

Modelling the Dynamics of an Arc-shaped Kite for Control Law Design

*Design of a Rigid Body Model for Real-Time Simulation using
a Multi-Body Reference*

S.G.C. de Groot, BSc.

May 6, 2010

Modelling the Dynamics of an Arc-shaped Kite for Control Law Design

**Design of a Rigid Body Model for Real-Time Simulation using a
Multi-Body Reference**

MASTER OF SCIENCE THESIS

For obtaining the degree of Master of Science in Aerospace
Engineering at Delft University of Technology

S.G.C. de Groot, BSc.

May 6, 2010



Delft University of Technology

Copyright © S.G.C. de Groot, BSc.
All rights reserved.

DELFT UNIVERSITY OF TECHNOLOGY
DEPARTMENT OF
AEROSPACE FOR SUSTAINABLE ENGINEERING AND TECHNOLOGY

The undersigned hereby certify that they have read and recommend to the Faculty of Aerospace Engineering for acceptance a thesis entitled “**Modelling the Dynamics of an Arc-shaped Kite for Control Law Design**” by **S.G.C. de Groot, BSc.** in partial fulfillment of the requirements for the degree of **Master of Science**.

Dated: May 6, 2010

Readers:

Prof. Dr. W.J. Ockels

Dr. Ir. A.L. Schwab

Dr.-Ing. R. Schmehl

Ir. J. Breukels

Summary

The need and interest for sustainable energy solutions is rising. A new branch in this field is high altitude wind power (HAWP). One novel concept is the Laddermill under development at the ASSET institute (TU Delft). The Laddermill uses kites to reel a tether from a drum which drives a generator. One of the key factors for success is the ability to control kites automatically. Currently successful tests have been conducted with leading edge inflatable or arc-shaped kites. Arc-shaped kites are extensively used and developed in the field of kite surfing. Due to their high traction and control capabilities arc-shaped kites are the choice for the Laddermill prototypes.

A literature review is conducted to obtain an overview of the current status of technology regarding arc-shaped kite modelling and control. For automatic control of kites several advanced control techniques exist like model predictive control and nonlinear dynamic inversion. Different kite models exist with specific applications. An example is the complex Multi-Body Kite model designed in MSC. ADAMS. It is concluded that fast models are required for online implementation.

A formal methodology is developed to reduce the Multi-Body Arc-shaped Kite model to a Rigid Body Arc-shaped Kite model. In more general terms: any flying object modelled with multi-bodies can be reduced to a set of rigid body states.

The numerous states of the Multi-Body model designed in ADAMS are reduced to a set of states describing the motion as a rigid body. For every body, flexible and rigid, holds that the inertial linear and rotational acceleration follow Newton's second law: the sum of external forces is equal to the time derivative of the linear momentum and the sum of external moments is equal to the time derivative of the angular momentum. On this principle the state reduction is applied and verified for the Multi-Body model. The acceleration, velocity and displacement components are obtained on the basis of conservation of linear momentum. The inertia tensor and angular momentum are derived with a particle based method. It is proven that the particle based method makes up a very good approximation to derive the rotational quantities.

The Rigid Body model is developed to describe the dynamic motion of an arc-shaped kite. It is attempted to reduce the aerodynamics and structural deformation of the Multi-Body Kite model to a parametric aerodynamic model and a quasi-static structural model. To accomplish the reduction of the Multi-Body Kite model to a Rigid Body Kite model it is required that the aerodynamics and the structural properties can be formulated by a set of rigid body states. The rigid body states are defined by the state reduction process. Due to the tight interaction between the flight condition and kite shape the aerodynamic model and structural model are variant with the flight condition.

The aerodynamic model is formulated on the basis of Taylor expansions and written in dimensionless form. This results in a linear decomposition of the dependency of each state. The effective

contribution of each aerodynamic state is given by respective dimensionless aerodynamic derivatives. The aerodynamic derivatives are obtained with the parameter identification technique. Flight test simulations are performed to identify the aerodynamic model.

The structural model is constituted on a quasi-static basis by formulating functions describing the initial conditions of the flight test simulations. Functions are formulated for the inertia tensor properties, mean wing chord, wing span, projected surface area and the tether attachment points.

Test simulations are performed to validate the Rigid Body model with respect to the Multi-Body model. The validation proves that the proposed methodology for model reduction is a qualitative manner for model reduction of the Multi-Body Kite model and for multi-body model reduction of flying objects in general. It results in kite models almost ten times faster than real-time, whereas simulating the Multi-Body Kite model in ADAMS takes more than ten times real-time. The development of an arc-shaped kite model which is appropriate for controller design has come to a detailed level. Control techniques which require fast and accurate models like model predictive control and nonlinear dynamic inversion can be designed on the basis of this modelling approach. For future work it is recommended to investigate on advanced model identification techniques and to perform a structural modal analysis.

Acknowledgements

The accomplishment of the master thesis is an exciting, hard work, but above all, a very educational experience. It forms the final assignment for obtaining the Master's Degree in Aerospace Engineering at the Delft University of Technology. It is a pleasure and an honor to express my gratitude to all individuals who have assisted me during this project.

I would like to thank Prof. Dr. Wubbo J. Ockels for his remarks and useful advice. Furthermore I would like to thank my first supervisor Jeroen Breukels for his inspiring ideas, professional guidance and close involvement. I am sincerely grateful to my other supervisors Roland Schmehl and Arend Schwab.

Other persons have made great contributions to bring this thesis to a qualitative end. I would like to thank Chris Verheul for his teaching and support of the multi-body application software MSC. ADAMS. I would like to thank Barend Lubbers for his guidance and critical remarks on model identification.

Grateful thanks goes to the Laddermill group within ASSET. I want to show my appreciation to Nana Saaneh, Aart de Wachter, Rolf van der Vlugt, Edwin Terink, John van den Heuvel, Roland Verheul, Lyssandre Rammos, Jorn Baayen and Thomas Frenkel.

Last but not least I want to thank my family, friends and my parents in special for their loving encouragement and support.

Nomenclature

Latin Symbols

a_k	identifiable parameter	[-]
b	wing span	m
c	damping constant	N·s/m
\bar{c}	mean wing chord	m
c_m	dimensionless airfoil moment coefficient about local Y -axis	[-]
c_x	dimensionless airfoil force coefficient along local X -axis	[-]
c_z	dimensionless airfoil force coefficient along local Z -axis	[-]
d_{ta}	control variable along kite tip from LE to TE	m
e	vector of residuals	[-]
e_t	tether unit vector	[-]
g_G	gravitational acceleration constant, 9.80665 m/s ²	m/s ²
k	spring constant	N/m
l_t	tether length	m
m	mass	kg
m_c	mass control unit	kg
p	roll rate in body-fixed reference frame	rad/s
q	pitch rate in body-fixed reference frame	rad/s
r	yaw rate in body-fixed reference frame	rad/s
r_t	radius of tether cross section	m
r_{ta}	position of the tether attachment point w.r.t. cg in body axes	m
t	time	s
u	velocity in X_b -direction	m/s
v	velocity in Y_b -direction	m/s
w	velocity in Z_b -direction	m/s
x_k	observation variable	[-]

$x_{taL/R}$	control variable or tether attachment point along X_b -axis	m
y	dependent variable	[-]
$y_{taL/R}$	control variable or tether attachment point along Y_b -axis	m
$z_{taL/R}$	control variable or tether attachment point along Z_b -axis	m
A	inertial acceleration	m/s ²
B	inertial angular momentum	N·m·s
C_L	lift coefficient	[-]
C_l	dimensionless moment coefficient about X_b -axis	[-]
C_m	dimensionless moment coefficient about Y_b -axis	[-]
C_n	dimensionless moment coefficient about Z_b -axis	[-]
C_X	dimensionless force coefficient along X_b -axis	[-]
C_{x_y}	dimensionless aerodynamic or stability derivative of force or moment ' x ' w.r.t. variable ' y '	[-]
C_Y	dimensionless force coefficient along Y_b -axis	[-]
C_Z	dimensionless force coefficient along Z_b -axis	[-]
D	resultant aerodynamic drag force	N
D_c	dimensionless time	[-]
E_t	Tether elasticity modulus	N/m ²
F	operational mode function	
F	tether force along X_b -axis	N
F_a	aerodynamic (air-path) reference frame	
F_b	body-fixed reference frame	
F_{CD}	control force Centroid Dummy	N
F_E	normal earth-fixed reference frame	
F_{ext}	sum of external forces	N
F_k	kinematic (flight-path) reference frame	
F_O	vehicle carried normal earth reference frame	
F_r	vehicle reference frame	
F_t	tether-fixed reference frame	
G	tether force along Y_b -axis	N
H	tether force along Z_b -axis	N
\mathbb{I}	mass matrix of inertia	kg·m ²
I_x	mass moments of inertia about respective ' x '-axis	kg·m ²
J_{xy}	mass products of inertia relative to ' x ' and ' y ' axes	kg·m ²
K_x	non-dimensional radius of gyration about respective ' x '-axis	[-]
K_{xy}	non-dimensional product of inertia relative to ' x ' and ' y ' axes	[-]
L	aerodynamic moment about X_b -axis	N·m
L	resultant aerodynamic lift force	N
M	Mach number	[-]
M	aerodynamic moment about Y_b -axis	N·m
\mathcal{M}_{bridle}	resultant bridle moment	N·m
\mathcal{M}_{ext}	sum of external moments	N·m
\mathcal{N}	normal distributed	
N	aerodynamic moment about Z_b -axis	N·m

O	origin of reference frame	
P	mechanical power	N·m/s
P	tether moment about X_b -axis	N·m
Q	tether moment about Y_b -axis	N·m
R	resultant aerodynamic force	N
R	tether moment about Z_b -axis	N·m
Re	Reynolds Number	[-]
S	projected surface area	m ²
T	reference frame transformation matrix	
T_t	resultant tether force	N
U	input vector	[-]
V_a	aerodynamic velocity	m/s
V_C	crosswind velocity	m/s
V_k	kinematic velocity	m/s
V_L	tether reel out speed	m/s
V_W	wind speed	m/s
V_∞	undisturbed wind velocity	m/s
W	weight	N
W_x	wind velocity in X_E direction	m/s
W_y	wind velocity in Y_E direction	m/s
W_z	wind velocity in Z_E direction	m/s
X	aerodynamic force along X_b -axis	N
X	observation matrix of observation variables	[-]
X	state vector	[-]
X_x	x -axis of respective ' x '-reference frame	
Y	output vector	[-]
Y	vector with dependent variables y	[-]
Y	aerodynamic force along Y_b -axis	N
Y_x	y -axis of respective ' x '-reference frame	
Z	aerodynamic force along Z_b -axis	N
Z_x	z -axis of respective ' x '-reference frame	

Greek Symbols

α	aerodynamic angle of attack	rad
α_0	angle of attack at $t = 0$ s	rad
α_0	angle of attack at zero lift	rad
β	aerodynamic side slip angle	rad
γ_a	aerodynamic pitch angle	rad
γ_k	kinematic pitch angle	rad
δ	angle of control input	rad
δ	tether elongation	m
ε	error variable	

ζ	body deformation parameter	
λ	eigenvalue	[-]
θ	body pitch angle w.r.t. earth	rad
θ_t	tether zenith angle	rad
κ	body pitch angle w.r.t. tether	rad
κ_a	aeroelastic deflection angle	rad
μ_c	dimensionless mass	[-]
μ_a	aerodynamic roll angle	rad
μ_k	kinematic roll angle	rad
ξ	body yaw angle w.r.t. tether	rad
ρ	air density	kg/m ³
σ_{a_k}	standard deviation of parameter a_k	
τ	body roll angle w.r.t. tether	rad
ϕ	body roll angle w.r.t. earth	rad
χ_a	aerodynamic yaw angle	rad
χ_k	kinematic yaw angle	rad
ψ	body yaw angle w.r.t. earth	rad
ψ_t	tether azimuth angle	rad
Ω	angular velocity	rad/s

Subscripts

Subscripts define normally the kind of the respective parameter, for example the small letter a in V_a defines that it is the *aerodynamic* velocity. Or it defines the point or object it refers to, for example cg in \mathbf{B}_{cg}^E defines that it is the inertial angular momentum about the *center of gravity*.

Superscripts

Superscripts define normally the kind of reference frame the parameter is expressed in, for example b in \dot{x}_t^b defines that it is the tether velocity component in X -direction, \dot{x}_t , expressed in the *body-fixed reference frame*.

Abbreviations

μAV	Micro Aerial Vehicle
2D	Two Dimensional
3D	Three Dimensional
ac	Aerodynamic center
ADAMS	Automatic Dynamic Analysis of Mechanical Systems
am	ADAMS function measure

ASSET	Aerospace for Sustainable Engineering and Technology
as	ADAMS state variable
CD	Centroid Dummy
CFD	Computational Fluid Dynamics
cg	Center of Gravity
DOF	Degree of freedom
DUT	Delft University of Technology
EKF	Extended Kalman filter
ER	Evolutionary Robotics
FEM	Finite Element Method
FSI	Fluid Structure Interaction
GF	ADAMS General Force
GPS	Global Positioning System
GSE	ADAMS General State Equation
GUI	Graphical User Interface
GUM	General Use Macros
GWEC	Global Wind Energy Council
HAWP	High Altitude Wind Power
HPV	Human Powered Vehicle
KPT	Kiteplane Toolbox
L/D	Lift over drag ratio
LE	Leading edge
LQR	Linear Quadratic Regulator
LTA	Light Transport Aircraft
LTI	Linear Time Invariant
mac	Mean Aerodynamic Chord
MPC	Model Predictive Control
NMPC	Nonlinear Model Predictive Control
pb	Particle based
PID	Proportional, Integral, Derivative
rp	Arbitrary reference point
ta	Tether attachment point
TE	Trailing edge
TKC	Toolkit Creator
UAV	Unmanned Aerial Vehicle
UDE	User Defined Entity
UKF	Unscented Kalman filter
WWEA	World Wind Energy Association

Contents

Summary	v
Acknowledgements	vii
Nomenclature	ix
1 Introduction	1
I Literature Review	3
2 The Laddermill, Kites & Modelling	5
2-1 The Laddermill	5
2-2 Arc-shaped kites	6
2-3 Kite system modelling	7
2-4 Kite control	18
2-5 Crosswind power	20
2-6 Other considerations	23
2-7 Conclusions	26
3 ADAMS and Multi-Body Kite Model Overview	29
3-1 A short introduction to ADAMS	29
3-2 The Kite Simulation Toolbox	30
3-3 Aerodynamic model	32
3-4 Structural model	34
4 Thesis Goal & Approach	37
4-1 Goal	37
4-2 Requirements	37
4-3 Approach	38

II Kite Modelling	39
5 Definitions, Reference Frames and Wind Kinematics	41
5-1 Reference frames	41
5-2 Transformation between reference frames and angular velocity vectors	44
5-3 The tether position and velocity in spherical coordinates	50
5-4 Wind kinematics	51
6 Rigid Body Kite Model	55
6-1 Derivation of the equations of motion	55
6-2 External forces and moments	56
6-3 Complete set of equations	62
6-4 Simulink Implementation	69
7 Linearized Kite Model Equations	73
7-1 Linearization about arbitrary flight condition	74
7-2 Linearized equations of motion no initial velocity	79
8 Verification of Rigid Body Kite model	95
8-1 Aircraft simulation	95
8-2 Citation-Kite simulation	101
8-3 Conclusions	107
9 Multi-Body Kite Model	109
9-1 Model description	109
9-2 GUM files	117
9-3 Transformation of measures to body-fixed reference	125
9-4 Verification of created measures	128
10 Aerodynamic & Structural Model Identification	141
10-1 Theory of parameter identification	141
10-2 Aerodynamic model	143
10-3 Inertia tensor & structural properties	153
11 Validation Rigid Body Kite Model	157
12 Conclusions & Recommendations	161
References	165
A Additional Information Multi-Body Kite Model	169
B Examples of flight test simulations	173
C Aerodynamic derivatives	179
C-1 Derivatives of the symmetric forces and moment	180
C-2 Derivatives of the asymmetric force and moments	184

D Moments and product of inertia and structural properties	189
E Response curves aircraft and Citation-Kite simulations	193
E-1 Aircraft	193
E-2 Citation-Kite	200

Chapter 1

Introduction

Kites have been around for many years and their fun factor is well known. The application of kites to use them as a serious traction or pulling device is coming more and more under attention. With the invention of the aircraft in the beginning of the 20th century, the research on kites has moved to the background. To date, many research groups and companies have gained interest in kites again to use them for pulling ships to reduce the fuel consumption or to extract wind energy from higher altitudes. The latter is called high altitude wind power HAWP. Terink, reference [30], made a summary about the history of kites. O’Gairbhith, reference [27], gives an overview of kite research groups and companies and the current status of technology.

The conventional wind energy market has been growing with an average rate of about 30% the last 10 years. All wind turbines installed by the end of 2008 worldwide are generating 260 TWh per year, equalling only 1,5% of the global electricity consumption. In the World Wind Energy report of 2008 of the World Wind Energy Association (WWEA), USA has taking over the top of the list from Germany with an installed capacity of 25.2 TW, whereas The Netherlands are ranked 12th with an installed power of 2225 MW. It is predicted by the WWEA that the installed capacity will be 152 TW by the end of the year 2009. Based on accelerated development and further improved policies, a global capacity of more than 1,500 TW is possible by the year 2020. Reference [40].

Basically the whole wind energy market makes use of horizontal axis wind turbines for the extraction of wind energy. They are positioned relatively close to the ground, but the potential to extract wind energy from higher altitudes is much larger. This is due to the fact that the wind velocity increases with altitude and the wind power increases with increasing wind speed to the third power. One of the reasons the wind speed is lower close to the surface is due to the earth’s boundary layer effect. Therefore the potential of extracting wind energy at higher altitudes is obvious and is one of the reasons why research to extracting wind energy from higher altitudes is exciting and interesting.

The Laddermill is a novel concept to extract wind energy from higher altitudes (reference [25]). The basic system uses one kite to pull a tether form a drum which drives a generator producing electricity. Currently successful tests have been performed with a 20 kW system at the TU Delft at ASSET. This system is controlled manually to fly the kite crosswind. Crosswind enhances the tether force on the same principle a wind turbine rotates the blades in crosswind direction. To automate the control of the kite and to let the kite fly a well-predefined path an automatic control system is required.

The first part of the thesis forms the literature review and is focused on the current status of technology with respect to kite modelling and control law design. Chapter 2 describes the definition

of the kite system, kite models and modelling approaches, control law design techniques and several general aspects with respect to the Laddermill and kites. In the last section the central thesis question is formulated. Chapter 2 is succeeded by a description of a multi-body model designed in the multi-body dynamics application MSC. ADAMS. An introduction to ADAMS, the kite simulation toolbox as well as the multi-body arc-shaped kite model is given. The first part concludes by formulating the modelling approach.

In the second part the modelling approach and results are discussed in detail. Chapter 5 defines reference frames, transformation matrices and kinematic relations with respect to a rigid body, a straight tether and the wind velocity and acceleration. Chapter 6 describes the system equations and modelling aspects of the new kite model based on a rigid body with a straight tether. Linear time invariant models of a kite system are derived in chapter 7. The verification of the Rigid Body model is conducted in chapter 8. Chapter 9 describes the state reduction methodology to reduce the numerous states of the Multi-Body model to a set of rigid body states. The rigid body states comprise the inertia tensor, angular momentum, translation and orientation quantities, aerodynamic forces and moments. In chapter 10 flight test simulations are performed to identify the aerodynamic models as a function of aerodynamic variables constructed from the rigid body states. The validation of the model reduction is shown in chapter 11. Chapter 12 presents the conclusions and recommendations.

Part I

Literature Review

The Laddermill, Kites & Modelling

The literature review commences with a formal overview of the current status of technology with respect to kite modelling and controller design. First the Laddermill concept is explained followed by the definition of a kite system.

2-1 The Laddermill

One novel concept of extracting wind energy from higher altitudes is the Laddermill. The Laddermill is an idea by prof. dr. W.J. Ockels [25]. In the 90's initial calculations were done to study the feasibility of power production and costs. Around 2005 real research started on the Laddermill concept, followed by publishing the first academic papers in 2006 [16]. In 2007 the first Laddermill prototype was successfully tested [14]. By the end of 2010 a successful demonstration is to be expected with a power capacity of 20 kW.

Already in 1980 Loyd, reference [19], investigated the potential of kite power. He proved that flying kites crosswind would be far more efficient than flying a kite up and down. Even more he showed that extracting wind energy by kites have far more potential than using conventional wind turbines. Furthermore a kite system does not need a tower with a hub and turbine blades, and is supposed to use less and cheaper materials than conventional wind turbines. This fact suggests that the Laddermill can be more cost effective than the wind energy extraction systems in operation today.

The Laddermill, figure 2-1, extracts wind energy by flying kites pulling a tether from a drum. While pulling the kites are in ascending phase and produce high lift. In descending the phase the kites produce less lift in order to be able to reel-in the tether. The difference in lift between the ascending and descending phase will result in a net power production. After the kites have descent to a certain altitude the cycle repeats again.

As explained by Loyd, section 2-5, flying a kite in crosswind motion will increase the efficiency drastically. Other research found out that flying figure of eights would be realistic and efficient in order to achieve crosswind motion (references [39] and [9]). Based on this the ability to control a kite flying an optimal path is evident.

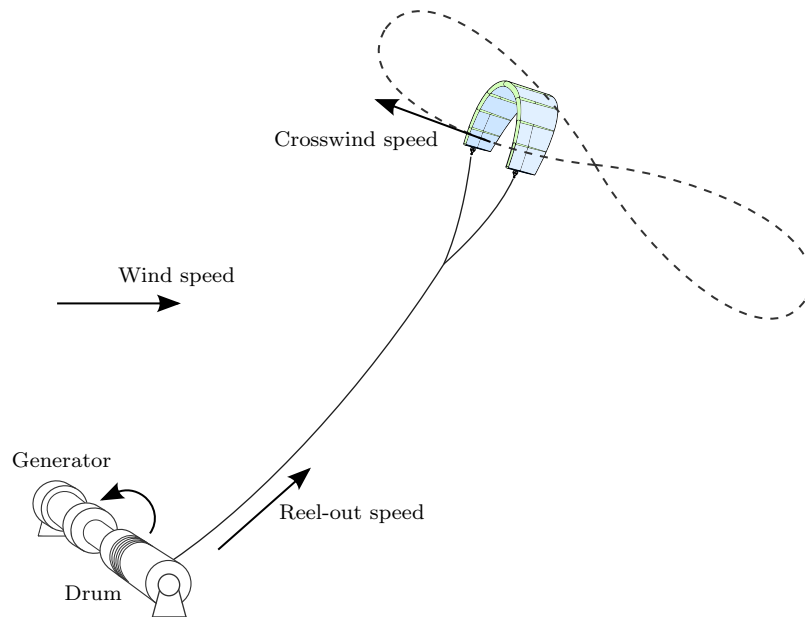


Figure 2-1: Laddermill concept with kite flying figure of eight

2-2 Arc-shaped kites

All kind of kites exist for many different purposes. The most valuable kites for use with the Laddermill are the kites which have a high pulling force and are relatively easy to control. The kites that have these properties are found in the world of kite surfing. Some athletes are able to perform jumps of over 25 m above the water, which illustrates the potential of these kites as a traction device. These modern kites are arc-shaped and supported by an inflatable structure. Therefore also called leading edge inflatable or LEI Kite.

Figure 2-2 shows a leading edge supported 25 m² LEI Kite. A LEI Kite consists of three basic elements: a leading edge (LE) tube, strut tubes and a canopy. The LE and strut tubes give structural stiffness and additionally the LE tube defines the shape of the nose of the wing. The canopy completes the wing and is responsible for the wing loading.

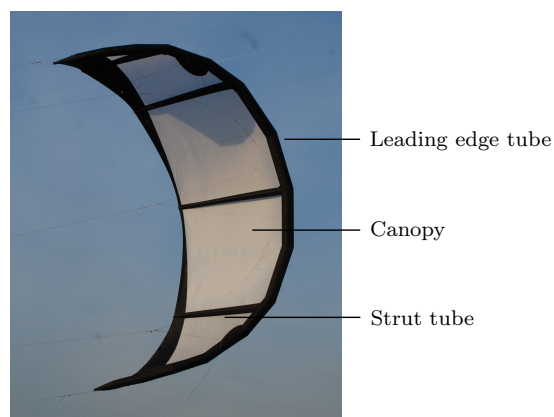


Figure 2-2: Leading edge supported 25 m² LEI Kite

2-3 Kite system modelling

In this thesis a kite system is defined by the following components (see figure 2-3):

- A lifting surface
- A tether with bridle lines
- A control mechanism
- A ground station

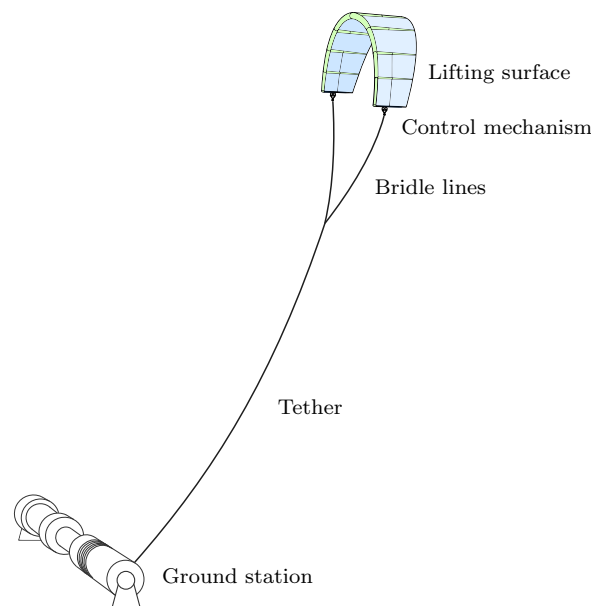


Figure 2-3: Definition of Kite System

In literature several theories and ideas are proposed and studied for modelling the different components of a kite system. This thesis will not go into detail about the dynamics of the ground station, but assumes that it can give a predefined force on the tether or reeling velocity. An overview of the current status of technology for modelling the other components is given in subsequent sections.

As is already discussed an arc-shaped kite is used for testing the Laddermill concept, it must be noted that it is not unlikely that other kite shapes are used in future prototypes. One of the possibilities that has to be brought under attention is the 'Kiteplane'. The 'Kiteplane' is a conceptual name for an inflatable kite, which can ascend like a kite and descend like an airplane. The flight dynamics of the 'Kiteplane'-concept are thoroughly discussed in Reference [30].

2-3-1 Arc-shaped kite models

This section discusses the possibilities for modelling a lifting surface in the form of an arc-shaped traction kite. They can be categorized by *point mass models*, *rigid body models*, and *high fidelity models*. Point mass models only have mass and no inertia properties. Rigid body models have inertia properties, but are in general invariable. High-fidelity models have multiple point masses or bodies, which are connected by joints and strings.

Point mass model

The most simple way to model a kite is using a point mass with a lift and drag force acting at a point mass placed at the center of gravity. The model neglects the attitude dynamics and flexible modes completely. Therefore Williams states, reference [39], that this model is not appropriate for high fidelity simulation and extremely limited for control law design. But it could be used for preliminary analysis of flight trajectories and rough performance analysis of kite systems. The motion control is modelled by manipulating the angle of attack and roll angle thereby changing the orientation of the lift and drag vector.

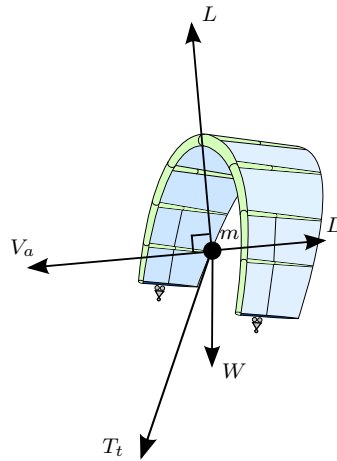


Figure 2-4: Point mass kite model, Ref. [39]

Figure 2-4 shows the concept of the point mass kite model with the aerodynamic velocity V_a , lift L , drag D , resulting tether force T_t and weight of the point mass W . The lift force is always defined perpendicular to the aerodynamic velocity vector. The last degree of freedom of the lift vector is defined by the roll angle of the kite. The roll angle of the kite is treated as a pseudocontrol. The roll angle is a pseudocontrol because there is no actual control mechanism model.

It must be noted that V_a is defined as the *aerodynamic velocity* of the kite, which is the velocity of the kite with respect to the air. This is a usual convention when discussing dynamical systems instead of the term *apparent wind speed* which is defined as the velocity of the air with respect to the object as found in literature about aerodynamics. Both are equal in magnitude, but opposite in direction.

Rigid body models

The next step in modelling a kite is using a rigid body model. Aircraft can be regarded to a great extent as a rigid body and are therefore mostly modelled by rigid body models. Evidently, by modelling a kite as a rigid body aircraft models can be used as a reference. As aircraft models have been developed for a long time profit can be made from this knowledge.

Figure 2-5 shows illustrative the principle of a rigid body model, where compared to the point mass model mass moments and products of inertia \mathbb{I} and a resulting aerodynamic moment M_a have been added. A rigid body has six degrees of freedom resulting in a set of six equations of motion, three for translation and three for rotation.

A 9-DOF model by Houska Houska, reference [12], proposes essentially a mixture of a point mass model and a rigid body model by taking only the tether inertia properties into account.

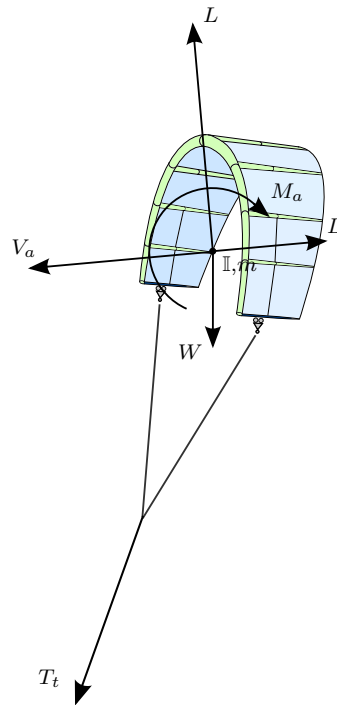


Figure 2-5: Rigid body kite model

According to Houska this can be allowed, because the main contribution to the mass comes from the tethers and partially from the control mechanism. So the equations of motion are derived on the basis that the kite inertia is much smaller than the combined tether and equivalent inertia of the kite as a point mass (mL^2 effect).

The model uses effective aerodynamic coefficients, which can be obtained by integrating over the aerodynamic properties of all kite pieces. These coefficients are actually *aerodynamic derivatives* as are often used for aerodynamic aircraft models (reference [24] and [23]).

Additionally, deformations can be superimposed by introducing the bending of the arc shape as an additional state. For example the typical *jellyfish* oscillations of an arc-shaped traction kite can be introduced by a second order differential equation. The jellyfish motion is characterized by the motion of the kite tips moving periodically towards and away from each other.

Altogether, the three DOFs of the body, the three DOFs of the tether model, the two DOFs from the control mechanism and one DOF for the jellyfish motion results in a 9-DOF kite system model.

A 6-DOF model by Williams Williams, reference [39], describes an approach for a rigid body model. Compared to Houska's model the description only focuses on the body with incorporation of the inertia properties resulting in six degrees of freedom.

The influence of arc-shape of the kite on the aerodynamics is included by using an aerodynamic analysis with the aid of the Tornado vortex-lattice method, reference [21]. With this software a fast initial guess can be made of the aerodynamic properties including aerodynamic derivatives of any rigid body consisting of $2D$ -airfoil shapes. The resulting aerodynamic derivatives are used to describe the aerodynamic forces and moment functions.

The limitations of the point mass and rigid body model become apparent by realizing that a surf kite does not produce the directional changes entirely through a roll, pitch or yaw manoeuvre but instead the kite is also structurally deformed. The deformations induce additional changes to the direction of forces and moments as well as changing inertia properties.

Aerodynamic models based on aerodynamic derivatives Both Houska and Williams use aerodynamic derivatives to describe the aerodynamic forces. Therefore a short introduction is given here to specify the principle. The approach results in functions which can be evaluated very fast for dynamic computations and is therefore widely used for modelling the dynamics of aircraft. The model structure shown by equations (2-1) are frequently used in aircraft literature.

The derivation of the functions is for example explained in Reference [24]. The derivation starts by defining the aerodynamic states which the aerodynamic forces and moments depend on. This is based on experience. The aerodynamic forces and moments are dependent on the entire history of the states. To decrease the complexity Taylor expansions are made. It appears, at least for aircraft, that most higher order terms have a negligible effect. The complete expression is made dimensionless by dividing by the dynamic pressure times geometric properties. This results in the dimensionless aerodynamic derivatives as show in equations (2-1) given by C_{x_y} where ‘ x ’ is the force or moment and ‘ y ’ the aerodynamic state. More details and an initial analysis for kites are given in chapter 6.

Equations (2-1) apply to nonlinear aerodynamic models in which the aerodynamic force and moment derivatives are variant and dependent on the dimensionless aerodynamic states by themselves (Reference [7]). The forces and moments are expressed in the body-fixed reference frame and are given by the dimensionless variables C_X , C_Y , C_Z , C_l , C_m and C_n respectively. The nonlinear equations for aircraft are usually given by equations (2-1) where it is assumed that the symmetric states have no influence on the asymmetric forces and moments and vice versa:

$$\begin{aligned}
C_X &= C_{X_0} + C_{X_\alpha} \cdot \alpha + C_{X_{\dot{\alpha}}} \cdot \frac{\dot{\alpha}\bar{c}}{V_a} + C_{X_q} \cdot \frac{q\bar{c}}{V_a} + C_{X_\delta} \cdot \delta_c \\
C_Y &= C_{Y_0} + C_{Y_\beta} \cdot \beta + C_{Y_{\dot{\beta}}} \cdot \frac{\dot{\beta}b}{V_a} + C_{Y_p} \cdot \frac{pb}{2V_a} + C_{Y_r} \cdot \frac{rb}{2V_a} + C_{Y_\delta} \cdot \delta_c \\
C_Z &= C_{Z_0} + C_{Z_\alpha} \cdot \alpha + C_{Z_{\dot{\alpha}}} \cdot \frac{\dot{\alpha}\bar{c}}{V_a} + C_{Z_q} \cdot \frac{q\bar{c}}{V_a} + C_{Z_\delta} \cdot \delta_c \\
C_l &= C_{l_0} + C_{l_\beta} \cdot \beta + C_{l_{\dot{\beta}}} \cdot \frac{\dot{\beta}b}{V_a} + C_{l_p} \cdot \frac{pb}{2V_a} + C_{l_r} \cdot \frac{rb}{2V_a} + C_{l_\delta} \cdot \delta_c \\
C_m &= C_{m_0} + C_{m_\alpha} \cdot \alpha + C_{m_{\dot{\alpha}}} \cdot \frac{\dot{\alpha}\bar{c}}{V_a} + C_{m_q} \cdot \frac{q\bar{c}}{V_a} + C_{m_\delta} \cdot \delta_c \\
C_n &= C_{n_0} + C_{n_\beta} \cdot \beta + C_{n_{\dot{\beta}}} \cdot \frac{\dot{\beta}b}{V_a} + C_{n_p} \cdot \frac{pb}{2V_a} + C_{n_r} \cdot \frac{rb}{2V_a} + C_{n_\delta} \cdot \delta_c
\end{aligned} \tag{2-1}$$

where the forces and moments are a function of the attitude variables angle of attack α , side slip angle β , body rotational rates p , q and r and some control input parameter δ_c .

Usually the following is assumed for C_{X_0} and C_{Z_0} :

$$\begin{aligned}
C_{X_0} &= -C_{D_0} \\
C_{Z_0} &= -C_{L_\alpha} \cdot \alpha_0
\end{aligned}$$

where α_0 is the angle of attack at zero lift and where C_{D_0} is the drag at zero angle of attack from the general drag formula:

$$C_D = C_{D_0} + \frac{(C_{L_\alpha}\alpha)^2}{\pi A e} \tag{2-2}$$

Because inflatable arc-shaped kites are flexible it is likely that these equations are not valid for kites. It is possible that additional states or coupled terms need to be included.

High fidelity models

A way to incorporate structural deformation to a higher extend is to use high fidelity models. Examples exist in the form of models based on multiple plates, lumped parameters with point masses, multi-body and/or combined with fluid structure interaction.

Multi-plate model The third model described in reference [39] by Williams is the multi-plate flexible model. More details are given in reference [34].

The multi-plate model tries to model some of the fundamental behaviour of real kites, which rigid body kite models neglect. This is the continuous deformation of a kite to control inputs. The consequence of the deformation is that the angle of attack and sideslip angle are difficult to define and the center of gravity is not fixed.

The multi-plate model proposes to incorporate the deformations of the kite's structure in a crude way. The kite is divided into a series of flat plates spherically joined at the leading edge as shown in figure 2-6.

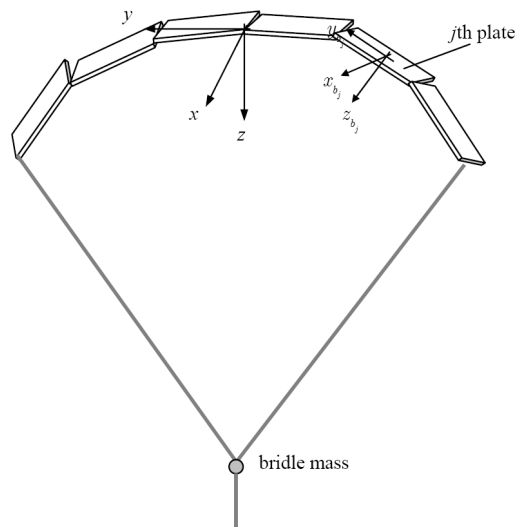


Figure 2-6: Multi-plate kite model, Ref. [39]

One degree of freedom of the spherical joints is removed in the form of a constraint such that the yaw angle of each plate with respect to the other plates is constant. The shape of the kite is approximated by allowing the pitch and roll angles of each plate to be different. Steering is accomplished by movable attachment points on the side of the kite. The equations of motion are based on the method of Lagrange.

According to Williams [34] a disadvantage of this mathematical model is that it can be difficult to establish an equilibrium configuration. A correct balance has to be found for a certain flight condition between the lift and drag forces, gravity, tether tension and aerodynamic moment. Furthermore the equations of motion are highly nonlinear and complicated making it hard to find analytic solutions in general. Numerical solution techniques are used and symmetry is enforced to find equilibrium positions. However, still a various combinations of attachment point positions were found to give different equilibrium positions. To solve this problem an initial condition of the attachment point must be chosen.

On one hand, this kite model consists of multiple bodies and therefore is able to incorporate the deformation effects, it is likely that, on the other hand, it is limited in its validity due to the fact that it only consists of plates. And to be able to get a resemblance of kite behaviour the relations for the moments acting at the joints have to be tuned on a trial and error basis.

Lumped parameter model Another option to simulate the kite's flexible structure due to a steering input is a lumped parameter model in the form of discretization of the kite into a series of point masses connected by viscoelastic springs.

This method used by Furey, reference [10] and [11], can also be called a particle based simulation. The motivation for using this model is to provide a framework which allows explicit consideration of variation in the kite configuration in terms of kite shape, bridle setup and physical properties such as relative rigidity and mass of the kite components.

The model consists of repeated rows of equidistant particles in a semicircular arc as shown in figure 2-7, which illustrates the default setup of two rows of 5 particles.

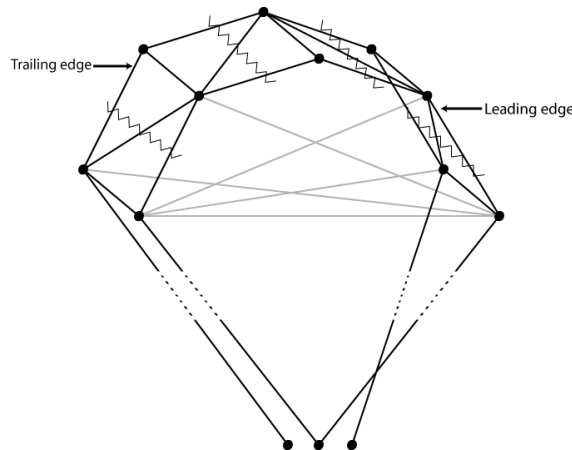


Figure 2-7: Lumped Parameter based kite model, Ref. [10]

The light grey constraints reinforce the arc shape of the kite to simulate the jellyfish type flapping motion and so effectively performing the same role as the inflatable ribs that maintain the shape of LEI kites. The zigzag lines indicate the positions at which the canopy is sliced for aerodynamic calculations. The lift and drag coefficients of each slice are calculated depending on the local angle of attack. The resulting aerodynamic forces are then distributed and act at particle positions.

Multi-body dynamics model A multi-body dynamics model uses building blocks like rigid bodies, joints and strings. Degrees of freedom can be constrained by joints. Nonlinear relations can be imposed on the joints and strings to model the complex load-deflection interaction.

Breukels, reference [2], constructed a kite model using the multi-body dynamics simulation program MSC. ADAMS. Additionally, a *Kite Simulation Toolbox* is developed to automatize the construction of kites and also tethers. Basically, any kind of kite, inflatable structure or tether can be constructed and simulated. For more details refer to chapter 3.

Fluid structure interaction To take into account the interaction between the air and structure fluid structure interaction FSI can be added to a multi-body model. The kite's surface is discretized into a mesh to apply finite element method FEM together with computational fluid dynamics CFD. In this way it is possible to simulate aeroelastic phenomena. The downside is that this method is heavily computation intensive as it requires iterative procedures to solve the equations at every time step. There has been no attempt yet to model a kite system using FSI.

2-3-2 Tether modelling

Performing accurate calculations on tethers is not straight forward. Taking full account for aerodynamic drag and dynamic behaviour requires complex nonlinear models. Most models discretize the tether in smaller elements.

Static models

Reference [41] describes a tether model where the change in tether tension along the tether is approximated by dividing the tether in small segments.

Figure 2-8 shows a tether with external forces acting on the tether ends, where T_k is the resultant kite force and T_0 the reaction force on the bottom end. The top end and bottom end forces are not equal, which is the result of a distributed aerodynamic drag force along the tether and a distributed force due to the tether mass. These distributed forces are also the cause for *tether sag*.

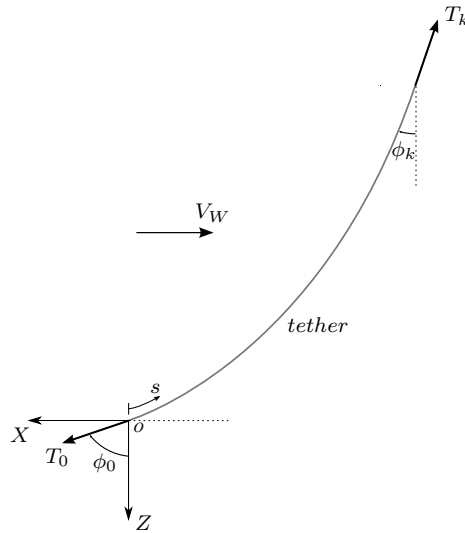


Figure 2-8: Tether with external forces and sag, Ref. [41]

Figure 2-9 shows a tether segment n with the tension forces T_n and T_{n-1} . The drag D and weight W forces for the segment are displayed along their tangential and perpendicular component. The resultant change in tension force between T_n and T_{n-1} is a result of the tangential and perpendicular components ΔF_p^n and ΔF_t^n , which are on their turn a result of a ΔD and ΔW acting on segment n .

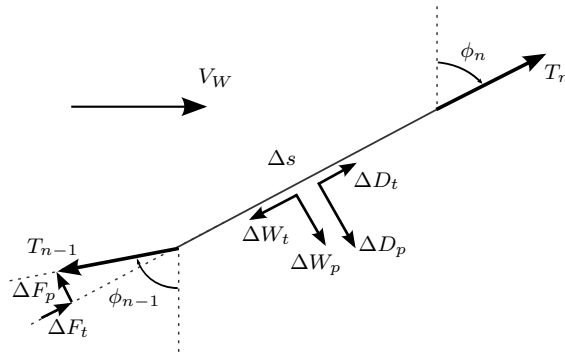


Figure 2-9: Free Body Diagram of a tether segment, Ref. [41]

The drag forces on tether segment n in perpendicular direction and tangential direction are defined

by:

$$\Delta D_p^n = C_{d_p} \frac{1}{2} \rho V_p^2 d_t \Delta s_n \quad (2-3)$$

$$\Delta D_t^n = C_{d_t} \frac{1}{2} \rho V_t^2 d_t \Delta s_n \quad (2-4)$$

where C_{d_p} and C_{d_t} are the perpendicular and tangential drag coefficient of the tether respectively, ρ the air density, V_p and V_t the apparent wind speed in perpendicular and tangential direction respectively, d_t the tether diameter and Δs_n the length of tether segment. The apparent wind speed is a combination of the wind speed V_W and the speed of tether segment relative to the ground.

And for the weight components can be written:

$$\Delta W_p^n = m_n \cdot g_G \cdot \sin \phi_n \quad (2-5)$$

$$\Delta W_t^n = m_n \cdot g_G \cdot \cos \phi_n \quad (2-6)$$

where m_n is the weight of the tether segment n , g_G the gravitational acceleration constant and ϕ_n the angle with the vertical of segment n . The equations have to be evaluated from the top end to the bottom end of the tether to determine the complete shape and total drag force.

In reality the wind speed and air density are a function of altitude. In reference [41] a linear relation is assumed for the wind speed as well as the air density. Figure 2-10 shows the average wind speed in The Netherlands as a function of altitude, where can be seen that a linear approximation is justifiable till 1 km altitude.

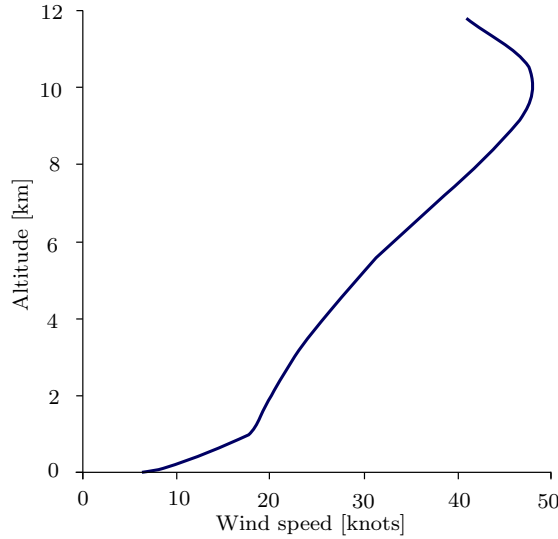


Figure 2-10: Average wind speed in The Netherlands as a function of altitude, Ref. [15]

Dynamic models

The equations (2-3) to (2-6) for the tether forces are on a static basis. One way of modelling the dynamic behaviour of a tether is using a spring-damper model. This can be accomplished by using a second order differential equation for the displacement of the tether along the tangential s-direction:

$$m_n \ddot{s}_n + c_t \dot{s}_n + k_t s_n = F_n \quad (2-7)$$

where m_n is the mass of the particular tether segment, c_t a linear damping coefficient for the velocity and k_t an elastic coefficient for the displacement.

An overview of existing tether models with increasing complexity is given below.

Straight line When tether sag is assumed small a straight line model can be regarded valid. One option is to constrain the kite to move on a sphere, another option is to model the tether force by the spring-damper equation (2-7) where variable spring and damper coefficients could be considered for a nonlinear behaviour.

Point masses with inelastic or elastic links In reference [36] the dynamic modelling of a tether kite system is depicted and develops a tether model based on the lumped mass approach. The tether is modeled by dividing it into a series of point masses connected by inelastic links. Figure 2-11 shows the concept of the flexible tether model with point masses and links. Reference [38] depicts that treating the tether as inelastic makes it more difficult to handle cases in which one or both end bodies are constrained by forces that are a function of the tether tension.

Therefore, elastic links can be used by using Hook's law with linear strain function for each element and the strain can vary along the tether length. Another advantage of elastic elements is that the equations of motion are decoupled. This means that the computation of the state derivatives for integration is very efficient. In such a case it is simpler to determine the tension forces using Hook's law.

But the major drawback with elastic links, according to Williams [38], particularly with high stiffness, is that small integration steps must be used in order to capture the high frequency vibrations. There is a large difference between the longitudinal modes and the tether string/pendulum modes. This can make elastic models problematic for control law design and trajectory optimization.

There are three different approaches which can generate the same physical model, but with different implications in terms of complexity and numerical cost. The first is to use Lagrange's equations or Kane's equations. The second approach is to derive the equations directly via Newton's second law in Cartesian coordinates. Constraint equations are added to the system and the dynamic and constraint equations have to be solved simultaneously.

Multi-body dynamics tether An application that utilizes the second approach, using Newton's second law directly, is the multi-body dynamics simulation program MSC. ADAMS. Breukels, reference [1], developed a toolbox to easily create multi-body tethers.

The model consists of a chain of discrete elements. The elements have mass and are infinitely stiff. The stiffness is justified within the scope of this model, because the strain for high-tension fibers like Dyneema¹ and Aramid is small. The elements are hinged together using hook joints allowing the elements to hinge in every direction, but are prevented from twisting. The frequency of twisting is much higher than bending, so leaving the twisting motion out results in faster simulations. Furthermore, the flight dynamics of the kite are almost independent of the twisting of the tether.

The damping of the tether can be split into two forms: aerodynamic damping and material-based damping. The aerodynamic damping is caused by the aerodynamic drag of the tether and the material-based damping is the dissipation of kinetic energy through heat caused by the tether fibers rubbing against each other. In the model the material-based damping is introduced by torsion dampers. The aerodynamic drag is given by equations (2-3) and (2-4) (for the 2D case).

¹used for the Laddermill

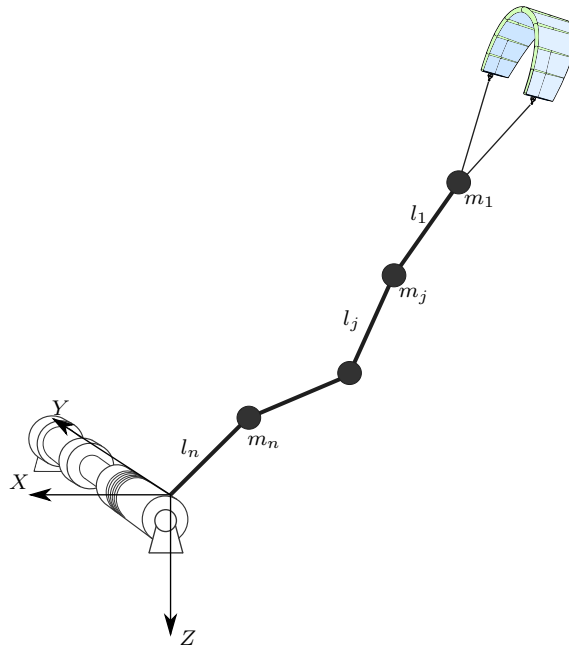


Figure 2-11: Flexible tether modelled as point masses and links, Ref. [36]

2-3-3 Control mechanism

To control the kite system which uses an arc-shape lifting surface two control mechanism are being researched at ASSET. The first option uses two carts on a rail like a rack and pinion system positioned at the tips of the kite to move the tether attachment points. The second system is a pod positioned at the bridle point of the tether and controls the kite with steering lines and two power lines for depower.

This thesis focuses on modelling the cart and rail control system. Figure 2-12 shows the 2009 version on the left and a schematic representation on the right. Figure 2-13 shows the control mechanism in operation during one of the Laddermill tests with a Foil Kite.

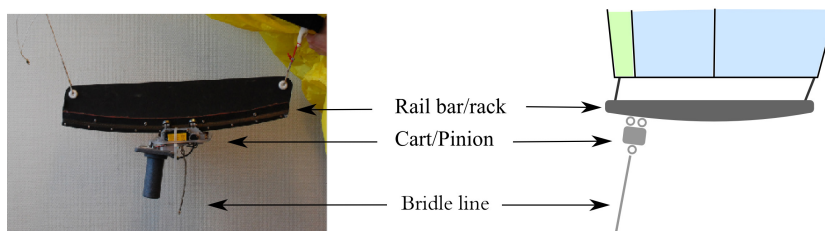


Figure 2-12: Cart and rail control mechanism to move the tether attachment points

The control mechanism regulates the pitch angle effectively changing the angle of attack by moving the tow points symmetrically. Moving the attachment points asymmetrically results in a dominant yaw rotation together with a roll motion allowing the kite to make turns. The system is operated by remote control.



Figure 2-13: Control mechanism in operation during Laddermill test with a Foil Kite

The specifications of the 2009 version are depicted as follows. The maximum pulling force along the rail is 80 N. For the system shown in figure 2-12, the weight of rack bar is 0.6 kg and the pinion carts weigh 0.99 kg each. The rail is curved to follow the changing angle of the line when the angle of attack changes.

The control mechanism works physically in the same way as the control of a surf kite by four lines. The four lines of a surf kite are connected to the four corners at the tips. When no steering is applied the tension is on the two most forward lines. Then when steering is applied the tension force in the two back lines will increase. This of course increases the magnitude of the tension force, but also changes the effective point of action of the tension force. The point of action will move backwards. The rack and pinion system is designed to accomplish the same effect. This is illustrated schematically in figures 2-14 and 2-15.

Figure 2-14 shows the left tip of a kite with the power and steering lines. On the left picture no steering is applied and the force on the power is larger than the force in the steering line. On the right picture steering is applied and the force in the power line has decreased and the force in the steering line has increased.

Figure 2-15 shows the left tip of a kite with the control mechanism. The left picture shows again the situation when no steering is applied and the right when steering is applied. The position of the pinion cart is shifted towards the trailing edge when steering is applied. The forces as they would result with four lines is shown with dashed arrows.

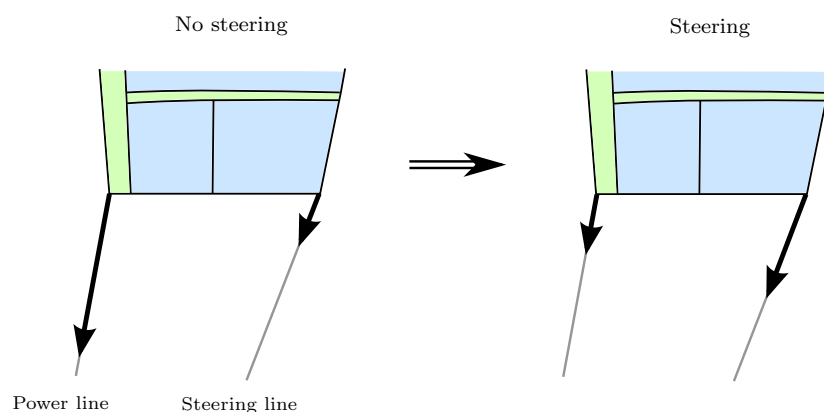


Figure 2-14: Principle of steering a kite with four lines

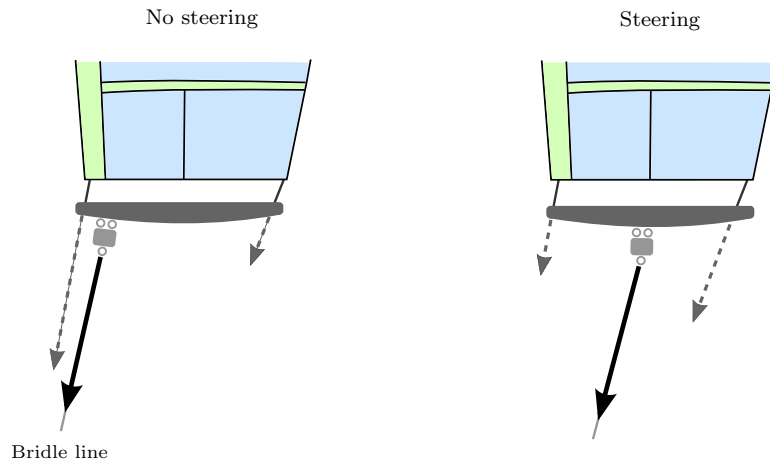


Figure 2-15: Principle of steering a kite with the control mechanism

2-4 Kite control

Now that the kite system with control mechanism is defined the question rises which control techniques are available for the basis for control law design. Secondly, other aspects are discussed, namely the influence of the model, the control variables, state and wind estimation for the control system.

2-4-1 Classical or linear control

Classical control is based on linear control, which uses the difference between the reference value and the desired value to set the value of the controlled parameter. This value is obtained by applying a proportional action (P), integral action (I), derivative action (D) or usually a combination of the three. Using all three results in a PID-controller.

Examples of PID-control to control a point mass kite model to fly along a predefined trajectory are found in references [15] and [39]. Furthermore Williams in reference [34] uses a linear controller to keep the multi-plate kite model at zenith position. Full state feedback is assumed to control the position and the orientation.

2-4-2 Advanced control algorithms

When dealing with complex nonlinear systems linear controllers will not suffice and some advanced control algorithm needs to be applied. Three advanced control algorithms are discussed in this section: model predictive control, nonlinear dynamic inversion and neural networks.

Model predictive control

Model predictive control MPC is a form of advanced control algorithm where the future trajectory of the system is predicted for a certain time interval. The controller tries to minimize the difference of a predicted trajectory to the reference trajectory by adapting the control inputs for some certain time interval in the future.

Williams in [37] uses a nonlinear predictive control algorithm for a point mass kite model. The nonlinear feedback controller stabilizes the kite motion from a set of noisy measurements of the

system. Predefined trajectories are uploaded to a virtual flight computer and the tracking controller implements a nonlinear predictive control algorithm for minimizing the deviation of the kite trajectory from the reference.

Also Diehl, reference [6], suggests to use nonlinear model predictive control NMPC for controlling kites. Another way to describe NMPC is as a feedback control based on real-time trajectory optimization of nonlinear process models. The robustness and excellent real-time performance of the method is demonstrated in a numerical experiment by controlling an unstable system: a kite that flies loops.

Only recently Fagiano, reference [8], presented his Phd. thesis on controlling kites using NMPC. For complex systems determining the optimal solution on-line requires a high computation effort. Therefore Fagiano suggests to use off-line computed solutions. Still a trade-off needs to be done between accuracy and computation speed.

Nonlinear dynamic inversion

Nonlinear dynamic inversion NDI compensates for the nonlinear dynamics via inverse model equations in the control laws. The model output equations need to be differentiated once to arrive at an analytical relation with the control inputs that can be inverted. The desired dynamics can be obtained using a linear outer loop controller. A major drawback of NDI is poor robustness to uncertainties in the dynamic model. Although, Looye in reference [18] discusses techniques to counteract this disadvantage.

Neural networks

Neural networks or evolutionary robotics ER is a control algorithm that basically learns itself how to control a system. Neural networks do not require deep knowledge about the dynamical system. This can be an advantage if very complex systems need to be controlled. On the other hand this can be a disadvantage if some dynamic phenomena are to be investigated and analyzed.

The use of neural networks on kite systems are shown by the study of Furey [10], where he uses the technique for controlling the lumped parameter kite model. It is demonstrated that the application of ER techniques to kite control produces controllers that fly the kite in stable figure eight trajectories. Evolved robust neuro-controllers maintain these trajectories during significant deviations of wind speed. These results suggest that it is worth pursuing ER for kite control systems.

2-4-3 Other aspects

Before a certain control topology is chosen it is vital to know which states are available for control feedback and how accurate these can be measured.

Influence of the model

In reference [17] a synthesis for real-time robust flexible structure controllers is shown. It is stated there that in general the main problem with controllers for large flexible structures is caused by the modelling error. The modelling error is caused due to two reasons:

- Truncating the original infinite dimensional model, i.e. the real world
- The lack of accurate knowledge of the parameters

The first is a problem for every model, as every model will neglect some dynamic phenomena because they are insignificant and therefore negligible. The difficulty in this is how to determine which influences are acceptable to neglect and which are not. This depends entirely on the purpose of the model. One aspect can be the difference in the frequency of the eigenmodes. For example high frequency vibrations in the tether are not interesting if the low frequent pendulum motion of a kite is to be investigated. Basically, the phenomena on which research can be done depends on the ability to model the required influences that cause those phenomena.

The second depends on the ability to set up the required tests for determining the parameters. Parameters can be obtained from wind tunnel tests [32], but might also be obtained from high fidelity models. High fidelity models incorporate more dynamic phenomena and therefore estimations can be made for parameters to be incorporated in lower fidelity models.

Both modelling errors will have an effect on controller design. When testing in practice the optimized controller based on the model has to be tuned in order to perform well.

Control variables

Almost any control system needs input data about the current state of the system to be able influence the state of the next time step. The amount of state variables needed to control the system is preferred to be small to minimize complexity of the control system, but the amount of state variables that can be measured is preferred to be large such that the control system can utilize them all. The latter is called the *observability* of the system.

In contrast *controllability* is the possibility of forcing the system into a particular state using an appropriate control signal. If a particular uncontrollable state is involved with an unstable eigenmode the complete system is uncontrollable. So the *stability* of the system is another important aspect.

State and wind estimation

Even when the required states can be measured or reconstructed from other measurements, the results are prone to errors and biases. The general term for minimizing the errors is called filtering. Another property of filtering is the ability to adapt the frequency of the measurements to the frequency suited for the controller.

Kalman filtering [35] is a well-known method to estimate the states of the kind and the wind speed from measurements. A normal Kalman filter is suited for linear systems in which the probabilistic distributions for the variables are Gaussian. For most nonlinear systems the extended Kalman filter EKF is suitable, but due to the complexity of the kite system the EKF is difficult to apply, according to Williams [35], and suggests to use another nonlinear filtering called the unscented Kalman filter (UKF).

2-5 Crosswind power

As explained in section 2-1 more power can be generated by the Laddermill by flying a kite in crosswind direction. This is explained as follows. Flying a kite in crosswind means that the apparent wind speed on the kite is increased. A higher apparent wind speed gives more lift and if there is more lift there will be more tension in the tether, which will increase the power generated because the power is given by the force times the reel-out speed of the tether:

$$P = T_t \cdot V_L \quad (2-8)$$

where T_t is the tether tension force, V_L the reel-out speed of the tether and P the power generated.

2-5-1 Crosswind motion

The principle and advantage for power generation of crosswind motion is first explained by Loyd, reference [19].

Figure 2-16 shows the forces and velocities on a weightless kite in crosswind motion. Equilibrium of forces is obtained by the lift L , the drag D and the tether tension T_t . The velocities shown are the wind speed V_W , the speed of the line V_L , the crosswind velocity of the kite V_C and the aerodynamic velocity of the kite with respect to the air V_a .

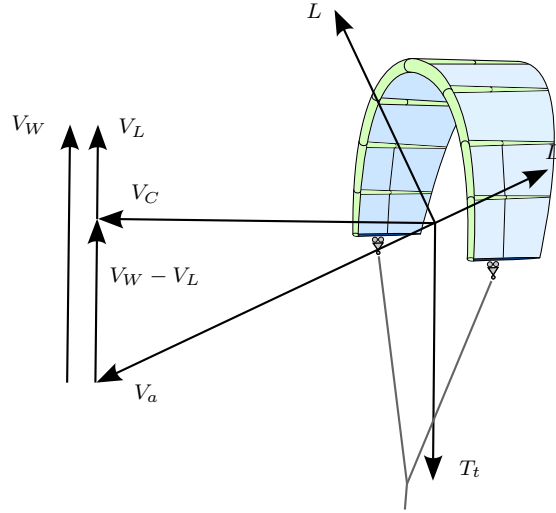


Figure 2-16: Forces and velocities on a kite in crosswind motion

From the figure a relation can be obtained for the apparent wind speed:

$$V_a = (V_W - V_L) \left(\frac{L}{D} \right)_K \quad (2-9)$$

where $(L/D)_K$ is the lift over drag ratio of the kite.

The lift force can be defined as:

$$\begin{aligned} L &= C_L \cdot \frac{1}{2} \rho V_a^2 S \\ &= C_L \cdot \frac{1}{2} \rho (V_W - V_L)^2 \left(\frac{L}{D} \right)_K^2 S \end{aligned} \quad (2-10)$$

where C_L is the lift coefficient, ρ the air density and S the projected surface area of the kite.

From this can be seen that the lift increases with the square of the lift over drag ratio. Further Loyd states that the power produced can be given as:

$$P = C_L \frac{1}{2} \rho V_W^3 S \cdot F \quad (2-11)$$

where F is a function describing the operational mode of the kite. In this case the kite is flying in crosswind motion, which is the most useful operational mode for the Laddermill. Loyd assumes that the inclination angle with the earth's surface is zero and that the kite is in perfect crosswind motion. The equation F for crosswind motion is given by:

$$F_{crosswind} = \left(\frac{L}{D} \right)_K^2 \left(\frac{V_L}{V_W} \right) \left(1 - \frac{V_L}{V_W} \right)^2 \quad (2-12)$$

The maximum value of this relation is:

$$F^{\max} = \frac{4}{27} \left(\frac{L}{D} \right)_K^2 \quad (2-13)$$

which occurs at,

$$V_L/V_W = 1/3$$

F^{\max} is again dependent on the square of the lift over drag ratio of the kite. So Loyd concluded that the $(L/D)_K$ is the parameter to maximize to extract the most wind energy in crosswind motion.

For a more thorough analysis about static crosswind power models refer to [26] and [30].

2-5-2 Crosswind power production

The most important aspect of the Laddermill is its power output. The analysis of Loyd in the previous section is only a static analysis of crosswind motion. For the complete Laddermill operation optimal trajectories as well as cycle strategies have to be determined to optimize power generation. Williams in reference [38] states that optimal power generation is most sensitive to the cycle time, the tether length and the wind speed. The dependency of these parameters on the power generation are given below for a kite of 50 kg, 25 m² and a tether length of 2000 m.

The dependence on the cycle time is illustrated in figure 2-17.

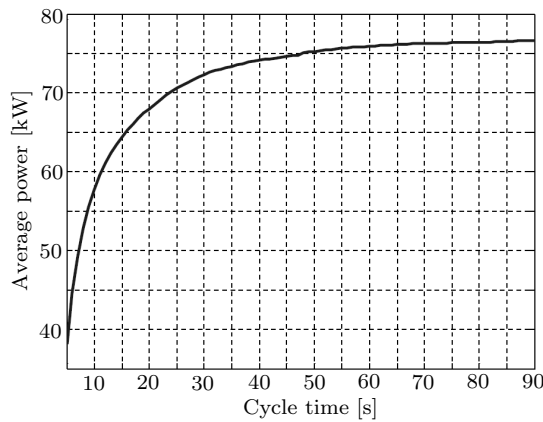


Figure 2-17: Average power production as a function of cycle time, Ref. [38]

It appears that the average power production increases approximately logarithmic to the cycle time with an asymptote of approximately 80 kW.

The key parameter for power production is proper selection of the tether length. The reason for this is the combined reduction in weight and drag. The power output increases almost exponentially as the tether length decreases, but the power output does not decrease significantly if the tether is made longer than its nominal value of 2000 m.

Finally, the power output for power production is roughly proportional to the cube of the wind speed. This already resulted from the static analysis on crosswind motion, see equation (2-11). The effect of variations in wind speed in the wind model shows that the wind speed at the kite's altitude plays a very significant role in the amount of power that can be generated by the system. From this can be concluded that it is vital to include wind variations if accurate power output has to be determined.

2-6 Other considerations

Several aspects of a kite system and the Laddermill operation have been assessed. This section considers some other subjects of kite systems regarding the wind, inflatable structures, aerodynamic deformations, aeroelasticity, the flight regime and model validation

2-6-1 The wind

The wind is of course a very important aspect of a Laddermill system. The purpose of the Laddermill is to harvest wind energy and wind fluctuations will have a profound role in the dynamic behaviour of such a system. The concept of the wind window, the wind profile and robustness related to wind variations are discussed.

Wind window

The wind window of a kite system indicates the domain for the kite to fly in. The boundaries of the wind window are given by the azimuth angle ranging from -90 deg to $+90$ deg and the zenith angle ranging from 0 deg to 90 deg. Figure 2-18 illustrates the wind window to show where the most powerful regions are. More powerful is indicated by $+$ or $++$ and less powerful by $-$. The cause of the higher potential in the middle is due to the fact that the kite flies in almost pure crosswind motion.

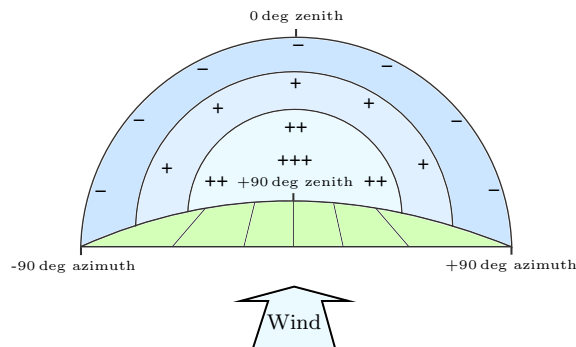


Figure 2-18: The wind window of a kite system, Ref. [9]

This knowledge could be advantageous in the control procedure between the reeling out and reeling in phase. In the reeling out phase as much power as possible should be extracted and by reeling in as less power as possible should be used. By reeling out in the $++$ area and reeling in on the edge of window should maximize the power production of the Laddermill.

Another issue could be that the most powerful region would result in too high tension on system. In this case the most powerful region should be avoided.

Wind profile

The wind profile is the relation between the average wind speed as a function of altitude. The average wind speed in The Netherlands was already shown in figure 2-10.

The most important aspect of the wind profile is the ground effect. The ground effect is caused by the boundary layer of the wind at the ground. Therefore the wind speed is normally lower at lower altitudes than at higher altitudes. The wind direction at higher altitudes is not generally defined as even wind speed reversals can occur between different altitudes.

Wind variations

Unfortunately the wind speed is not constant but fluctuates continuously with short period of time intervals. The behaviour of the wind is important as the wind speed greatly affects the power produced by a kite system, reference [38].

It following suggests that in normal operation the wind variation has little effect on the apparent wind speed and the angle of attack of the kite. This can be seen as follows. It is known from section 2-5 that the most power is extracted by flying the kite in crosswind motion. In crosswind motion the aerodynamic velocity V_a of the kite is determined by the wind speed component V_W and the crosswind velocity component V_C . If the wind speed variation is defined by ΔV_W the following can be stated:

$$|\mathbf{V}_A + \Delta \mathbf{V}_A| = \sqrt{(V_W + \Delta V_W \mathbf{i})^2 + (V_C + \Delta V_W \mathbf{j})^2} \quad (2-14)$$

$$\alpha + \Delta \alpha = \arctan \left(\frac{V_W + \Delta V_W \mathbf{i}}{V_C + \Delta V_W \mathbf{j}} \right) \quad (2-15)$$

In normal operation the wind speed variation is about 10-20% of the wind speed and the wind speed itself is a couple times smaller than the crosswind velocity. Looking at equation (2-14) the relative change in apparent wind speed is small with wind speed variations as well as the relative change in angle of attack by investigating equation (2-15). This is an advantage for controller design because less wind speed variation means that the system is more easy to control.

Wind modelling

Wind modelling is a difficult matter as it involves the understanding of stochastic processes as wind speed variations are highly random. For testing a controller wind models are important in order to find out the limitations of the controller. For example, for testing wind turbine controllers wind speed variation tests with different profiles are performed in order to test the response and robustness of the controller to these wind speed variations. These tests comprise gradual wind speed increase, step wise wind speed increase and inclusion of gust and turbulence models.

2-6-2 Inflatable structures

Modern arc-shaped kites are constructed with inflatable structures, for example the LEI surf kite. Several theories and models exist to simulate their bending behaviour. Two methods are depicted: using finite elements and multiple bodies

Finite element

Reference [33] describes the theory behind inflatable beams. First two kinds of inflatable prototypes are discussed: flat panels and tubes. Experiments show that their behaviour is a linear combination of yarn and beam shapes. Also their deformation pattern depends mainly on the inflation pressure and applied load. The usual theory of collapse analysis is then applied to the computation of wrinkling loads.

Multi-body

Breukels in reference [2] uses a multi-body dynamics approach to simulate inflatable beams. Beams are approximated by rigid elements, connected by spherical joints and 3-dimensional torque vectors. The stiffness of the torque vector determines the bending behaviour of the beam. The

stiffness possesses a nonlinear relationship with the deflection. It is dependent on internal pressure and beam radius. By varying the stiffness of the torsion springs, the nonlinear behavior of a complete inflatable structure can be simulated. Functions for the stiffness of the torsion springs are obtained by matching to existing measured data. In this way a variety of complex structures can be simulated.

Figure 2-19 shows the resulting bending moment with respect to the beam deflection. The figure illustrates that there is a linear part followed by a curved part where wrinkling is present and finally the beam collapses and is unable to give a sufficient bending moment.

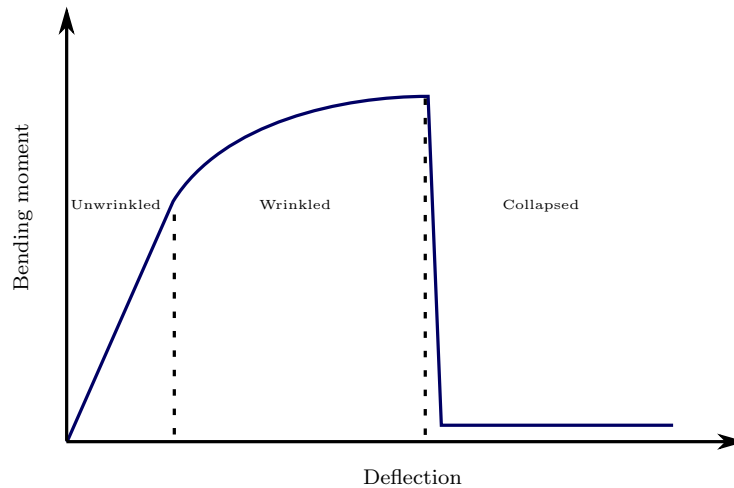


Figure 2-19: Load-deflection curve of inflatable beams, Ref. [2]

The wrinkled part poses a challenge on simulating the structure of inflatable beams. The wrinkled state is characterized by nonlinearities and local effects which influence the behaviour of the entire structure.

The advantage of a multi-body dynamics approach is that it is more suitable for dynamic simulations compared to the finite element method. The finite element method will be time consuming, where detailed knowledge about the places where wrinkles occur are necessary for mesh generation.

2-6-3 Aeroelasticity

Aeroelasticity is defined as the interaction between the aerodynamic forces and the structural forces resulting in local dynamic behaviour of the structure. Aeroelasticity can have non-negligible effect on the overall dynamic behaviour of a system. Flexible structures like kites are more prone to aeroelastic phenomena.

Aeroelastic phenomena arise when structural deformations induce additional aerodynamic forces. These additional aerodynamic forces may produce additional structural deformations which induce still greater aerodynamic forces. One example is the jellyfish motion with arc-shaped kites. These interactions have the potential for instability of the structure that will result in a catastrophic failure. The onset of this phenomenon occurs when the change in aerodynamic loads comes close to the natural eigenfrequency of the structure. Elastic deformation of wings due to flight loads can have a profound influence on the performance, handling qualities, flight stability, structural load distribution, and control effectiveness/reversal phenomena [28].

2-6-4 Flight regime and airfoil L/D

Figure 2-20 shows an overview of the flight regimes of aerial vehicles with respect to Mach number M and Reynolds number Re . Kites are placed between the domains of the birds and the hanggliders & ultralights, which is estimated for velocities between 5 and 20 m/s and for mean aerodynamic chord (mac) lengths between 0.5 and 3.0 m using air conditions at sea-level.

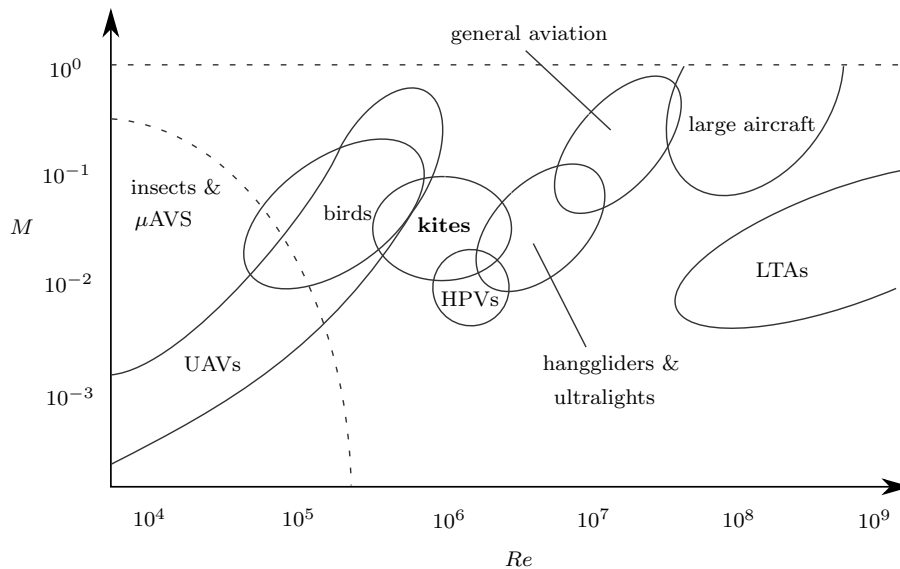


Figure 2-20: Flight Regimes of different vehicles by Mach and Reynolds number, Ref. [29]

Additionally, figure 2-21 shows the relation between the maximum L/D and Reynolds number of rough and smooth airfoils. For good performance the L/D ratio is preferred to be high. The airfoil of a kite can be regarded more rough than smooth due to the material and flexibility of the foil. From the figure can be concluded that a kite does not suffer from the L/D drop in the ‘Low Re Transitional Range’, because this does not apply to rough airfoils and the Re number of kites is just above this region. Another remark can be made with respect to the absolute values of the L/D . Figure 2-21 shows that the L/D of airfoils are quite high with respect to the L/D of a complete vehicle. Because regular aircraft have a L/D of approximately 10 to 15 and the $(L/D)^{max}$ of arc-shaped kites range from 5 to 8 for very efficient ones.

2-7 Conclusions

An overview of different aspects related to the Laddermill project, arc-shaped kite modelling and kite control is given in this chapter. The breakdown in figure 2-22 shows the various aspects that are involved in arc-shaped kite system design and arc-shaped kite modelling. The literature review forms the basis for the central thesis question and thesis goal.

Arc-shaped traction kites are the only type of kites which have been used extensively for testing the Laddermill concept. Several approaches for modelling an arc-shaped kite are explored. The most extensive model available is a multi-body kite model designed with the simulation software MSC. ADAMS. The model uses a variety of bodies, strings and joints and the structural bending and internal moment relations as well as the aerodynamics are based on measurements, empirical data and CFD calculations. The downside of the model is that it is quite computation intensive and seems therefore not very applicable for controller design. Furthermore the model is not quite transparent as it is hard to find relations between the model parameters and the resulting

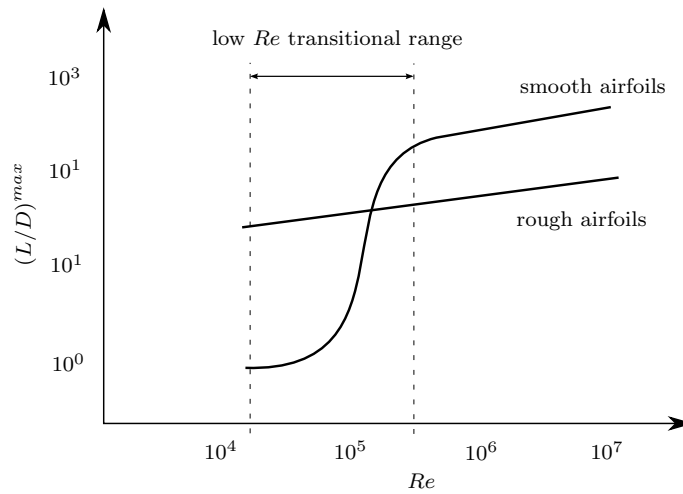


Figure 2-21: $(L/D)^{max}$ versus Reynolds number for airfoils, Ref. [13]

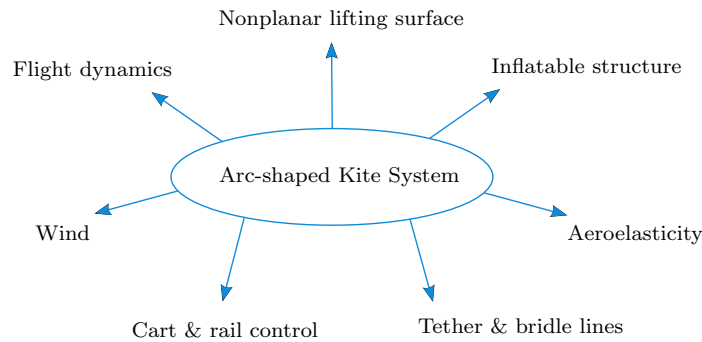


Figure 2-22: Breakdown of arc-shaped kite system

dynamics. Rigid body models are more transparent and faster to solve. In these models the aerodynamic model is based on aerodynamic derivatives and variables. But in general kites are not rigid and no aerodynamic models are available. The dynamics will change due to structural deformations.

Different control techniques are discussed like PID, MPC, NDI and neural networks. The first three require knowledge about the system equations for tuning the controller to obtain the required dynamics. Neural networks do not require accurate models and treat the model more like a black box. Detailed physical phenomena are harder to analyze. Referring to the references of Williams and Furey it is likely that PID is not sufficient to control a kite system. MPC and NDI are the favourable options.

For higher efficiency of the system a kite can be flown in crosswind motion. A kite can be flown loops or figures of eight to achieve crosswind motion. But this is not trivial. For complete Laddermill cycles the most important parameters determining the efficiency of power generation are the cycle time, the tether length and off course the wind speed. When control laws are designed the efficiency can be increased with trajectory optimization. This is a mathematical challenge due to changing wind conditions and kite dynamics. Trajectory optimization requires a fast model for dynamic calculations.

Modelling tethers can be a challenge, because of the complex dynamic behaviour. Especially longer tethers, due to tether drag and sag and delayed responses. Several approaches are presented to model a tether using discrete elements: point masses connected by links and multi-bodies. It is often assumed that short tethers behave as a straight line which requires only a simple spring-

damper model.

The thesis central question is formed on the following conclusions. For real-time automatic control, on-line implementation and flight-path optimization a fast model is required. A physics based model is preferred for more detailed analysis. The multi-body kite model designed in ADAMS is the most advanced model, but is not fast enough for control design. In contrast, rigid body models of aircraft have proven to be fast, accurate and useful for control law design. The aerodynamic model structures are often formed by Taylor series to obtain parameter based functions. A similar approach is imaginable for kites (reference [12] and [39]). The central question of this thesis is stated as:

‘Is it possible to simulate the overall dynamic behaviour of a flexible arc-shaped kite model with a rigid body model?’

The reference for the rigid body model will be the flexible multi-body arc-shaped kite model designed in the application MSC. ADAMS. Therefore chapter 3 is devoted to give an introduction to ADAMS and the multi-body kite model.

ADAMS and Multi-Body Kite Model Overview

MSC. ADAMS [22] is a multi-body dynamics simulation application. Many dynamical systems can be modelled in ADAMS from simple cranes and conveyor belts to full systems like cars, aircraft and wind turbines with most detailed complexity from a dynamical viewpoint. Even other from FEM analysis and CFD calculations can be coupled to the software. ADAMS seems a useful tool for modelling kite systems and kite designs.

To decrease the model design time system parts can be generated and assembled at once, instead of connecting the basic ADAMS elements over and over again. This can also be applied to kite system design because the basic system parts are tethers, inflatable tubes and foils. Therefore a kite design toolbox is developed to automatize the generation of these basic system parts. Even complete kite designs can be created including Arc-shaped LEI Kites and the Kiteplane concept, see figure 3-1.

3-1 A short introduction to ADAMS

ADAMS is a multi-body dynamics simulation application where models are created from building elements instead of programming the model equations yourself.

The basic elements of a model are:

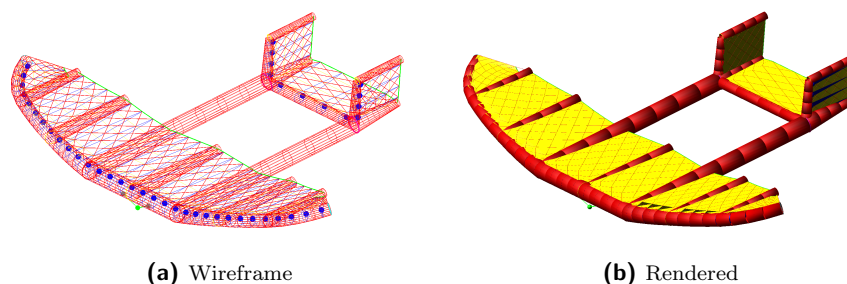


Figure 3-1: ADAMS Kiteplane model

- Markers
- Parts (rigid bodies)
- Joints & constraints
- Forces

Markers define a location as well as a local 3D reference. Markers can be created unlimited without decrease in simulation speed. Markers are always connected to parts or ground to define their location and orientation.

Parts have mass and geometry properties. The mass and the geometry can be configured dependent or independent. It is possible to specify a part without a geometry, but it is not possible to have a part with no mass or inertia properties. Many common shapes like links, cubes, cylinders and spheres can be created. It is advised to create models on a parametric basis such that the location and orientation of a part is specified with respect to another part.

Joints connect the parts together and specify the degrees of freedom that are allowed. Many predefined joints can be selected like revolute joints, hooke joints, fixed joints, translational joints and spherical joints. If one of these joints are not satisfying user-defined constraints can be specified as well.

To complete a model some external forces (including gravity) need to be created in order to start motion. Forces are categorized by applied forces, translational and torsional spring-dampers, contact forces and special forces like tire forces and gravity.

Additionally, variables can be introduced. Variables come in two basic forms: design variables and state variables. Design variables can be used to parameterize for example the physical, geometric or visualization properties of a part or other object. A design variable can be set to four different types: real, integer, string or object. ADAMS state variables (as) are always given by real values. State variables define the state of a specific variable. The input is set by a function dependent of time or another variable. State variables can be used to give an input to the system or to monitor the output (or state). State variables are required when using the ADAMSControls plugin. The function expression can include the result of ADAMS function measures and function commands to compute for example distances, angles and forces.

ADAMS function measures (am) are used to measure or monitor the result of a simulation after or during the simulation. The function defining the function measures can be specified by predefined function commands. The same as for the state variables. Many function commands exist from displacements, velocities and accelerations to measuring forces or computing math functions.

Beginners start building their models in the GUI ADAMS/View. In ADAMS/View the basic elements as mentioned above can be easily created and changes are immediately visible. When simulating models ADAMS/Solver is called solving the model equations which are automatically generated from the created model. The ADAMS/PostProcessor is convenient to thoroughly analyze the simulation results. Another extension to ADAMS which is frequently used for control applications is ADAMS/Controls.

Advanced users find out that creating models in the ADAMS/View environment is not always satisfactory. Therefore models can also be created with a command script or so called 'macro' file. The markers, parts, joints and forces can be created from a specific ADAMS script language. Additionally, the ADAMS/View interface can be modified with user-defined buttons and menus to call the user-created macro files. On this basis the *Kite Simulation Toolbox* is created.

3-2 The Kite Simulation Toolbox

With the Kite Simulation Toolbox tubes, cables, chords, foils and complete assemblies can be created. The Kite Simulation Toolbox started as the Kiteplane Toolkit (KPT) as part of the

Toolkit Creator (TKC). Later other models like the LEI Surf Kite have been added. Figure 3-2 gives an overview of the Kiteplane Toolkit and Toolkit Creator Shared Macros file and folder structure and hierarchy.

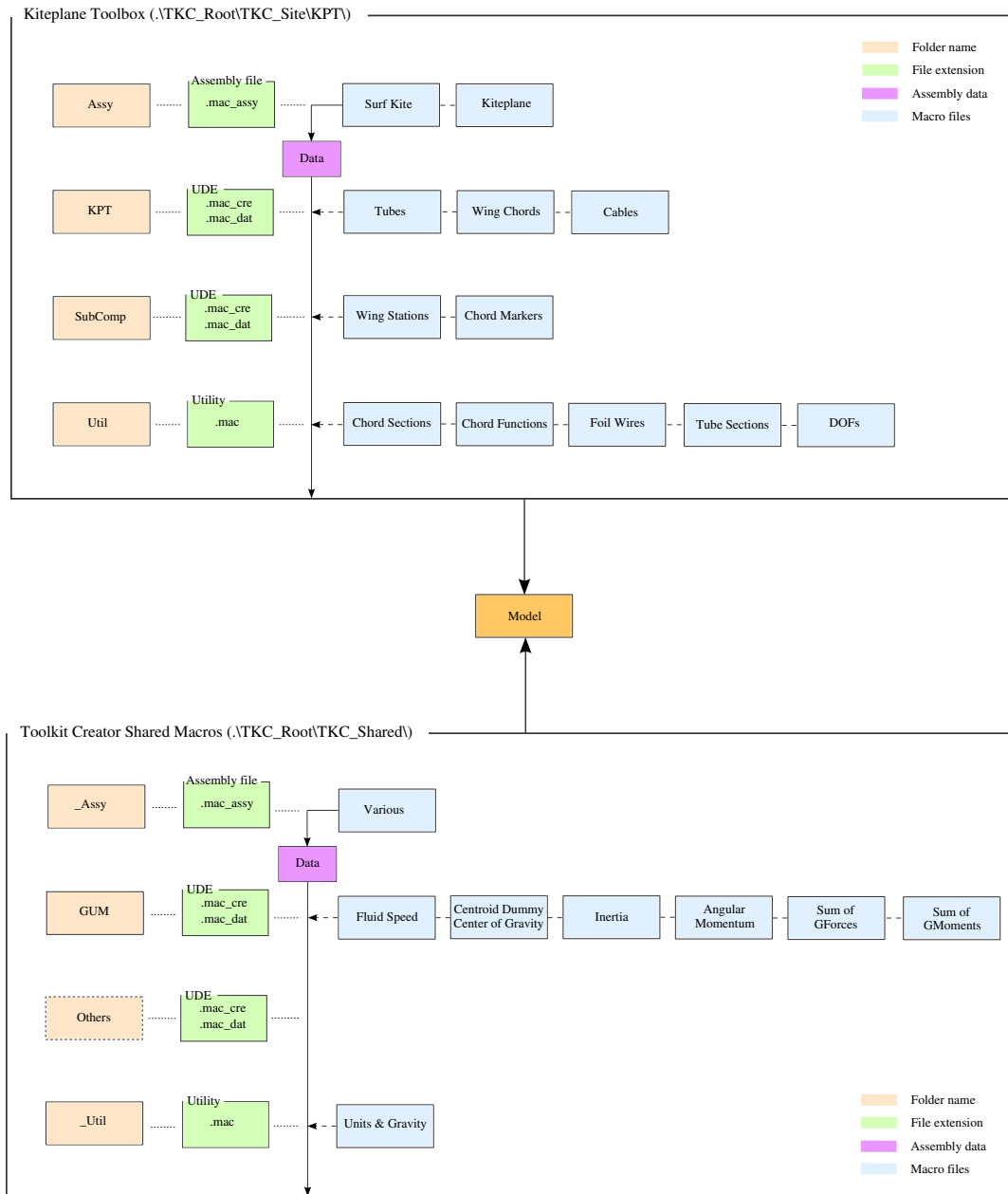


Figure 3-2: Overview of the KPT and TKC Shared file and folder structure

Assembly files can create User Defined Entities (UDE) and can call sub-component macro files (SubComp) as well as utility files (Util) to create a model. The default data specified in the UDEs can be overwritten by the assembly data to specify the model dimension or other properties. The assembly file is not restricted to call macro files within its root folder. The General Use Macros (GUM) and Shared utilities (.Util) are accessible via the Toolkit Creator Shared folder. The dependency of the macro files is more strict than shown in figure 3-2, because most UDEs do not work properly without the sub-component macros and utility macros. Additionally, macro files

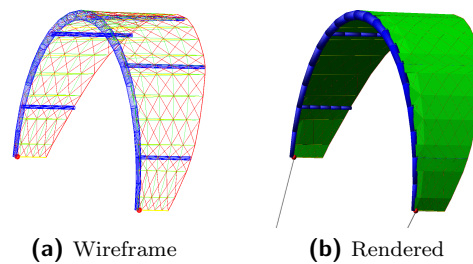


Figure 3-3: ADAMS LEI Surf Kite model

can be called via shortcut or fill-in menus. Generally the input data can be specified or altered.

The macro files shown under the GUM folder are modified or created for this thesis. Detailed explanation about the applied equations is given in chapter 9. Many more macro files are available in GUM as well as in other folders. The overview shown in figure 3-2 applies to this thesis.

The Surf Kite assembly file creates the LEI Surf Kite model as shown in figure 3-3. The assembly file is loaded with the ‘Assembly Loader Dialog’. In this menu options are given to specify the aerodynamic model, the tether model, the number of tube segments for structural discretization, geometry parameters and initial conditions.

For discretization of the model two basic parameters are given in the assembly loader: ‘LE Segments’ and ‘Side Segments’. The aerodynamic and structural model are related by the fact that the parameter ‘LE Segments’ determines the aerodynamic and structural discretization of the wing in span-wise direction. The parameter ‘Side Segments’ determines the discretization of the chord tubes also known as struts. Figure 3-4 shows that one LE Segment has one airfoil for aerodynamic calculations. In chord-wise direction the wing is always divided in five segments making the airfoil consisting of five rigid bodies and five pairs of Foil Cross Wires. Additionally, the structural elements of the foil are shown. The interaction with the other elements of the model is established with the Foil Wires and the TE Wires. The Foil Outline has only graphical purposes.

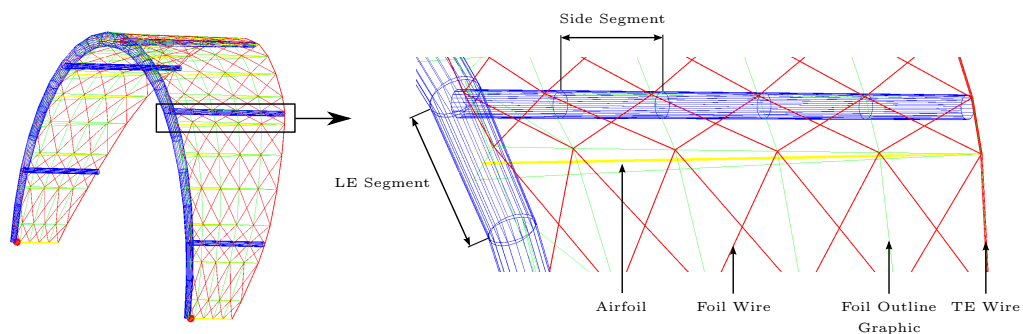


Figure 3-4: Elements of a chord segment of the ADAMS Surf Kite

3-3 Aerodynamic model

For the aerodynamic model three options are given in the assembly loader for specifying the ‘Wing Type’ via a drop down menu: ‘Rigid’, ‘Discrete’ and ‘None’. Rigid creates foils with one resultant force for each chord segment, Discrete creates foils with five forces at each chord segment and None creates no foils at all.

Aerodynamic forces and moments on a 2D airfoil can be represented by the frequently used c_l , c_d and c_m coefficients. The airfoil segment of a real LEI Kite is given in figure 3-5a. The model of the airfoil segment as used in ADAMS is given in figure 3-5b, from reference [3]. The changing shape of the airfoil during flight due to the flexibility of the foil has significant influence on the aerodynamic coefficients. Therefore the influence of the shape of the airfoil on the aerodynamic forces is taken into account by the camber line in the model. Other parameters that influence the 2D aerodynamic coefficients are angle of attack and the airfoil thickness. The airfoil thickness in the model is given by the tube thickness and the chord length. For different values of the angle of attack, airfoil thickness and for the shape of the camber line CFD calculations are performed to derive the corresponding c_l , c_d and c_m values. The resulting relations are fitted to polynomials to incorporate the aerodynamic coefficients c_l , c_d and c_m for each airfoil. The resulting values for the coefficients in the polynomials are available in ADAMS.

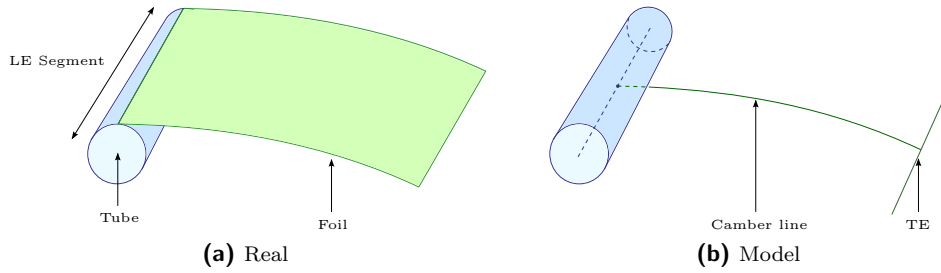


Figure 3-5: Airfoil segment, Ref. [3]

In ADAMS the airfoil segment model in figure 3-5b is split into five rigid elements as shown in figure 3-6. The aerodynamic coefficients apply to the quarter chord point and are determined from the local angle of attack, airfoil thickness and camber of each airfoil at every time step. The quarter chord point is frequently used as an approximation for the aerodynamic center (ac). Additionally, a 3D correction to each c_l value is applied depending on the position of the airfoil in span-wise direction. Using the angle of attack the c_l and c_d values are transformed to c_z and c_x which are perpendicular and parallel along the chord respectively. The coefficient c_m is incorporated by fractioning the c_z value over the five nodes. The contribution of c_x to c_m is neglected. So there are five resulting forces acting on the airfoil nodes, i.e action points. The relative value of each force is determined by a weighing function ($w_n + u_n \cdot a$) for $n = 1$ to $n = 5$. The sum of all w_n equals 1 and the sum of all u_n equals 0 such that the sum of all $c_{z,n}$ is c_z . The values of all w_n and u_n are known by assuming a general shape for the pressure distribution. Since the total moment is known, the value for a can be determined by setting up the moment equilibrium equation. The $c_{z,n}$ value for each node is now known and the c_x coefficient is also divided in 5 fractions using the same weighing terms. The actual force that is applied in ADAMS at the nodes is given by multiplying each $c_{z,n}$ and $c_{x,n}$ by $\frac{1}{2}\rho V_a^2 S$.

The aerodynamic model can be summarized into the following statement:

$$c_{x,j}, c_{z,j}, c_{m,j} \rightarrow f(\alpha_j, \zeta_j) \quad \text{for } j = 1 \dots n \quad (3-1)$$

where n is the number of airfoils and ζ_j a deformation vector containing the camber and airfoil thickness.

The previous applies to the ‘Discrete’ aerodynamic model. It is also possible to choose for a ‘Rigid’ aerodynamic model. In this case there is only one resulting force on each airfoil acting at the quarter chord point. So the aerodynamic moment of the airfoil is not incorporated. The ‘Rigid’ model is used if simulation speed is preferred above accuracy.

Reference [5] describes the simulation of a full flexible sail wing with an inflated tubular spar. For the Surf Kite the wing is curved like an arc and therefore 3D effects are taken into account

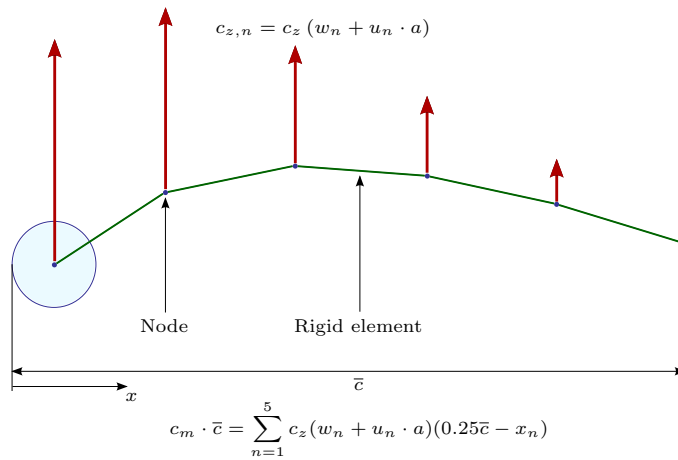


Figure 3-6: Airfoil model 'Discrete', Ref. [3]

in a different manner, but other aspects that apply for the straight sail wing also apply for an arc-shaped wing.

Figure 3-7 shows an example of the arc-shaped LEI Surf Kite in simulation with the resulting aerodynamic forces in blue.

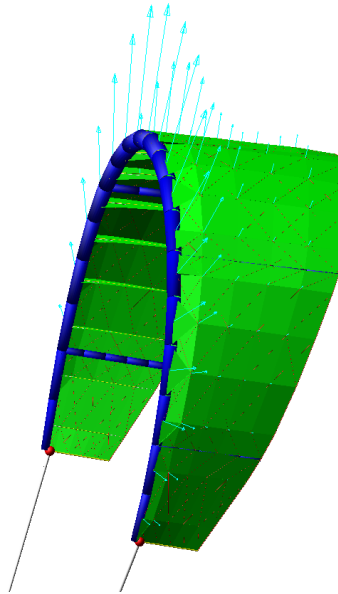


Figure 3-7: ADAMS Surf Kite model in simulation

3-4 Structural model

The structural model consists of a LE tube discretized in a number of LE segments, strut or chord tubes discretized in a number of side segments and foil modelled by TE wires and cross wires (figure 3-4).

The interaction between the LE segments and side segments is given by load-deflection relations applied on the joints. The typical load-deflection curve for inflatable beams was already shown

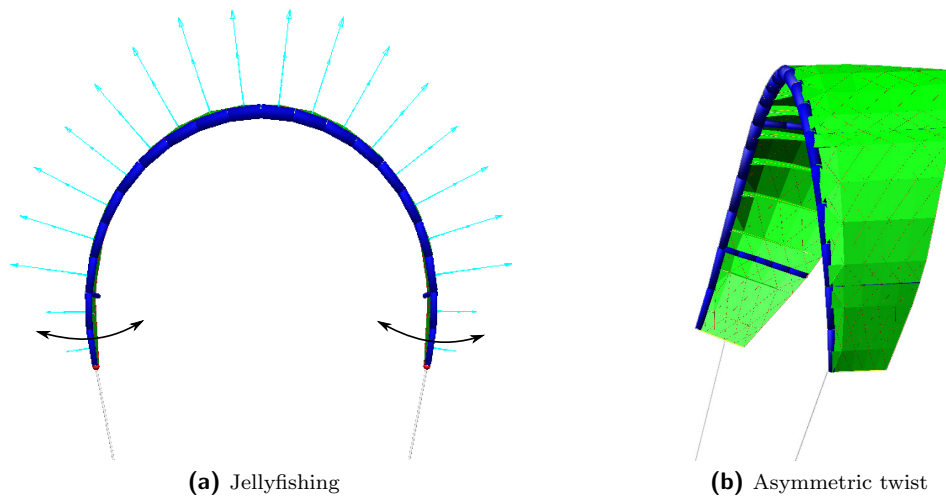


Figure 3-8: Structural modes

in figure 2-19. The load-deflection curves can be adjusted for internal pressure and radius of the cross-section. The models for the TE and cross wires consist of spring-damper systems. The damping in the system is adjustable to obtain a 'kite like' behaviour.

The resulting structure is able to simulate some characteristic modes of an arc-shaped kite like jellyfish motion and asymmetric twist. See figure 3-8. These modes are the consequence of a tightly interaction between the aerodynamic forces, tether forces and structural deformation. The jellyfish motion typically occurs in symmetric flight. The asymmetric twist is merely a result of steering input.

Thesis Goal & Approach

In the literature review a broad overview is given of the current status of kite research. Based on the literature review the central thesis question was formed. In the extension of the thesis question the thesis goal is formed. In the following the thesis goal is used to specify the requirements and approach.

4-1 Goal

The goal of this thesis is stated as follows:

‘To establish a model of an arc-shaped traction kite which is appropriate for controller design’

4-2 Requirements

Controlling kites is accomplished by a complex interaction between control inputs, tether forces, structure deformation and aerodynamic forces. To have more insight on which control techniques are required to control a kite is of vital importance. Advanced control techniques are available which might be appropriate. The most feasible ones are: Model Predictive Control (MPC) and Nonlinear Dynamic Inversion (NDI). MPC and NDI require models which can simulate the dynamic behaviour of the system accurately. This dynamic behaviour comprises the overall motion of the kite which can be described by a limited set of states. MPC and NDI require information of the system dynamics to be available online. If the simulation solutions are generated online the model simulation time must be faster than real-time. Another possibility is to obtain the solution space off-line, but also in this case a fast model is advantageous.

The model is more useful if it is appropriate to simulate other kites. This requires that the model is designed on a parametric basis, where the structure and aerodynamics are modelled by a limited set of parameters which completely describe the kite characteristics.

The requirements of the arc-shaped kite model are itemized as follows:

- Able to simulate the dynamic behaviour described by a limited set of states
- Suitable to gain more knowledge about the system dynamics

- Appropriate for real-time simulation and online implementation
- Applicable to simulate different kites
- The aerodynamics and structural properties are modelled on a parametric basis

4-3 Approach

Chapter 3 describes the capability to model an arc-shaped kite with the multi-body dynamics simulation tool MSC. ADAMS. The main purpose of the ADAMS Multi-Body model is to be used as a design tool. Models can be made with many degrees of freedom such that many dynamical phenomena can be studied. This results in simulations which are relatively time consuming. This also implies that it is hard to create tangible conclusions about the dominant influences on the dynamics of the system. Therefore it can be stated that an arc-shaped kite modelled in ADAMS does not fulfill the requirements.

Therefore a new kite model is proposed, where the equations of motion will be based on an rigid body.

For this Rigid Body kite model the aerodynamics are based on an approach as is custom for aircraft. These methods make use of so called aerodynamic derivatives. The aerodynamic derivatives represent the change of force or moment to a specific aerodynamic variable. The aerodynamic derivatives are obtained with a fitting procedure called parameter identification using flight test techniques. Due to limited capabilities for measurements on real kites the ADAMS Multi-Body Kite model is used as a reference.

Because of the flexible structure the inertia tensor, mean wing chord, wing span and projected surface area vary as well. The variation of the inertia tensor components, mean wing chord, wing span and projected surface area is taken into account on a quasi static basis. The inertia tensor and structural properties adapt to the respective flight condition.

For the Rigid Body model and the Multi-Body model the tether is simulated by a spring-damper model. This has two reasons. There are no differences between both models with respect to the tether and the dynamic influence on the system is predictable.

Modelling the aerodynamic forces and structural properties on a parametric basis assumes that the aerodynamic functions are only dependent on external aerodynamic states and not on internal structural (dynamic) states. These aerodynamic states are a function of rigid body states. This requires that the aerodynamics and structural properties can be written as a function of rigid body states. To reduce the numerous states of the Multi-Body Kite model to a set of rigid body states a formal methodology is required.

The verification of the Rigid Body kite model is based on known dynamics of a rigid body aircraft. For validation of the reduction of the Multi-Body Kite model to a Rigid Body Kite model test simulations are performed.

Part II

Kite Modelling

Definitions, Reference Frames and Wind Kinematics

Before the actual modelling part can start a basis is required with respect to definitions for reference frames, angles as well as the kinematic relations for a straight tether and wind kinematics. The first section defines the reference frames needed for modelling a kite system. Secondly the derivation of the transformation matrices and vectors for the orientation and angular velocity is given. The chapter concludes with discussing the tether and wind kinematic relations.

5-1 Reference frames

A reference frame defines the position and/or orientation of a point, body, force or moment in space. The reference frames, which are relevant when modeling kite systems are the normal earth-fixed reference frame F_E , the body-fixed reference frame F_b , the aerodynamic reference frame F_a , the kinematic reference frame F_k , the tether-fixed reference frame F_t and the vehicle reference frame F_r . More information can be found in reference [24]. Except for the tether-fixed reference frame which is defined for this thesis. The term ‘vehicle’ is sometimes used and is representative for kite.

Normal earth-fixed reference frame F_E

The normal earth-fixed reference frame ($OX_EY_EZ_E$) is a right-handed orthogonal axis-system, where the origin is fixed to the earth. The X_EY_E plane is tangent to the earth's surface and the X_E -axis is directed to the north. When the earth is considered a sphere, the Z_E -axis points to the center of the earth.

In aircraft literature another reference frame is defined which is similar to the normal earth-fixed reference frame: the vehicle carried normal earth reference frame F_O . The origin is at the same position, but the Z_O -axis points in the direction of the local gravity vector as seen by the vehicle center of gravity cg . When deriving the equations of motion for aircraft usually the assumption is made that the earth is flat and non-rotating. For kite systems the same assumption is made. With this assumption the Normal earth-fixed reference frame and the vehicle carried normal earth reference frame coincide.

Body-fixed reference frame F_b

The body-fixed reference frame ($cgX_bY_bZ_b$) is a right-handed orthogonal axis-system with the origin at the vehicle's reference point. Usually the center of mass of the vehicle is the vehicle's reference point. The reference frame is fixed to the vehicle even in perturbed motion. The direction of the axis can be chosen arbitrarily. In general the X_b -axis is in the symmetry plane of the vehicle and points forward. The actual direction is still arbitrary and can be chosen situation dependent, which influences the definition of the angle of attack. The Z_b -axis is also situated in the symmetry plane and points downward. The Y_b -axis is directed to the right, perpendicular to the symmetry plane.

Often in flight dynamics literature the stability is investigated for specific flight conditions. The X_b -axis will then be defined in the direction of the aerodynamic velocity (see aerodynamic reference frame) projected on the symmetry plane of the vehicle. The body-fixed reference frames defined in this way are called *stability reference frames*.

Aerodynamic (air-path) reference frame F_a

The aerodynamic or air-path reference frame is coupled to the aerodynamic velocity vector \mathbf{V}_a . The aerodynamic velocity is defined as the velocity of the vehicle's reference point relative to the undisturbed air. It is a right-handed orthogonal reference frame where the origin is the same as for the Body-fixed reference frame, the X_a -axis is in the direction of the aerodynamic velocity vector and the Z_a -axis is in the plane of symmetry. The aerodynamic velocity vector in the aerodynamic reference frame is:

$$\mathbf{V}_a^a = \begin{bmatrix} u_a^a \\ v_a^a \\ w_a^a \end{bmatrix} = \begin{bmatrix} V_a \\ 0 \\ 0 \end{bmatrix} \quad (5-1)$$

In the body-fixed reference frame the aerodynamic velocity vector is:

$$\mathbf{V}_a^b = \begin{bmatrix} u_a^b \\ v_a^b \\ w_a^b \end{bmatrix} = \begin{bmatrix} u_a \\ v_a \\ w_a \end{bmatrix} \quad (5-2)$$

The equations of motion derived in chapter 6 are written in the body-fixed reference frame. Therefore the convention is made that after this section the quantities u , v and w are always written in the body-fixed reference frame.

Kinematic (flight-path) reference frame F_k

The kinematic reference frame is coupled to the kinematic velocity \mathbf{V}_k , which is the velocity of the vehicle relative to the normal earth-fixed reference frame. GPS-systems measure the kinematic velocity. It is the position of the center of mass O_{cg} relative to the normal earth-fixed reference frame F_E :

$$\mathbf{V}_{k,cg} = \mathbf{V}_{k,E} = \frac{d\mathbf{O}_{cg}^E}{dt} \quad (5-3)$$

The origin is the same as for body-fixed reference frame. The X_k -axis is in the direction of the kinematic velocity \mathbf{V}_k , the Z_k -axis is in the symmetry plane of the vehicle and the Y_k -axis is perpendicular to the X_kZ_k -plane to complete the right-orthogonal axis system. The angles to describe the orientation of the kinematic reference frame with respect to the body-fixed reference frame are the kinematic angle of attack α_k and the kinematic side slip angle β_k . The kinematic velocity expressed in the kinematic reference frame is denoted as:

$$\mathbf{V}_k^k = \begin{bmatrix} u_k^k \\ 0 \\ 0 \end{bmatrix} \quad (5-4)$$

Tether-fixed reference frame F_t

To describe the orientation of the tether with respect to the earth and the vehicle a tether-fixed reference frame F_t can be defined. This is a right handed reference where the Z_t -axis is directed perpendicular along the tether and the X_t -axis lies in the X_OZ_O -plane of the Vehicle Carried Normal earth reference frame. See figure 5-1. The angles ψ_t and θ_t describe the orientation of tether with respect to the earth-fixed reference frame. The angles ξ , κ and τ describe the orientation of the kite with respect to the tether.

Note that when a tether with sag is considered the orientation of the tether-fixed reference depends on the position on the tether.

Figure 5-1 gives an abstract visualization of the kite system with the position of the earth-fixed reference frame, the body-fixed reference frame and the tether-fixed reference frame.

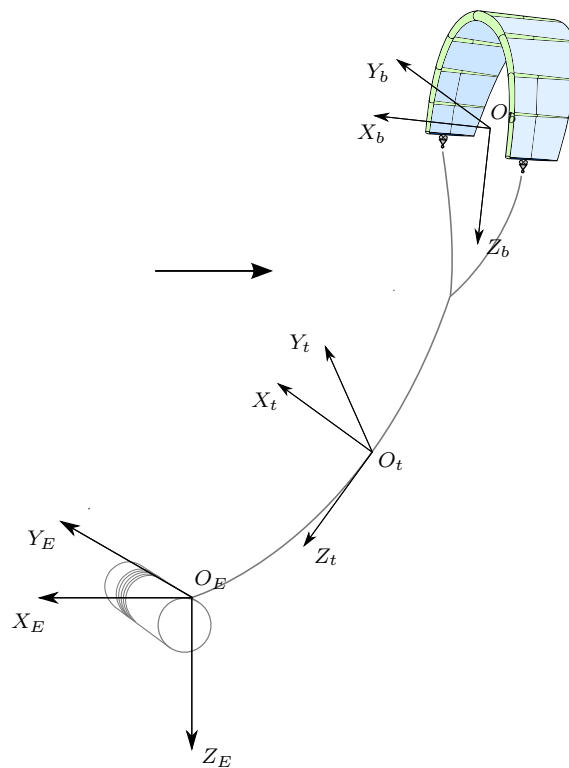


Figure 5-1: Laddermill with definition of F_E , F_b and F_t

Vehicle reference frame F_r

The vehicle frame of reference (O_r, X_r, Y_r, Z_r) for kites is a right-handed orthogonal axis system with the origin at a fixed position to the vehicle. Here the origin is chosen at the most downward position central between the two tips, see figure 5-2. This reference frame is convenient when defining the geometry of a vehicle.

For a kite the direction of the X_r -axis will be parallel to the plane of symmetry and points to the rear of the vehicle. The Y_r -axis is directed parallel to the symmetry plane and points to the right. And the Z_r -axis is defined perpendicular to the X_r, Y_r -plane and points upwards. The actual position of the origin and the orientation of the X_r and Z_r -axes is user defined, but one option is to choose the origin at the most forward low central position and the Z_r -axis parallel to the leading edge. Figure 5-2 shows the vehicle reference frame for an arbitrary kite.

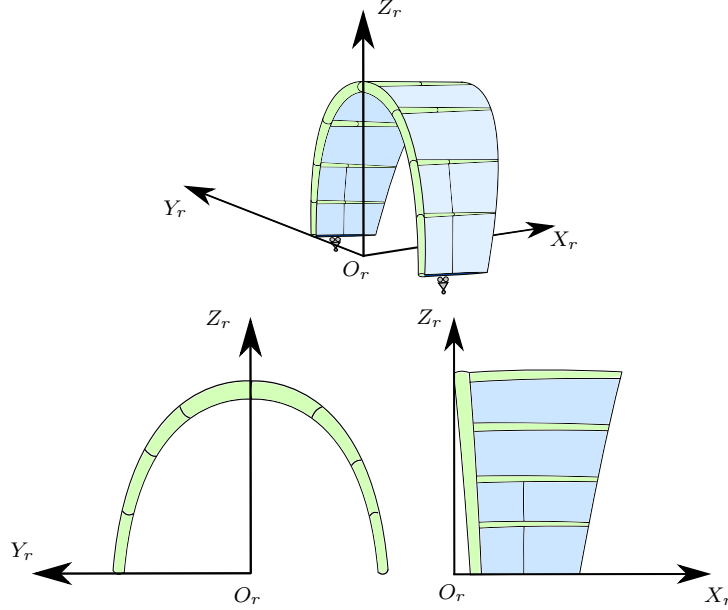


Figure 5-2: Vehicle reference frame with front and side view

5-2 Transformation between reference frames and angular velocity vectors

To transform a vector from one reference to another transformation matrices are defined. The specification of the attitude parameters is based on the Euler angles representation. Most transformations are based on the {3-2-1} rotation sequence as is common for modelling aircraft. This means that the first rotation is about the Z -axis, the second about the Y -axis and the third about the X -axis. The rotations and angle declarations are specified for every defined transformation.

Secondly angular velocity vectors are obtained, which define the relative rotational speed between two reference frames. The angular velocity vector is a function of the Euler angles and the time derivative of the Euler angles between two reference frames.

5-2-1 Transformation from F_E to F_b and derivation of Ω_{bE}^b

In the aerospace industry the rotation sequence $\psi \rightarrow \theta \rightarrow \phi$ is most commonly used for the rotation from F_E to F_b , where

- ψ is the yaw angle, rotation about the Z_{E} -axis
- θ is the pitch angle, rotation about the $Y_{E'}$ -axis
- ϕ is the roll angle, rotation about the X_b -axis ($=X_{E''}$ -axis)

where the $Y_{E'}$ -axis and $X_{E''}$ -axis are the axes of the intermediate reference frame $F_{E'}$ and $F_{E''}$ respectively. The complete rotation defines the following reference frames:

$$F_E \rightarrow F_{E'} \rightarrow F_{E''} \rightarrow F_b$$

Note that F_E has been assumed equal to F_O , so the rotation matrix for the rotation from F_E to F_b is the same as for F_O to F_b .

The transformation matrix for the rotation from F_E to F_b is given by,

$$\mathbb{T}_{bE} = \mathbf{T}_{bE''} \mathbf{T}_{E''E'} \mathbf{T}_{E'E} \quad (5-5)$$

$$\begin{aligned} &= \begin{bmatrix} 1 & 0 & 0 \\ 0 & \cos \phi & \sin \phi \\ 0 & -\sin \phi & \cos \phi \end{bmatrix} \begin{bmatrix} \cos \theta & 0 & -\sin \theta \\ 0 & 1 & 0 \\ \sin \theta & 0 & \cos \theta \end{bmatrix} \begin{bmatrix} \cos \psi & \sin \psi & 0 \\ -\sin \psi & \cos \psi & 0 \\ 0 & 0 & 1 \end{bmatrix} \\ &= \begin{bmatrix} \cos \theta \cos \psi & \cos \theta \sin \psi & -\sin \theta \\ \left(\begin{array}{l} \sin \phi \sin \theta \cos \psi \\ -\cos \phi \sin \psi \end{array} \right) & \left(\begin{array}{l} \sin \phi \sin \theta \sin \psi \\ +\cos \phi \cos \psi \end{array} \right) & \sin \phi \cos \theta \\ \left(\begin{array}{l} \cos \phi \sin \theta \cos \psi \\ +\sin \phi \sin \psi \end{array} \right) & \left(\begin{array}{l} \cos \phi \sin \theta \sin \psi \\ -\sin \phi \cos \psi \end{array} \right) & \cos \phi \cos \theta \end{bmatrix} \end{aligned} \quad (5-6)$$

The angular velocity of the body-fixed reference frame F_b with respect to the normal earth-fixed reference frame F_E expressed in F_b is obtained using the rotational speed of the previous defined angles. This results in:

$$\begin{aligned} \Omega_{bE}^b &= \mathbb{T}_{bE'} \Omega_{E'E}^{E'} + \mathbb{T}_{bE''} \Omega_{E''E'}^{E''} + \Omega_{bE''}^b \\ &= \begin{bmatrix} \dot{\phi} - \dot{\psi} \sin \theta \\ \dot{\theta} \cos \phi + \dot{\psi} \sin \phi \cos \theta \\ -\dot{\theta} \sin \phi + \dot{\psi} \cos \phi \cos \theta \end{bmatrix} \\ &= \begin{bmatrix} 1 & 0 & -\sin \theta \\ 0 & \cos \phi & \sin \phi \cos \theta \\ 0 & -\sin \phi & \cos \phi \cos \theta \end{bmatrix} \begin{bmatrix} \dot{\phi} \\ \dot{\theta} \\ \dot{\psi} \end{bmatrix} \\ &= \begin{bmatrix} p \\ q \\ r \end{bmatrix} \end{aligned} \quad (5-7)$$

where p , q and r are the body rotational rates in the body-fixed reference frame.

5-2-2 Transformation from F_E to F_a and derivation of Ω_{aE}^a

The transformation from the normal earth-fixed reference frame F_E to the aerodynamic reference frame F_a consist of three sequential rotations:

- rotation χ_a , aerodynamic yaw angle, about the Z_E -axis
- rotation γ_a , aerodynamic pitch angle, about the $Y_{E'}$ -axis
- rotation μ_a , aerodynamic roll angle, about the X_a -axis ($=X_{E''}$ -axis)

The reference frames obtained during the transformation are defined by:

$$F_E \rightarrow F_{E'} \rightarrow F_{E''} \rightarrow F_a$$

The transformation matrix for the rotation from F_E to F_a is given by,

$$\begin{aligned} \mathbb{T}_{aE} &= \begin{bmatrix} 1 & 0 & 0 \\ 0 & \cos \mu_a & \sin \mu_a \\ 0 & -\sin \mu_a & \cos \mu_a \end{bmatrix} \begin{bmatrix} \cos \gamma_a & 0 & -\sin \gamma_a \\ 0 & 1 & 0 \\ \sin \gamma_a & 0 & \cos \gamma_a \end{bmatrix} \begin{bmatrix} \cos \chi_a & \sin \chi_a & 0 \\ -\sin \chi_a & \cos \chi_a & 0 \\ 0 & 0 & 1 \end{bmatrix} \\ &= \begin{bmatrix} \cos \gamma_a \cos \chi_a & \cos \gamma_a \sin \chi_a & -\sin \gamma_a \\ \left(\begin{array}{l} \sin \mu_a \sin \gamma_a \cos \chi_a \\ -\cos \mu_a \sin \chi_a \end{array} \right) & \left(\begin{array}{l} \sin \mu_a \sin \gamma_a \sin \chi_a \\ +\cos \mu_a \cos \chi_a \end{array} \right) & \sin \mu_a \cos \gamma_a \\ \left(\begin{array}{l} \cos \mu_a \sin \gamma_a \cos \chi_a \\ +\sin \mu_a \sin \chi_a \end{array} \right) & \left(\begin{array}{l} \cos \mu_a \sin \gamma_a \sin \chi_a \\ -\sin \mu_a \cos \chi_a \end{array} \right) & \cos \mu_a \cos \gamma_a \end{bmatrix} \end{aligned} \quad (5-8)$$

The angular velocity of the aerodynamic reference frame F_a with respect to the normal earth-fixed reference frame F_E expressed in F_a is obtained using the rotational speed of the previous defined angles. This results in:

$$\begin{aligned}\boldsymbol{\Omega}_{aE}^a &= \mathbb{T}_{aE'} \boldsymbol{\Omega}_{E'E}^{E'} + \mathbb{T}_{aE''} \boldsymbol{\Omega}_{E''E'}^{E''} + \boldsymbol{\Omega}_{aE''}^a \\ &= \begin{bmatrix} \dot{\mu}_a - \dot{\chi}_a \sin \gamma_a \\ \dot{\gamma}_a \cos \mu_a + \dot{\chi}_a \sin \mu_a \cos \gamma_a \\ -\dot{\gamma}_a \sin \mu_a + \dot{\chi}_a \cos \mu_a \cos \gamma_a \end{bmatrix}\end{aligned}\quad (5-9)$$

5-2-3 Transformation from F_E to F_k and derivation of $\boldsymbol{\Omega}_{kE}^k$

The transformation from the normal earth-fixed reference frame F_E to the kinematic reference frame F_k consist of three sequential rotations:

- rotation χ_k , kinematic yaw angle, about the Z_E -axis
- rotation γ_k , kinematic pitch angle, about the $Y_{E'}$ -axis
- rotation μ_k , kinematic roll angle, about the X_k -axis (= $X_{E''}$ -axis)

The derivation of transformation matrix \mathbb{T}_{kE} and angular velocity vector $\boldsymbol{\Omega}_{kE}^k$ are analogue to derivation of \mathbb{T}_{aE} and $\boldsymbol{\Omega}_{aE}^a$ and can be obtained by replacing the subscripts a by k .

$$\begin{aligned}\mathbb{T}_{kE} &= \begin{bmatrix} 1 & 0 & 0 \\ 0 & \cos \mu_k & \sin \mu_k \\ 0 & -\sin \mu_k & \cos \mu_k \end{bmatrix} \begin{bmatrix} \cos \gamma_k & 0 & -\sin \gamma_k \\ 0 & 1 & 0 \\ \sin \gamma_k & 0 & \cos \gamma_k \end{bmatrix} \begin{bmatrix} \cos \chi_k & \sin \chi_k & 0 \\ -\sin \chi_k & \cos \chi_k & 0 \\ 0 & 0 & 1 \end{bmatrix} \\ &= \begin{bmatrix} \cos \gamma_k \cos \chi_k & \cos \gamma_k \sin \chi_k & -\sin \gamma_k \\ \begin{pmatrix} \sin \mu_k \sin \gamma_k \cos \chi_k \\ -\cos \mu_k \sin \chi_k \end{pmatrix} & \begin{pmatrix} \sin \mu_k \sin \gamma_k \sin \chi_k \\ +\cos \mu_k \cos \chi_k \end{pmatrix} & \sin \mu_k \cos \gamma_k \\ \begin{pmatrix} \cos \mu_k \sin \gamma_k \cos \chi_k \\ +\sin \mu_k \sin \chi_k \end{pmatrix} & \begin{pmatrix} \cos \mu_k \sin \gamma_k \sin \chi_k \\ -\sin \mu_k \cos \chi_k \end{pmatrix} & \cos \mu_k \cos \gamma_k \end{bmatrix}\end{aligned}\quad (5-10)$$

$$\begin{aligned}\boldsymbol{\Omega}_{kE}^k &= \mathbb{T}_{kE'} \boldsymbol{\Omega}_{E'E}^{E'} + \mathbb{T}_{kE''} \boldsymbol{\Omega}_{E''E'}^{E''} + \boldsymbol{\Omega}_{kE''}^k \\ &= \begin{bmatrix} \dot{\mu}_k - \dot{\chi}_k \sin \gamma_k \\ \dot{\gamma}_k \cos \mu_k + \dot{\chi}_k \sin \mu_k \cos \gamma_k \\ -\dot{\gamma}_k \sin \mu_k + \dot{\chi}_k \cos \mu_k \cos \gamma_k \end{bmatrix}\end{aligned}\quad (5-11)$$

5-2-4 Transformation from F_b to F_a and derivation of $\boldsymbol{\Omega}_{ab}^a$

The transformation from the body-fixed reference frame to the aerodynamic reference frame consists of two sequential rotations:

- rotation $-\alpha_a$ aerodynamic angle of attack about Y_b -axis
- rotation β_a aerodynamic side slip angle about Z_a -axis

These angles are expressed in aerodynamic velocity components by equations (5-12) and (5-13).

$$\alpha_a = \arctan\left(\frac{w_a}{u_a}\right) \quad (5-12)$$

$$\beta_a = \arcsin\left(\frac{v_a}{V_a}\right) \quad (5-13)$$

with

$$V_a = \sqrt{u_a^2 + v_a^2 + w_a^2} \quad (5-14)$$

where u_a , v_a and w_a are written in body-fixed reference frame.

The rotation defines the following reference frames:

$$F_b \rightarrow F_{b'} \rightarrow F_a$$

The transformation matrix for the rotation from F_b to F_a is given by,

$$\begin{aligned} \mathbb{T}_{ab} &= \begin{bmatrix} \cos \beta_a & \sin \beta_a & 0 \\ -\sin \beta_a & \cos \beta_a & 0 \\ 0 & 0 & 1 \end{bmatrix} \begin{bmatrix} \cos \alpha_a & 0 & \sin \alpha_a \\ 0 & 1 & 0 \\ -\sin \alpha_a & 0 & \cos \alpha_a \end{bmatrix} \\ &= \begin{bmatrix} \cos \beta_a \cos \alpha_a & \sin \beta_a & \cos \beta_a \sin \alpha_a \\ -\sin \beta_a \cos \alpha_a & \cos \beta_a & -\sin \beta_a \sin \alpha_a \\ -\sin \alpha_a & 0 & \cos \alpha_a \end{bmatrix} \end{aligned} \quad (5-15)$$

And the angular velocity vector of the aerodynamic reference frame F_a with respect to the body-fixed reference frame F_b expressed in F_a using the rotational speed of the same rotations is given by:

$$\begin{aligned} \boldsymbol{\Omega}_{ab}^a &= \mathbb{T}_{ab'} \boldsymbol{\Omega}_{b'b}^{b'} + \boldsymbol{\Omega}_{ab'}^a \\ &= \begin{bmatrix} -\dot{\alpha}_a \sin \beta_a \\ -\dot{\alpha}_a \cos \beta_a \\ \dot{\beta}_a \end{bmatrix} \end{aligned} \quad (5-16)$$

The derivatives of the aerodynamic angles, α_a and β_a , are obtained by the relations given in equations (5-17) and (5-18) (Reference [23]).

$$\dot{\alpha}_a = \frac{u\dot{w} - w\dot{u}}{u^2 + w^2} \quad (5-17)$$

$$\dot{\beta}_a = \frac{(u^2 + w^2)\dot{v} - v(u\dot{u} + w\dot{w})}{(u^2 + v^2 + w^2)\sqrt{u^2 + v^2}} \quad (5-18)$$

where all velocities and accelerations are aerodynamic quantities, the subscript 'a' is omitted for convenience.

5-2-5 Transformation from F_b to F_k and derivation of $\boldsymbol{\Omega}_{kb}^k$

The transformation from the body-fixed reference frame to the aerodynamic reference frame consist of two rotations:

- rotation $-\alpha_k$ kinematic angle of attack about Y_b -axis
- rotation β_k kinematic sideslip angle about Z_k -axis

The rotation defines the following reference frames:

$$F_b \rightarrow F_{b'} \rightarrow F_k$$

The transformation matrix for the rotation from F_b to F_k is given by,

$$\begin{aligned} \mathbb{T}_{kb} &= \begin{bmatrix} \cos \beta_k & \sin \beta_k & 0 \\ -\sin \beta_k & \cos \beta_k & 0 \\ 0 & 0 & 1 \end{bmatrix} \begin{bmatrix} \cos \alpha_k & 0 & \sin \alpha_k \\ 0 & 1 & 0 \\ -\sin \alpha_k & 0 & \cos \alpha_k \end{bmatrix} \\ &= \begin{bmatrix} \cos \beta_k \cos \alpha_k & \sin \beta_k & \cos \beta_k \sin \alpha_k \\ -\sin \beta_k \cos \alpha_k & \cos \beta_k & -\sin \beta_k \sin \alpha_k \\ -\sin \alpha_k & 0 & \cos \alpha_k \end{bmatrix} \end{aligned} \quad (5-19)$$

The derivation of the angular velocity vector of Ω_{kb}^k is analogue to the derivation of Ω_{ab}^a :

$$\begin{aligned} \Omega_{kb}^k &= \mathbb{T}_{kb'} \Omega_{b'b}^{b'} + \Omega_{kb'}^k \\ &= \begin{bmatrix} -\dot{\alpha}_k \sin \beta_k \\ -\dot{\alpha}_k \cos \beta_k \\ \dot{\beta}_k \end{bmatrix} \end{aligned} \quad (5-20)$$

5-2-6 Transformation from F_E to F_t and derivation of Ω_{tE}^t

The transformation from earth-fixed reference frame F_E to the tether-fixed reference frame F_t is done by two sequential rotations:

- rotation ψ_t , tether yaw angle, about Z_E -axis
- rotation θ_t , tether pitch angle, about Y_t -axis

See figure 5-3 for the rotations and 5-4 for the complete picture.

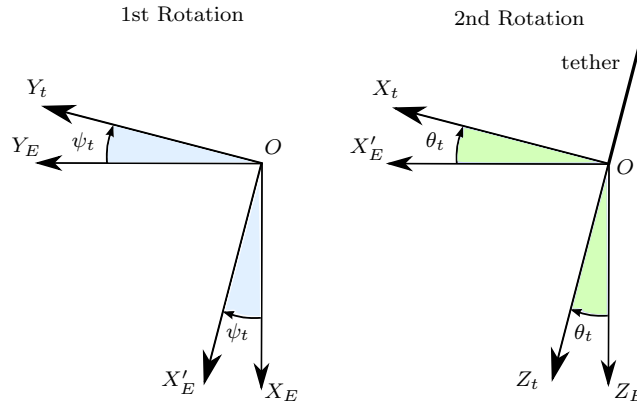


Figure 5-3: 1st rotation and 2nd rotation of the transformation from F_E to F_t

The rotation defines the following reference frames:

$$F_E \rightarrow F_{E'} \rightarrow F_t$$

One can see from figure 5-3 that the first rotation, the tether yaw angle ψ_t , defines the so called azimuth angle. The direction of the axis for the second rotation, Y_t , is now defined and the second

rotation gives the zenith angle. This way of defining the angles is convenient, because in every situation the value of the tether angles can be directly observed, i.e. a direct measure of the orientation of the tether with respect to the earth-fixed reference frame gives the azimuth and zenith angle. This in contrast to where one would first do a rotation about the Y_E -axis and then about the Z_t -axis.

The transformation matrix for the rotation from F_E to F_t is given by:

$$\begin{aligned} \mathbb{T}_{tE} &= \begin{bmatrix} \cos \theta_t & 0 & -\sin \theta_t \\ 0 & 1 & 0 \\ \sin \theta_t & 0 & \cos \theta_t \end{bmatrix} \begin{bmatrix} \cos \psi_t & \sin \psi_t & 0 \\ -\sin \psi_t & \cos \psi_t & 0 \\ 0 & 0 & 1 \end{bmatrix} \\ &= \begin{bmatrix} \cos \theta_t \cos \psi_t & \cos \theta_t \sin \psi_t & -\sin \theta_t \\ -\sin \psi_t & \cos \psi_t & 0 \\ \sin \theta_t \cos \psi_t & \sin \theta_t \sin \psi_t & \cos \theta_t \end{bmatrix} \end{aligned} \quad (5-21)$$

And the angular velocity vector of the tether reference frame F_t with respect to the earth-fixed reference frame F_E expressed in F_t using the rotational speed of the same rotations is given by:

$$\begin{aligned} \boldsymbol{\Omega}_{tE}^t &= \mathbb{T}_{tE'} \boldsymbol{\Omega}_{E'E}^{E'} + \boldsymbol{\Omega}_{tE'}^t \\ &= \begin{bmatrix} -\dot{\psi}_t \sin \theta_t \\ \dot{\theta}_t \\ \dot{\psi}_t \cos \theta_t \end{bmatrix} \end{aligned} \quad (5-22)$$

5-2-7 Transformation from F_t to F_b and derivation of $\boldsymbol{\Omega}_{tb}^t$

The transformation from tether-fixed reference frame F_t to the body-fixed reference frame F_b is done by three sequential rotations:

- rotation ξ , body yaw angle w.r.t. the tether, about Z_t -axis
- rotation κ , body pitch angle w.r.t. the tether, about $Y_{t'}$ -axis
- rotation τ , body roll angle w.r.t. the tether, about X_b -axis

The rotation defines the following reference frames:

$$F_t \rightarrow F_{t'} \rightarrow F_{t''} \rightarrow F_b$$

The transformation matrix for the rotation from F_t to F_b is given by:

$$\begin{aligned} \mathbb{T}_{bt} &= \begin{bmatrix} 1 & 0 & 0 \\ 0 & \cos \tau & \sin \tau \\ 0 & -\sin \tau & \cos \tau \end{bmatrix} \begin{bmatrix} \cos \kappa & 0 & -\sin \kappa \\ 0 & 1 & 0 \\ \sin \kappa & 0 & \cos \kappa \end{bmatrix} \begin{bmatrix} \cos \xi & \sin \xi & 0 \\ -\sin \xi & \cos \xi & 0 \\ 0 & 0 & 1 \end{bmatrix} \\ &= \begin{bmatrix} \cos \kappa \cos \xi & \cos \kappa \sin \xi & -\sin \kappa \\ \begin{pmatrix} \sin \tau \sin \kappa \cos \xi \\ -\cos \tau \sin \xi \end{pmatrix} & \begin{pmatrix} \sin \tau \sin \kappa \sin \xi \\ +\cos \tau \cos \xi \end{pmatrix} & \sin \tau \cos \kappa \\ \begin{pmatrix} \cos \tau \sin \kappa \cos \xi \\ +\sin \tau \sin \xi \end{pmatrix} & \begin{pmatrix} \cos \tau \sin \kappa \sin \xi \\ -\sin \tau \cos \xi \end{pmatrix} & \cos \tau \cos \kappa \end{bmatrix} \end{aligned} \quad (5-23)$$

The angular velocity vector of the body-fixed reference frame F_b with respect to the tether-fixed reference frame F_t expressed in F_t using the rotational speed of the same rotations is given by:

$$\begin{aligned} \boldsymbol{\Omega}_{bt}^b &= \mathbb{T}_{bt'} \boldsymbol{\Omega}_{t't}^{t'} + \mathbb{T}_{bt''} \boldsymbol{\Omega}_{t''t'}^{t''} + \boldsymbol{\Omega}_{bt''}^b \\ &= \begin{bmatrix} \dot{\tau} - \dot{\xi} \sin \kappa \\ \dot{\kappa} \cos \tau + \dot{\xi} \sin \tau \cos \kappa \\ -\dot{\kappa} \sin \tau + \dot{\xi} \cos \tau \cos \kappa \end{bmatrix} \end{aligned} \quad (5-24)$$

Now the angular velocity of the body-fixed reference frame with respect to the earth-fixed reference frame can also be written as:

$$\boldsymbol{\Omega}_{bE}^b = \boldsymbol{\Omega}_{bt}^b + \mathbb{T}_{bt} \boldsymbol{\Omega}_{tE}^t \quad (5-25)$$

and the transformation matrix from F_E to F_b can also be written as:

$$\mathbb{T}_{bE} = \mathbb{T}_{bt} \mathbb{T}_{tE} \quad (5-26)$$

The inverse of the transformations given in this section can be obtained by taking the inverse of the transformation matrices. Since all transformation matrices are orthogonal, i.e. orthonormal row and column vectors, the inverse of the transformation matrices is equal to their transpose, i.e. $\mathbb{T}^{-1} = \mathbb{T}^\top$.

5-3 The tether position and velocity in spherical coordinates

To define the position of the tether it is convenient to define a spherical coordinate system. The transformation from F_E to F_t is given by the two angles ψ_t and θ_t . To define the position of the top end of the tether an additional coordinate is needed. This coordinate is the absolute length of the tether denoted l_t . This defines the spherical coordinates as, see also figure 5-4:

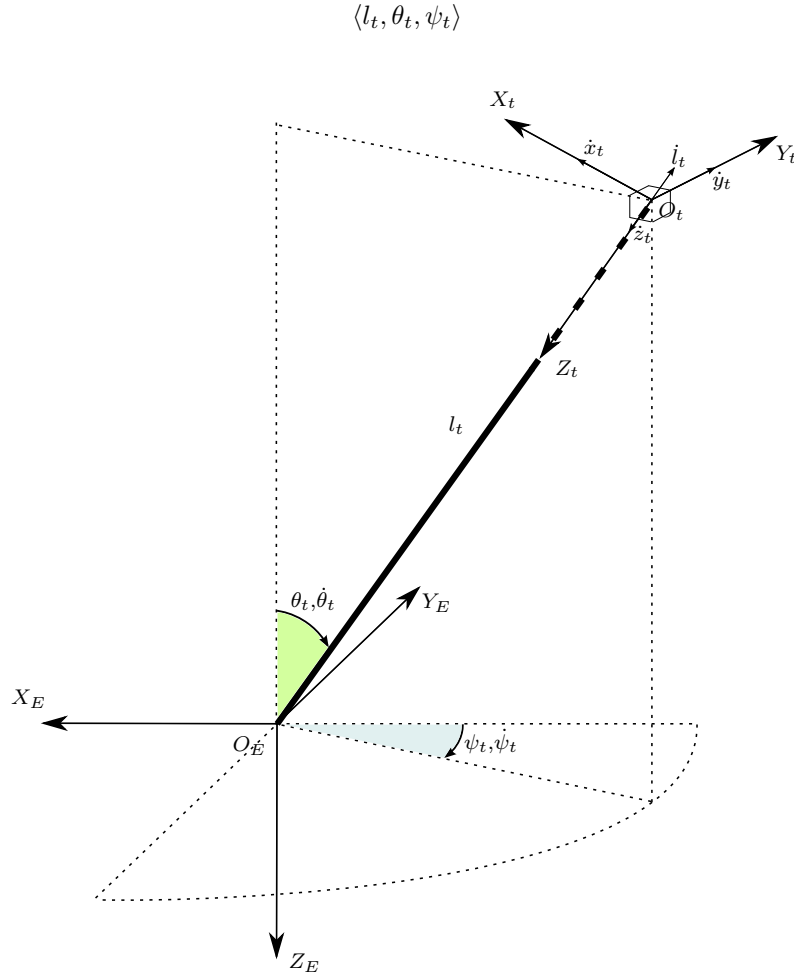


Figure 5-4: Tether position and velocity in spherical coordinates

It must be noted that due to the chosen rotation order of the angles ψ_t and θ_t that the X_t -axis always crosses the negative Z_E -axis. Furthermore it must be noted that the position of the tether can only be captured by these three coordinates if the tether is assumed to be a straight line.

The previously defined coordinates can be determined by the relations given in equation (5-27), which are obtained by investigating figure 5-4:

$$\begin{aligned} l_t &= \sqrt{(x_t^E)^2 + (y_t^E)^2 + (z_t^E)^2} \\ \theta_t &= \arctan\left(\frac{x_t^E}{z_t^E \cos \psi_t}\right) \quad \text{for} \quad -\frac{1}{2}\pi < \theta_t < \frac{1}{2}\pi \\ \psi_t &= \arctan\left(\frac{y_t^E}{x_t^E}\right) \quad \text{for} \quad -\frac{1}{2}\pi < \psi_t < \frac{1}{2}\pi \end{aligned} \quad (5-27)$$

where the coordinates $\langle x_t^E, y_t^E, z_t^E \rangle$ determine the position of the end point of the tether in the earth-fixed reference frame.

There are several limitations to the formulae in (5-27). The angles θ_t and ψ_t cannot become exactly $+\pi$ or $-\pi$ for singularity reasons. The second limitation is when the Y_E -axis is crossed ψ_t changes from $+\pi$ to $-\pi$ or vice versa. For the Rigid Body Kite model, chapter 6, this is overcome by integrating the time derivative of $\langle l_t, \theta_t, \psi_t \rangle$. \dot{l}_t , $\dot{\theta}_t$ and $\dot{\psi}_t$ are derived as follows.

If the kite is assumed to be a rigid body the velocity of the end point of the tether expressed in the tether-fixed reference frame $\langle \dot{x}_t^t, \dot{y}_t^t, \dot{z}_t^t \rangle$ is determined from the kinematic velocity of the kite and the rotational speed of the kite. From the theory of the planar motion of rigid bodies in reference [31] as a first approximation for a body with one tether attachment point equation (5-28) is derived:

$$\begin{bmatrix} \dot{x}_t^b \\ \dot{y}_t^b \\ \dot{z}_t^b \end{bmatrix} = \begin{bmatrix} u_k^b \\ v_k^b \\ w_k^b \end{bmatrix} + \boldsymbol{\Omega}_{bE}^b \times \mathbf{r}_{ta} \quad (5-28)$$

where \mathbf{r}_{ta} is the average position of the two tether attachment points relative to the center of gravity of the kite in body-fixed axes. An explanation of \mathbf{r}_{ta} with respect to \mathbf{r}_{taL} and \mathbf{r}_{taR} is given in section 6-3-3.

If the velocity of the end point of the tether in earth axes is known, than the velocity of the end point of the tether can be transformed in tether-fixed axes by equation (5-29):

$$\begin{bmatrix} \dot{x}_t^t \\ \dot{y}_t^t \\ \dot{z}_t^t \end{bmatrix} = \mathbb{T}_{tb} \begin{bmatrix} \dot{x}_t^b \\ \dot{y}_t^b \\ \dot{z}_t^b \end{bmatrix} \quad (5-29)$$

The time derivative of $\langle l_t, \theta_t, \psi_t \rangle$ is than given by equation (5-30), see figure 5-4:

$$\begin{aligned} \dot{l}_t &= -\dot{z}_t^t \\ \dot{\theta}_t &= -\frac{\dot{x}_t^t}{l_t} \\ \dot{\psi}_t &= -\frac{\dot{y}_t^t}{l_t \sin \theta_t} \end{aligned} \quad (5-30)$$

5-4 Wind kinematics

Since a kite flies under the influence of the wind, wind relations are required which describe the influence of the wind on the aerodynamic velocity and acceleration. The resulting equations are called the wind kinematics.

The aerodynamic velocity \mathbf{V}_a i.e. the actual wind velocity experienced by the kite, is given by the kinematic velocity of the kite \mathbf{V}_k and the wind speed \mathbf{V}_W . See figure 5-5.

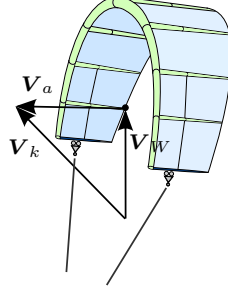


Figure 5-5: Wind velocity relation

The wind velocity vector is defined as the velocity of an undisturbed air particle W in the center of gravity cg expressed in the vehicle carried normal earth reference or the normal earth-fixed reference frame F_E for a flat and non-rotating earth:

$$\mathbf{V}_W = \mathbf{V}_{W,cg} = \frac{d\mathbf{W}_{cg}^E}{dt} = \begin{bmatrix} W_x \\ W_y \\ W_z \end{bmatrix}$$

The kinematic velocity is the velocity of the kite relative to the earth, which determines the actual displacements in x , y and z -direction. The aerodynamic velocity can be split up in the kinematic velocity and the wind velocity expressed in the earth-fixed reference frame by:

$$\begin{aligned} \mathbf{V}_a &= \mathbf{V}_k - \mathbf{V}_w \\ \mathbb{T}_{Eb} \begin{bmatrix} u_a \\ v_a \\ w_a \end{bmatrix} &= \mathbb{T}_{Eb} \begin{bmatrix} u_k \\ v_k \\ w_k \end{bmatrix} - \begin{bmatrix} W_x \\ W_y \\ W_z \end{bmatrix} \end{aligned} \quad (5-31)$$

The equations of motion will be written in the body-fixed reference frame. The aerodynamic velocity in the body-fixed reference frame is given by:

$$\begin{bmatrix} u_a \\ v_a \\ w_a \end{bmatrix} = \begin{bmatrix} u_k \\ v_k \\ w_k \end{bmatrix} - \mathbb{T}_{bE} \begin{bmatrix} W_x \\ W_y \\ W_z \end{bmatrix} \quad (5-32)$$

where the wind velocity in body-fixed reference frame is equivalent to:

$$\mathbf{V}_W^b = \mathbb{T}_{bE} \mathbf{V}_W^E$$

To derive the aerodynamic acceleration the time derivative of the wind velocity in body axes needs to be known. Use is made of the theory of the transformation of the derivative of a vector, reference [7]:

$$\begin{aligned} \frac{d\mathbf{V}_W^b}{dt} &= \frac{d}{dt} (\mathbb{T}_{bE} \mathbf{V}_W^E) \\ \dot{\mathbf{V}}_W^b &= \mathbb{T}_{bE} \frac{d\mathbf{V}_W^E}{dt} + \frac{d\mathbb{T}_{bE}}{dt} \mathbf{V}_W^E \\ \dot{\mathbf{V}}_W^b &= \mathbb{T}_{bE} \cdot \dot{\mathbf{V}}_W^E + \mathbb{T}_{bE} (\boldsymbol{\Omega}_{Eb}^E \times \mathbf{V}_W^E) \\ \dot{\mathbf{V}}_W^b &= \mathbb{T}_{bE} \cdot \dot{\mathbf{V}}_W^E - \boldsymbol{\Omega}_{bE}^b \times \mathbb{T}_{bE} \mathbf{V}_W^E \end{aligned} \quad (5-33)$$

Equation (5-32) can now be differentiated with respect to time to obtain the expression for the aerodynamic acceleration vector in terms of the kinematic velocity vector, the wind acceleration vector and the wind velocity vector:

$$\begin{aligned}\frac{d\mathbf{V}_a^b}{dt} &= \frac{d\mathbf{V}_k^b}{dt} - \frac{d}{dt} \left(\mathbb{T}_{bE} \mathbf{V}_W^E \right) \\ \dot{\mathbf{V}}_a^b &= \dot{\mathbf{V}}_k^b - \mathbb{T}_{bE} \cdot \dot{\mathbf{V}}_W^E + \boldsymbol{\Omega}_{bE}^b \times \mathbb{T}_{bE} \mathbf{V}_W^E\end{aligned}\quad (5-34)$$

Rigid Body Kite Model

This chapter derives the equations of motion for the Rigid Body Kite model. The equations describe a rigid body model attached to a straight line tether with two bridle lines. The tether attachment points control the kite like the cart and rail control system as discussed in chapter 2. The steps are partially analogue to the theory of flight dynamics for aircraft. Reference material for aircraft flight dynamics theory is found in [7], [23] and [24].

6-1 Derivation of the equations of motion

The derivation of the equations of motion is based on a single rigid body approach using Newton's second law. An arc-shaped LEI Surf Kite is a flexible body and is steered by deformation of the structure (reference [4]). The model is required to describe the dynamic motion as a function of rigid body states.

Newton's second law

The general force and moment equations expressed in the earth-fixed reference are according to Newton's second law:

$$m\mathbf{A}_{E,cg} = \mathbf{F}_{ext} \quad (6-1)$$

$$\frac{d\mathbf{B}_{cg}^E}{dt} = \mathcal{M}_{ext,cg} \quad (6-2)$$

where $\mathbf{A}_{E,cg}$ and $\frac{d\mathbf{B}_{cg}^E}{dt}$ are the inertial translational acceleration and the derivative of the inertial angular momentum respectively and \mathbf{F}_{ext} and $\mathcal{M}_{ext,cg}$ are the applied external forces and moments respectively.

The center of gravity (cg) is chosen as the reference point for the body in equations (6-1) and (6-2). Note that these equations hold for any body, flexible and rigid.

In flight dynamics the equations of motion are commonly expressed in the body-fixed reference frame. This is especially convenient when modelling the aerodynamic forces and moments of the body.

Translational and angular acceleration

The inertial translational acceleration in the body-fixed reference frame can be expressed as:

$$\begin{aligned} \mathbf{A}_{E,cg}^b &= \frac{d\mathbf{V}_{E,cg}^b}{dt} + \boldsymbol{\Omega}_{bE}^b \times \mathbf{V}_{E,cg}^b \\ &= \begin{bmatrix} \dot{u}_k \\ \dot{v}_k \\ \dot{w}_k \end{bmatrix} + \begin{bmatrix} p \\ q \\ r \end{bmatrix} \times \begin{bmatrix} u_k \\ v_k \\ w_k \end{bmatrix} \end{aligned} \quad (6-3)$$

$$= \begin{bmatrix} \dot{u}_k + qw_k - rv_k \\ \dot{v}_k + ru_k - pw_k \\ \dot{w}_k + pv_k - qu_k \end{bmatrix} \quad (6-4)$$

The time derivative of the inertial angular momentum in the body-fixed reference frame can be written as:

$$\begin{aligned} \left(\frac{d\mathbf{B}_{cg}^E}{dt} \right)^b &= \frac{d\mathbf{B}_{cg}^b}{dt} + \boldsymbol{\Omega}_{bE}^b \times \mathbf{B}_{cg}^b \\ &= \mathbb{I}_{cg}^b \frac{d\boldsymbol{\Omega}_{bE}^b}{dt} + \frac{d\mathbb{I}_{cg}^b}{dt} \boldsymbol{\Omega}_{bE}^b + \boldsymbol{\Omega}_{bE}^b \times \left(\mathbb{I}_{cg}^b \boldsymbol{\Omega}_{bE}^b \right) \end{aligned} \quad (6-5)$$

where $\boldsymbol{\Omega}_{bE}^b$ and \mathbb{I}_{cg}^b are the rotational velocity and the inertia tensor respectively given by:

$$\boldsymbol{\Omega}_{bE}^b = \begin{bmatrix} p \\ q \\ r \end{bmatrix} \quad (6-6)$$

$$\mathbb{I}_{cg}^b = \begin{bmatrix} I_{xx} & -J_{xy} & -J_{xz} \\ -J_{yx} & I_{yy} & -J_{yz} \\ -J_{zx} & -J_{zy} & I_{zz} \end{bmatrix} \quad (6-7)$$

For a rigid body model the time derivative of the inertia tensor is zero.

6-2 External forces and moments

The translational and angular acceleration are driven by external forces and moments. Firstly the forces and moments are defined expressed in the body-fixed reference frame. Secondly a general state dependency analysis is performed for the forces and moments. The analysis is used to justify the modelling assumptions.

6-2-1 Definition of external forces and moments

There are three types of external forces acting on a kite:

1. Aerodynamic forces
2. Tether forces
3. Gravity

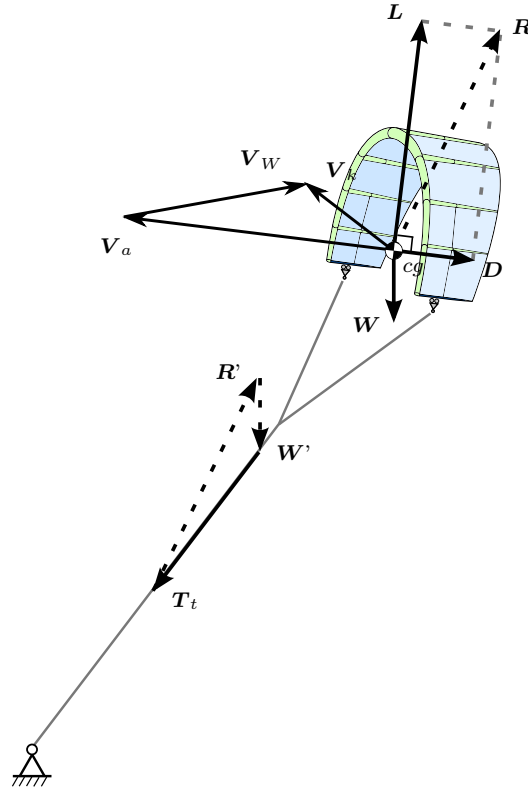


Figure 6-1: Forces acting on a kite

The aerodynamic forces and gravity are distributed forces by nature. These distributed forces can be replaced by point forces acting on particular points on the body simplifying the equations of motion. The tether forces are already point forces acting on the so called tether attachment points (ta). The resultant aerodynamic force \mathbf{R} , the resultant tether force \mathbf{T} and gravity (weight) \mathbf{W} are shown in figure 6-1.

The direction of the lift vector \mathbf{L} is defined perpendicular to the direction of the aerodynamic velocity \mathbf{V}_a and the direction of the drag vector \mathbf{D} is defined tangential and opposite to the direction of the aerodynamic velocity. The aerodynamic velocity is the resultant of the wind component \mathbf{V}_w and the kinematic velocity \mathbf{V}_k (see equation (5-32)). The tether force \mathbf{T} the aerodynamic force \mathbf{R} and the weight \mathbf{W} are in equilibrium when the kite is not accelerating.

The aerodynamic force vector in the body-fixed reference frame is given by:

$$\mathbf{R}^b = \mathbf{F}_{aero}^b = \begin{bmatrix} X \\ Y \\ Z \end{bmatrix} \quad (6-8)$$

The tether force vector in the body-fixed reference frame is defined as:

$$\mathbf{T}_t^b = \mathbf{F}_{tether}^b = \begin{bmatrix} F \\ G \\ H \end{bmatrix} \quad (6-9)$$

The gravity vector in the body-fixed reference frame is given by:

$$\begin{aligned}\mathbf{W}_G^b &= m \cdot \mathbb{T}_{bE} \mathbf{g}_G^E \\ &= m \cdot g_G \begin{bmatrix} -\sin \theta \\ \sin \phi \cos \theta \\ \cos \phi \cos \theta \end{bmatrix}\end{aligned}\quad (6-10)$$

The external forces generate external moments about the center of gravity. The aerodynamic moment vector in the body-fixed reference frame is defined as:

$$\mathcal{M}_{aero, cg}^b = \begin{bmatrix} L \\ M \\ N \end{bmatrix}\quad (6-11)$$

The tether moment vector in the body-fixed reference frame is defined as:

$$\mathcal{M}_{tether, cg}^b = \begin{bmatrix} P \\ Q \\ R \end{bmatrix} = \mathbf{r}_{ta} \times \mathbf{F}_{tether}^b\quad (6-12)$$

where \mathbf{r}_{ta} is the position of the tether attachment point relative to the center of gravity in the body fixed reference frame.

6-2-2 External forces and moments state dependency analysis

All forces and moments are dependent on the *entire time history* of the body states. The question is which states influence which forces and moments and to what extend contributes the time history. With the state dependency analysis an attempt is made to find an initial guess on which states the aerodynamic forces and moments and tether forces and moments depend on.

In general for rigid body aircraft models the aerodynamic forces and moments are assumed to be dependent on the components of the *aerodynamic motion variables* and *control deflections*. Because the body is rigid there is no influence of body deformation states. Off course, the shape of the body influences the aerodynamics. Therefore for flexible kites the structural deformation is possibly non-negligible. The state vector ζ is defined which includes all possible *deformation parameters*, like mean aerodynamic chord \bar{c} , wing span b , projected surface area S and others. For example an aeroelastic deflection angle κ_a .

The tether forces and moments acting on the body are a reaction of the aerodynamic forces and gravity dependent on the shape of the tether and the position of the tether attachment points. All these forces influence the body shape. And the body shape influences the aerodynamic forces and moments and thereby the tether forces. Resulting in a recursive loop.

The state dependency of the aerodynamic forces and moments can be stated as follows:

$$\begin{aligned}X, Y, Z, L, M, N, F, G, H, P, Q, R \rightarrow \\ f(\mathbf{W}_G^b, u_a(\cdot), v_a(\cdot), w_a(\cdot), p(\cdot), q(\cdot), r(\cdot), \mathbf{r}_{taL}(\cdot), \mathbf{r}_{taR}(\cdot), \zeta(\cdot), l_t(\cdot), \mathbf{e}_{t,E}(\cdot), \mathbf{e}_{t,b}(\cdot), V_W(\cdot))\end{aligned}\quad (6-13)$$

where (\cdot) denotes that the function contains information about the entire time history of the kite system. $u_a(\cdot)$, $v_a(\cdot)$, $w_a(\cdot)$, $p(\cdot)$, $q(\cdot)$ and $r(\cdot)$ are defined in chapter 5. \mathbf{r}_{taL} and \mathbf{r}_{taR} are the positions of the pinion on the left and right tip respectively with respect to the center of gravity. $l_t(\cdot)$ is the length of the tether and $\mathbf{e}_{t,E}(\cdot)$ and $\mathbf{e}_{t,b}(\cdot)$ are the unit vectors of the tether at the origin of the earth-fixed reference frame and at the two top ends point of the tether respectively denoting the direction of the tether at the bottom end and the average direction of the two top ends of the tether. It is assumed that these three tether states determine the complete shape of the tether.

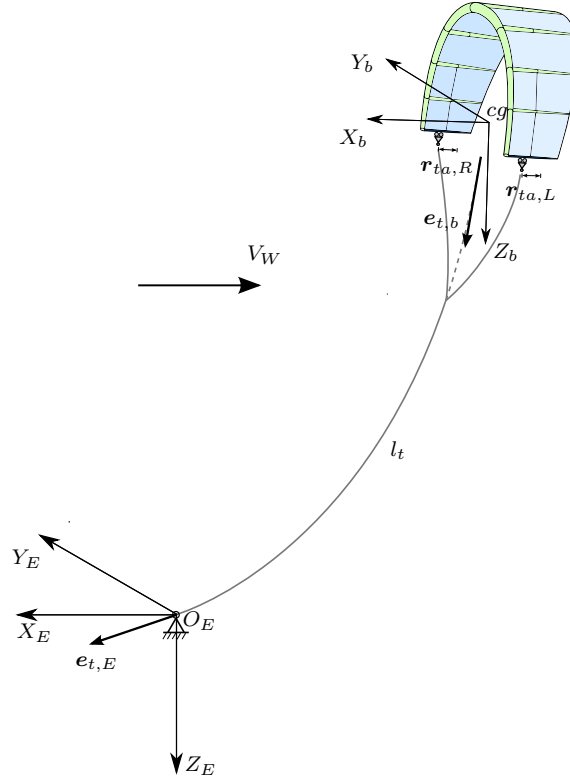


Figure 6-2: Definition of tether and control parameters

Figure 6-2 shows the definition of the tether and control parameters $l_t(\cdot)$, $e_{t,E}(\cdot)$, $e_{t,b}(\cdot)$, $r_{taL}(\cdot)$ and $r_{taR}(\cdot)$. The wind velocity $V_W(\cdot)$ is not only acting at the reference point of the body but along the entire tether length l_t .

The first assumption that is applied is that there is no coupling between the aerodynamic forces and moments and the tether forces and moments. In other words, the aerodynamic forces and moments are independent of the tether forces. This can be seen as follows. The aerodynamic variables cause a resultant aerodynamic force and moment. The aerodynamic force causes a resultant tether force. For flexible bodies the tether force will change the body shape. The change in body shape will have an influence on the aerodynamic forces and moments. With this assumption the influence of the *time derivatives* of the resultant tether force on the body shape is neglected. Taking this effect into account results in an algebraic loop, which should be solved by an iteration process every time step. Iterative processes are unwanted, because they slow down the simulation speed of the model. Instead the *static* solutions of this iterative process are taken into account by the aerodynamic derivatives. The aerodynamic derivatives are explained in section 6-3-2.

Secondly, for most flight conditions the aerodynamic and tether forces are at least several times larger than the weight of the body making the influence of the weight on the body shape practically insignificant.

For the function expression in equation (6-13) can now be written:

$$X, Y, Z, L, M, N \rightarrow f(u_a(\cdot), v_a(\cdot), w_a(\cdot), p(\cdot), q(\cdot), r(\cdot), r_{taL}(\cdot), r_{taR}(\cdot), \zeta(\cdot)) \quad (6-14)$$

$$F, G, H, P, Q, R \rightarrow f(r_{taL}(\cdot), r_{taR}(\cdot), l_t(\cdot), e_{t,E}(\cdot), e_{t,b}(\cdot), V_W(\cdot)) \quad (6-15)$$

To unravel the time history dependent state variables Taylor expansions are made. This results

in functions given by a summation of different contributions. For example for $u_a(\cdot)$ this becomes:

$$u_a(\cdot) = u_a(t) + \sum_{i=1}^{\infty} \frac{1}{i!} \frac{d^i u_a}{dt^i} \Delta t^i \quad (6-16)$$

For aircraft, practice has shown that the influence of most time derivatives is limited and can be neglected, i.e. the summation in equation (6-16). But there are a few exceptions, see reference [24], like $\dot{\alpha}$ and $\dot{\beta}$. These parameters are damping terms and are very likely to influence the dynamics of kites as well. Furthermore, as the arc-shaped kite is deformable it is also likely that higher order terms play a significant role. Additionally, cross terms can be important as well. Cross terms define the coupling between two or more states.

Since there is no reference for modelling the aerodynamics of kites, the analysis for the aerodynamic forces stops here. An attempt to find an aerodynamic model for an arc-shaped kite is given in chapter 10. The aerodynamic velocity components are usually written in the spherical coordinates V_a , α and β as given by equations (5-12), (5-13), (5-17) and (5-18) for the first derivative with respect to time.

An example of the time dependency of the aerodynamic states can be given when an arc-shaped kite is flying with a changing side slip angle. The tip of the kite which is turned into the wind is slightly more upwind than the other kite tip. The upwind kite tip will change the wind stream around the kite and the wind on the downstream tip some time Δt later. The pressure distribution on the downstream will change and therefore also the resultant aerodynamic forces and moments.

For the tether it is assumed that it can be represented by a straight line, that is there is no cable sag. This assumption results in the fact that the tether is relatively short. For short tethers, as a first approximation, it is reasonable to assume that the wind speed has no influence on the tether forces. For the states influencing the tether force this means that $e_{t,E}^b(\cdot) = e_{t,b}^b(\cdot)$ and that $V_w(\cdot)$ are neglected. Furthermore the resultant tether moment is a function of the tether force and the position of the tether attachment points $\mathbf{r}_{taL}(\cdot)$ and $\mathbf{r}_{taR}(\cdot)$, where the tether force is independent of the tether attachment points.

The tether unit vector \mathbf{e}_t expressed in the body-fixed reference frame is defined by three angles τ , κ and ξ as defined by the transformation from F_t to F_b . The transformation of the tether force in the tether-fixed reference frame to the body-fixed reference frame is given by:

$$\begin{aligned} \mathbf{T}^b &= \mathbb{T}_{bt} \mathbf{T}^t \\ \begin{bmatrix} F \\ G \\ H \end{bmatrix} &= \mathbb{T}_{bt} \begin{bmatrix} 0 \\ 0 \\ T_t \end{bmatrix} \\ \begin{bmatrix} F \\ G \\ H \end{bmatrix} &= T_t \begin{bmatrix} -\sin \kappa \\ \sin \tau \cos \kappa \\ \cos \tau \cos \kappa \end{bmatrix} \end{aligned} \quad (6-17)$$

Note that there is no influence of the angle ξ on the tether forces. As κ and τ are transformation angles, they do not influence the resultant tether T_t directly.

For the control positions, see section 6-3-3, it is assumed that the carts are constrained to move in X_b direction. This implies that the states for the control positions can be given by $x_{taL}(\cdot)$ and $x_{taR}(\cdot)$. As the controls move the center of gravity shifts relative to the body due to the weight of the carts. This results in the fact that the reference point of the aerodynamic forces and moments changes with respect to the body (read: aerodynamic body). So it can be concluded that not only the deformation induced results in a change in aerodynamic forces and moments but also the shift of the center of gravity.

This results in the following states for the aerodynamic and tether forces and moments:

$$X, Y, Z, L, M, N \rightarrow f(V_a(\cdot), \alpha(\cdot), \beta(\cdot), p(\cdot), q(\cdot), r(\cdot), x_{taL}(\cdot), x_{taR}(\cdot), \zeta(\cdot)) \quad (6-18)$$

$$F, G, H, P, Q, R \rightarrow f(l_t(\cdot), \tau, \kappa, \mathbf{r}_{taL}, \mathbf{r}_{taR}) \quad (6-19)$$

With the following assumptions:

- The tether is a straight line $\mathbf{e}_{t,E}^b(\cdot) = \mathbf{e}_{t,b}^b(\cdot)$
- The wind speed $V_W(\cdot)$ has no influence on the tether forces
- States influencing aerodynamic forces and moments have no direct influence on the resultant tether force T_t and the tether force has no influence on the aerodynamic forces and moments
- The control positions are constrained to move in X_b direction

The kite system model with the given assumptions and the definition of the reference frames is illustrated in figure 6-3.

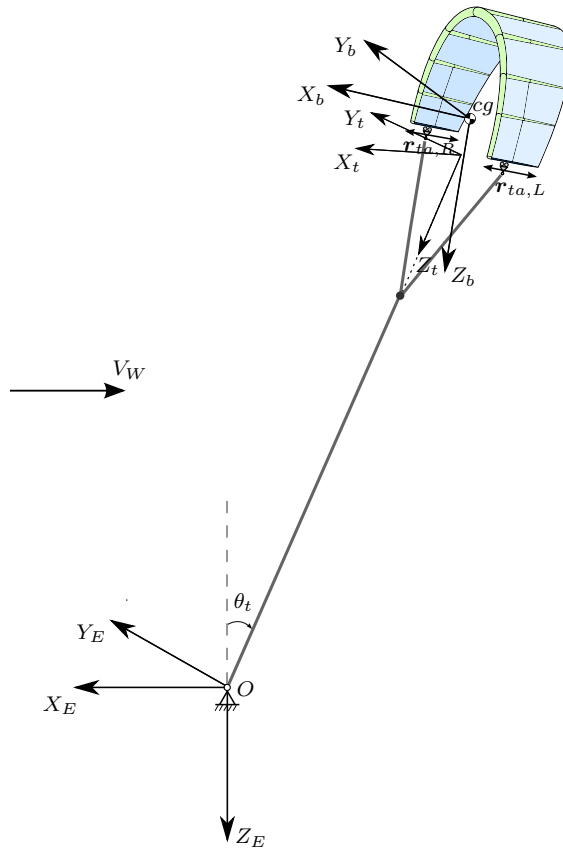


Figure 6-3: Kite system model and definition of reference frames

6-3 Complete set of equations

6-3-1 Equations of motion and kinematic relations

The equations of motion in the body-fixed reference frame are:

$$m \begin{bmatrix} \dot{u}_k + qw_k - rv_k \\ \dot{v}_k + ru_k - pw_k \\ \dot{w}_k + pv_k - qu_k \end{bmatrix} = mg_G \begin{bmatrix} -\sin\theta \\ \sin\phi \cos\theta \\ \cos\phi \cos\theta \end{bmatrix} + \begin{bmatrix} X \\ Y \\ Z \end{bmatrix} + \begin{bmatrix} F \\ G \\ H \end{bmatrix} \quad (6-20)$$

$$\mathbb{I}_{cg}^b \frac{d\Omega_{bE}^b}{dt} + \Omega_{bE}^b \times (\mathbb{I}_{cg}^b \Omega_{bE}^b) = \begin{bmatrix} L \\ M \\ N \end{bmatrix} + \begin{bmatrix} P \\ Q \\ R \end{bmatrix} \quad (6-21)$$

The kinematic relations for the rotational rates of the body can be obtained from equations (5-7) and (6-6):

$$\begin{bmatrix} \dot{\phi} \\ \dot{\theta} \\ \dot{\psi} \end{bmatrix} = \begin{bmatrix} 1 & \sin\phi \tan\theta & \cos\phi \tan\theta \\ 0 & \cos\phi & -\sin\phi \\ 0 & \frac{\sin\phi}{\cos\theta} & \frac{\cos\phi}{\cos\theta} \end{bmatrix} \begin{bmatrix} p \\ q \\ r \end{bmatrix} \quad (6-22)$$

Furthermore additional kinematic relations due to the tether are given by equations (5-28), (5-29) and (5-30):

$$\begin{bmatrix} \dot{x}_t^t \\ \dot{y}_t^t \\ \dot{z}_t^t \end{bmatrix} = \mathbb{T}_{tb} \left(\begin{bmatrix} u_k \\ v_k \\ w_k \end{bmatrix} + \Omega_{bE}^b \times \mathbf{r}_{ta}^b \right) \quad (6-23)$$

$$\begin{bmatrix} \dot{l}_t \\ \dot{\theta}_t \\ \dot{\psi}_t \end{bmatrix} = \begin{bmatrix} 0 & 0 & -1 \\ -\frac{1}{l_t} & 0 & 0 \\ 0 & -\frac{1}{l_t \sin\theta_t} & 0 \end{bmatrix} \begin{bmatrix} \dot{x}_t^t \\ \dot{y}_t^t \\ \dot{z}_t^t \end{bmatrix} \quad (6-24)$$

The aerodynamic forces and moments are dependent on the aerodynamic velocity and acceleration. So the set completes by adding the wind relations describing the aerodynamic velocity (5-32) and aerodynamic acceleration (5-34):

$$\begin{bmatrix} u_a \\ v_a \\ w_a \end{bmatrix} = \begin{bmatrix} u_k \\ v_k \\ w_k \end{bmatrix} - \mathbb{T}_{bE} \begin{bmatrix} W_x \\ W_y \\ W_z \end{bmatrix} \quad (6-25)$$

$$\begin{bmatrix} \dot{u}_a \\ \dot{v}_a \\ \dot{w}_a \end{bmatrix} = \begin{bmatrix} \dot{u}_k \\ \dot{v}_k \\ \dot{w}_k \end{bmatrix} - \mathbb{T}_{bE} \cdot \begin{bmatrix} \dot{W}_x \\ \dot{W}_y \\ \dot{W}_z \end{bmatrix} + \begin{bmatrix} p \\ q \\ r \end{bmatrix} \times \mathbb{T}_{bE} \begin{bmatrix} W_x \\ W_y \\ W_z \end{bmatrix} \quad (6-26)$$

6-3-2 Nonlinear aerodynamic model

The aerodynamic forces and moments in the body-fixed reference frame are given by X , Y , Z , L , M and N .

The aerodynamic forces and moments are a function of specific aerodynamic states as given by (6-14). As discussed in the previous section the forces and moments depend on the entire time history of the states. The question is which states and which derivatives of these states should be

taken into account to model a kite significantly accurate. For now, the only reference there is is the analysis of previous section and the resulting relation given by equation (6-18):

$$X, Y, Z, L, M, N \rightarrow f(V_a(\cdot), \alpha(\cdot), \beta(\cdot), p(\cdot), q(\cdot), r(\cdot), x_{taL}(\cdot), x_{taR}(\cdot), \zeta(\cdot))$$

The following step is to write the forces and moments in dimensionless form by dividing by $\frac{1}{2}\rho V_a^2 S$ for the forces, by $\frac{1}{2}\rho V_a^2 S \bar{c}$ for the symmetric moments and by $\frac{1}{2}\rho V_a^2 S b$ for the asymmetric moments. In this way the forces and moments become independent of the dynamic pressure $\frac{1}{2}\rho V_a^2$ and the geometric properties S , \bar{c} and b . This results in the dimensionless coefficients C_X , C_Y , C_Z , C_l , C_m and C_n . Note that S , \bar{c} and b are variable due to the flexible structure of an arc-shaped LEI Kite.

The procedure continues by applying Taylor expansions on the dimensionless functions. This results in an infinite amount of summation terms. The effect of most higher order terms are negligible. The remaining states are written in dimensionless form as well. This results in functions with nonlinear summation terms dependent on dimensionless states and aerodynamic coefficients C_{x_y} .

The aerodynamic coefficients themselves are dependent on the reference condition for the Taylor expansion. With aircraft flight test techniques the aerodynamic coefficient are identified by a fitting procedure for the measured aerodynamic forces and moments. Reference [23] can be consulted for this *parameter identification* technique using a *linear regression* method. With this method the flight tests always start from a stationary statically stable condition. The resulting linear aerodynamic functions are than only valid for some specific domain around the initial condition. To increase the validity domain of the aerodynamic model more flight tests are performed at other initial conditions. All resulted aerodynamic functions can be ‘tied together’ to form the aerodynamic model. In this way the parameters in the model become a function of some set of static variables. Additionally this technique can be applied to obtain nonlinear functions as well. With nonlinear functions the validity range of the function is increased.

Equation (2-1) shows an example of an aerodynamic model structure for *aircraft*. In these equations there is no coupling between the symmetric and asymmetric forces and moments, which means that that the symmetric states have no influence on the asymmetric forces and moments and vice versa. These assumptions are applicable to most aircraft models. A methodology for the derivation of aerodynamic models for *kites* is given in chapter 10 where the ADAMS multi-body model is used as a reference.

6-3-3 Definition of control positions

The position of the tether attachment points or the control units expressed in the body-fixed reference frame are given by:

$$\mathbf{r}_{taL} = \begin{bmatrix} x_{taL} \\ y_{taL} \\ z_{taL} \end{bmatrix} \quad \mathbf{r}_{taR} = \begin{bmatrix} x_{taR} \\ y_{taR} \\ z_{taR} \end{bmatrix} \quad (6-27)$$

Figure 6-4 shows the definition of the control positions in an illustrative way.

Based on this definition it is possible to define an ‘average’ or central position. This is convenient when the controls are moved symmetrically and only one control variable has to be defined:

$$\mathbf{r}_{ta} = \begin{bmatrix} \frac{x_{taL} + x_{taR}}{2} \\ \frac{y_{taL} + y_{taR}}{2} \\ \frac{z_{taL} + z_{taR}}{2} \end{bmatrix} \quad (6-28)$$

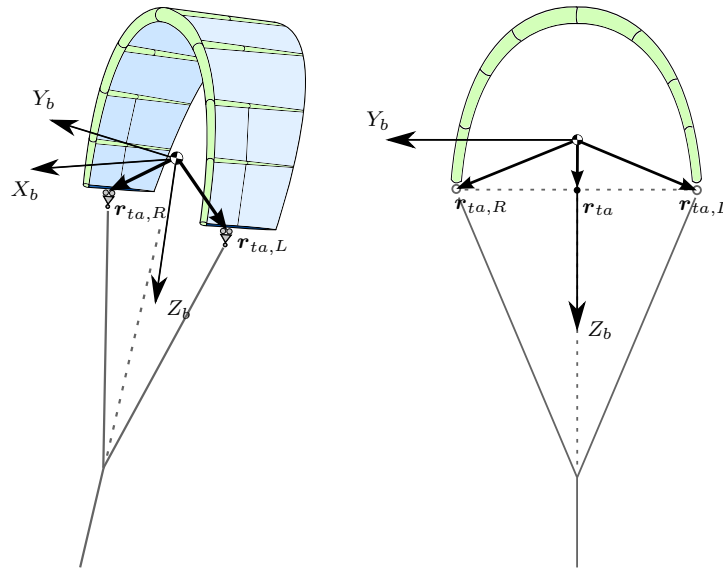


Figure 6-4: Definition of the control parameters

Furthermore this central control position r_{ta} defines the position of the action point of the main tether. See the right picture of figure 6-4.

For simplicity it is assumed that x_{taL} and x_{taR} are the only varying parameters. This holds when the displacement of the control positions in Y_b or Z_b direction is relatively small and the X_b -axis is parallel to the rail.

Figure 6-5 shows the definition of the control position relative to the leading edge of the tip d_{ta} . d_{ta} is expressed in the local coordinate system F_r . d_{taL} and d_{taR} for left and right position respectively are the actual control inputs for a real kite and for the ADAMS model.

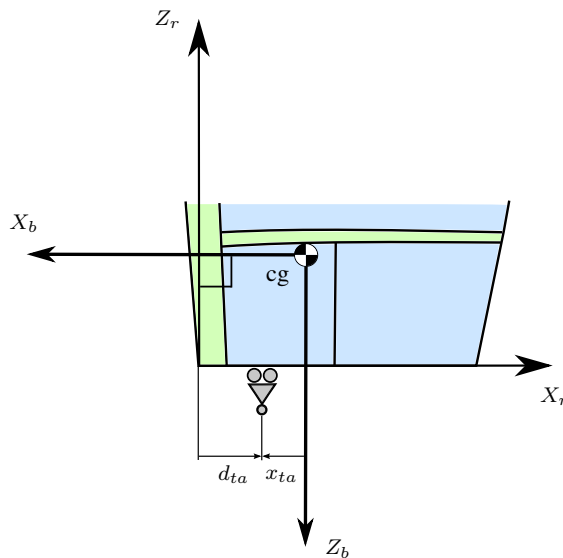


Figure 6-5: Definition of control parameter d_{ta}

In ADAMS it is possible to measure r_{taL} and r_{taR} . Because the control carts have weight the center of gravity position shifts when applying a control input. Therefore a relation is required

between x_{ta} and d_{ta} for the Rigid Body model. The derived relation between x_{taL} and d_{taL} and between x_{taR} and d_{taR} is given in chapter 9.

6-3-4 Tether model

The tether forces and moments are a function of the states given by (6-19):

$$F, G, H, P, Q, R \rightarrow f(l_t(\cdot), \tau, \kappa, \mathbf{r}_{taL}, \mathbf{r}_{taR})$$

Main tether

The main tether force is modelled as a spring-damper and this is represented by equation (6-29):

$$T_t(\delta l_t(t), \dot{l}_t(t)) = k_t \cdot \delta l_t(t) + c_t \cdot \dot{l}_t(t) \quad (6-29)$$

where k_t and c_t are the spring and damper constants of the respective tether and are invariant.

The initial tether length at ' $t = 0$ s' is given by the formula in (6-30):

$$l_{t0} = l_{t, \delta l_t=0} + \delta l_{t0} \quad (6-30)$$

where $l_{t, \delta l_t=0}$ is the unstretched tether length and δl_{t0} the initial tether elongation.

The tether forces and moments in the body-fixed reference frame are determined by equations (6-17) and (6-12) respectively. In (6-12) \mathbf{r}_{ta}^b is the position of the tether attachment point or control input. How this is modelled for the two independent control points \mathbf{r}_{taL} and \mathbf{r}_{taR} is given below in the section about the bridle lines.

Bridle lines

This section gives a method to model the change in forces in the bridle lines. The bridle lines constrain the kite in a mix of roll (p) and yaw (r) motion depending on the body pitch angle with respect to the tether κ . See figures 6-6, 6-7 and 6-8.

For simplicity of implementation the bridle lines are not explicitly modelled by two spring-dampers for example, but rather by a moment caused by the main tether force in Y_b -direction: G . The tether force in body components is shown in figure 6-7.

When the tether has a tether force T and the tether is in the symmetric plane of the kite, that is τ and ξ are zero, the vertical components of the forces in the bridle lines are equal to $\frac{1}{2}T$. Furthermore the tether force in Y_b -direction G is zero, so $\frac{1}{2}T$ is equal to $\frac{1}{2}\sqrt{F^2 + H^2}$.

Two assumptions are made for modelling the forces in the bridle lines:

1. The forces act in the $Y_t Z_t$ -plane or parallel to this plane
2. The bridle angle ϑ is invariant

From the first assumption follows that the angle between the bridle line and the main line in the $X_t Z_t$ -plane stays small. From the second assumption follows that the elastic elongation of the bridle lines stays small.

The absolute value of the tether forces in the bridle lines are given by the parameters T_L and T_R for the left and right bridle line respectively. The vertical components in the $Y_t Z_t$ -plane are given by the parameters T_L^v and T_R^v . The horizontal components in the $Y_t Z_t$ -plane are given by the

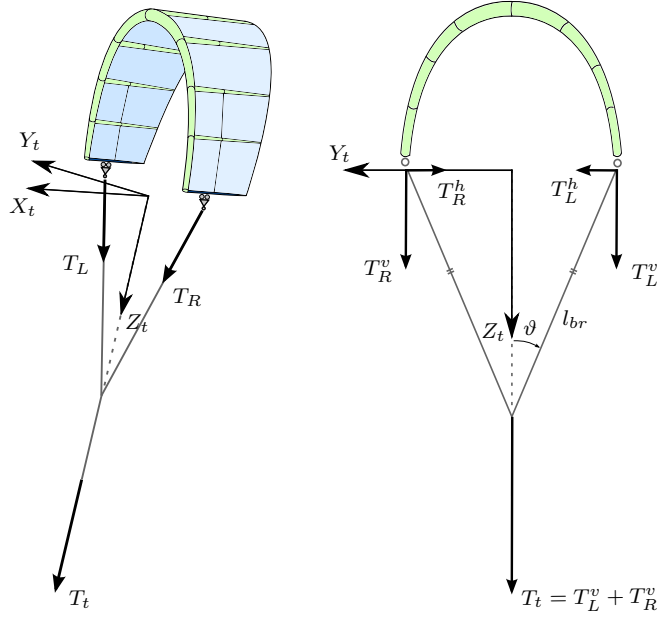


Figure 6-6: Bridle line forces, $G = 0$

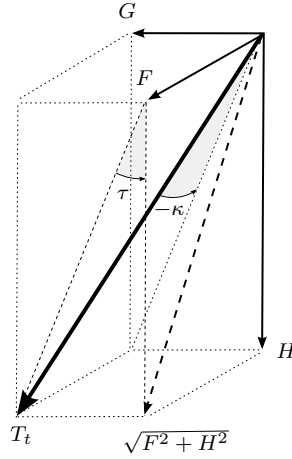


Figure 6-7: Tether force T_t in body components F , G and H

parameters T_L^h and T_R^h . See figure 6-6. Furthermore the bridle angle is specified by ϑ as shown in figure 6-6. The absolute value of the forces in the bridle lines can be written as:

$$\begin{aligned} T_L &= \sqrt{T_L^v{}^2 + T_L^h{}^2} \\ T_R &= \sqrt{T_R^v{}^2 + T_R^h{}^2} \end{aligned} \quad (6-31)$$

Now when the tether force component G has a nonzero value the forces in the bridle lines will not be equal anymore. A moment acting in the $X_t Z_t$ -plane will result to counteract this asymmetric condition.

This moment, given by \mathcal{M}_{bridle} , is simply equal to:

$$\mathcal{M}_{bridle} = -G \cdot l_{br} \cos \vartheta \quad (6-32)$$

where l_{br} is the length of one of the bridle lines. See figure 6-8.

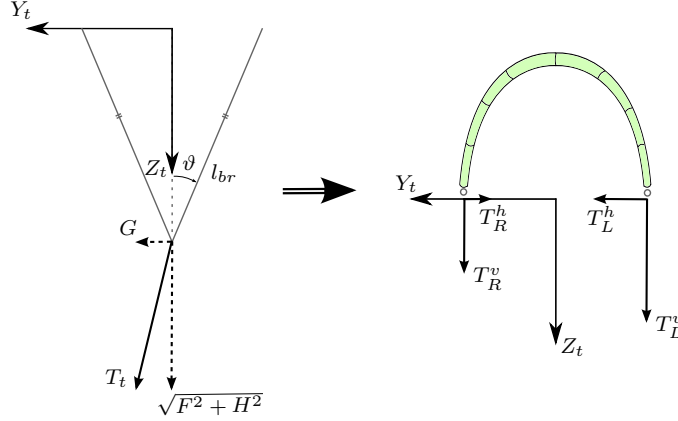


Figure 6-8: Bridle line forces, $G \neq 0$

As this moment is actually caused by a difference in the bridle line forces, this moment is transferred by the bridle line forces T_L and T_R to the body. Only the change in the vertical components of the bridle lines will transfer this moment, as the horizontal components do not act about the arm l_{br} , because they act about $\langle x_{taL}, z_{taL} \rangle$ and $\langle x_{taR}, z_{taR} \rangle$. The change in the vertical components will cause a moment given by:

$$\mathcal{M}_{bridle} = (\Delta T_R^v - \Delta T_L^v) \cdot l_{br} \sin \vartheta$$

Because it is assumed that ϑ is constant, it means that ΔT_R^v is equal to $-\Delta T_L^v$. From this follows that:

$$\Delta T_L^v = -\Delta T_R^v = \frac{1 \cos \vartheta}{2 \sin \vartheta} \cdot G = \frac{G}{2 \tan \vartheta}$$

Now the vertical components of the bridle forces are given by equations (6-33):

$$\begin{aligned} T_L^v &= \frac{1}{2} T_{G=0} + \Delta T_L^v \\ &= \frac{1}{2} \left(\sqrt{F^2 + H^2} + \frac{G}{\tan \vartheta} \right) \\ T_R^v &= \frac{1}{2} T_{G=0} + \Delta T_R^v \\ &= \frac{1}{2} \left(\sqrt{F^2 + H^2} - \frac{G}{\tan \vartheta} \right) \end{aligned} \tag{6-33}$$

The horizontal components of the bridle T_L^h and T_R^h follow from force equilibrium and the fact that ϑ is constant:

$$\begin{aligned} T_L^h &= T_{L,G=0}^h + \frac{1}{2} G \\ &= \frac{1}{2} T_{G=0} \tan \vartheta + \frac{1}{2} G \\ T_R^h &= T_{R,G=0}^h - \frac{1}{2} G \\ &= \frac{1}{2} T_{G=0} \tan \vartheta - \frac{1}{2} G \end{aligned} \tag{6-34}$$

If the bridle line forces are given in components of the body-fixed reference frame $\langle F_L, G_L, H_L \rangle$

and $\langle F_R, G_R, H_R \rangle$ than the bridle line moments \mathcal{M}_{tL} and \mathcal{M}_{tR} are obtained by equations (6-35):

$$\begin{aligned}\mathcal{M}_{tL} &= \begin{bmatrix} P_L \\ Q_L \\ R_L \end{bmatrix} = \mathbf{r}_{taL} \times \begin{bmatrix} F_L \\ G_L \\ H_L \end{bmatrix} \\ \mathcal{M}_{tR} &= \begin{bmatrix} P_R \\ Q_R \\ R_R \end{bmatrix} = \mathbf{r}_{taR} \times \begin{bmatrix} F_R \\ G_R \\ H_R \end{bmatrix}\end{aligned}\quad (6-35)$$

where \mathbf{r}_{taL} and \mathbf{r}_{taR} are the left and right position vectors of the tether attachment point with respect to the center of gravity in the body-fixed reference frame. They are given by equations (6-36):

$$\begin{aligned}\mathbf{r}_{taL} &= \begin{bmatrix} x_{taL} \\ -l_{br} \sin \vartheta \\ z_{taL} \end{bmatrix} \\ \mathbf{r}_{taR} &= \begin{bmatrix} x_{taR} \\ l_{br} \sin \vartheta \\ z_{taR} \end{bmatrix}\end{aligned}\quad (6-36)$$

where it is assumed that y_{taL} is equal to $-y_{taR}$ by the fact that ϑ is invariable.

The total tether moment \mathcal{M}_t is obtained by adding the moments of the bridle lines $\mathcal{M}_{t,L}$ and $\mathcal{M}_{t,R}$, so:

$$\mathcal{M}_t = \begin{bmatrix} P \\ Q \\ R \end{bmatrix} = \begin{bmatrix} P_L \\ Q_L \\ R_L \end{bmatrix} + \begin{bmatrix} P_R \\ Q_R \\ R_R \end{bmatrix}\quad (6-37)$$

Writing the bridle forces T_L and T_R in body components is done by:

$$\begin{aligned}\begin{bmatrix} F_L \\ G_L \\ H_L \end{bmatrix} &= \mathbf{e}_L^b \cdot T_L \\ \begin{bmatrix} F_R \\ G_R \\ H_R \end{bmatrix} &= \mathbf{e}_R^b \cdot T_R\end{aligned}\quad (6-38)$$

where \mathbf{e}_L^b and \mathbf{e}_R^b are the unit vectors of the left and right bridle line respectively.

The direction of the bridle lines are determined by the angles κ and ϑ and their unit vectors are computed by:

$$\begin{aligned}\mathbf{e}_L^b &= \begin{bmatrix} -\sin \kappa \cos \vartheta \\ \sin \vartheta \\ \cos \kappa \cos \vartheta \end{bmatrix} \\ \mathbf{e}_R^b &= \begin{bmatrix} -\sin \kappa \cos \vartheta \\ -\sin \vartheta \\ \cos \kappa \cos \vartheta \end{bmatrix}\end{aligned}\quad (6-39)$$

where κ is a rotation about $Y_{t'}$ -axis and is given by (see figure 6-7):

$$\kappa = \arctan \left(-\frac{F}{\sqrt{G^2 + H^2}} \right) \quad \text{for} \quad -\frac{1}{2}\pi < \kappa < \frac{1}{2}\pi \quad (6-40)$$

The body roll angle with respect to the tether τ can be obtained by:

$$\tau = \arctan \left(\frac{G}{H} \right) \quad \text{for} \quad -\frac{1}{2}\pi < \kappa < \frac{1}{2}\pi \quad (6-41)$$

τ is a rotation about X_b -axis. Since the tether force T_t is directed in the Z_t -axis, the body yaw angle with respect to the tether ξ has no influence on the body components of the tether force.

6-4 Simulink Implementation

To simulate the Rigid Body Kite system equations the model is created in the software application SIMULINK.

Model structure

For each set of equations a ‘subsystem’ block is constructed. The equations of motion and kinematic relations define each a set of equations and can be viewed in their respective ‘subsystem’ block. These subsystem blocks are by themselves part of other subsystem blocks. And the latter are again part of other blocks. Eventually leading to a ‘top level’ block. Basically, in this way, various model ‘levels’ are created.

The top level is a block with an input vector \mathbf{U} and output vector \mathbf{Y} . This is illustrated in figure 6-9. The input vector consists of the wind input and the controls input. The wind input can be given in terms of the wind velocity \mathbf{V}_W in the earth-fixed reference frame. The control inputs consists of the time derivative of the position of the two control units \dot{d}_{ta}^L and \dot{d}_{ta}^R .

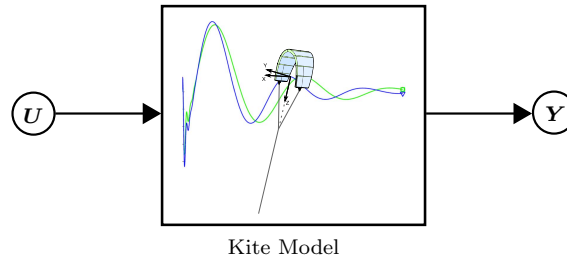


Figure 6-9: ‘Top level’ block

The second level consists of the output block, see figure 6-10. The output block has as input the state vector from a feedback signal, the wind input and the controls input. The output is given by the state vector, the time derivative of the state vector and additional aerodynamic variables: V_a , α and β .

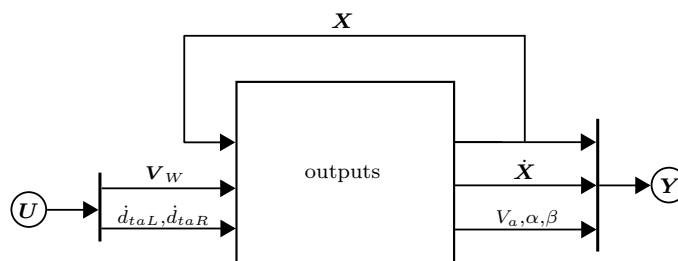


Figure 6-10: ‘Output’ block

The following underlying level contains a subsystem with all system equations and an integrator to obtain the state vector from the time derivative of the state vector, see figure 6-11. The initial condition of the state vector at ‘ $t = 0$ s’ is denoted \mathbf{X}_0 . $\dot{\mathbf{X}}$ is also fed back to the system equations block. Furthermore there is a function to limit the tether azimuth angle ψ_t . When the top end of the tether crosses the positive X_E -axis 2π will be added or subtracted to limit ψ_t between $-\pi$ and $+\pi$. See section 5-3 and figure 5-4 for more details.

The state vector \mathbf{X} is formed by the following 15 states:

$$\mathbf{X} = \langle u_k, v_k, w_k, x, y, z, p, q, r, \phi, \theta, \psi, l_t, \theta_t, \psi_t, \mathbf{x}_{taL}, \mathbf{x}_{taR} \rangle$$

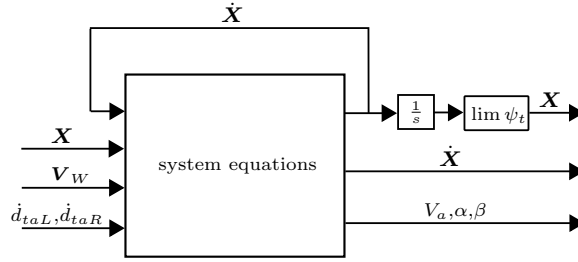


Figure 6-11: 'System equations' block

which defines $\dot{\mathbf{X}}$ as:

$$\dot{\mathbf{X}} = \langle \dot{u}_k, \dot{v}_k, \dot{w}_k, \dot{x}, \dot{y}, \dot{z}, \dot{p}, \dot{q}, \dot{r}, \dot{\phi}, \dot{\theta}, \dot{\psi}, \dot{l}_t, \dot{\theta}_t, \dot{\psi}_t, \dot{\mathbf{x}}_{taL}, \dot{\mathbf{x}}_{taR} \rangle$$

And the output vector \mathbf{Y} is given by the following variables:

$$\mathbf{Y} = \langle \dot{\mathbf{X}}, \mathbf{X}, V_a, \alpha, \beta \rangle$$

If the system equations block is opened the following blocks are found:

- kinematic relations
- wind relations
- equations of motion

At this level and in the 'lower' levels each signal represents a vector of three components. For example, the signal 'sphere' consists of the three spherical tether coordinates $\langle l_t, \theta_t, \psi_t \rangle$.

Review and final remarks

In this chapter the Rigid Body model equations are derived to describe the dynamics of an arc-shaped kite system.

The equations of motion are based on Newton's second law expressed in Cartesian and spherical coordinates. The system equations are expressed in the body fixed reference frame with its origin at the center of gravity of the kite. An analysis is given for the state dependency of the aerodynamic forces and moments as well as for the tether forces and moments. The functions describing the aerodynamic forces and moments are still undefined. A first estimate for these functions will be done in chapter 10 based on a arc-shaped LEI Kite simulated by a Multi-Body model in ADAMS. Functions for the inertia tensor properties are derived in chapter 10 as well on a quasi static basis.

An overview of the applied assumptions for the Rigid Body model is given below:

- The variation of the inertia tensor can be taken into account on a quasi static basis
- The aerodynamic forces and moments can be represented by Taylor series
- The tether is a straight line and is modelled by a spring-damper system with invariant coefficients
- The wind speed has no influence on the tether forces
- The roll constraint due to the bridle is modelled by a counteracting moment as a function of the main tether force T_t

- States influencing aerodynamic forces and moments have no direct influence on the resultant tether force T_t and vice versa
- The control positions are constrained to move in X_b direction given by x_{taL} and x_{taR}

The verification of the model is performed by simulating an aircraft model of the Cessna ‘Citation’ and by simulating the aircraft attached to a tether in chapter 8.

To conclude the model is illustrated in figure 6-12.

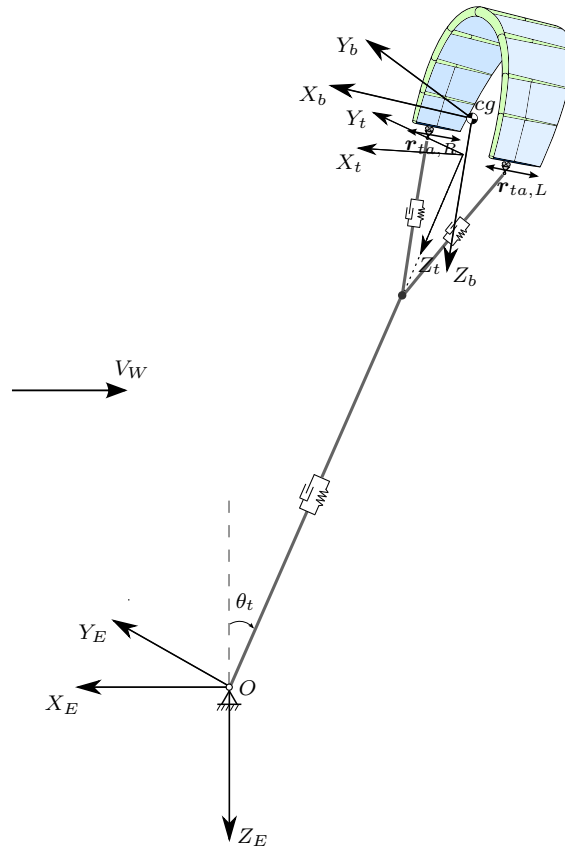


Figure 6-12: Rigid Body Kite system model

Linearized Kite Model Equations

The nonlinear Rigid Body model equations derived in chapter 6 are linearized in this chapter. Use is made of the linearization method for aircraft flight dynamics as broadly described in reference [24]. The system is linearized around a stationary statically stable condition. This results in two linear time invariant (LTI) models: one for the symmetric motions and one for the asymmetric motions. The linear models are compared with the Rigid Body model and used to investigate the effect of linearization of the Rigid Body model in chapter 8.

In general linearization can be used to investigate the dynamics of a system at a particular initial condition or around a particular initial condition where the linearization still suffice. Influences of sufficiently small disturbances can be analyzed as well. The influences of the states and control inputs will be captured in so called stability and control derivatives respectively. They describe the change of a force or moment as function of a small change of a particular state or control input.

One has to keep in mind that linearization is only valid within a certain region around the chosen flight condition. The main goal of linearization is to find the stability in this particularly flight condition. But it might be that a system is highly nonlinear, that the linearization is only valid in a very small domain and that already a small disturbance will push the system out of the confidence region. See figure 7-1 for the definition of the confidence region. In this case linearization becomes practically useless. Although the usefulness of linearization on a kite system is still unanswered, using the theory of linearization might give more insight and understanding of the dynamics and stability of the system.

In practice linearization is usually performed around equilibrium positions. If the system is in a stable and equilibrium condition the system will remain close to this condition. But if the system is unstable or not in equilibrium the system will deviate quickly from the chosen condition and out of the region of confidence. Therefore it is necessary to perform linearization from a statically stable initial condition.

In this chapter, first the equations of motion will be linearized about an arbitrary flight condition. Secondly the result of the first part will be used to obtain a linearized system or so called LTI (linear time invariant) state-space model about a motionless steady straight symmetric flight condition for the symmetric (longitudinal) and asymmetric (lateral) motions.

First, an additional assumption is made to the equations of motion with respect to the mass moments and products of inertia. The body is assumed to be invariable and symmetric and the body-fixed reference frame is chosen such that J_{xy} and J_{yz} are zero. Invariable means that the

time derivative of the inertia tensor is zero and that the inertia tensor is constant. This results in the fact that the derivative of the inertial angular momentum in the body-fixed reference frame can be written as:

$$\begin{aligned} \left(\frac{d\mathbf{B}_{cg}^E}{dt} \right)^b &= \left(\frac{\mathbf{B}_{cg}^E}{dt} \right)^b + \boldsymbol{\Omega}_{bE}^b \times \mathbf{B}_{cg}^b \\ &= \mathbb{I}_{cg}^b \frac{d\boldsymbol{\Omega}_{bE}^b}{dt} + \boldsymbol{\Omega}_{bE}^b \times \left(\mathbb{I}_{cg}^b \boldsymbol{\Omega}_{bE}^b \right) \\ &= \begin{bmatrix} I_{xx}\dot{p} + (I_{zz} - I_{yy})qr - J_{xz}(pq + \dot{r}) \\ I_{yy}\dot{q} + (I_{xx} - I_{zz})pr + J_{xz}(p^2 - r^2) \\ I_{zz}\dot{r} + (I_{yy} - I_{xx})pq + J_{xz}(qr - \dot{p}) \end{bmatrix} \end{aligned} \quad (7-1)$$

where $\boldsymbol{\Omega}_{bE}^b$ and \mathbb{I}_{rp}^b are the rotational velocity and the mass moment of inertia respectively given by:

$$\boldsymbol{\Omega}_{bE}^b = \begin{bmatrix} p \\ q \\ r \end{bmatrix} \quad (7-2)$$

$$\mathbb{I}_{rp}^b = \begin{bmatrix} I_{xx} & 0 & -J_{xz} \\ 0 & I_{yy} & 0 \\ -J_{xz} & 0 & I_{zz} \end{bmatrix} \quad (7-3)$$

Now, the equations of motion (6-20) and (6-21) can be written in the following set of equations:

$$\begin{aligned} F_x &= -W \sin \theta + X + F &= m(\dot{u}_k + qw_k - rv_k) \\ F_y &= W \cos \theta \sin \phi + Y + G &= m(\dot{v}_k + ru_k - pw_k) \\ F_z &= W \cos \theta \cos \phi + Z + H &= m(\dot{w}_k + pv_k - qu_k) \\ \mathcal{M}_x &= L + P &= I_{xx}\dot{p} + (I_{zz} - I_{yy})qr - J_{xz}(pq + \dot{r}) \\ \mathcal{M}_y &= M + Q &= I_{yy}\dot{q} + (I_{xx} - I_{zz})pr + J_{xz}(p^2 - r^2) \\ \mathcal{M}_z &= N + R &= I_{zz}\dot{r} + (I_{yy} - I_{xx})pq + J_{xz}(qr - \dot{p}) \end{aligned} \quad (7-4)$$

where $W = mg_C$ has been used.

The kinematic relations accompanying this set of equations are equations (6-22), (6-23), (6-24) and the wind relations (6-25) and (6-26) completes the set.

7-1 Linearization about arbitrary flight condition

In general linearization can be performed on any function, which is differentiable. The method is to apply a Taylor expansion about the state vector \mathbf{X} and only take the initial condition (first term) and the first derivative (second term) into account. For a two dimensional state $\mathbf{X} = (x, u)$ the Taylor expansion about state (x_0, u_0) of a real function can be written as:

$$\begin{aligned} y &= f(x_0, u_0) + [f_x(x_0, u_0)\Delta x + f_u(x_0, u_0)\Delta u] \\ &+ \frac{1}{2!} [f_{xx}(x_0, u_0)\Delta x^2 + 2f_{xu}(x_0, u_0)\Delta x\Delta u + f_{uu}(x_0, u_0)\Delta u^2] \\ &+ \dots \end{aligned} \quad (7-5)$$

where f_x denotes the first derivative of f with respect to x and f_u the first derivative with respect to u . When applying linearization all terms with higher derivatives than 1 will be ignored. For a

general n -dimensional state X the linearized function about point X_0 becomes:

$$Y = f(\mathbf{X}_0) + \sum_{i=1}^n f_{x_i}(\mathbf{X}_0)\Delta x_i \quad (7-6)$$

Figure 7-1 gives a graphical representation of the concept of linearization for the function $y = f(x)$ about x_0 . The confidence region defines the domain the linearized representation of $y = f(x)$ about x_0 is within the allowed error margin.

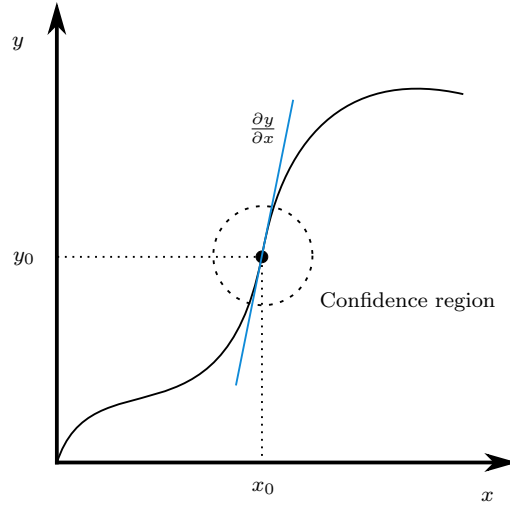


Figure 7-1: Linearization of $y = f(x)$ about x_0

7-1-1 Linearization of acceleration terms

The linearization of the acceleration terms of the equations of motion (7-4) can be written in terms of the initial condition and the first derivative by:

$$\begin{aligned} F_x &= F_x(\mathbf{X}_0) + F_x(\Delta\mathbf{X}) \\ F_y &= F_y(\mathbf{X}_0) + F_y(\Delta\mathbf{X}) \\ F_z &= F_z(\mathbf{X}_0) + F_z(\Delta\mathbf{X}) \\ \mathcal{M}_x &= \mathcal{M}_x(\mathbf{X}_0) + \mathcal{M}_x(\Delta\mathbf{X}) \\ \mathcal{M}_y &= \mathcal{M}_y(\mathbf{X}_0) + \mathcal{M}_y(\Delta\mathbf{X}) \\ \mathcal{M}_z &= \mathcal{M}_z(\mathbf{X}_0) + \mathcal{M}_z(\Delta\mathbf{X}) \end{aligned} \quad (7-7)$$

with

$$\begin{aligned} F_x(\mathbf{X}_0) &= m(\dot{u}_{k,0} + q_0 w_{k,0} - r_0 v_{k,0}) \\ F_y(\mathbf{X}_0) &= m(\dot{v}_{k,0} + r_0 u_{k,0} - p_0 w_{k,0}) \\ F_z(\mathbf{X}_0) &= m(\dot{w}_{k,0} + p_0 v_{k,0} - q_0 u_{k,0}) \\ \mathcal{M}_x(\mathbf{X}_0) &= I_x \dot{p}_0 + (I_z - I_y) q_0 r_0 - J_{xz} (\dot{r}_0 + p_0 q_0) \\ \mathcal{M}_y(\mathbf{X}_0) &= I_y \dot{q}_0 + (I_x - I_z) p_0 r_0 + J_{xz} (p_0^2 + r_0^2) \\ \mathcal{M}_z(\mathbf{X}_0) &= I_z \dot{r}_0 + (I_y - I_x) p_0 q_0 - J_{xz} (\dot{p}_0 - q_0 r_0) \end{aligned} \quad (7-8)$$

and

$$\begin{aligned}
F_x(\Delta \mathbf{X}) &= m(\Delta \dot{u}_k - r_0 \Delta v_k + q_0 \Delta w_k + w_{k,0} \Delta q - v_{k,0} \Delta r) \\
F_y(\Delta \mathbf{X}) &= m(\Delta \dot{v}_k + r_0 \Delta u_k - p_0 \Delta w_k - w_{k,0} \Delta p + u_{k,0} \Delta r) \\
F_z(\Delta \mathbf{X}) &= m(\Delta \dot{w}_k - q_0 \Delta u_k + p_0 \Delta v_k + v_{k,0} \Delta p - u_{k,0} \Delta q) \\
\mathcal{M}_x(\Delta \mathbf{X}) &= I_x \Delta \dot{p} - J_{xz} \Delta \dot{r} - J_{xz} q_0 \Delta p + [(I_z - I_y) r_0 - J_{xz} p_0] \Delta q + (I_z - I_y) q_0 \Delta r \\
\mathcal{M}_y(\Delta \mathbf{X}) &= I_y \Delta \dot{q} + [(I_x - I_z) r_0 + J_{xz} p_0] \Delta p + [(I_x - I_z) p_0 - J_{xz} r_0] \Delta r \\
\mathcal{M}_z(\Delta \mathbf{X}) &= I_z \Delta \dot{r} - J_{xz} \Delta \dot{p} + (I_y - I_x) q_0 \Delta p + [(I_y - I_x) p_0 - J_{xz} r_0] \Delta q + J_{xz} q_0 \Delta r
\end{aligned} \tag{7-9}$$

Note that the right hand side of the equations of motion are dependent on the kinematic velocities, but that the aerodynamic forces and moments are dependent on the aerodynamic velocities. The linearization of forces and moments is derived in the following section.

7-1-2 Linearization of forces and moments

The forces and moments are a function of the following states:

$$\begin{aligned}
F_x &= f(\theta, u_a, \dot{u}_a, w_a, \dot{w}_a, q, \mathbf{r}_{ta}^L, \mathbf{r}_{ta}^R, l_t, \dot{l}_t, \kappa,) \\
F_y &= f(\phi, \theta, v_a, \dot{v}_a, p, r, \mathbf{r}_{ta}^L, \mathbf{r}_{ta}^R, l_t, \dot{l}_t, \tau, \kappa) \\
F_z &= f(\phi, \theta, u_a, \dot{u}_a, w_a, \dot{w}_a, q, \mathbf{r}_{ta}^L, \mathbf{r}_{ta}^R, l_t, \dot{l}_t, \tau, \kappa) \\
M_x &= f(v_a, \dot{v}_a, p, r, \mathbf{r}_{ta}^L, \mathbf{r}_{ta}^R, l_t, \dot{l}_t, \tau, \kappa) \\
M_y &= f(u_a, \dot{u}_a, w_a, \dot{w}_a, q, \mathbf{r}_{ta}^L, \mathbf{r}_{ta}^R, l_t, \dot{l}_t, \tau, \kappa) \\
M_z &= f(v_a, \dot{v}_a, p, r, \mathbf{r}_{ta}^L, \mathbf{r}_{ta}^R, l_t, \dot{l}_t, \tau, \kappa)
\end{aligned} \tag{7-10}$$

where ϕ and θ come from the gravity terms.

The control quantities \mathbf{r}_{ta}^L and \mathbf{r}_{ta}^R consist both of three components x_{ta} , y_{ta} and z_{ta} as explained in section 6-3-3. The only variable components are x_{ta}^L and x_{ta}^R . Linearization of the control quantities will result in a dependency only of Δx_{ta}^L and Δx_{ta}^R .

Linearizing the forces and moments to the defined states leads to:

$$\begin{aligned}
F_x &= F_x(\mathbf{X}_0) + F_x(\Delta \mathbf{X}) \\
F_y &= F_y(\mathbf{X}_0) + F_y(\Delta \mathbf{X}) \\
F_z &= F_z(\mathbf{X}_0) + F_z(\Delta \mathbf{X}) \\
M_x &= M_x(\mathbf{X}_0) + M_x(\Delta \mathbf{X}) \\
M_y &= M_y(\mathbf{X}_0) + M_y(\Delta \mathbf{X}) \\
M_z &= M_z(\mathbf{X}_0) + M_z(\Delta \mathbf{X})
\end{aligned} \tag{7-11}$$

with

$$\begin{aligned}
F_x(\mathbf{X}_0) &= -W \sin \theta_0 + X_0 + F_0 \\
F_y(\mathbf{X}_0) &= W \cos \theta_0 \sin \phi_0 + Y_0 + G_0 \\
F_z(\mathbf{X}_0) &= W \cos \theta_0 \cos \phi_0 + Z_0 + H_0 \\
M_x(\mathbf{X}_0) &= L_0 + P_0 \\
M_y(\mathbf{X}_0) &= M_0 + Q_0 \\
M_z(\mathbf{X}_0) &= N_0 + R_0
\end{aligned} \tag{7-12}$$

and

$$\begin{aligned}
F_x(\Delta \mathbf{X}) &= -W \cos \theta_0 \cdot \Delta \theta \\
&\quad + X_u \cdot \Delta u_a + X_w \cdot \Delta w_a + X_{\dot{w}} \cdot \Delta \dot{w}_a + X_q \cdot \Delta q \\
&\quad + F_{\delta_L} \cdot \Delta x_{ta}^L + F_{\delta_R} \cdot \Delta x_{ta}^R + F_l \cdot \Delta l_t \\
&\quad + F_j \cdot \Delta \dot{l}_t + F_\kappa \cdot \Delta \kappa \\
F_y(\Delta \mathbf{X}) &= -W \sin \theta_0 \sin \phi_0 \cdot \Delta \theta + W \cos \theta_0 \cos \phi_0 \cdot \Delta \phi \\
&\quad + Y_v \cdot \Delta v_a + Y_{\dot{v}} \cdot \Delta \dot{v}_a + Y_p \cdot \Delta p + Y_r \cdot \Delta r \\
&\quad + G_{\delta_L} \cdot \Delta x_{ta}^L + G_{\delta_R} \cdot \Delta x_{ta}^R + G_l \cdot \Delta l_t + G_j \cdot \Delta \dot{l}_t \\
&\quad + G_\kappa \cdot \Delta \kappa + G_\tau \cdot \Delta \tau \\
F_z(\Delta \mathbf{X}) &= -W \sin \theta_0 \cos \phi_0 \cdot \Delta \theta - W \cos \theta_0 \sin \phi_0 \cdot \Delta \phi \\
&\quad + Z_u \cdot \Delta u_a + Z_w \cdot \Delta w_a + Z_{\dot{w}} \cdot \Delta \dot{w}_a + Z_q \cdot \Delta q \\
&\quad + H_{\delta_L} \cdot \Delta x_{ta}^L + H_{\delta_R} \cdot \Delta x_{ta}^R + H_l \cdot \Delta l_t + H_j \cdot \Delta \dot{l}_t \\
&\quad + H_\kappa \cdot \Delta \kappa + H_\tau \cdot \Delta \tau \\
M_x(\Delta \mathbf{X}) &= L_v \cdot \Delta v_a + L_{\dot{v}} \cdot \Delta \dot{v}_a + L_p \cdot \Delta p + L_r \cdot \Delta r \\
&\quad + P_{\delta_L} \cdot \Delta x_{ta}^L + P_{\delta_R} \cdot \Delta x_{ta}^R + P_l \cdot \Delta l_t + P_j \cdot \Delta \dot{l}_t \\
&\quad + P_\kappa \cdot \Delta \kappa + P_\tau \cdot \Delta \tau \\
M_y(\Delta \mathbf{X}) &= M_u \cdot \Delta u_a + M_w \cdot \Delta w_a + M_{\dot{w}} \cdot \Delta \dot{w}_a + M_q \cdot \Delta q \\
&\quad + Q_{\delta_L} \cdot \Delta x_{ta}^L + Q_{\delta_R} \cdot \Delta x_{ta}^R + Q_l \cdot \Delta l_t + Q_j \cdot \Delta \dot{l}_t \\
&\quad + Q_\kappa \cdot \Delta \kappa + Q_\tau \cdot \Delta \tau \\
M_z(\Delta \mathbf{X}) &= N_v \cdot \Delta v_a + N_{\dot{v}} \cdot \Delta \dot{v}_a + N_p \cdot \Delta p + N_r \cdot \Delta r \\
&\quad + R_{\delta_L} \cdot \Delta x_{ta}^L + R_{\delta_R} \cdot \Delta x_{ta}^R + R_l \cdot \Delta l_t + R_j \cdot \Delta \dot{l}_t \\
&\quad + R_\kappa \cdot \Delta \kappa + R_\tau \cdot \Delta \tau
\end{aligned} \tag{7-13}$$

Linear aerodynamic models

In linear aerodynamic models the dimensionless coefficients C_{x_y} are called stability derivatives, are constant and derived from a specific flight condition. A linear aerodynamic is derived by linearizing equations (2-1).

Linearization is usually performed at a stable and steady condition, i.e. forces and moments are in equilibrium. This results in the fact that C_{X_0} , C_{Z_0} and C_{m_0} have a different meaning in linear models than in nonlinear models. This also holds for the asymmetric variants C_{Y_0} , C_{l_0} and C_{n_0} . In linear models the subscript '0' denotes the value of the forces and moments at $t = 0$ s, whereas in nonlinear models the subscript '0' denotes the value of the forces and moments when all the states are zero. The linear variants of C_{X_0} and C_{Z_0} is given by their nonlinear variants at trim condition:

$$\begin{aligned}
C_{X_0}^{lin} &= C_{X_0} + C_{X_\alpha} \cdot \alpha^{tr} + C_{X_\delta} \cdot \delta_c \\
C_{Z_0}^{lin} &= C_{Z_0} + C_{Z_\alpha} \cdot \alpha^{tr} + C_{Z_\delta} \cdot \delta_c
\end{aligned} \tag{7-14}$$

In linear models one should take the variation of airspeed into account. This results in the stability derivatives C_{X_u} , C_{Z_u} and C_{m_u} . According to reference [24] C_{X_u} is defined as:

$$C_{X_u} = \frac{1}{\frac{1}{2}\rho V_0 S} \frac{\partial X}{\partial V}$$

There is also:

$$X = C_X \cdot \frac{1}{2} \rho V_a^2 S$$

differentiating with respect to V gives:

$$\frac{\partial X}{\partial V} = C_X \rho V_0 S + \frac{\partial C_X}{\partial V} \frac{1}{2} \rho V_0^2 S$$

so, by consequence,

$$C_{X_u} = 2C_X + \frac{\partial C_X}{\partial V} V_0 \quad (7-15)$$

where C_X is C_X at the initial condition for linearization, so equation (7-15) can be written as:

$$C_{X_u} = 2C_{X_0}^{lin} + \frac{\partial C_X}{\partial V} V_0 \quad (7-16)$$

Note that there is a distinction between V_a and V_0 . V_a is the general aerodynamic velocity and is variable, whereas V_0 is the initial aerodynamic velocity at $t = 0$ s and is constant. This distinction comes from the linearization process. In linear models V_0 is used and the change in velocity comes from the stability derivatives with respect to u .

In equation (7-16) $\frac{\partial C_X}{\partial V}$ has to be derived still. This is the derivative of the first of equations (2-1).

The derivation of C_{Z_u} and C_{m_u} is analogue to C_{X_u} , so:

$$C_{Z_u} = 2C_{Z_0}^{lin} + \frac{\partial C_Z}{\partial V} V_0 \quad (7-17)$$

$$C_{m_u} = 2C_{m_0}^{lin} + \frac{\partial C_m}{\partial V} V_0 \quad (7-18)$$

The partial derivatives of velocity in 7-16, 7-17 and 7-18 have several contributions as found in reference [24], like variation in Mach number, Reynolds number, thrust coefficient and aeroelastic deformation. For kites aeroelastic deformation is the only contribution with has influence.

The previous results in the forces and moments equations for linear models given in (7-19):

$$\begin{aligned} \Delta C_X &= C_{X_u} \cdot \hat{u} + C_{X_\alpha} \cdot \alpha + C_{X_{\dot{\alpha}}} \cdot \frac{\dot{\alpha} \bar{c}}{V_0} + C_{X_q} \cdot \frac{q \bar{c}}{V_0} + C_{X_\delta} \cdot \delta_c \\ \Delta C_Y &= C_{Y_\beta} \cdot \beta + C_{Y_{\dot{\beta}}} \cdot \dot{\beta} + C_{Y_p} \cdot \frac{pb}{2V_0} + C_{Y_r} \cdot \frac{rb}{2V_0} + C_{Y_\delta} \cdot \delta_c \\ \Delta C_Z &= C_{Z_u} \cdot \hat{u} + C_{Z_\alpha} \cdot \alpha + C_{Z_{\dot{\alpha}}} \cdot \frac{\dot{\alpha} \bar{c}}{V_0} + C_{Z_q} \cdot \frac{q \bar{c}}{V_0} + C_{Z_\delta} \cdot \delta_c \\ \Delta C_l &= C_{l_\beta} \cdot \beta + C_{l_{\dot{\beta}}} \cdot \dot{\beta} + C_{l_p} \cdot \frac{pb}{2V_0} + C_{l_r} \cdot \frac{rb}{2V_0} + C_{l_\delta} \cdot \delta_c \\ \Delta C_m &= C_{m_u} \cdot \hat{u} + C_{m_\alpha} \cdot \alpha + C_{m_{\dot{\alpha}}} \cdot \frac{\dot{\alpha} \bar{c}}{V_0} + C_{m_q} \cdot \frac{q \bar{c}}{V_0} + C_{m_\delta} \cdot \delta_c \\ \Delta C_n &= C_{n_\beta} \cdot \beta + C_{n_{\dot{\beta}}} \cdot \dot{\beta} + C_{n_p} \cdot \frac{pb}{2V_0} + C_{n_r} \cdot \frac{rb}{2V_0} + C_{n_\delta} \cdot \delta_c \end{aligned} \quad (7-19)$$

where the Δ is written to make clear that the functions describe a deviation on the initial condition.

Again the obtained dimensionless forces and moments are multiplied with $\frac{1}{2} \rho V_0^2 S$ and $\frac{1}{2} \rho V_0^2 S \bar{c}$ or $\frac{1}{2} \rho V_0^2 S b$ respectively to get the dimensional forces and moments, where V_0 is the aerodynamic trim velocity and is constant.

7-1-3 Linearization of kinematic relations

The linearization of the kinematic relations relating to the body (6-22) can be found in reference [24] and is repeated here:

$$\begin{aligned}\dot{\phi} &= \dot{\phi}(\mathbf{X}_0) + \dot{\phi}(\Delta\mathbf{X}) \\ \dot{\theta} &= \dot{\theta}(\mathbf{X}_0) + \dot{\theta}(\Delta\mathbf{X}) \\ \dot{\psi} &= \dot{\psi}(\mathbf{X}_0) + \dot{\psi}(\Delta\mathbf{X})\end{aligned}\quad (7-20)$$

with

$$\begin{aligned}\dot{\phi}(\mathbf{X}_0) &= p_0 + q_0 \sin \phi_0 \tan \theta_0 + r_0 \cos \phi_0 \tan \theta_0 \\ \dot{\theta}(\mathbf{X}_0) &= q_0 \cos \phi_0 - r_0 \sin \phi_0 \\ \dot{\psi}(\mathbf{X}_0) &= q_0 \frac{\sin \phi_0}{\cos \theta_0} + r_0 \frac{\cos \phi_0}{\cos \theta_0}\end{aligned}\quad (7-21)$$

and

$$\begin{aligned}\dot{\phi}(\Delta\mathbf{X}) &= \Delta p + \sin \phi_0 \tan \theta_0 \Delta q + q_0 \cos \phi_0 \tan \theta_0 \Delta \phi + q_0 \frac{\sin \phi_0}{\cos^2 \theta_0} \Delta \theta \\ &\quad + \cos \phi_0 \tan \theta_0 \Delta r - r_0 \sin \phi_0 \tan \theta_0 \Delta \phi + r_0 \frac{\cos \phi_0}{\cos^2 \theta_0} \Delta \theta \\ \dot{\theta}(\Delta\mathbf{X}) &= \cos \phi_0 \Delta q - q_0 \sin \phi_0 \Delta \phi - \sin \phi_0 \Delta r - r_0 \cos \phi_0 \Delta \phi \\ \dot{\psi}(\Delta\mathbf{X}) &= \frac{\sin \phi_0}{\cos \theta_0} \Delta q + q_0 \frac{\cos \phi_0}{\cos \theta_0} \Delta \phi + q_0 \frac{\sin \phi_0}{\cos \theta_0} \tan \theta_0 \Delta \theta \\ &\quad + \frac{\cos \phi_0}{\cos \theta_0} \Delta r - r_0 \frac{\sin \phi_0}{\cos \theta_0} \Delta \phi + r_0 \frac{\cos \phi_0}{\cos \theta_0} \tan \theta_0 \Delta \theta\end{aligned}\quad (7-22)$$

The linearization of the first of the kinematic relations relating to the the tether, equation (6-23), is quite extensive. It is in this case more convenient to perform the linearization together with the application of the initial condition. This is done in subsequent sections.

The linearization of the second of the kinematic relations relating to the tether, equation (6-24), is given by equation (7-23):

$$\begin{aligned}\dot{l}_t &= \dot{l}_t(\mathbf{X}_0 + \Delta\mathbf{X}) = -\dot{z}_{t0}^t - \Delta\dot{z}_t^t \\ \dot{\theta}_t &= \dot{\theta}_t(\mathbf{X}_0 + \Delta\mathbf{X}) = -\frac{\dot{x}_{t0}^t}{l_{t0}} - \frac{1}{l_{t0}} \Delta\dot{x}_t^t + \frac{\dot{x}_{t0}^t}{l_{t0}^2} \Delta l_t \\ \dot{\psi}_t &= \dot{\psi}_t(\mathbf{X}_0 + \Delta\mathbf{X}) = -\frac{\dot{y}_{t0}^t}{l_{t0} \sin \theta_{t0}} - \frac{1}{l_{t0} \sin \theta_{t0}} \Delta\dot{y}_t^t \\ &\quad + \frac{\dot{y}_{t0}^t}{l_{t0}^2 \sin \theta_{t0}} \Delta l_t + \frac{\dot{y}_{t0}^t \cos \theta_{t0}}{l_{t0} \sin^2 \theta_{t0}} \Delta \theta_t\end{aligned}\quad (7-23)$$

Finally the linearization of wind relations, equations (6-25) and (6-26) needs to be done. The linearization of these relations is also quite extensive. Also these relations are linearized together with applying the initial condition.

7-2 Linearized equations of motion no initial velocity

The linearized equations of motions derived in the previous section can form a basis to study the dynamic stability of kites. In this section the equations of motion will be derived for the steady symmetric case, where the kite has no initial kinematic velocity. In the following first the symmetric equations of motion will be derived followed by the asymmetric equations of motion.

Initial condition

The flight condition to be linearized is a steady straight symmetric flight condition where the initial kinematic velocity of the kite is zero. The initial condition is given by following parameters in the body-fixed reference frame except for the wind velocity components:

$$\begin{array}{cccccc}
 u_a \neq 0 & u_k = 0 & \dot{u}_k = 0 & W_x \neq 0 & p = 0 & \dot{p} = 0 \\
 v_a = 0 & v_k = 0 & \dot{v}_k = 0 & W_y = 0 & q = 0 & \dot{q} = 0 \\
 w_a = 0 & w_k = 0 & \dot{w}_k = 0 & W_z = 0 & r = 0 & \dot{r} = 0 \\
 \\
 \phi = 0 & \dot{\phi} = 0 & \delta l_t \neq 0 & \dot{l}_t = 0 & \tau = 0 & \dot{\tau} = 0 \\
 \theta \neq 0 & \dot{\theta} = 0 & \theta_t \neq 0 & \dot{\theta}_t = 0 & \kappa \neq 0 & \dot{\kappa} = 0 \\
 \psi = 0 & \dot{\psi} = 0 & \psi_t = 0 & \dot{\phi}_t = 0 & \xi = 0 & \dot{\xi} = 0 \\
 \\
 X \neq 0 & F \neq 0 & L = 0 & p = 0 & & \\
 Y = 0 & G = 0 & M \neq 0 & Q \neq 0 & & \\
 Z \neq 0 & H \neq 0 & N = 0 & R = 0 & &
 \end{array}$$

The initial state of linearization is in equilibrium which means that the terms with \mathbf{X}_0 cancel in the equations of the previous section. These equations are used to determine the values of the non-zero initial parameters.

7-2-1 Matrix notation of symmetric equations of motion

In this section the linearized symmetric or longitudinal equations of motion are obtained. Figure 7-2 shows a graphical representation of this system with the definition of the angles κ , θ_t and θ .

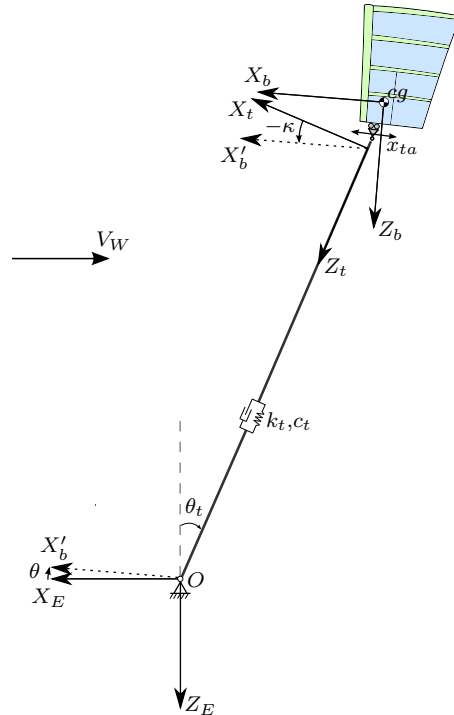


Figure 7-2: Symmetric state-space kite system

Accelerations

The linearized acceleration terms or right hand side of the equations of motion (7-9) are given by:

$$\begin{aligned} F_x(\Delta \mathbf{X}) &= m \cdot \Delta \dot{u}_k \\ F_z(\Delta \mathbf{X}) &= m \cdot \Delta \dot{w}_k \\ \mathcal{M}_y(\Delta \mathbf{X}) &= I_y \cdot \Delta \dot{q} \end{aligned} \quad (7-24)$$

Forces and moments

The forces and moments for the symmetric case are a function of:

$$\begin{aligned} W &\rightarrow f(\theta) \\ X, Z, M &\rightarrow f(u_a, w_a, \dot{w}_a, q) \\ F, H, Q &\rightarrow f(x_t a, l_t, \dot{l}_t, \kappa, \dot{\kappa}) \end{aligned}$$

where the left and right pinion positions have been replaced by one parameter $x_t a$, because they move synchronously for the symmetric case.

The linearized symmetric forces and moment of equation (7-13) become:

$$\begin{aligned} F_x(\Delta \mathbf{X}) &= -W \cos \theta_0 \cdot \Delta \theta + X_u \cdot \Delta u_a + X_w \cdot \Delta w_a + X_{\dot{w}} \cdot \Delta \dot{w}_a + X_q \cdot \Delta q \\ &\quad + F_\delta \cdot \Delta \delta + F_l \cdot \Delta l_t + F_{\dot{l}} \cdot \Delta \dot{l}_t + F_\kappa \cdot \Delta \kappa + F_{\dot{\kappa}} \cdot \Delta \dot{\kappa} \\ F_z(\Delta \mathbf{X}) &= -W \sin \theta_0 \cdot \Delta \theta + Z_u \cdot \Delta u_a + Z_w \cdot \Delta w_a + Z_{\dot{w}} \cdot \Delta \dot{w}_a + Z_q \cdot \Delta q \\ &\quad + H_\delta \cdot \Delta \delta + H_l \cdot \Delta l_t + H_{\dot{l}} \cdot \Delta \dot{l}_t + H_\kappa \cdot \Delta \kappa + H_{\dot{\kappa}} \cdot \Delta \dot{\kappa} \\ M_y(\Delta \mathbf{X}) &= M_u \cdot \Delta u_a + M_w \cdot \Delta w_a + M_{\dot{w}} \cdot \Delta \dot{w}_a + M_q \cdot \Delta q \\ &\quad + Q_\delta \cdot \Delta \delta + Q_l \cdot \Delta l_t + Q_{\dot{l}} \cdot \Delta \dot{l}_t + Q_\kappa \cdot \Delta \kappa + Q_{\dot{\kappa}} \cdot \Delta \dot{\kappa} \end{aligned} \quad (7-25)$$

The derivatives of the tether forces and moment are derived from the tether model.

Tether forces and moments

Expressions for the tether forces and moments with respect to a change in κ , l_t , \dot{l}_t and δ can be derived. The tether is modelled as a spring-damper given by the values k_t and c_t for the spring and damping constant respectively. The tether force is given by, see equation 6-29:

$$T_t = k_t \cdot \delta l_t + c_t \cdot \dot{l}_t$$

where δl_t is the elastic elongation at $t = 0$ s.

Writing this in the body axes by the transformation \mathbb{T}_{bt} gives:

$$\begin{aligned} F &= -k_t \sin \kappa \cdot \delta l_t - c_t \sin \kappa \cdot \dot{l}_t \\ H &= k_t \cos \kappa \cdot \delta l_t + c_t \cos \kappa \cdot \dot{l}_t \end{aligned} \quad (7-26)$$

These forces give the tether moment by:

$$Q = F \cdot z_{ta} - H \cdot x_{ta} \quad (7-27)$$

Linearizing the previous expressions, (7-26) and (7-27), gives:

$$\begin{aligned} F(\mathbf{X}_0) &= -k_t \sin \kappa_0 \cdot \delta l_{t0} - c_t \sin \kappa_0 \cdot \dot{l}_{t0} \\ H(\mathbf{X}_0) &= k_t \cos \kappa_0 \cdot \delta l_{t0} + c_t \cos \kappa_0 \cdot \dot{l}_{t0} \\ Q(\mathbf{X}_0) &= F_0 \cdot z_{ta} - H_0 \cdot x_{ta0} \end{aligned} \quad (7-28)$$

and

$$\begin{aligned}
F(\Delta \mathbf{X}) &= -H_0 \cdot \Delta \kappa - k_t \sin \kappa_0 \cdot \Delta l_t - c_t \sin \kappa_0 \cdot \Delta \dot{l}_t \\
H(\Delta \mathbf{X}) &= F_0 \cdot \Delta \kappa + k_t \cos \kappa_0 \cdot \Delta l_t + c_t \cos \kappa_0 \cdot \Delta \dot{l}_t \\
Q(\Delta \mathbf{X}) &= z_{ta} F_\kappa \cdot \Delta \kappa - z_{ta} k_t \sin \kappa_0 \cdot \Delta l_t \\
&\quad - z_{ta} c_t \sin \kappa_0 \cdot \Delta \dot{l}_t - x_{ta0} H_\kappa \cdot \Delta \kappa \\
&\quad - x_{ta0} k_t \cos \kappa_0 \cdot \Delta l_t - x_{ta0} c_t \cos \kappa_0 \cdot \Delta \dot{l}_t \\
&\quad - H_0 \cdot \Delta x_{ta}
\end{aligned} \tag{7-29}$$

where $F_\kappa = -H_0$ and $H_\kappa = F_0$.

Kinematic relations

Equation (7-22) of the kinematic relations with the initial conditions is:

$$\dot{\theta}(\Delta \mathbf{X}) = \Delta q \tag{7-30}$$

The linearization of the first of the kinematic relations of the tether, equation (6-23), is done by first writing equation (6-23) as a function of the symmetric parameters.

$$\begin{aligned}
\begin{bmatrix} \dot{x}_t^t \\ \dot{y}_t^t \\ \dot{z}_t^t \end{bmatrix} &= \mathbb{T}_{tb} \left(\begin{bmatrix} u_k^b \\ v_k^b \\ w_k^b \end{bmatrix} + \boldsymbol{\Omega}_{bE}^b \times \mathbf{r}_{ta}^b \right) \\
&= \mathbb{T}_{tb} \left(\begin{bmatrix} \dot{x}_k^b \\ 0 \\ \dot{z}_k^b \end{bmatrix} + \begin{bmatrix} q \cdot z_{ta} \\ 0 \\ -q \cdot x_{ta} \end{bmatrix} \right) \\
&= \mathbb{T}_{bt}^\top \begin{bmatrix} u_t^b \\ 0 \\ w_t^b \end{bmatrix} \\
&= \begin{bmatrix} \cos \kappa \cdot \dot{x}_t^b + \sin \kappa \cdot \dot{z}_t^b \\ 0 \\ -\sin \kappa \cdot \dot{x}_t^b + \cos \kappa \cdot \dot{z}_t^b \end{bmatrix}
\end{aligned}$$

This gives:

$$\begin{aligned}
\dot{x}_t^t &= \cos \kappa (u_k + q \cdot z_{ta}) + \sin \kappa (w_k - q \cdot x_{ta}) \\
\dot{z}_t^t &= -\sin \kappa (u_k + q \cdot z_{ta}) + \cos \kappa (w_k - q \cdot x_{ta})
\end{aligned}$$

Linearizing this equation gives for \mathbf{X}_0 and $\Delta \mathbf{X}$:

$$\begin{aligned}
\dot{x}_t^t(\mathbf{X}_0) &= \cos \kappa_0 (u_{k0} + q_0 \cdot z_{ta}) + \sin \kappa_0 (w_{k0} - q_0 \cdot x_{ta0}) \\
\dot{z}_t^t(\mathbf{X}_0) &= -\sin \kappa_0 (u_{k0} + q_0 \cdot z_{ta}) + \cos \kappa_0 (w_{k0} - q_0 \cdot x_{ta0})
\end{aligned} \tag{7-31}$$

$$\begin{aligned}
\dot{x}_t^t(\Delta \mathbf{X}) &= \cos \kappa_0 \cdot \Delta u_k + z_{ta} \cos \kappa_0 \cdot \Delta q \\
&\quad + \sin \kappa_0 \cdot \Delta w_k - x_{ta0} \sin \kappa_0 \cdot \Delta q \\
\dot{z}_t^t(\Delta \mathbf{X}) &= -\sin \kappa_0 \cdot \Delta u_k - z_{ta} \sin \kappa_0 \cdot \Delta q \\
&\quad + \cos \kappa_0 \cdot \Delta w_k - x_{ta0} \cos \kappa_0 \cdot \Delta q
\end{aligned} \tag{7-32}$$

where the initial condition has been applied and z_{ta} is assumed constant as defined in section 6-3-3

The linearization of the second of the kinematic relations relating to the tether, equation (7-23), for the symmetric case is given by:

$$\begin{aligned} \dot{l}_t(\Delta \mathbf{X}) &= -\Delta \dot{z}_t^t \\ \dot{\theta}_t(\Delta \mathbf{X}) &= -\frac{1}{l_{t0}} \Delta \dot{x}_t^t \end{aligned} \quad (7-33)$$

From the kinematic relation (5-24) one can obtain a relation between the rotational velocities of the body and the tether, which is used to remove the state κ and to be replaced by θ and θ_t . Linearization for the symmetric case with the initial conditions gives:

$$q(\Delta \mathbf{X}) = \Delta \dot{\kappa} + \Delta \dot{\theta}_t \quad (7-34)$$

Wind kinematics

The wind kinematic relations (6-25) can be written as:

$$\begin{aligned} \mathbf{V}_a &= \mathbf{V}_k - \mathbf{V}_W \\ \begin{bmatrix} u_a \\ v_a \\ w_a \end{bmatrix} &= \begin{bmatrix} u_k \\ v_k \\ w_k \end{bmatrix} - \mathbb{T}_{bE} \begin{bmatrix} W_x \\ 0 \\ 0 \end{bmatrix} \end{aligned} \quad (7-35)$$

Evaluating the previous with the initial conditions gives :

$$\begin{aligned} u_a^b &= u_k^b - W_x \cos \theta \\ w_a^b &= w_k^b - W_x \sin \theta \end{aligned} \quad (7-36)$$

Applying linearization on equation (7-36) results in:

$$\begin{aligned} u_a(\mathbf{X}_0) &= u_{k,0} - W_{x0} \cos \theta_0 \\ w_a(\mathbf{X}_0) &= w_{k,0} - W_{x0} \sin \theta_0 \end{aligned} \quad (7-37)$$

and

$$\begin{aligned} u_a(\Delta \mathbf{X}) &= \Delta u_k - \cos \theta_0 \cdot \Delta W_x + W_{x0} \sin \theta_0 \cdot \Delta \theta \\ w_a(\Delta \mathbf{X}) &= \Delta w_k - \sin \theta_0 \cdot \Delta W_x - W_{x0} \cos \theta_0 \cdot \Delta \theta \end{aligned} \quad (7-38)$$

Furthermore for the linearization of the wind acceleration, equation (6-26), holds:

$$\begin{aligned} \dot{u}_a^b(\mathbf{X}_0) &= \dot{u}_{k,0} + q_0 \sin \theta_0 W_{x,0} \\ \dot{w}_a^b(\mathbf{X}_0) &= \dot{w}_{k,0} - q_0 \cos \theta_0 W_{x,0} \end{aligned} \quad (7-39)$$

and

$$\begin{aligned} \dot{u}_a^b(\Delta \mathbf{X}) &= \Delta \dot{u}_k + W_{x0} \sin \theta_0 \Delta q \\ \dot{w}_a^b(\Delta \mathbf{X}) &= \Delta \dot{w}_k - W_{x0} \cos \theta_0 \Delta q \end{aligned} \quad (7-40)$$

Linearized symmetric equations

Taking the previously obtained equations as a function of $\Delta \mathbf{X}$ together and dropping the Δ 's the following set of equations is obtained:

$$\begin{aligned}
-W \cos \theta_0 \cdot \theta + X_u \cdot u_a + X_{\dot{u}} \cdot \dot{u}_a + X_w \cdot w_a + X_{\dot{w}} \cdot \dot{w}_a + X_q \cdot q \\
+ F_\delta \cdot \delta + F_l \cdot l_t + F_i \cdot \dot{l}_t + F_\kappa \cdot \kappa &= m \cdot \dot{u}_k \\
-W \sin \theta_0 \cdot \theta + Z_u \cdot u_a + Z_{\dot{u}} \cdot \dot{u}_a + Z_w \cdot w_a + Z_{\dot{w}} \cdot \dot{w}_a + Z_q \cdot q \\
+ H_\delta \cdot \delta + H_l \cdot l_t + H_i \cdot \dot{l}_t + H_\kappa \cdot \kappa &= m \cdot \dot{w}_k \\
M_u \cdot u_a + M_{\dot{u}} \cdot \dot{u}_a + M_w \cdot w_a + M_{\dot{w}} \cdot \dot{w}_a + M_q \cdot q \\
+ Q_\delta \cdot \delta + Q_l \cdot l_t + Q_i \cdot \dot{l}_t + Q_\kappa \cdot \kappa &= I_y \cdot \dot{q} \\
\dot{\theta} &= q \\
\cos \kappa_0 \cdot u_k + z_{ta} \cos \kappa_0 \cdot q + \sin \kappa_0 \cdot w_k - x_{ta0} \sin \kappa_0 \cdot q &= -l_{t0} \cdot \dot{\theta}_t \\
- \sin \kappa_0 \cdot u_k - z_{ta} \sin \kappa_0 \cdot q + \cos \kappa_0 \cdot w_k - x_{ta0} \cos \kappa_0 \cdot q &= -\dot{l}_t \\
\dot{\kappa} + \dot{\theta}_t &= q \\
u_k - \cos \theta_0 \cdot W_x + W_{x0} \sin \theta_0 \cdot \theta &= u_a \\
w_k - \sin \theta_0 \cdot W_x - W_{x0} \cos \theta_0 \cdot \theta &= w_a \\
\dot{u}_k + W_{x0} \sin \theta_0 \cdot q &= \dot{u}_a \\
\dot{w}_k - W_{x0} \cos \theta_0 \cdot q &= \dot{w}_a
\end{aligned} \tag{7-41}$$

These 10 equations can be reduced to 6 equations. The equations for u_a and w_a can be used to replace the aerodynamic velocities in the force and moment equations. The same holds for \dot{u}_a .

Furthermore a relation between κ , θ and θ_t is obtained by integrating equation 7.

$$\begin{aligned}
q &= \dot{\kappa} + \dot{\theta}_c \\
\frac{d}{dt} \cdot \theta &= \frac{d}{dt} \cdot \kappa + \frac{d}{dt} \cdot \theta_c \\
\theta &= \kappa + \theta_c \\
\kappa &= \theta - \theta_c
\end{aligned} \tag{7-42}$$

where the integration constant is omitted, because it is represented in the initial state of equilibrium \mathbf{X}_0 .

Reducing the equations in (7-41) and collecting terms the following set of equations is obtained:

$$\begin{aligned}
& X_u \cdot u_k + X_{\dot{u}} \cdot \dot{u}_k + X_w \cdot w_k + X_{\dot{w}} \cdot \dot{w}_k \\
& + (-W \cos \theta_0 + X_u W_{x0} \sin \theta_0 - X_w W_{x0} \cos \theta_0 + F_\kappa) \cdot \theta \\
& + (X_q + X_{\dot{u}} W_{x0} \sin \theta_0 - X_{\dot{w}} W_{x0} \cos \theta_0) \cdot q + F_l \cdot l_t + F_i \cdot \dot{l}_t \\
& - F_\kappa \cdot \theta_t + (-X_w \sin \theta_0 - X_u \cos \theta_0) \cdot W_x + F_\delta \cdot x_{ta} = m \cdot \dot{u}_k \\
& Z_u \cdot u_k + Z_{\dot{u}} \cdot \dot{u}_k + Z_w \cdot w_k + Z_{\dot{w}} \cdot \dot{w}_k \\
& + (-W \sin \theta_0 + Z_u W_{x0} \sin \theta_0 - Z_w W_{x0} \cos \theta_0 + H_\kappa) \cdot \theta \\
& + (Z_q + Z_{\dot{u}} W_{x0} \sin \theta_0 - Z_{\dot{w}} W_{x0} \cos \theta_0) \cdot q + H_l \cdot l_t + H_i \cdot \dot{l}_t \\
& - H_\kappa \cdot \theta_t + (-Z_w \sin \theta_0 - Z_u \cos \theta_0) \cdot W_x + H_\delta \cdot x_{ta} = m \cdot \dot{w}_k \\
& M_u \cdot u_k + M_{\dot{u}} \cdot \dot{u}_k + M_w \cdot w_k + M_{\dot{w}} \cdot \dot{w}_k \\
& + (M_u W_{x0} \sin \theta_0 - M_w W_{x0} \cos \theta_0 + Q_\kappa) \cdot \theta \\
& + (M_q + M_{\dot{u}} W_{x0} \sin \theta_0 - M_{\dot{w}} W_{x0} \cos \theta_0) \cdot q + Q_l \cdot l_t + Q_i \cdot \dot{l}_t \\
& - Q_\kappa \cdot \theta_t + (-M_w \sin \theta_0 - M_u \cos \theta_0) \cdot W_x + Q_\delta \cdot x_{ta} = I_y \cdot \dot{q} \\
& q = \dot{\theta} \\
& \cos \kappa_0 \cdot u_k + \sin \kappa_0 \cdot w_k + (z_{ta} \cos \kappa_0 - x_{ta0} \sin \kappa_0) \cdot q = -l_{t0} \cdot \dot{\theta}_t \\
& - \sin \kappa_0 \cdot u_k + \cos \kappa_0 \cdot w_k - (z_{ta} \sin \kappa_0 + x_{ta0} \cos \kappa_0) \cdot q = -\dot{l}_t
\end{aligned} \tag{7-43}$$

For aircraft the equations of motion are made dimensionless because the aerodynamic forces and moments are expressed in non-dimensional coefficients. In this way the flying characteristics of different type of aircraft can be compared. Since kites also generate aerodynamic forces and moments and to be able to compare the flying characteristics of different type of kites the equations of motion for kites are made dimensionless as well.

The equations can be made dimensionless according to the divisors given in table 7-1 for the symmetric and asymmetric equations of motion.

	Symmetric motions	Asymmetric motions
Length [l]	\bar{c}	b
Velocity [lt^{-1}]	V_0	V_0
Mass [m]	$\rho S \bar{c}$	$\rho S b$

Table 7-1: Divisors for the dimensionless linearized equations of motion

In table 7-1 ρ is the air density, S the projected surface area, \bar{c} the mean aerodynamic chord and b the wing span.

In the symmetric equations (7-43) the force equations will be divided by $\frac{1}{2}\rho V_0^2 S$ and the moment equation by $\frac{1}{2}\rho V_0^2 S \bar{c}$. In this process the states as well as the derivatives become dimensionless. For example for the velocity component u becomes $u/V_0 = \hat{u}$. More details can be found in reference [24].

The result is:

$$\begin{aligned}
& (C_{X_u} + C_{X_{\dot{u}}} D_c) \cdot \hat{u}_k + (C_{X_w} + C_{X_{\dot{w}}} D_c) \cdot \hat{w}_k \\
& + (C_{Z_0} + C_{H_0} + C_{X_u} \hat{w}_{z_0} - C_{X_w} \hat{w}_{x_0} + C_{F_\kappa}) \cdot \theta \\
& + (C_{X_q} + C_{X_{\dot{u}}} \hat{w}_{z_0} - C_{X_w} \hat{w}_{x_0}) \cdot \frac{q\bar{c}}{V_a} + C_{F_l} \cdot \frac{l_t}{\bar{c}} + C_{F_i} \cdot \frac{i_t}{V_a} - C_{F_\kappa} \cdot \theta_t \\
& + (-C_{X_w} \sin \theta_0 - C_{X_u} \cos \theta_0) \cdot W_x + C_{F_\delta} \cdot x_{ta} = 2\mu_c D_c \cdot \hat{u}_k \\
& (C_{Z_u} + C_{Z_{\dot{u}}} D_c) \cdot \hat{u}_k + (C_{Z_w} + C_{Z_{\dot{w}}} D_c) \cdot \hat{w}_k \\
& + (-C_{X_0} - C_{F_0} + C_{Z_u} \hat{w}_{z_0} - C_{Z_w} \hat{w}_{x_0} + C_{H_\kappa}) \cdot \theta \\
& + (C_{Z_q} + C_{Z_{\dot{u}}} \hat{w}_{z_0} - C_{Z_w} \hat{w}_{x_0}) \cdot \frac{q\bar{c}}{V_a} + C_{H_l} \cdot \frac{l_t}{\bar{c}} + C_{H_i} \cdot \frac{i_t}{V_a} - C_{H_\kappa} \cdot \theta_t \\
& + (-C_{Z_w} \sin \theta_0 - C_{Z_u} \cos \theta_0) \cdot W_x + C_{H_\delta} \cdot x_{ta} = 2\mu_c D_c \cdot \hat{w}_k \quad (7-44) \\
& \frac{q\bar{c}}{V_a} = D_c \cdot \theta \\
& (C_{m_u} + C_{m_{\dot{u}}} D_c) \cdot \hat{u}_k + (C_{m_w} + C_{m_{\dot{w}}} D_c) \cdot \hat{w}_k \\
& + (C_{m_u} \hat{w}_{z_0} - C_{m_w} \hat{w}_{x_0} + C_{Q_\kappa}) \cdot \theta \\
& + (C_{m_q} + C_{m_{\dot{u}}} \hat{w}_{z_0} - C_{m_w} \hat{w}_{x_0}) \cdot \frac{q\bar{c}}{V_a} + C_{Q_l} \cdot \frac{l_t}{\bar{c}} + C_{Q_i} \cdot \frac{i_t}{V_a} - C_{Q_\kappa} \cdot \theta_t \\
& + (-C_{m_w} \sin \theta_0 - C_{m_u} \cos \theta_0) \cdot W_x + C_{Q_\delta} \cdot x_{ta} = 2\mu_c K_Y^2 D_c \cdot \frac{q\bar{c}}{V_a} \\
& \cos \kappa_0 \cdot \hat{u}_k + \sin \kappa_0 \cdot \hat{w}_k + \frac{z_{ta} \cos \kappa_0 - x_{ta0} \sin \kappa_0}{\bar{c}} \cdot \frac{q\bar{c}}{V_a} = -\frac{l_{t0}}{\bar{c}} D_c \cdot \theta_t \\
& - \sin \kappa_0 \cdot \hat{u}_k + \cos \kappa_0 \cdot \hat{w}_k - \frac{z_{ta} \sin \kappa_0 + x_{ta0} \cos \kappa_0}{\bar{c}} \cdot \frac{q\bar{c}}{V_a} = -D_c \cdot \frac{l_t}{\bar{c}}
\end{aligned}$$

with:

$$\begin{aligned}
\hat{u}_k &= \frac{u_k}{V_0} & C_{Z_0} + C_{H_0} &= -\frac{W \cos \theta_0}{\frac{1}{2} \rho V_0^2 S} \\
\hat{w}_k &= \frac{w_k}{V_0} & -C_{X_0} - C_{F_0} &= -\frac{W \sin \theta_0}{\frac{1}{2} \rho V_0^2 S} \\
\mu_c &= \frac{m}{\rho S \bar{c}} & \hat{w}_{x_0} &= \frac{W_{x_0} \cos \theta_0}{V_0} \\
\mu_c K_Y^2 &= \frac{I_y}{\rho S \bar{c}^3} & \hat{w}_{z_0} &= \frac{W_{x_0} \sin \theta_0}{V_0} \\
D_c &= \frac{\bar{c}}{V_0} \frac{d}{dt}
\end{aligned}$$

and

$$\begin{aligned}
C_{F_\kappa} &= -C_{H_0} & C_{F_l} &= -\frac{k_t \bar{c} \sin \kappa_0}{\frac{1}{2} \rho V_0^2 S} \\
C_{H_\kappa} &= C_{F_0} & C_{H_l} &= \frac{k_t \bar{c} \cos \kappa_0}{\frac{1}{2} \rho V_0^2 S} \\
C_{Q_\kappa} &= \frac{z_{ta}}{\bar{c}} C_{F_\kappa} - \frac{x_{ta0}}{\bar{c}} C_{H_\kappa} & C_{Q_l} &= -\frac{z_{ta} k_t \sin \kappa_0 + x_{ta0} k_t \cos \kappa_0}{\frac{1}{2} \rho V_0^2 S} \\
C_{F_i} &= -\frac{c_t \sin \kappa_0}{\frac{1}{2} \rho V_0 S} & C_{F_\delta} &= 0 \\
C_{H_i} &= \frac{c_t \cos \kappa_0}{\frac{1}{2} \rho V_0 S} & C_{H_\delta} &= 0 \\
C_{Q_i} &= -\frac{z_{ta} c_t \sin \kappa_0 + x_{ta0} c_t \cos \kappa_0}{\frac{1}{2} \rho V_0 S \bar{c}} & C_{Q_\delta} &= -C_{H_0}
\end{aligned}$$

where the terms with the weight W come from the force equilibrium.

The dimensionless aerodynamic force and moment derivatives have to be known for the specific kite to be studied. They can be obtained from experimental data, other models or flight tests.

The next step is to write the equations in matrix notation depending on the dimensionless states \hat{u}_k , \hat{w}_k , θ , $\frac{q\bar{c}}{V_0}$, θ_t and $\frac{l_t}{\bar{c}}$ with $\frac{W_x}{V_0}$ and $\frac{x_{ta}}{\bar{c}}$ as inputs:

$$\begin{aligned}
& \begin{bmatrix} C_{X_u} + (C_{X_{\dot{u}}} - 2\mu_c)D_c & C_{X_w} + C_{X_{\dot{w}}}D_c & c_{x_\theta} & c_{x_q} & -C_{F_\kappa} & C_{F_l} + C_{F_l}D_c \\ C_{Z_u} + C_{Z_{\dot{u}}}D_c & C_{Z_w} + (C_{Z_{\dot{w}}} - 2\mu_c)D_c & c_{z_\theta} & c_{z_q} & -C_{Z_\kappa} & C_{H_l} + C_{H_l}D_c \\ 0 & 0 & -D_c & 1 & 0 & 0 \\ C_{m_u} + C_{m_{\dot{u}}}D_c & C_{m_w} + C_{m_{\dot{w}}}D_c & c_{m_\theta} & c_{m_q} - 2\mu_c K_Y^2 D_c & -C_{Q_\kappa} & C_{Q_l} + C_{Q_l}D_c \\ \cos \kappa_0 & \sin \kappa_0 & 0 & \frac{z_{ta} \cos \kappa_0 - x_{ta0} \sin \kappa_0}{\bar{c}} & \frac{l_{t0}}{\bar{c}} D_c & 0 \\ -\sin \kappa_0 & \cos \kappa_0 & 0 & -\frac{z_{ta} \sin \kappa_0 + x_{ta0} \cos \kappa_0}{\bar{c}} & 0 & D_c \end{bmatrix} \begin{bmatrix} \hat{u}_k \\ \hat{w}_k \\ \theta \\ \frac{q\bar{c}}{V_0} \\ \theta_t \\ \frac{l_t}{\bar{c}} \end{bmatrix} \\
& = \begin{bmatrix} c_{x_W} & -C_{F_\delta} \\ c_{z_W} & -C_{H_\delta} \\ 0 & 0 \\ c_{m_W} & -C_{Q_\delta} \\ 0 & 0 \\ 0 & 0 \end{bmatrix} \begin{bmatrix} \frac{W_x}{V_0} \\ \frac{x_{ta}}{\bar{c}} \end{bmatrix} \quad (7-45)
\end{aligned}$$

with:

$$\begin{aligned}
c_{x_\theta} &= C_{Z_0} + C_{H_0} + C_{X_u} \hat{w}_{z_0} - C_{X_w} \hat{w}_{x_0} + C_{F_\kappa} \\
c_{z_\theta} &= -C_{X_0} - C_{F_0} + C_{Z_u} \hat{w}_{z_0} - C_{Z_w} \hat{w}_{x_0} + C_{H_\kappa} \\
c_{m_\theta} &= C_{m_u} \hat{w}_{z_0} - C_{m_w} \hat{w}_{x_0} + C_{Q_\kappa} \\
c_{x_q} &= C_{X_q} + C_{X_{\dot{u}}} \hat{w}_{z_0} - C_{X_{\dot{w}}} \hat{w}_{x_0} \\
c_{z_q} &= C_{Z_q} + C_{Z_{\dot{u}}} \hat{w}_{z_0} - C_{Z_{\dot{w}}} \hat{w}_{x_0} \\
c_{m_q} &= C_{m_q} + C_{m_{\dot{u}}} \hat{w}_{z_0} - C_{m_{\dot{w}}} \hat{w}_{x_0} \\
c_{x_W} &= C_{X_w} \sin \theta_0 + C_{X_u} \cos \theta_0 \\
c_{z_W} &= C_{Z_w} \sin \theta_0 + C_{Z_u} \cos \theta_0 \\
c_{m_W} &= C_{m_w} \sin \theta_0 + C_{m_u} \cos \theta_0
\end{aligned}$$

7-2-2 Matrix notation of asymmetric equations of motion

The derivation of the asymmetric LTI model for the given initial condition is given in this section.

States

Linearizing the right hand side of the equations of motion (7-9) for the asymmetric case with the initial condition gives:

$$\begin{aligned} F_y(\Delta \mathbf{X}) &= m \cdot \Delta \dot{v}_k \\ \mathcal{M}_x(\Delta \mathbf{X}) &= I_x \cdot \Delta \dot{p} - J_{xz} \cdot \Delta \dot{r} \\ \mathcal{M}_z(\Delta \mathbf{X}) &= I_z \cdot \Delta \dot{r} - J_{xz} \cdot \Delta \dot{p} \end{aligned} \quad (7-46)$$

Forces and moments

The forces and moments for the asymmetric case are a function of:

$$\begin{aligned} W &\rightarrow f(\phi) \\ Y, L, N &\rightarrow f(v_a, \dot{v}_a, p, r) \\ G, P, R &\rightarrow f(x_{ta}^L, x_{ta}^R, \tau) \end{aligned}$$

where x_{ta}^L and x_{ta}^R are the displacements of the left and right tether attachment points.

The linearized asymmetric forces and moments of equations (7-13) become:

$$\begin{aligned} F_y(\Delta \mathbf{X}) &= W \cos \theta_0 \cdot \Delta \phi \\ &\quad + Y_v \cdot \Delta v_a + Y_{\dot{v}} \cdot \Delta \dot{v}_a + Y_p \cdot \Delta p + Y_r \cdot \Delta r \\ &\quad + G_{\delta_L} \cdot \Delta x_{ta}^L + G_{\delta_R} \cdot \Delta x_{ta}^R + G_\tau \cdot \Delta \tau \\ \mathcal{M}_x(\Delta \mathbf{X}) &= L_v \cdot \Delta v_a + L_{\dot{v}} \cdot \Delta \dot{v}_a + L_p \cdot \Delta p + L_r \cdot \Delta r \\ &\quad + P_{\delta_L} \cdot \Delta x_{ta}^L + P_{\delta_R} \cdot \Delta x_{ta}^R + P_\tau \cdot \Delta \tau \\ \mathcal{M}_z(\Delta \mathbf{X}) &= N_v \cdot \Delta v_a + N_{\dot{v}} \cdot \Delta \dot{v}_a + N_p \cdot \Delta p + N_r \cdot \Delta r \\ &\quad + R_{\delta_L} \cdot \Delta x_{ta}^L + R_{\delta_R} \cdot \Delta x_{ta}^R + R_\tau \cdot \Delta \tau \end{aligned} \quad (7-47)$$

Tether forces and moments

Expressions for derivatives of the tether forces and moments can be found by linearizing the equations for the bridle lines given in section 6-3-4.

From equation (6-17) can be obtained by applying the initial conditions $\tau_0 = 0$ and $\kappa_0 \neq 0$:

$$\begin{aligned} \Delta F &= -\sin \kappa_0 \cdot \Delta T_t - T_{t0} \cos \kappa_0 \cdot \Delta \kappa \\ \Delta G &= T_{t0} \cos \kappa_0 \cdot \Delta \tau \\ \Delta H &= \cos \kappa_0 \cdot \Delta T_t - T_{t0} \sin \kappa_0 \cdot \Delta \kappa \end{aligned} \quad (7-48)$$

Since T_t and κ are symmetric quantities ΔT_t and $\Delta \kappa$ are zero for the asymmetric motions, so only ΔG is not zero.

Linearizing equations (6-38) the derivative of the bridle force components in body-fixed reference is obtained:

$$\begin{aligned} F_L(\Delta \mathbf{X}) &= -\sin \kappa_0 \cos \vartheta \cdot \Delta T_L & F_R(\Delta \mathbf{X}) &= -\sin \kappa_0 \cos \vartheta \cdot \Delta T_R \\ G_L(\Delta \mathbf{X}) &= \sin \vartheta \cdot \Delta T_L & G_R(\Delta \mathbf{X}) &= -\sin \vartheta \cdot \Delta T_R \\ H_L(\Delta \mathbf{X}) &= \cos \kappa_0 \cos \vartheta \cdot \Delta T_L & H_R(\Delta \mathbf{X}) &= \cos \kappa_0 \cos \vartheta \cdot \Delta T_R \end{aligned} \quad (7-49)$$

Linearizing the equations for T_L and T_R gives:

$$\begin{aligned} T_L(\Delta \mathbf{X}) &= \frac{T_{br0}^v}{\sqrt{T_{br0}^{v2} + T_{br0}^{h2}}} \cdot \Delta T_L^v + \frac{T_{br0}^h}{\sqrt{T_{br0}^{v2} + T_{br0}^{h2}}} \cdot \Delta T_L^h \\ T_R(\Delta \mathbf{X}) &= \frac{T_{br0}^v}{\sqrt{T_{br0}^{v2} + T_{br0}^{h2}}} \cdot \Delta T_R^v + \frac{T_{br0}^h}{\sqrt{T_{br0}^{v2} + T_{br0}^{h2}}} \cdot \Delta T_R^h \end{aligned} \quad (7-50)$$

where br stands for the left and right bridle line and where is used that $T_{L0}^v = T_{R0}^v = T_{br0}^v$ and $T_{L0}^h = T_{R0}^h = T_{br0}^h$ for the initial condition where G is zero.

Linearizing the vertical and horizontal components of T_L and T_R gives:

$$\begin{aligned} T_L^v(\Delta \mathbf{X}) &= \frac{1}{2 \tan \vartheta} \cdot \Delta G & T_R^v(\Delta \mathbf{X}) &= -\frac{1}{2 \tan \vartheta} \cdot \Delta G \\ T_L^h(\Delta \mathbf{X}) &= \frac{1}{2} \cdot \Delta G & T_R^h(\Delta \mathbf{X}) &= -\frac{1}{2} \cdot \Delta G \end{aligned} \quad (7-51)$$

Linearizing equations (6-35) for the asymmetric left and right bridle moments P_L , P_R , R_L and R_R results in:

$$\begin{aligned} P_L(\Delta \mathbf{X}) &= y_{ta}^L \cdot \Delta H_L - z_{ta}^L \cdot \Delta G_L \\ P_R(\Delta \mathbf{X}) &= y_{ta}^R \cdot \Delta H_R - z_{ta}^R \cdot \Delta G_R \\ R_L(\Delta \mathbf{X}) &= x_{ta0}^L \cdot \Delta G_L + G_{L0} \cdot \Delta x_{ta}^L - y_{ta}^L \cdot \Delta F_L \\ R_R(\Delta \mathbf{X}) &= x_{ta0}^R \cdot \Delta G_R + G_{R0} \cdot \Delta x_{ta}^R - y_{ta}^R \cdot \Delta F_R \end{aligned} \quad (7-52)$$

Finally the resulting moments on the body P and R are than given by:

$$\begin{aligned} P(\Delta \mathbf{X}) &= \Delta P_L + \Delta P_R \\ R(\Delta \mathbf{X}) &= \Delta R_L + \Delta R_R \end{aligned} \quad (7-53)$$

Finally condensing the previously obtained equations will give the first derivatives of G , P and R as a function of τ , x_{ta}^L and x_{ta}^R :

$$\begin{aligned} G_\tau &= T_{t0} \cos \kappa_0 \\ P_\tau &= -\frac{z_{ta} \sin \vartheta \cos \kappa_0 \sqrt{T_{t0}^2 (1 + \tan^2 \vartheta)}}{\tan \vartheta} + \frac{y_{ta}^L \cos \vartheta \cos^2 \kappa_0 \sqrt{T_{t0}^2 (1 + \tan^2 \vartheta)}}{\tan \vartheta} \\ R_\tau &= \frac{y_{ta}^L \cos \vartheta \sin \kappa_0 \cos \kappa_0 \sqrt{T_{t0}^2 (1 + \tan^2 \vartheta)}}{\tan \vartheta} + \frac{x_{ta0} \sin \vartheta \cos \kappa_0 \sqrt{T_{t0}^2 (1 + \tan^2 \vartheta)}}{\tan \vartheta} \\ R_{\delta_L} &= T_{br0} \sin \vartheta \\ R_{\delta_R} &= -T_{br0} \sin \vartheta \end{aligned} \quad (7-54)$$

where the fact is used that $y_{ta}^L = -y_{ta}^R$ and $z_{ta}^L = z_{ta}^R = z_{ta}$. Note that G_{δ_L} , G_{δ_R} , P_{δ_L} and P_{δ_R} are zero.

Kinematic relations

Equation (7-22) of the kinematic relations with the initial conditions is:

$$\begin{aligned} \dot{\phi}(\Delta \mathbf{X}) &= \Delta p + \tan \theta_0 \cdot \Delta r \\ \dot{\psi}(\Delta \mathbf{X}) &= \frac{1}{\cos \theta_0} \cdot \Delta r \end{aligned} \quad (7-55)$$

The kinematic relations relating to the tether, equations (6-23) and (7-23), for the asymmetric motion are linearized as follows.

Equation (6-23) is written as a function of only the asymmetric degree of freedom, \dot{y}_t^t :

$$\begin{aligned} \begin{bmatrix} \dot{x}_t^t \\ \dot{y}_t^t \\ \dot{z}_t^t \end{bmatrix} &= \mathbb{T}_{tb} \left(\begin{bmatrix} u_k^b \\ v_k^b \\ w_k^b \end{bmatrix} + \boldsymbol{\Omega}_{bE}^b \times \mathbf{r}_{ta}^b \right) \\ &= \mathbb{T}_{tb} \left(\begin{bmatrix} 0 \\ v_k \\ 0 \end{bmatrix} + \begin{bmatrix} 0 \\ r \cdot x_{ta} - p \cdot z_{ta} \\ 0 \end{bmatrix} \right) \\ &= \mathbb{T}_{bt}^\top \begin{bmatrix} 0 \\ \dot{y}_t^b \\ 0 \end{bmatrix} \\ &= \begin{bmatrix} 0 \\ \cos \tau \cdot \dot{y}_t^b \\ 0 \end{bmatrix} \end{aligned}$$

This gives:

$$\dot{y}_t^t = \cos \tau \cdot (v_k + r \cdot x_{ta} - p \cdot z_{ta})$$

Linearizing this equation gives for \mathbf{X}_0 and $\Delta \mathbf{X}$:

$$\dot{y}_t^t(\mathbf{X}_0) = -p_0 \cdot z_{ta} + r_0 \cdot x_{ta0} \quad (7-56)$$

where x_{ta0} is the initial cart position and z_{ta} is invariant.

$$\dot{y}_t^t(\Delta \mathbf{X}) = \Delta v_k - z_{ta} \cdot \Delta p + x_{ta0} \cdot \Delta r \quad (7-57)$$

The linearization of the second of the kinematic relations relating to the tether, equation (7-23), for the asymmetric variable results in:

$$\dot{\psi}_t(\Delta \mathbf{X}) = -\frac{1}{l_{t0} \sin \theta_{t0}} \Delta \dot{y}_t^t \quad (7-58)$$

Taking equations (7-57) and (7-58) together results in:

$$\Delta \dot{\psi}_t = -\frac{1}{l_{t0} \sin \theta_{t0}} \cdot \Delta v_k + \frac{z_{ta}}{l_{t0} \sin \theta_{t0}} \cdot \Delta p - \frac{x_{ta0}}{l_{t0} \sin \theta_{t0}} \cdot \Delta r \quad (7-59)$$

Another equation can be obtained from the kinematic relation (5-24) for a relation between the rotational velocities of the body and the tether, which is used to remove the state τ and to be replaced by θ and θ_t . The asymmetric body rotations p and r are given by:

$$\begin{aligned} p &= \dot{\tau} - \dot{\xi} \cdot \sin \kappa - \dot{\psi}_t \cdot (\sin \theta_t \cos \kappa \cos \xi + \cos \theta_t \sin \kappa) \\ r &= -\dot{\kappa} \cdot \sin \tau + \dot{\xi} \cdot \cos \tau \cos \kappa - \dot{\psi}_t \cdot \sin \theta_t (\cos \tau \sin \kappa \cos \xi + \sin \tau \sin \xi) \\ &\quad + \dot{\psi}_t \cos \theta_t \cos \tau \cos \kappa \end{aligned} \quad (7-60)$$

Linearizing these equations with the initial condition gives for $\Delta \mathbf{X}$:

$$\begin{aligned} p(\Delta \mathbf{X}) &= \Delta \dot{\tau} - \sin \kappa_0 \cdot \Delta \dot{\xi} - (\sin \theta_{t0} \cos \kappa_0 + \cos \theta_{t0} \sin \kappa_0) \cdot \Delta \dot{\psi}_t \\ r(\Delta \mathbf{X}) &= \cos \kappa_0 \cdot \Delta \dot{\xi} - (\sin \theta_{t0} \sin \kappa_0 - \cos \theta_{t0} \cos \kappa_0) \cdot \Delta \dot{\psi}_t \end{aligned} \quad (7-61)$$

Wind kinematics

The wind kinematics equation (6-25) can be written as:

$$\mathbf{V}_a^b = \mathbf{V}_k^b - \mathbf{V}_w^b$$

$$\begin{bmatrix} u_a \\ v_a \\ w_a \end{bmatrix} = \begin{bmatrix} u_k \\ v_k \\ w_k \end{bmatrix} - \mathbb{T}_{bE} \begin{bmatrix} W_x \\ W_y \\ 0 \end{bmatrix} \quad (7-62)$$

Evaluating the previous for v_a results in:

$$v_a = v_k - (\sin \phi \sin \theta \cos \psi - \cos \phi \sin \psi) \cdot W_x$$

$$- (\sin \phi \sin \theta \sin \psi + \cos \phi \cos \psi) \cdot W_y \quad (7-63)$$

Linearization of (7-63) with the initial conditions gives:

$$v_a(\mathbf{X}_0) = 0 \quad (7-64)$$

and

$$v_a(\Delta \mathbf{X}) = \Delta v_k - \Delta W_y - W_{x0} \sin \theta_0 \cdot \Delta \phi + W_{x0} \cdot \Delta \psi \quad (7-65)$$

For the wind acceleration, equation (6-26), with the initial conditions holds:

$$\dot{v}_a(\Delta \mathbf{X}) = W_{x0} \cos \theta_0 \cdot \Delta r - W_{x0} \sin \theta_0 \cdot \Delta p \quad (7-66)$$

Linearized asymmetric equations

Taking the previously obtained equations as a function of $\Delta \mathbf{X}$ together and dropping the Δ 's the following set of equations is obtained:

$$\begin{aligned} W \cos \theta_0 \cdot \phi + Y_v \cdot v_a + Y_{\dot{v}} \cdot \dot{v}_a + Y_p \cdot p + Y_r \cdot r \\ + G_\tau \cdot \tau &= m \cdot \dot{v}_k \\ L_v \cdot v_a + L_{\dot{v}} \cdot \dot{v}_a + L_p \cdot p + L_r \cdot r \\ + P_\tau \cdot \tau &= I_x \cdot \dot{p} - J_{xz} \cdot \dot{r} \\ N_v \cdot v_a + N_{\dot{v}} \cdot \dot{v}_a + N_p \cdot p + N_r \cdot r \\ + R_{\delta_L} \cdot x_{ta}^L + R_{\delta_R} \cdot x_{ta}^R + R_\tau \cdot \tau &= I_z \cdot \dot{r} - J_{xz} \cdot \dot{p} \\ p + \tan \theta_0 \cdot r &= \dot{\phi} \\ \frac{1}{\cos \theta_0} \cdot r &= \dot{\psi} \\ -v_k + z_{ta} \cdot p - x_{ta0} \cdot r &= l_{t0} \sin \theta_{t0} \cdot \dot{\psi}_t \\ \tau - \sin \kappa_0 \cdot \dot{\xi} - (\sin \theta_{t0} \cos \kappa_0 + \cos \theta_{t0} \sin \kappa_0) \cdot \dot{\psi}_t &= p \\ \cos \kappa_0 \cdot \dot{\xi} - (\sin \theta_{t0} \sin \kappa_0 - \cos \theta_{t0} \cos \kappa_0) \cdot \dot{\psi}_t &= r \\ v_k - W_y - W_{x0} \sin \theta_0 \cdot \phi + W_{x0} \cdot \psi &= v_a \\ \dot{v}_k - W_{x0} \sin \theta_0 \cdot p + W_{x0} \cos \theta_0 \cdot r &= \dot{v}_a \end{aligned} \quad (7-67)$$

These 10 relations can be reduced to a set of 6 equations, depending on the states v_k , ϕ , p , ψ , r and ψ_t .

A relation can be found for τ depending on ϕ , ψ and ψ_t by taking equations 4,5,7 and 8 of (7-67) together:

$$\dot{\tau} = \dot{\phi} + (-\sin \theta_0 + \tan \kappa_0 \cos \theta_0) \cdot \dot{\psi} + \frac{\sin \theta_{t0}}{\cos \kappa_0} \cdot \dot{\psi}_t$$

and equation (7-68) can be integrated to obtain:

$$\tau = \phi + t_\psi \cdot \psi + t_{\psi_t} \cdot \psi_t \quad (7-68)$$

with

$$\begin{aligned} t_\psi &= -\sin \theta_0 + \tan \kappa_0 \cos \theta_0 \\ t_{\psi_t} &= \frac{\sin \theta_{t0}}{\cos \kappa_0} \end{aligned}$$

Reducing the 10 equations to 6 and collecting terms the following set of equations is obtained:

$$\begin{aligned} Y_v \cdot v_k + Y_{\dot{v}} \cdot \dot{v}_k + (W \cos \theta_0 - W_x \sin \theta_0 Y_v + G_\tau) \cdot \phi \\ + (-Y_{\dot{v}} W_x \sin \theta_0 + Y_p) \cdot p + (Y_v W_x + G_\tau t_\psi) \cdot \psi \\ + (Y_{\dot{v}} W_x \cos \theta_0 + Y_r) \cdot r + G_\tau t_{\psi_t} \cdot \psi_t - Y_v \cdot W_y &= m \cdot \dot{v}_k \\ p + \tan \theta_0 \cdot r &= \dot{\phi} \\ L_v \cdot v_k + L_{\dot{v}} \cdot \dot{v}_k + (-W_x \sin \theta_0 L_v + P_\tau) \cdot \phi \\ + (-L_{\dot{v}} W_x \sin \theta_0 + L_p) \cdot p + (L_v W_x + P_\tau t_\psi) \cdot \psi \\ + (L_{\dot{v}} W_x \cos \theta_0 + L_r) \cdot r + P_\tau t_{\psi_t} \cdot \psi_t - L_v \cdot W_y &= I_x \cdot \dot{p} - J_{xz} \cdot \dot{r} \\ \frac{1}{\cos \theta_0} \cdot r &= \dot{\psi} \\ N_v \cdot v_k + N_{\dot{v}} \cdot \dot{v}_k + (-W_x \sin \theta_0 N_v + P_\tau) \cdot \phi \\ + (-N_{\dot{v}} W_x \sin \theta_0 + N_p) \cdot p + (N_v W_x + R_\tau t_\psi) \cdot \psi \\ + (N_{\dot{v}} W_x \cos \theta_0 + N_r) \cdot r + R_\tau t_{\psi_t} \cdot \psi_t - N_v \cdot W_y \\ + R_{\delta_L} \cdot x_{ta}^L + R_{\delta_R} \cdot x_{ta}^R &= I_z \cdot \dot{r} - J_{xz} \cdot \dot{p} \\ -v_k + z_{ta} \cdot p - x_{ta0} \cdot r &= l_{t0} \sin \theta_{t0} \cdot \dot{\psi}_t \end{aligned} \quad (7-69)$$

As for the symmetric equations of motion the asymmetric equations are made dimensionless as well. The divisors are given in table 7-1. The forces are divided by $\frac{1}{2}\rho V_0^2 S$ and the moments by $\frac{1}{2}\rho V_0^2 S b$. The dimensionless quantities of p and r are $\frac{pb}{2V_0}$ and $\frac{rb}{2V_0}$ respectively. There is no specific reason for this way, but more a custom in flight dynamics.

The dimensionless equations of motion can be written as:

$$\begin{aligned}
& (C_{Y_v} + C_{Y_v} D_b) \cdot \hat{v}_k + (-C_{Z_0} - C_{H_0} - C_{Y_v} \hat{w}_{z_0} + C_{G_\tau}) \cdot \phi \\
& + (-2C_{Y_{\hat{v}}} \hat{w}_{z_0} + C_{Y_p}) \cdot \frac{pb}{2V_0} + (C_{Y_v} \frac{W_x}{V_0} + C_{G_\tau} t_\psi) \cdot \psi \\
& + (2C_{Y_{\hat{v}}} \hat{w}_{x_0} + C_{Y_r}) \cdot \frac{rb}{2V_0} + C_{G_\tau} t_{\psi_t} \cdot \psi_t - C_{Y_v} \cdot \frac{W_y}{V_0} = 2\mu_b D_b \cdot \hat{v}_k \\
& \qquad \qquad \qquad 2 \frac{pb}{2V_0} + 2 \tan \theta_0 \cdot \frac{rb}{2V_0} = D_b \cdot \phi \\
& (C_{l_v} + C_{l_v} D_b) \cdot \hat{v}_k + (-C_{l_v} \hat{w}_{z_0} + C_{P_\tau}) \cdot \phi \\
& + (-2C_{l_{\hat{v}}} \hat{w}_{z_0} + C_{l_p}) \cdot \frac{pb}{2V_0} + (C_{l_v} \frac{W_x}{V_0} + C_{P_\tau} t_\psi) \cdot \psi \\
& + (2C_{l_{\hat{v}}} \hat{w}_{x_0} + C_{l_r}) \cdot \frac{rb}{2V_0} + C_{P_\tau} t_{\psi_t} \cdot \psi_t - C_{l_v} \cdot \frac{W_y}{V_0} = 4\mu_b K_X^2 D_b \cdot \frac{pb}{2V_0} - 4\mu_b K_{XZ} D_b \cdot \frac{rb}{2V_0} \\
& \qquad \qquad \qquad \frac{2}{\cos \theta_0} \cdot \frac{rb}{2V_0} = D_b \cdot \psi \\
& (C_{n_v} + C_{n_v} D_b) \cdot \hat{v}_k + (-C_{n_v} \hat{w}_{z_0} + C_{P_\tau}) \cdot \phi \\
& + (-2C_{n_{\hat{v}}} \hat{w}_{z_0} + C_{n_p}) \cdot \frac{pb}{2V_0} + (C_{n_v} \frac{W_x}{V_0} + C_{R_\tau} t_\psi) \cdot \psi \\
& + (2C_{n_{\hat{v}}} \hat{w}_{x_0} + C_{n_r}) \cdot \frac{rb}{2V_0} + C_{R_\tau} t_{\psi_t} \cdot \psi_t - C_{n_v} \cdot \frac{W_y}{V_0} \\
& \qquad \qquad \qquad + C_{R_{\delta_L}} \cdot \frac{x_{ta}^L}{b} + C_{R_{\delta_R}} \cdot \frac{x_{ta}^R}{b} = 4\mu_b K_Z^2 D_b \cdot \frac{rb}{2V_0} - 4\mu_b K_{XZ} D_b \cdot \frac{pb}{2V_0} \\
& - \frac{v_k}{V_0} + 2 \frac{z_{ta}}{b} \cdot \frac{pb}{2V_0} - 2 \frac{x_{ta0}}{b} \cdot \frac{rb}{2V_0} = \frac{l_{t0} \sin \theta_{t0}}{b} D_b \cdot \psi_t
\end{aligned} \tag{7-70}$$

where $W \cos \theta_0$ has been replaced by $-Z_0 - H_0$ as was done in the symmetric equations.

The next step is to write the equations in matrix notation depending on the dimensionless states \hat{v}_k , ϕ , $\frac{pb}{2V_0}$, ψ , $\frac{rb}{2V_0}$ and ψ_t with $\frac{W_y}{V_0}$, $\frac{x_{ta}^L}{b}$ and $\frac{x_{ta}^R}{b}$ as inputs:

$$\begin{aligned}
& \begin{bmatrix} C_{Y_v} + (C_{Y_{\hat{v}}} - 2\mu_b) D_b & c_{y_\phi} & c_{y_p} & C_{Y_v} \frac{W_x}{V_0} + C_{G_\tau} t_\psi & c_{y_r} & C_{G_\tau} t_{\psi_t} \\ 0 & -D_b & 2 & 0 & 2 \tan \theta_0 & 0 \\ C_{l_v} + C_{l_{\hat{v}}} D_b & c_{l_\phi} & c_{l_p} - 4\mu_b K_X^2 D_b & C_{l_v} \frac{W_x}{V_0} + C_{P_\tau} t_\psi & c_{l_r} + 4\mu_b K_{XZ} D_b & C_{P_\tau} t_{\psi_t} \\ 0 & 0 & 0 & -D_b & \frac{2}{\cos \theta_0} & 0 \\ C_{n_v} + C_{n_{\hat{v}}} D_b & c_{n_\phi} & c_{n_p} + 4\mu_b K_{XZ} D_b & C_{n_v} \frac{W_x}{V_0} + C_{R_\tau} t_\psi & c_{n_r} - 4\mu_b K_Z^2 D_b & C_{R_\tau} t_{\psi_t} \\ 1 & 0 & -2 \frac{z_{ta}}{b} & 0 & 2 \frac{x_{ta0}}{b} & \frac{l_{t0} \sin \theta_{t0}}{b} D_b \end{bmatrix} \begin{bmatrix} \hat{v}_k \\ \phi \\ \frac{pb}{2V_0} \\ \psi \\ \frac{rb}{2V_0} \\ \psi_t \end{bmatrix} \\
& = \begin{bmatrix} C_{Y_v} & 0 & 0 \\ 0 & 0 & 0 \\ C_{l_v} & 0 & 0 \\ 0 & 0 & 0 \\ C_{n_v} & -C_{R_{\delta_L}} & -C_{R_{\delta_R}} \\ 0 & 0 & 0 \end{bmatrix} \begin{bmatrix} \frac{W_y}{V_0} \\ \frac{x_{ta}^L}{b} \\ \frac{x_{ta}^R}{b} \end{bmatrix}
\end{aligned} \tag{7-71}$$

where

$$\begin{aligned}
c_{y_\phi} &= -C_{Z_0} - C_{H_0} - C_{Y_v} \hat{w}_{z_0} + C_{G_\tau} \\
c_{l_\phi} &= -C_{l_v} \hat{w}_{z_0} + C_{P_\tau} \\
c_{n_\phi} &= -C_{n_v} \hat{w}_{z_0} + C_{R_\tau} \\
c_{y_p} &= -2 \cdot C_{Y_{\hat{v}}} \hat{w}_{z_0} + C_{Y_p} \\
c_{l_p} &= -2 \cdot C_{l_{\hat{v}}} \hat{w}_{z_0} + C_{l_p} \\
c_{n_p} &= -2 \cdot C_{n_{\hat{v}}} \hat{w}_{z_0} + C_{n_p} \\
c_{y_r} &= 2 \cdot C_{Y_{\hat{v}}} \hat{w}_{x_0} + C_{Y_r} \\
c_{l_r} &= 2 \cdot C_{l_{\hat{v}}} \hat{w}_{x_0} + C_{l_r} \\
c_{n_r} &= 2 \cdot C_{n_{\hat{v}}} \hat{w}_{x_0} + C_{n_r}
\end{aligned}$$

The equations of motion can also be given in state-space form given by equation (7-72).

7-2-3 Equations of motion in state space form

To simulate the models in MATLAB the matrix notation is written in the standard state space form given by equation (7-72):

$$\begin{aligned}\dot{\mathbf{x}} &= \mathbf{A}\mathbf{x} + \mathbf{B}\mathbf{u} \\ \mathbf{y} &= \mathbf{C}\mathbf{x} + \mathbf{D}\mathbf{u}\end{aligned}\tag{7-72}$$

where \mathbf{A} is the state-matrix, \mathbf{B} the input-matrix, \mathbf{C} the output matrix and \mathbf{D} the direct matrix. Furthermore \mathbf{x} is the state vector, \mathbf{y} the output vector and \mathbf{u} the input vector.

The state space form is obtained by rearranging equation (7-45). First, all terms without the differential operator D_c are put to the right hand side and the differential operator D_c is replaced by $\frac{c}{V_a} \frac{d}{dt}$. This results in a equation of the form:

$$P \frac{d\mathbf{x}}{dt} = P\dot{\mathbf{x}} = Q\mathbf{x} + R\mathbf{u}$$

The state space form is than obtained by:

$$\dot{\mathbf{x}} = P^{-1}Q\mathbf{x} + P^{-1}R\mathbf{u} = \mathbf{A}\mathbf{x} + \mathbf{B}\mathbf{u}$$

Note that the resultant output variables are dimensionless. Each variable must be multiplied by its respective dimensional multiplier.

Review & remarks

The linearization process at the specified flight condition shows that the symmetric and asymmetric equations of motion result in two decoupled LTI models. This holds with the assumption that the aerodynamic states are decoupled.

The theory in this chapter could be of valuable use for stability analysis and controller design purposes. The LTI models can be used for stability analysis on a parametric basis. By computing the characteristic equation of the state-matrix \mathbf{A} the eigenvalues of the system can be derived. Routh and Hurwitz derived criteria which the coefficients of an algebraic equation have to satisfy for all real eigenvalues and the real parts of the complex eigenvalues to be negative (reference [24]). With this method the influence of the stability derivatives on the stability of the system can be analyzed.

Simulations of the LTI models are performed in chapter 8.

Verification of Rigid Body Kite model

The verification of the Rigid Body model is done by simulating the Cessna Ce500 ‘Citation’ aircraft as well as a light version of this aircraft attached to a tether. The latter system is called ‘Citation-Kite’. As reference for the aircraft simulations a linear aircraft model is used as given in reference [24]. For the Citation-Kite a comparison is made between the linear kite models as derived in chapter 7 and the nonlinear Rigid Body Kite model as described in chapter 6. Additionally, the simulation results are shown in appendix E.

8-1 Aircraft simulation

The aircraft verification is performed by simulating the Cessna Ce500 ‘Citation’ aircraft. In reference [24] linear time invariant (LTI) models are derived for the symmetric and asymmetric motions of an aircraft at a steady, straight, symmetric flight condition. These models are used to simulate the Cessna Citation aircraft. Here, the same aircraft is simulated with similar LTI models. Additionally, the models are adapted to have the wind speed as input on the system as well. The LTI models have the same dynamics if the initial wind speed and initial kinematic velocities are set right. Therefore the LTI models serve as a reference for the nonlinear model Rigid Body.

The LTI model simulations are used to verify the Rigid Body Kite model of chapter 6. The nonlinear kite model is adapted such that it simulates an aircraft instead of a kite by eliminating the tether forces. The aerodynamic force and moment functions are derived from the linear stability and control derivatives given in reference [24]. The Rigid Body model is linearized to compare the model with the LTI models and to investigate the effect of linearization on the nonlinear model. The models used for the simulations are itemized below:

- LTI model in parametric state-space form
- Nonlinear model: Rigid Body Kite model modified to simulate an aircraft
- Linearized model: automatic linearized version of the nonlinear model

The equilibrium equations for the nonlinear model will determine the values for the initial condition. To be able to make a comparison between the models, the chosen flight condition should be the same for all models.

8-1-1 LTI model in state-space representation

The LTI models in reference [24] are adapted to have the wind speed as input to the system as well. Actually, the symmetric and asymmetric LTI model are given by equations (7-45) and (7-71) with the tether degrees of freedom removed. The aircraft is trimmed at a steady straight symmetric flight condition as described in the part about the nonlinear model.

The linear aerodynamic functions are derived from the nonlinear aerodynamic model given in equation (2-1). Tables 8-1 and 8-2 give the resulted stability and control derivatives. Note that the coefficients in nonlinear aerodynamic models are called aerodynamic derivatives and in nonlinear models stability and control derivatives. The linear model is represented in matrix form as given by equations (8-1) and (8-3) for the longitudinal and lateral motions.

To simulate the LTI models, the matrix notation of the models are written in state-space form as described in chapter 7. Representing the equations of motion in state-space form is also convenient for determining the eigenvalues of the state matrix A . The eigenvalues λ of the system can be determined with the MATLAB routine `eig.m` (for the state matrix A).

Longitudinal equations of motion

The equations of motion for the symmetric motions are given by equation (8-1), which is obtained from equation (7-45) by removing the tether degrees of freedom, θ_t and l_t . Additionally, terms have been added to the linearized accelerations in equation (7-24) due to a nonzero initial kinematic velocity effect given by $m \cdot w_{k0} \cdot \Delta q$ and $-m \cdot u_{k0} \cdot \Delta q$. These nonzero initial kinematic velocities result from the force equilibrium, that is the initial condition.

$$\begin{aligned} \begin{bmatrix} C_{X_u} + (C_{X_{\dot{u}}} - 2\mu_c)D_c & C_{X_w} + C_{X_{\dot{w}}}D_c & c_{x_\theta} & c_{x_q} - 2\mu_c\hat{w}_{k0} \\ C_{Z_u} + C_{Z_{\dot{u}}}D_c & C_{Z_w} + (C_{Z_{\dot{w}}} - 2\mu_c)D_c & c_{z_\theta} & c_{z_q} + 2\mu_c\hat{u}_{k0} \\ 0 & 0 & -D_c & 1 \\ C_{m_u} + C_{m_{\dot{u}}}D_c & C_{m_w} + C_{m_{\dot{w}}}D_c & c_{m_\theta} & c_{m_q} - 2\mu_cK_Y^2D_c \end{bmatrix} \begin{bmatrix} \hat{u}_k \\ \hat{w}_k \\ \theta \\ \frac{q\bar{c}}{V_0} \end{bmatrix} \\ = \begin{bmatrix} -C_{X_{\delta_e}} \\ -C_{Z_{\delta_e}} \\ 0 \\ -C_{m_{\delta_e}} \end{bmatrix} [\delta_e] \end{aligned} \quad (8-1)$$

where

$$\begin{aligned} c_{x_\theta} &= C_{Z_0} + C_{x_u}\hat{w}_{z0} - C_{X_w}\hat{w}_{x0} \\ c_{z_\theta} &= -C_{X_0} + C_{Z_u}\hat{w}_{z0} - C_{Z_w}\hat{w}_{x0} \\ c_{m_\theta} &= C_{m_u}\hat{w}_{z0} - C_{m_w}\hat{w}_{x0} \\ c_{x_q} &= C_{X_q} + C_{X_{\dot{u}}}\hat{w}_{z0} - C_{X_{\dot{w}}}\hat{w}_{x0} \\ c_{z_q} &= C_{Z_q} + C_{Z_{\dot{u}}}\hat{w}_{z0} - C_{Z_{\dot{w}}}\hat{w}_{x0} \\ c_{m_q} &= C_{m_q} + C_{m_{\dot{u}}}\hat{w}_{z0} - C_{m_{\dot{w}}}\hat{w}_{x0} \end{aligned}$$

and

$$\begin{aligned}
 \hat{u}_k &= \frac{u_k}{V_0} & C_{Z_0} &= -\frac{W \cos \theta_0}{\frac{1}{2}\rho V_0^2 S} \\
 \hat{w}_k &= \frac{w_k}{V_0} & C_{X_0} &= \frac{W \sin \theta_0}{\frac{1}{2}\rho V_0^2 S} \\
 \mu_c &= \frac{m}{\rho S \bar{c}} & \hat{w}_{x_0} &= \frac{W_{x_0} \cos \theta_0}{V_0} \\
 \mu_c K_Y^2 &= \frac{I_Y}{\rho S \bar{c}^3} & \hat{w}_{z_0} &= \frac{W_{x_0} \sin \theta_0}{V_0} \\
 D_c &= \frac{\bar{c}}{V_0} \frac{d}{dt}
 \end{aligned}$$

In section 8-1-3 the results to a step elevator deflection are shown. The responses of the states V_a and α are shown, instead of u_k and w_k , which is conventional in aircraft simulations. V_a and α are obtained by equations (8-2):

$$\begin{aligned}
 V_a &= \sqrt{u_a^2 + w_a^2} \\
 \alpha &= \arctan\left(\frac{w_a}{u_a}\right)
 \end{aligned} \tag{8-2}$$

where u_a and w_a are given by adding equations (7-37) and (7-38).

The symmetric stability and control derivatives together with the trim condition and mass properties are given in table 8-1.

V_0	=	59.9 m/s	m	=	4547.8 kg	μ_c	=	102.7
S	=	24.2 m ²	K_Y^2	=	0.980	\bar{c}	=	2.022 m
C_{X_0}	=	0.0821	C_{Z_0}	=	-1.1330	C_{m_0}	=	0.0
C_{X_u}	=	0.0825	C_{Z_u}	=	-1.3605	C_{m_u}	=	0.0755
$C_{X_{\dot{u}}}$	=	0.0	$C_{Z_{\dot{u}}}$	=	0.2509	$C_{m_{\dot{u}}}$	=	0.6493
C_{X_w}	=	0.4653	C_{Z_w}	=	-5.1600	C_{m_w}	=	-0.4300
$C_{X_{\dot{w}}}$	=	0.0	$C_{Z_{\dot{w}}}$	=	-1.4078	$C_{m_{\dot{w}}}$	=	-3.6426
C_{X_q}	=	0.0	C_{Z_q}	=	-3.8600	C_{m_q}	=	-7.0400
$C_{X_{\delta_e}}$	=	0.0	$C_{Z_{\delta_e}}$	=	-0.6238	$C_{m_{\delta_e}}$	=	-1.5530

Table 8-1: Symmetric stability and control derivatives, Cessna Ce500 ‘Citation’

These values are determined by linearizing the nonlinear aerodynamic model functions in equation (2-1). The linear model can be found in chapter 7.

The air density ρ is determined from the formula for μ_c , which gives:

$$\rho = 0.9050 \text{ kg/m}^3$$

With these values the eigenvalues for the symmetric motions are:

$$\begin{aligned}
 \lambda_{1,2} &= -0.0078 \pm 0.1971 i \\
 \lambda_{3,4} &= -1.1388 \pm 1.1258 i
 \end{aligned}$$

$\lambda_{1,2}$ corresponds to a low frequent slow damping periodic motion, i.e. the ‘phugoid’ eigenmotion, and $\lambda_{3,4}$ corresponds to a high frequent fast damping periodic motion, i.e. the ‘short period’ eigenmotion.

Lateral equations of motion

The equations of motion for the asymmetric motions in matrix notation is given by equation (8-3), which is obtained from (7-71) by removing the tether angle degree of freedom ψ_t . Additionally, terms have been added to the linearized accelerations in equation (7-24) due to a nonzero initial kinematic velocity effect given by $-m \cdot w_{k0} \cdot \Delta p$.

$$\begin{aligned} \begin{bmatrix} C_{Y_v} + (C_{Y_{\dot{v}}} - 2\mu_b)D_b & -C_{Z_0} - C_{Y_v}\hat{w}_{z0} & c_{y_p} & C_{Y_v}\hat{w}_{E0} & c_{y_r} \\ 0 & -D_b & 2 & 0 & 2 \tan \theta_0 \\ C_{l_v} + C_{l_{\dot{v}}}D_b & -C_{l_v}\hat{w}_{z0} & c_{l_p} - 4\mu_b K_X^2 D_b & C_{l_v}\hat{w}_{E0} & c_{l_r} + 4\mu_b K_{XZ} D_b \\ 0 & 0 & 0 & -D_b & \frac{2}{\cos \theta_0} \\ C_{n_v} + C_{n_{\dot{v}}}D_b & -C_{n_v}\hat{w}_{z0} & c_{n_p} + 4\mu_b K_{XZ} D_b & C_{n_v}\hat{w}_{E0} & c_{n_r} - 4\mu_b K_Z^2 D_b \end{bmatrix} \begin{bmatrix} \hat{v}_k \\ \phi \\ \frac{pb}{2V_0} \\ \psi \\ \frac{rb}{2V_0} \end{bmatrix} \\ = \begin{bmatrix} -C_{Y_{\delta_a}} & -C_{Y_{\delta_r}} \\ 0 & 0 \\ -C_{l_{\delta_a}} & -C_{l_{\delta_r}} \\ 0 & 0 \\ -C_{n_{\delta_a}} & -C_{n_{\delta_r}} \end{bmatrix} \begin{bmatrix} \delta_a \\ \delta_r \end{bmatrix} \end{aligned} \quad (8-3)$$

where

$$\begin{aligned} c_{y_p} &= -C_{Y_{\dot{v}}}\hat{w}_{z0} + C_{Y_p} + 4\mu_b\hat{w}_{k0} \\ c_{l_p} &= -C_{l_{\dot{v}}}\hat{w}_{z0} + C_{l_p} \\ c_{n_p} &= -C_{n_{\dot{v}}}\hat{w}_{z0} + C_{n_p} \\ c_{y_r} &= 2C_{Y_{\dot{v}}}\hat{w}_{x0} + C_{Y_r} \\ c_{l_r} &= 2C_{l_{\dot{v}}}\hat{w}_{x0} + C_{l_r} \\ c_{n_r} &= 2C_{n_{\dot{v}}}\hat{w}_{x0} + C_{n_r} \end{aligned}$$

and

$$\begin{aligned} \hat{v}_k &= \frac{v_k}{V_0} & \hat{w}_{E0} &= \frac{W_{x0}}{V_0} \\ \mu_b &= \frac{m}{\rho S b} & \mu_b K_X^2 &= \frac{I_X}{\rho S b^3} \\ \mu_b K_Z^2 &= \frac{I_Z}{\rho S b^3} & \mu_b K_{XZ} &= \frac{J_{XZ}}{\rho S b^3} \\ D_b &= \frac{b}{V_0} \frac{d}{dt} \end{aligned}$$

Equation (8-3) is written in state-space form by equation (7-72). The resulting A matrix has a rank of 4, which means that there are two linear dependent rows or columns. This means that there will be at least one eigenvalue which is zero.

The asymmetric stability and control derivatives together with the trim condition and mass properties are given in table 8-2.

b	=	13.36 m	K_X^2	=	0.012	K_{XZ}	=	0.002
μ_b	=	15.5	K_Z^2	=	0.037			
C_{Y_0}	=	0.0	C_{l_0}	=	0.0	C_{n_0}	=	0.0
C_{Y_v}	=	-0.9896	C_{l_v}	=	-0.0772	C_{n_v}	=	0.1638
$C_{Y_{\dot{v}}}$	=	0.0	$C_{l_{\dot{v}}}$	=	0.0	$C_{n_{\dot{v}}}$	=	0.0
C_{Y_p}	=	-0.0870	C_{l_p}	=	-0.3444	C_{n_p}	=	-0.0108
C_{Y_r}	=	0.4300	C_{l_r}	=	0.2800	C_{n_r}	=	-0.1930
$C_{Y_{\delta_a}}$	=	0.0	$C_{l_{\delta_a}}$	=	-0.2349	$C_{n_{\delta_a}}$	=	0.0286
$C_{Y_{\delta_r}}$	=	0.3037	$C_{l_{\delta_r}}$	=	0.0286	$C_{n_{\delta_r}}$	=	-0.1261

Table 8-2: Asymmetric stability and control derivatives, Cessna Ce500 'Citation'

With these values the eigenvalues for the asymmetric motions are:

$$\begin{aligned}
 \lambda_1 &= -1.9452 \\
 \lambda_2 &= 0.0939 \\
 \lambda_{3,4} &= -0.3387 \pm 1.7990 i \\
 \lambda_5 &= 0.0
 \end{aligned}$$

λ_1 and λ_2 correspond both to an aperiodic mode. λ_1 is negative and relatively large, so this gives a rapid converging and stable behaviour. λ_2 is positive and relatively small, so this gives a slow diverging and unstable behaviour, known as the 'spiral motion'. The periodic mode is given by $\lambda_{3,4}$ and is generally called the 'Dutch roll' motion.

8-1-2 Nonlinear and linearized model

The nonlinear aircraft model covers the full equations of motion and kinematic relations as derived in chapter 6, but with the tether forces and moments set to zero.

For the nonlinear model the aerodynamic force and moment equations are given by equations (2-1), where δ_e , elevator input, is used as the symmetric input and δ_a , aileron input, and δ_r , rudder input, as the asymmetric inputs. The aerodynamic derivatives in the formulae are given in table 8-3. The dimensionless functions are multiplied with $\frac{1}{2}\rho V_a^2 S$ and $\frac{1}{2}\rho V_a^2 S \bar{c}$ for the forces and symmetric moments respectively and with $\frac{1}{2}\rho V_a^2 S b$ for the asymmetric moments to obtain their dimensional value. So the forces and moments are dependent on the aerodynamic velocity squared.

As explained in chapter 7, for linear models the change in velocity is captured by the stability derivatives with respect to the aerodynamic velocity component u_a . These terms are the partial derivatives with respect to u_a of the nonlinear aerodynamic functions and therefore there is no aerodynamic coefficient with respect to u in the nonlinear model.

V_0	=	59.9 m/s	m	=	4547.8 kg	μ_c	=	102.7
S	=	24.2 m ²	K_Y^2	=	0.980	\bar{c}	=	2.022 m
C_{X_0}	=	0.0821	C_{Z_0}	=	-1.1330	C_{m_0}	=	0.0
C_{X_α}	=	0.4653	C_{Z_α}	=	-5.1600	C_{m_α}	=	-0.4300
$C_{X_{\dot{\alpha}}}$	=	0.0	$C_{Z_{\dot{\alpha}}}$	=	-1.4300	$C_{m_{\dot{\alpha}}}$	=	-3.7000
C_{X_q}	=	0.0	C_{Z_q}	=	-3.8600	C_{m_q}	=	-7.0400
$C_{X_{\delta_e}}$	=	0.0	$C_{Z_{\delta_e}}$	=	-0.6238	$C_{m_{\delta_e}}$	=	-1.5530

Table 8-3: Symmetric aerodynamic derivatives, Cessna Ce500 'Citation'

b	=	13.36 m	K_X^2	=	0.012	K_{XZ}	=	0.002
μ_b	=	15.5	K_Z^2	=	0.037			
C_{Y_0}	=	0.0	C_{l_0}	=	0.0	C_{n_0}	=	0.0
C_{Y_β}	=	-0.9896	C_{l_β}	=	-0.0772	C_{n_β}	=	0.1638
$C_{Y_{\dot{\beta}}}$	=	0.0	$C_{l_{\dot{\beta}}}$	=	0.0	$C_{n_{\dot{\beta}}}$	=	0.0
C_{Y_p}	=	-0.0870	C_{l_p}	=	-0.3444	C_{n_p}	=	-0.0108
C_{Y_r}	=	0.4300	C_{l_r}	=	0.2800	C_{n_r}	=	-0.1930
$C_{Y_{\delta_a}}$	=	0.0	$C_{l_{\delta_a}}$	=	-0.2349	$C_{n_{\delta_a}}$	=	0.0286
$C_{Y_{\delta_r}}$	=	0.3037	$C_{l_{\delta_r}}$	=	0.0286	$C_{n_{\delta_r}}$	=	-0.1261

Table 8-4: Asymmetric aerodynamic derivatives, Cessna Ce500 'Citation'

The initial condition for the nonlinear model is given by equilibrium of forces for the steady straight symmetric flight condition. This results in a specific trim condition tr for the static variables α and δ_e . To specify the nonlinear variants of C_{X_0} , C_{Z_0} and C_{m_0} the subscript nl is added.

So an equilibrium between the symmetric and asymmetric aerodynamic forces and moments has to be determined for the given flight condition. Since the flight condition is steady straight and symmetric the asymmetric forces and moments are zero at $t = 0$ s. For the symmetric case the equations given in (8-4) have to be satisfied, where the aerodynamic contributions are obtained from equations (2-1):

$$\begin{aligned}
 \sum C_X = 0 &= -\frac{W \sin \theta_0}{qS} + C_{X_{0,nl}} + C_{X_\alpha} \cdot \alpha_{tr} + C_{X_{\delta_e}} \cdot \delta_{e,tr} \\
 \sum C_Z = 0 &= \frac{W \cos \theta_0}{qS} + C_{Z_{0,nl}} + C_{Z_\alpha} \cdot \alpha_{tr} + C_{Z_{\delta_e}} \cdot \delta_{e,tr} \\
 \sum C_m = 0 &= C_{m_{0,nl}} + C_{m_\alpha} \cdot \alpha_{tr} + C_{m_{\delta_e}} \cdot \delta_{e,tr}
 \end{aligned} \tag{8-4}$$

with $q = \frac{1}{2} \rho V_0^2$ and where tr stands for trimmed value. The contributions of $\dot{\alpha}$ and q can be omitted, because of the steady flight condition.

The values of $C_{X_{0,nl}}$, $C_{Z_{0,nl}}$ and $C_{m_{0,nl}}$ are given by:

$$\begin{aligned}
 C_{X_{0,nl}} &= 0.0 \\
 C_{Z_{0,nl}} &= -C_{Z_\alpha} \cdot \alpha_0 \\
 C_{m_{0,nl}} &= 0.07
 \end{aligned}$$

with

$$\alpha_0 = -0.0436 \text{ rad}$$

where α_0 is α at zero lift. $C_{X_{0,nl}}$ for the given flight condition can be estimated to be zero.

There are three unknowns, θ_0 , α^{tr} and δ_e^{tr} for the three equations in (8-4) to determine the trim condition. The solution for the trim condition is found by solving the three equations for the three unknowns:

$$\begin{aligned}
 \theta_0 &= 0.0723 \text{ rad} \\
 \alpha_{tr} &= 0.1764 \text{ rad} \\
 \delta_{e,tr} &= -0.0038 \text{ rad}
 \end{aligned}$$

Since there is a difference between α^{tr} and θ_0 the aircraft has an initial flight path angle γ_0 given by:

$$\gamma_0 = \theta_0 - \alpha_{tr} \tag{8-5}$$

The flight path angle of approximately -6.0 deg results in a descending flight. This has influence on the results given in section 8-1-3. In body-fixed reference the aerodynamic velocity is chosen

to be V_0 . In earth reference this results in a slightly smaller wind velocity and the aircraft will have an initial kinematic velocity downwards.

The wind velocities in earth reference are:

$$\begin{aligned} W_{x0} &= -59.553 \text{ m/s} \\ W_{y0} &= 0.0 \text{ m/s} \\ W_{z0} &= 0.0 \text{ m/s} \end{aligned}$$

and the initial kinematic velocities in body-fixed reference are:

$$\begin{aligned} u_{k0} &= -0.4494 \text{ m/s} \\ v_{k0} &= 0.0 \text{ m/s} \\ w_{k0} &= 6.2045 \text{ m/s} \end{aligned}$$

Linearized model

The linearized model is obtained by linearizing the nonlinear model by performing the MATLAB routine `linmod.m` at the specified flight condition. The use of the linear model is to verify the nonlinear model and to investigate the effect of linearization of the nonlinear model.

The eigenvalues given by MATLAB at the specified flight condition are:

$$\begin{aligned} \lambda_1 &= -1.9448 \\ \lambda_{2,3} &= -0.3386 \pm 1.7988 i \\ \lambda_4 &= 0.0937 \\ \lambda_{5,6} &= -1.1619 \pm 1.1111 i \\ \lambda_{7,8} &= -0.0077 \pm 0.1966 i \\ \lambda_9 &= 0.0246 \\ \lambda_{10} &= 0.0002 \end{aligned}$$

Comparing the eigenvalues with the eigenvalues of the state-space model it can be concluded that they make a very good match. The eigenvalues λ_1 , $\lambda_{2,3}$ and λ_4 correspond to the asymmetric motions and that $\lambda_{5,6}$ and $\lambda_{7,8}$ correspond to the symmetric motions. λ_9 is small but slightly unstable and is not present in the state-space models. λ_{10} is approximately zero and corresponds to λ_5 of the lateral state-space model.

8-1-3 Simulation results

The results of the symmetric simulations for the three models ‘state-space’, ‘linearized’ and ‘non-linear’ are obtained by performing a step elevator deflection $\Delta\delta_e$ of -0.005 rad. The results for the asymmetric motions are obtained by performing two simulations: one with a pulse rudder deflection $\Delta\delta_r$ of 0.025 rad during 1 s and one with a pulse aileron deflection $\Delta\delta_a$ of 0.025 rad during 1 s. These inputs are chosen to compare with the aircraft simulations in reference [24]. The response curves are given in appendix E.

Also for the asymmetric simulations the change in aerodynamic velocity V_a is given to show that the velocity is not constant for the nonlinear simulation. This results in a discrepancy of the responses due to an aileron deflection between the nonlinear model and the linear models.

8-2 Citation-Kite simulation

The Cessna Ce500 ‘Citation’ aircraft of previous section is attached to a 250 m long tether resulting in the system called ‘Citation-Kite’. An analysis is performed to verify the nonlinear model of chapter 6 and the LTI models of chapter 7.

8-2-1 Simulation setup

The analysis is performed by comparing three different models analogue to the aircraft simulations of the Cessna ‘Citation’:

- LTI model in parametric state-space form
- Nonlinear model: Rigid Body model with aircraft aerodynamic model
- Linearized model: automatic linearized version of the nonlinear model

The state-space model for the symmetric equations of motion is given by equation (7-45) and for the asymmetric equations of motion by (7-71). The structure and operation of the nonlinear model is explained in detail in chapter 6. Again, the linearized model is obtained by linearizing the nonlinear model with the MATLAB routine `linmod.m`.

Initial condition

The initial condition is given by the initial condition as defined in chapter 7 with the parametric values given in the previous section. The geometric properties and aerodynamic derivatives of the aircraft are given in table 8-3 and 8-4. For equilibrium of forces and moments an initial tether force will result.

There are three possibilities to have an initial tether force:

1. Increase the wind speed W_x to obtain more lift force
2. Change the geometric properties \bar{c} , b or S to increase the lift force
3. Decrease the weight of the vehicle

The aerodynamic derivatives are made dimensionless among others by the variables V_a , \bar{c} , b and S . This results in the fact that the aerodynamic derivatives are independent of these variables. In this case the derivatives are constant and obtained from a certain flight condition. In full nonlinear models the derivatives will vary dependent on certain (static) variables. To keep the flight condition for which the derivatives are obtained the third option is chosen. By decreasing the weight the aerodynamic derivatives are still valid, because the weight of the vehicle has no influence on the validity of the aerodynamic model.

A lift over weight value is specified to decrease the weight and to create a significant tether force:

$$\frac{L}{W} = 25.0$$

The initial condition is determined from equilibrium of forces and moments with the $\frac{L}{W}$ value to compute the weight. From the tether force the initial tether elongation δl_{t0} is computed to obtain the initial tether length at ‘ $t = 0$ [s]’, l_{t0} , by equations 6-29 and 6-30. The tether is specified by the following parameters:

$$\begin{aligned} l_{t,\delta l_t=0} &= 250 \text{ m} \\ d_t &= 2.0 \cdot 10^{-2} \text{ m} \\ r_t &= \frac{1}{2} \cdot d_t \text{ m} \\ E_t &= 9.8 \cdot 10^{10} \text{ N/m}^2 \\ c_t &= 2.08 \cdot 10^2 \text{ Ns/m} \end{aligned}$$

where d_t is the tether diameter, r_t the tether radius and E_t the elasticity modulus. The spring constant k_t is than given by $E_t \cdot \pi r_t^2 / l_{t,\delta l_t=0}$:

$$k_t = 1.232 \cdot 10^5 \text{ N/m}$$

Eigenvalues linear models

The symmetric aerodynamic derivatives for the nonlinear model are given in table 8-3. The symmetric stability and control derivatives of the state-space model for the symmetric motions are given in table 8-1. The mass of the Citation-Kite and the dimensionless mass are given by m_{kite} and $\mu_{c,kite}$ respectively. They are a factor $\frac{L}{W}$ smaller compared to the mass values for the Citation aircraft of section 8-1. The inertia value K_Y^2 is the same as it only depends on the aircraft shape, because it is dimensionless with respect to size and mass. With these stability derivatives the eigenvalues of the symmetric state-space model are:

$$\begin{aligned}\lambda_{1,2} &= -0.2360 \pm 1.0640 i \\ \lambda_{3,4} &= -5.8351 \pm 2.3751 \cdot 10^1 i \\ \lambda_5 &= -1.0412 \\ \lambda_6 &= -3.6810 \cdot 10^1\end{aligned}$$

$\lambda_{1,2}$ corresponds to a low frequent slow damping periodic motion and is called the ‘pendulum’ motion. It is inherently coupled to the phugoid motion of the aircraft. $\lambda_{3,4}$ corresponds to a high frequent fast damping periodic motion and is inherently coupled to the short period motion of the aircraft. It is called short period motion here as well. λ_5 and λ_6 correspond both to an aperiodic stable mode. λ_5 is relatively small and gives a slow converging behaviour. λ_6 is relatively very large and gives a very fast converging motion.

The asymmetric stability derivatives of the state-space model for the asymmetric motions are given in table 8-2. With these stability derivatives the eigenvalues of the asymmetric state-space model are:

$$\begin{aligned}\lambda_{1,2} &= -6.8900 \pm 6.4944 i \\ \lambda_{3,4} &= -2.4722 \cdot 10^1 \pm 3.7138 \cdot 10^1 i \\ \lambda_5 &= -0.1865 \\ \lambda_6 &= 0.1694\end{aligned}$$

$\lambda_{1,2}$ corresponds to a medium frequent medium damped periodic motion. $\lambda_{3,4}$ corresponds to a very high frequent very fast damping periodic motion. $\lambda_{3,4}$ will probably not be noticeable in the simulation results. λ_5 corresponds to a slow damped aperiodic stable mode and λ_6 corresponds to an undamped aperiodic unstable mode.

The eigenvalues of the linearized model are:

$$\begin{aligned}\lambda_{1,2} &= -0.2359 \pm 1.0639 i \\ \lambda_{3,4} &= -5.8233 \pm 2.3752 \cdot 10^1 i \\ \lambda_5 &= -1.0406 \\ \lambda_6 &= -3.6777 \cdot 10^1 \\ \lambda_{7,8} &= -6.8942 \pm 6.4561 i \\ \lambda_{9,10} &= -2.4712 \cdot 10^1 \pm 3.5510 \cdot 10^1 i \\ \lambda_{11} &= -0.1873 \\ \lambda_{12} &= 0.1690\end{aligned}$$

which is a very good match with the eigenvalues of the state-space models

8-2-2 Simulation results

The symmetric response curves given in the following figures are obtained for a wind step input of $\Delta W_x = -10$ m/s and for a control step input of $\Delta x_{ta} = 0.05$ m. The first plot is the path of the kite in the $X_E Z_E$ -plane from the nonlinear simulation. The second and third figures show the kinematic velocity component u_k illustrating the pendulum and short period modes. The asymmetric response curves given in the following figures are obtained for a wind step input in lateral direction of $\Delta W_y = 15$ m/s and for a control step input of $\Delta x_{ta}^L = 0.05$ m and $\Delta x_{ta}^R = -0.05$ m simultaneously. The first plot is the path of the kite in the $X_E Y_E$ -plane from the nonlinear simulation. The second figure shows the response curve of the side slip angle β .

Symmetric motions, wind step input

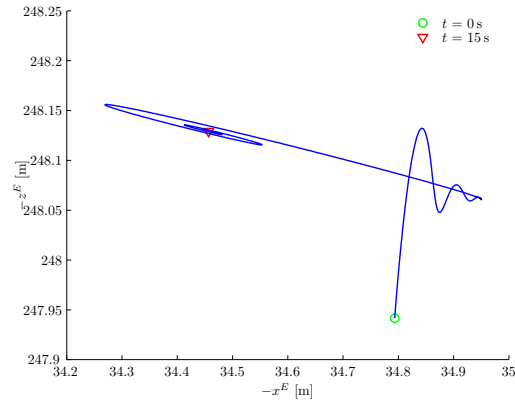


Figure 8-1: Path in $X_E Z_E$ -plane to a wind step input of $\Delta W_x = -10$ m/s of the 'Citation-Kite', nonlinear simulation

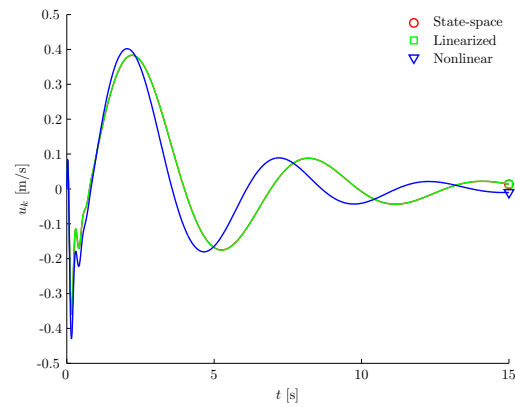


Figure 8-2: u_k -response curve to a wind step input of $\Delta W_x = -10$ m/s of the 'Citation-Kite', pendulum motion

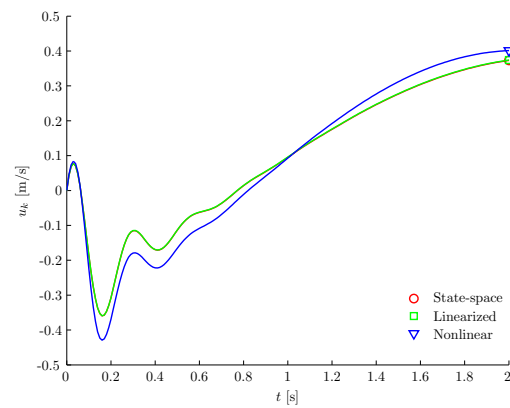


Figure 8-3: u_k -response curve to a wind step input of $\Delta W_x = -10$ m/s of the 'Citation-Kite', short period motion

Symmetric motions, control step input

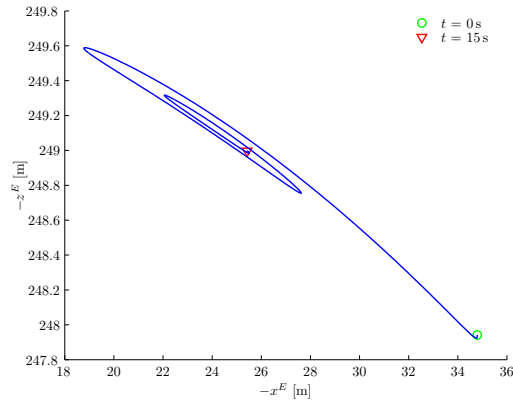


Figure 8-4: Path in $X_E Z_E$ -plane to a control step input of $\Delta x_{ta} = 0.05$ m of the 'Citation-Kite', nonlinear simulation

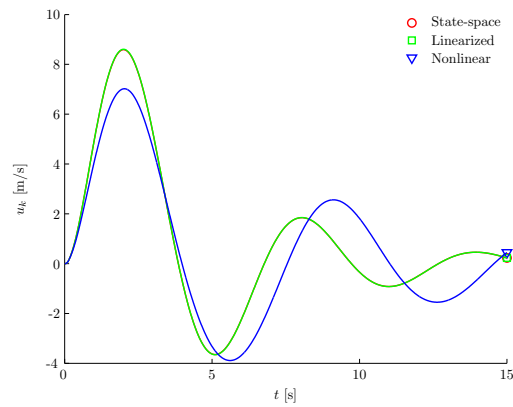


Figure 8-5: u_k -response curve to a control step input of $\Delta x_{ta} = 0.05$ m of the 'Citation-Kite', pendulum motion

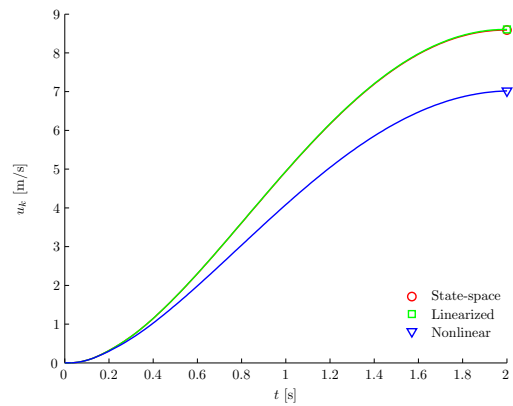


Figure 8-6: u_k -response curve to a control step input of $\Delta x_{ta} = 0.05$ m of the 'Citation-Kite', short period motion

Asymmetric motions, lateral wind step input

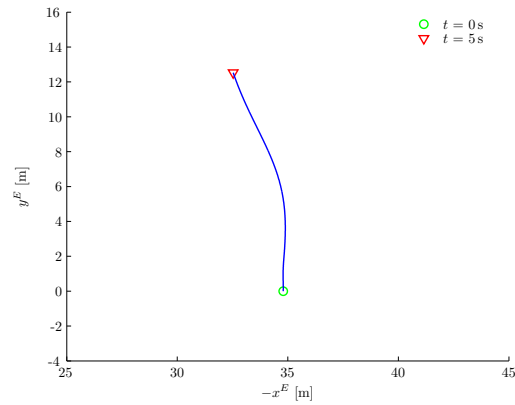


Figure 8-7: Path in $X_E Y_E$ -plane to a wind step input of $\Delta W_y = 15$ m/s of the 'Citation-Kite', nonlinear simulation

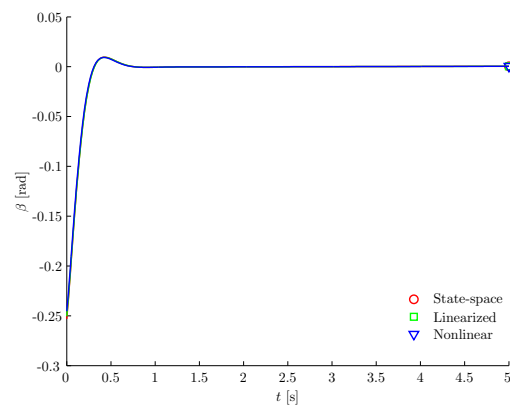


Figure 8-8: β -response curve to a wind step input of $\Delta W_y = 15$ m/s of the 'Citation-Kite'

Asymmetric motions, asymmetric control step input

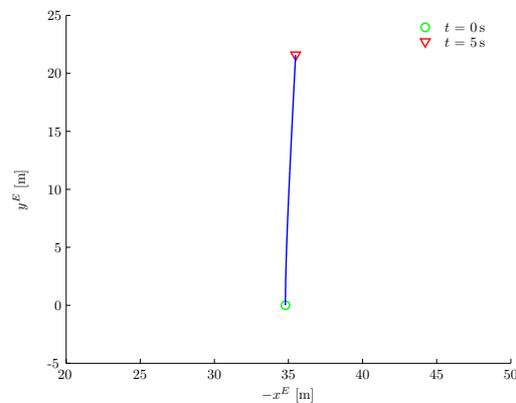


Figure 8-9: Path in $X_E Y_E$ -plane to a control step input of $\Delta x_{ta}^L = 0.05$ m and $\Delta x_{ta}^R = -0.05$ m simultaneously of the 'Citation-Kite', nonlinear simulation

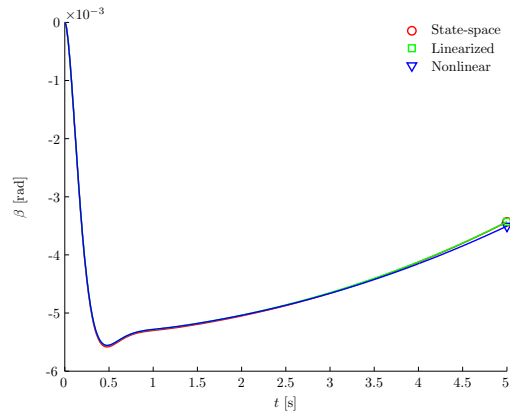


Figure 8-10: β -response curve to a control step input of $\Delta x_{ta}^L = 0.05$ m and $\Delta x_{ta}^R = -0.05$ m simultaneously of the 'Citation-Kite'

8-3 Conclusions

Comparing the eigenvalues of the aircraft simulation and the Citation-Kite simulation shows that there is a good match between the state-space models and the linearized models and, by consequence, the nonlinear model. The simulation graphs support this too. Additionally, the aircraft responses are very similar to the responses shown in reference [24].

Furthermore, the eigenmotions of the original aircraft are reflected in the eigenmotions of the Citation-Kite, which is an expected result. Note that the frequency of the responses are higher, which is a result of the L/W factor.

Looking closer to the responses of the Citation-Kite it can be seen that the linear models are not that accurate for the symmetric responses due to a control input compared to the responses of the other inputs. A clarification can be that the tether moments as a result of the shift of the control positions have a large nonlinear influence on the dynamics of the system. Although, it must be noted that the amplitude of the input has influence on the validity domain of the linear models.

Actually, the asymmetric motions can be very accurately simulated with the very fast linear models, which could be of use for control law design.

But the most important conclusion here is that the verification of the Rigid Body model is successful, which paves the way to simulate an arc-shaped kite.

Chapter 9

Multi-Body Kite Model

In chapter 3 an introduction to MSC. ADAMS as well as an introduction to the kite toolbox is given. This chapter continues by presenting the detailed Multi-Body model of an existing arc-shaped kite as well as describing the methodology to reduce the numerous states of the Multi-Body system to a limited set of rigid body states. These rigid body states comprises the angular momentum, the inertia tensor properties, the translational and rotational quantities and control translation. The sum of the aerodynamic forces and moments are derived as well. Furthermore, the components of the lumped parameters are expressed in the body-fixed reference frame. This defines the information required for the aerodynamic and structural model identification in chapter 10.

9-1 Model description

North Rhino Kite specifications

The arc-shaped LEI Kite chosen for the simulations is the ‘North Rhino’ Kite. In reference [4] the North Rhino Kite is used for testing and validation of the Multi-Body Surf Kite model. This kite has a wetted surface area of 16 m^2 and is shown in flight in figure 9-1.

The structural discretization and geometric parameters of this kite as they are entered into the ‘Assembly Loader’ (see chapter 3) to model the kite in ADAMS are specified in table 9-1.



Figure 9-1: 'North Rhino' arc-shaped LEI Kite in flight

LE Segments	10
Side Segments	5
Position Strut 1	4 segments
Position Strut 2	8 segments
Angle Chord 1	36.5 deg
Angle Chord 2	72.0 deg
Height	3.20 m
Span	5.80 m
Ang Tip	90.0 deg
Length Chord 0	1.93 m
Length Chord 1	1.67 m
Length Chord 2	1.08 m
Length Tip	0.65 m
LE Radius Mid	100 mm
LE Radius Tip	40 mm

Table 9-1: Geometric properties

The resulting model is shown in figure 9-2. Additional information of the multi-body system is given in appendix A.

Initial condition

The initial condition can be changed by specifying four parameters: tether zenith angle, body pitch angle and the initial position for the controls. Table 9-2 shows the values as specified in the Assembly Loader. The initial condition is defined as the state of the kite at $t = 0$ s in ADAMS. At this condition the kite is not in equilibrium, because all forces in the model are zero. When the simulation starts, the state of the kite will converge to the equilibrium condition initiated from the condition as specified in the table. The period from the initial condition to the equilibrium condition is defined as the *stabilization phase*.

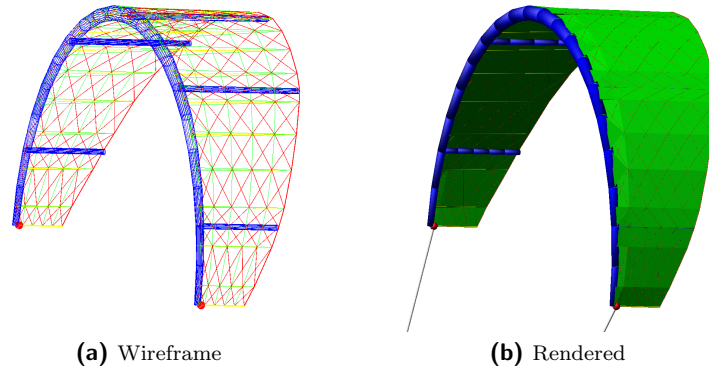


Figure 9-2: ADAMS 'North Rhino' Kite model

Zenith Angle, $\theta_{t,0}$	20.0 deg
Pitch Angle, θ_0	3.5 deg
Initial D_{taL}	0.275 m
Initial D_{taR}	0.275 m

Table 9-2: Initial condition

Control mechanism

The control mechanism is based on the cart and rail principle as explained in chapter 2.

The cart, modelled as a spherical body, is connected to a pivot arm which is driven by a torque motor such that the cart is forced to move on a curved path. But the cart is constraint to move along the rail bar or kite tip as well. The motor is positioned at a fixed distance l_{pivot} above the kite tip and relative to the kite tip such that the pivot arm is not a part but a position constraint. The torque of the motor is modelled by a rotational spring-damper system to control the position of the cart given by an angle δ_{cL} and δ_{cR} for the left and right cart respectively. The actual input is given by the position along the kite tip d_{taL} and d_{taR} respectively with the origin 0.05 m along the kite tip measured from the center of the leading edge tube. The initial position of the control carts is specified by the variables D_{taL} and D_{taR} respectively with the origin at the center of the kite tip.

Figure 9-3 shows schematically the model of the control system. Table A-5 shows the values of the cart mass and rail mass (kite tip) and table 9-3 gives an overview of the other control mechanism properties.

Pivot arm, l_{pivot}	3.0 m
Motor stiffness	$1.0 \cdot 10^3$ N·m/deg
Motor damping	$1.0 \cdot 10^2$ N·m·s/deg
Motor torque limit	$1.0 \cdot 10^3$ N·m

Table 9-3: Control mechanism properties

The values for the motor stiffness and damping in table 9-3 are verified from simulations. If the stiffness value is chosen too small (for example $1.0 \cdot 10^2$ N·m/deg) the motor is not able to hold the position of the cart for inputs between the center of the kite tip and the trailing edge. If the damping value is chosen too small (for example $2.0 \cdot 10^1$ N·s·m/deg) the damping on the control

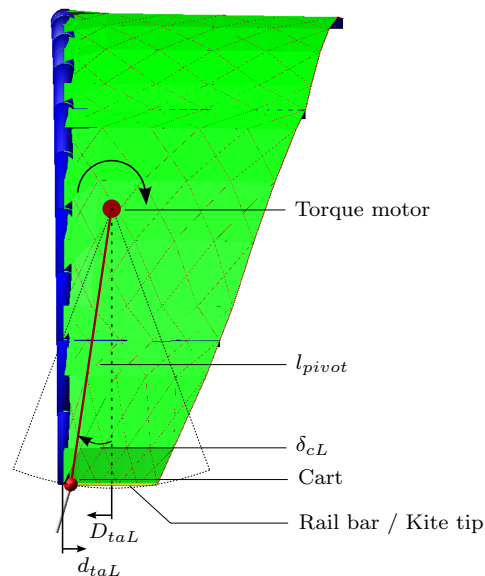


Figure 9-3: Control system model

position is low and this is reflected in the total acceleration of the center of gravity in the form of slowly damped oscillations.

Mass and inertia

A flexible kite has changing inertia properties under influence of changing aerodynamic conditions and control input. The change in inertia due to the controls is not only caused by the deformation introduced by the change of the tether attachment point but also by the fact that the controls have weight.

In ADAMS/View the mass and inertia properties of a model can be determined with the function `Aggregate Mass...`. This function is accessed by the drop down menu 'Tools'. Unfortunately this is only accessible in ADAMS/View and therefore not applicable during run-time simulations.

Another option is to evaluate this function every time step by using an user-defined subroutine. This can be accomplished by creating an executable and linking the executable to ADAMS/Solver. Executables can be created with the Fortran programming language. The downside of this option is that all mass elements in the model have to be linked to the subroutine and that the data is only accessible after the simulation. This means that the inertia properties can not be assigned to an ADAMS state variable or function measure.

For completion the mass and inertia properties at the initial condition ($t = 0$ s) obtained with the function `Aggregate Mass...` (exact value) are given in appendix A, see table A-5.

To evaluate the variation of the inertia properties during a simulation an estimate is made based on a mass particle approach. This *particle based* method (pb) is described in section 9-2. The results for the inertia properties at the initial condition are also given in table A-5. Additionally the error made with the particle method is shown as well. It can be concluded that the error gets larger as the absolute value of the inertia property gets smaller.

Tether model

For comparison the tether model in the multi-body model and rigid body model are based on a spring-damper model.

The tether properties that can be specified in the Assembly Loader are given in table 9-4. The meaning of the parameters ‘Bridle Point’ and ‘Cable Point’ is illustrated in figure 9-4. The dynamic properties are given by the spring constant k_t and damping constant c_t .

Bridle Point	12.0 m
Cable Point	40.0 m
k_t	$7.697 \cdot 10^3 \text{ N/m}$
c_t	$2.080 \cdot 10^2 \text{ N}\cdot\text{s/m}$

Table 9-4: Tether properties

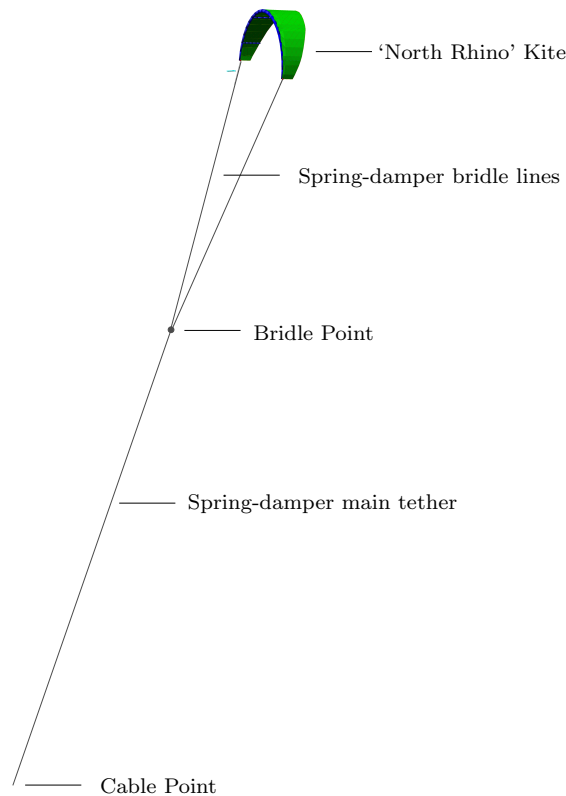


Figure 9-4: ADAMS tether model

To connect the bridle lines with the main tether a dummy part is required. The main tether and the bridle lines are modelled by so called direct single forces. The forces act between two points and are given by a specified function. In this case a spring-damper. In ADAMS forces can not be directly connected to another force, this has to be accomplished by adding a part. Actually, this is a consequence of Newton’s second law, $F = m \cdot a$. As the force is specified to act between two points, ADAMS needs two bodies or parts with mass on both action points of the force. Note that *ground* is treated as a part as well.

Bridle dummy stabilization A bridle dummy part, in the form of a small sphere, is introduced to establish the connection between the bridle lines and the main tether. It is preferred for the dummy part to have negligible mass and inertia properties. Because the question is to analyze the dynamics of the kite and, as ADAMS is used as a reference for Rigid Body, the differences with respect to the tether model must as small as possible. This is also the reason why there is no aerodynamic drag acting on the tether.

Unfortunately, small values for the mass introduces an unwanted dynamic phenomenon. The tether-fixed reference frame is formed by the tether attachment points and the connection point of the main tether with the ground, that is the Cable Point. These three points define the $Y_t Z_t$ -plane of the tether-fixed reference frame. In this plane the motion of the dummy part is driven by the bridle lines and the main tether and is stable. But the motion of the dummy part perpendicular to this plane is not stable. If, for some reason, the bridle dummy displacement lags the displacement of the $Y_t Z_t$ -plane a resultant force acts on the dummy part in the direction perpendicular to the $Y_t Z_t$ -plane. This force causes a motion towards the $Y_t Z_t$ -plane, but overshoots and the dummy part is in front of the $Y_t Z_t$ -plane. And, again, there is a resultant force towards the $Y_t Z_t$ -plane and the situation repeats itself. This motion is underdamped for too small masses.

At first it is tried to increase the mass of the dummy part. This has a positive result. Although, after changing other parameters with respect to the structural damping of the kite the phenomenon returned. At some point the mass of the dummy part had reached 2% of the total system mass. To be sure that the mass of the dummy part has a negligible effect on the dynamics of the system, the mass is not increased any further. Additionally, it is not sure if the problem would return in some cases or other phenomena would occur.

Another solution has been found. The solution is adding damping to the unstable motion. But the damping force should always act perpendicular to the $Y_t Z_t$ -plane. Therefore the tether-fixed reference frame needs to be defined. This is done by using the two tether attachment points and the connection with the ground. All vector quantities given below are expressed in the earth-fixed reference frame. The mass of the dummy part is set to $1.0 \cdot 10^{-3}$ kg and the mass moment of inertia to $1.0 \cdot 10^{-4}$ kg·m².

The direction of the X_t , Y_t and Z_t axes is given by the unit vectors $e_{t,x}$, $e_{t,y}$ and $e_{t,z}$, see figure 9-5. The direction of $e_{t,y}$ is given by the two tether attachment points, because the Y_t axis is defined parallel to the line through these two points. The distance between the tether attachment points is defined as l_c . Then, for $e_{t,y}$ can be written:

$$e_{t,y} = \begin{bmatrix} l_{c,x} \\ l_{c,y} \\ l_{c,z} \end{bmatrix} \frac{1}{|l_c|} \quad (9-1)$$

The average distance between the tether attachment points is defined by the point m . The distance between m and the Cable Point defines l_m . The corresponding unit vector is given by:

$$e_{t,z} = \begin{bmatrix} l_{m,x} \\ l_{m,y} \\ l_{m,z} \end{bmatrix} \frac{1}{|l_m|} \quad (9-2)$$

Now, the unit vector for the X_t axis is:

$$e_{t,x} = e_{t,y} \times e_{t,z} \quad (9-3)$$

The damping force applied at the bridle dummy is given by the difference in rotational speed of the tether about the Y_t -axis between point m , $\omega_{t,m}$, and the bridle point, point b , $\omega_{t,b}$. The rotational speed of the tether at point m is:

$$\omega_{t,m} = \frac{e_{t,x} \cdot \dot{l}_{t,m}}{|l_m|} \quad (9-4)$$

and the rotational speed of the tether at point b is:

$$\omega_{t,b} = \frac{e_{t,x} \cdot \dot{l}_{t,b}}{|l_b|} \quad (9-5)$$

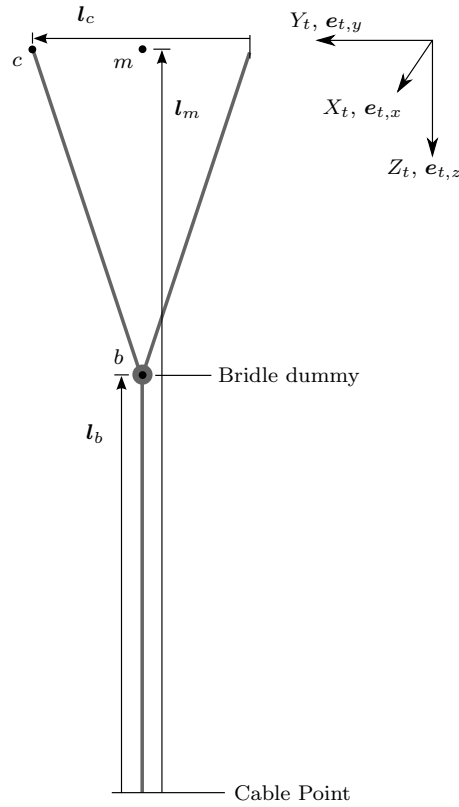


Figure 9-5: Bridle dummy, definition of tether-fixed reference frame

where $\dot{l}_{t,m}$ and $\dot{l}_{t,b}$ are the velocities of point m and b respectively.

Then, for the resultant damping force on the bridle dummy can be written by:

$$F_{dummy} = c_{dummy} \cdot (\omega_{t,m} - \omega_{t,b}) \tag{9-6}$$

where c_{dummy} is $1.0 \cdot 10^3$ N·s/rad.

In ADAMS the force is applied perpendicular to the $Y_t Z_t$ -plane and expressed in the earth-fixed reference frame. Therefore the resultant bridle force is transformed to act in the direction of the unit vector $e_{t,x}$:

$$\mathbf{F}_{dummy} = F_{dummy} \cdot \mathbf{e}_{t,x} \tag{9-7}$$

The effectiveness on the stabilization of the bridle dummy is illustrated in figure 9-6. The force in the main tether as well as the acceleration of the center of mass of the kite are shown for 2 s after the initial condition. It is clear that the dummy force effectively damps the oscillations. The resultant force required is shown in figure 9-7 for 10 s after the initial condition. The highest value of the absolute dummy force is smaller than 1 % of the force in the main tether and converges to zero quickly.

Performing simulations

Before one is able to fly kites in real life at some level of skill a learning process has to be initiated. The same can be said for the Multi-Body Kite model in ADAMS. This is not only because it is a kite, this is also because it is a complex model consisting of many parts and parameters. From the experience gained by performing simulations many issues have been resolved.

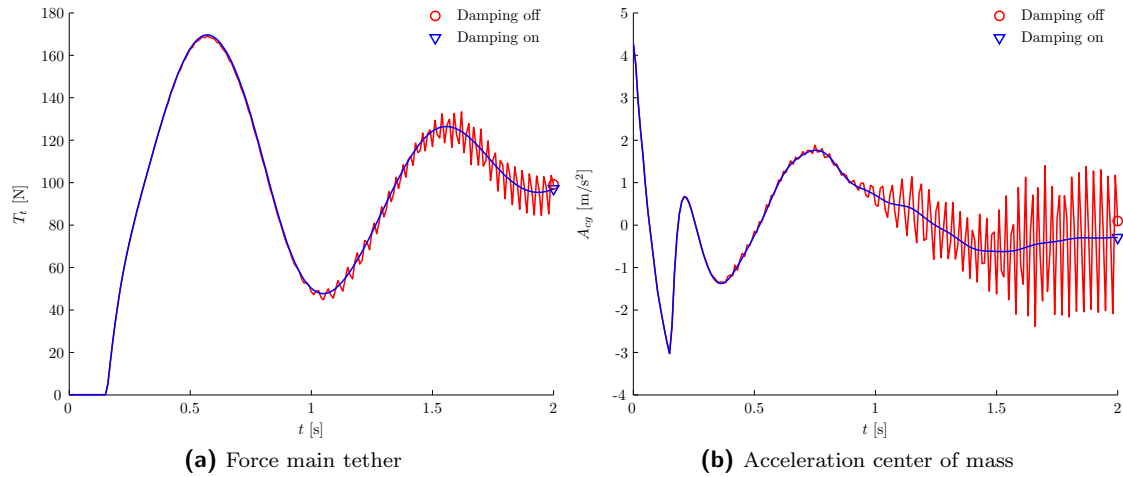


Figure 9-6: Effect of bridle dummy stabilization

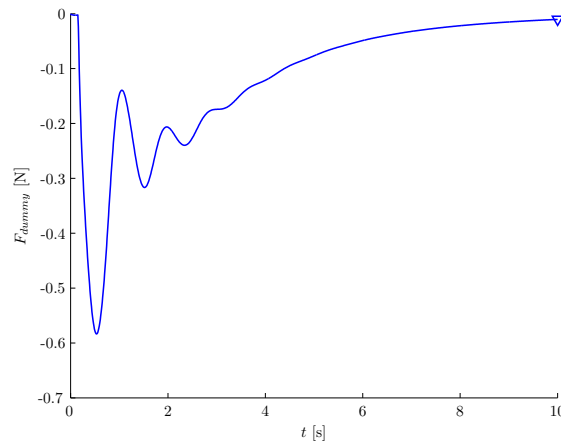


Figure 9-7: Resultant damping force on bridle dummy

When the simulation starts the kite has to find its equilibrium first. At the initial condition there are no forces applied to the model. For every wind speed there exists a kite shape based on the equilibrium between the aerodynamic forces and moments, tether forces and internal structural forces and moments. The time to reach the equilibrium is defined as the *stabilization time*.

At the moment the kite has reach its equilibrium point, the kite starts to slide to the side. This is caused by a critically damped lateral eigenmotion. The perturbation which initiates the motion is the integration error of the simulation solver. This error increases very fast as time passes. A *planar joint* is introduced and can be switched on when this motion is unwanted and only symmetric responses are to be simulated.

The simulation and solver settings used for all simulations of the Multi-Body Kite model are given in table 9-5. The value for the integrator error is based on the simulation time. The simulation time for the shown value is approximately 420 to 480 s for 30 s of simulation. Reducing the error increases the simulation time multi-fold.

Time step size	0.01 s
Dynamic integrator	GStiff, I3
Integrator error	$1.0 \cdot 10^{-3}$

Table 9-5: Simulation and solver settings

Structural stiffness and damping

The structural stiffness and damping properties have a great effect on the dynamic behaviour of the kite. The stiffness properties are based on real tubes and can not be changed (except for the foils), but the damping properties are not. Therefore the damping properties are altered such that the dynamic behaviour introduces less simulation issues and still behaves like a flexible arc-shaped kite.

The most benefit has been found with respect to:

- reduced stabilization time: from 30 to 15 s
- more direct response to control inputs
- faster damping of the ‘jellyfish’ motion

The values for the stiffness and damping are given in table 9-6. The units for the stiffness and damping properties are given by N and s respectively.

Tubes, Bending stiffness	Nonlinear function
Tubes, Bending damping	$5.0 \cdot 10^{-1} s$
Tubes, Torsional stiffness	Nonlinear function
Tubes, Torsional damping	$2.0 \cdot 10^{-1} s$
Foil wires, stiffness	$1.0 \cdot 10^3 N$
Foil wires, damping	$1.0 \cdot 10^{-2} s$
TE wires, stiffness	$1.0 \cdot 10^3 N$
TE wires, damping	$1.0 \cdot 10^{-2} s$

Table 9-6: Model verification

9-2 GUM files

Figure 3-2 in chapter 3 shows the TKC structure as is applicable to this thesis. In the GUM folder additional macro files have been programmed such that new User Defined Entities (UDEs) can be created in the Surf Kite Assembly file. The UDEs create ADAMS function measures (am) for implementing ‘virtual sensors’ for center of gravity position, inertia properties, angular momentum, sum of aerodynamic forces and moments expressed in the TKC global reference frame.

The TKC global reference frame is the fixed global inertial reference frame for every model created with TKC. For the GUM files the TKC global reference frame is regarded as the inertial earth-fixed reference frame F_E . Figure 9-8 shows the location of the TKC global reference frame marker. The location does not coincide with the convention of the earth-fixed reference as defined in chapter 5. This does not give any problem regarding the implementation of the ADAMS function measures created by the GUM files as long as all functions are applied with respect to the TKC global reference frame marker. The orientation is equal to the earth-fixed reference frame. Only when discussing the absolute position of the kite with respect to the global origin a correction has to be applied.

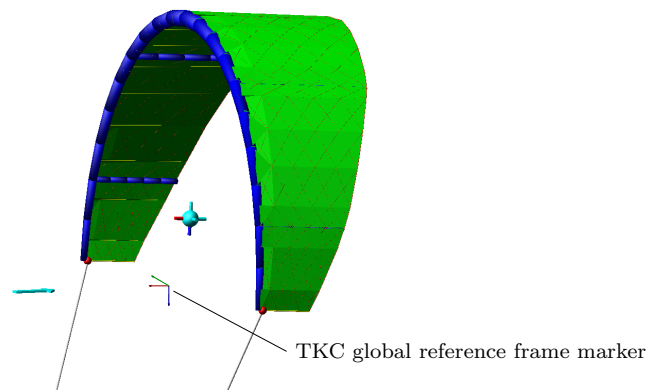


Figure 9-8: TKC global reference frame

ADAMS can only perform scalar computations and therefore all equations are evaluated in scalar form by the macro files. For convenience all equations in this section are given in vector or matrix form. Calculation of displacement, velocity, acceleration or force components of an element is done by specific function commands. The string lengths of the elements (for example parts or forces) have to be entered in the function commands. The string lengths are relatively long approximately 10 to 15 characters. The resulting summation terms of the macro equations are computed by ADAMS function measures (am) containing the function commands. Due to a limit string size of 1023 characters of these function measures the string size of the function measures is usually too short for all summation terms and the function measures have to be partitioned. The partitions are already shown in tables A-2, A-3 and A-4. For the Sum of General Moments macro the partitioning is automated, because manual partitioning resulted in more than 20 UDEs.

To keep the amount of partial function measures as small as possible the equations evaluated by the GUM files are all computed with respect to the TKC global origin and expressed in the TKC global reference frame. In this way the reference frame does not have to be specified in the function commands and the function commands are automatically evaluated with respect to the TKC global origin and expressed in the TKC global reference frame.

9-2-1 Fluid Speed macro

The Fluid Speed macro file defines the wind input for the Multi-Body model. The Fluid Speed macro file is located in the GUM folder of the Toolkit Creator Shared Macros, see figure 3-2.

The original macro file creates an arrow pointing in X_E direction as well as a 'fluid particle'. The fluid particle is a rigid body in the form of a sphere whose motion is given by a time dependent displacement function in X_E , Y_E and Z_E direction. During a simulation the velocity of the particle is measured and the result is used by the aerodynamic model.

The Fluid Speed macro file is adapted such that the wind input is directly given by a function defining the velocity in X_E , Y_E and Z_E direction. This is accomplished by removing the fluid particle and the displacement functions and by introducing three ADAMS state variables (as) defining the wind velocity in X_E , Y_E and Z_E direction. In this way the unnecessary motion of the fluid particle is removed and the wind speed can be given by a constant value or as a function of time. Additionally, the wind input can now be specified externally in case of co-simulating ADAMS with SIMULINK.

9-2-2 Centroid Dummy for Center of Gravity macro

The Centroid Center of Gravity macro `Centroid.CoG.mac.cre` creates measures for the center of gravity displacement, velocity and acceleration of selected parts in a model. Additionally a ‘Centroid Dummy’ (CD) is created. The Centroid Dummy is a visualization body to track the center of gravity position. The Centroid Dummy is a sphere with three axes attached to visualize the orientation, see figure 9-9.

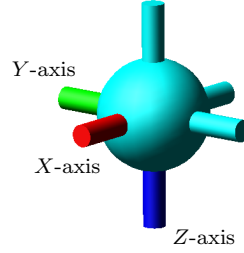


Figure 9-9: Centroid Dummy

The position of the center of mass for a particle system is determined by the average of the particle positions and weighted by their masses (Reference [31]). The system can be defined by n particles each with a mass m_j for $j = 1, 2, \dots, n$. The displacement vector of each particle \mathbf{r}_j is given with respect to a fixed set of global axes. In ADAMS the fixed global reference frame is called the TKC global reference frame. The center of mass of the system of particles is given by equation (9-8):

$$\mathbf{r}_{cg} = \frac{1}{m} \sum_{j=1}^n m_j \mathbf{r}_j \quad (9-8)$$

in which

$$m = \sum_{j=1}^n m_j$$

is the total mass of the system.

Taking successive time derivatives of equation 9-8, by realizing that the each m_j is invariable, the velocity of the center of mass results to be given by equation 9-9:

$$\dot{\mathbf{r}}_{cg} = \frac{1}{m} \sum_{j=1}^n m_j \dot{\mathbf{r}}_j \quad (9-9)$$

where the summation terms are the linear momenta of each particle.

In ADAMS all degrees of freedom of all bodies are required to be driven by forces. These forces can be introduced either by constraining certain degrees of freedom by joints or by applying a force or moments. The six degrees of freedom of the Centroid Dummy are controlled by a PD-controller. The orientation controller for the three rotational DOFs is explained in section 9-3. The function for the position PD-controller is based on a ‘spring-damper’ with gains given as a stiffness-constant k_{CD} and a damping-constant c_{CD} resulting in the control force \mathbf{F}_{CD} . The function minimizes both the displacement and velocity error and is given by equation (9-10):

$$\mathbf{F}_{CD} = -k_{CD} \cdot \boldsymbol{\varepsilon}_{CD} - c_{CD} \cdot \dot{\boldsymbol{\varepsilon}}_{CD} \quad (9-10)$$

with

$$\begin{aligned} \boldsymbol{\varepsilon}_{CD} &= \mathbf{r}_{CD} - \mathbf{r}_{cg} \\ \dot{\boldsymbol{\varepsilon}}_{CD} &= \dot{\mathbf{r}}_{CD} - \dot{\mathbf{r}}_{cg} \end{aligned}$$

where \mathbf{r}_{CD} and $\dot{\mathbf{r}}_{CD}$ are the displacement and velocity of the Centroid Dummy respectively and $\boldsymbol{\varepsilon}_{CD}$ and $\dot{\boldsymbol{\varepsilon}}_{CD}$ are the displacement error and the velocity error of the Centroid Dummy respectively.

The values for k_{CD} and c_{CD} are chosen based on verification of the simulations. During the simulation the kite is steered sideways such that it gains speed and is drifted away from the initial condition. By inspection the displacement and velocity errors are analyzed and are required not to cross a value of 10^{-6} . Based on these simulations the values for k_{CD} and c_{CD} are given in table 9-7:

k_{CD}	$1.0 \cdot 10^8 \text{ N/m}$
c_{CD}	$1.0 \cdot 10^5 \text{ N}\cdot\text{s/m}$

Table 9-7: Gains for Centroid Dummy position PD-controller

The Center of Gravity macro creates measures for the center of mass inertial acceleration as well. Again taking successive time derivatives of equation (9-9) for the acceleration vector is written:

$$\ddot{\mathbf{r}}_{cg} = \frac{1}{m} \sum_{j=1}^n m_j \ddot{\mathbf{r}}_j \quad (9-11)$$

Reference [31] states that the internal forces for a system of particles cancel out and that the inertial acceleration of the center of gravity $\ddot{\mathbf{r}}_{cg}$ is equal to the sum of the external forces:

$$\sum_{j=1}^n \mathbf{F}_j^{ext} = m \cdot \ddot{\mathbf{r}}_{cg} \quad (9-12)$$

where \mathbf{F}_j^{ext} is the resultant external force of particle j .

Note that equation (9-12) states the same as equation (6-1).

A particle is defined as a point mass and has therefore no rotational inertia properties. A rigid body is defined as a non-flexible homogeneous body. The mass and inertia properties of a rigid body can be given in terms of the concentrated mass positioned at the center of mass of the body and the mass moment and products of inertia about the center of mass. As the inertia properties of a body are unrelated to equations (9-8), (9-9), (9-11) and (9-12) these equations are also valid for a system of rigid bodies.

9-2-3 Inertia macro

Table A-5 shows the mass moments and products of inertia for the North Rhino Multi-Body Kite model derived with the ADAMS function `Aggregate Mass...`. As this function is only accessible in ADAMS/View for static conditions it cannot be used during dynamic simulations.

Because the Multi-Body Kite model is flexible the inertia properties change during dynamic simulations. The variation of the values for mass moments and products of inertia for different flight conditions have non-negligible effects on the dynamics of the system. Therefore the variation of the inertia properties under influence of the flight condition must be known. It would be advantageous to know the variation of the inertia properties dynamically or, in other words, as a function of time. The Inertia macro `Inertia.mac_cre` creates measures for the inertia properties as a function of time.

The mass moments and products of inertia are usually given in the mass matrix of inertia or inertia tensor. The inertia tensor with respect to the origin of the fixed global reference frame and

expressed in the fixed global reference frame is given by:

$$\mathbb{I}_{O_E}^E = \begin{bmatrix} I_{xx} & -J_{xy} & -J_{xz} \\ -J_{yx} & I_{yy} & -J_{yz} \\ -J_{zx} & -J_{zy} & I_{zz} \end{bmatrix} \quad (9-13)$$

The function `Aggregate Mass...` calculates the sum of the inertia properties of all rigid bodies with respect to a specified reference frame or marker. In ADAMS the inertia tensor of every rigid body is specified about its local body reference frame. To obtain the inertia tensor about the earth-fixed reference frame the inertia tensor has to be transformed. For the inertia tensor of some rigid body j with the TKC global frame as the reference marker can be written:

$$\mathbb{I}_{cg_j,j}^E = \mathbb{T}_{Eb,j} \mathbb{I}_{cg_j,j}^{b_j} \mathbb{T}_{Eb,j}^\top \quad (9-14)$$

where $\mathbb{T}_{Eb,j}$ is the transformation matrix for the transformation from the local body-fixed reference frame $F_{b,j}$ to the earth-fixed reference frame and cg_j the center of gravity of body j .

In the following step the inertia tensor $\mathbb{I}_{cg_j,j}^E$ is translated with the *Parallel Axis Theorem* (Reference [31]). The Parallel Axis Theorem is used to compute the inertia properties about another reference point:

$$\begin{aligned} I_{xx,j} &= I_{xx_{cg_j,j}} + m_j (d_y^2 + d_z^2)_j & I_{xy,j} &= I_{xy_{cg_j,j}} + m_j (d_x d_y)_j \\ I_{yy,j} &= I_{yy_{cg_j,j}} + m_j (d_x^2 + d_z^2)_j & I_{xz,j} &= I_{xz_{cg_j,j}} + m_j (d_x d_z)_j \\ I_{zz,j} &= I_{zz_{cg_j,j}} + m_j (d_x^2 + d_y^2)_j & I_{yz,j} &= I_{yz_{cg_j,j}} + m_j (d_y d_z)_j \end{aligned} \quad (9-15)$$

where m_j is the mass of body j , d_x , d_y and d_z the directed distances from the new axes to the centroidal axes and entering the results in equation (9-13) gives the inertia tensor $\mathbb{I}_{O_E,j}^E$.

Summing over all the bodies gives the total inertia tensor with respect to the specified marker:

$$\mathbb{I}_{O_E}^E = \sum_{j=1}^n \mathbb{I}_{O_E,j}^E \quad (9-16)$$

Equation (9-16) gives the exact inertia tensor and evaluated at every time step the dynamic variation is known as well. Unfortunately the function `Aggregate Mass...` is hard to be implemented for every time step as described in section 9-1. Additionally, ADAMS can only perform scalar computations and no vector operations. The implementation of equation 9-14 for every body in scalar form is a tedious job and requires the orientation as well as the inertia properties for every body at every time step. This results in a dramatic size for the amount of characters in the function measures and is almost practically impossible for ADAMS to handle.

Due to these programming issues in ADAMS for the computation of the inertia tensor the contribution of the first terms of the Parallel Axis Theorem, i.e. the inertia properties of each body about the local cg_j , is neglected. The resulting values for the mass moment and products of inertia will be an approximation of equation (9-16). The relative error will get smaller if the reference point is chosen further away from the bodies, because the second terms in (9-15) will become larger. For analyzing the variation of the inertia properties the inertia tensor needs to be known about the center of mass of all bodies as determined in section 9-2-2. So the reference point cannot be chosen arbitrary.

This method can also be described as the *particle based (pb)* method. This can be seen by inspecting equation (9-15) and realizing that a particle has no *local* inertia properties. To conclude

the moments and products of inertia determined with the Inertia macro are given by:

$$\begin{aligned}
 I_{xx,pb} &= \sum_{j=1}^n m_j (d_y^2 + d_z^2)_j & I_{xy,pb} &= \sum_{j=1}^n m_j (d_x d_y)_j \\
 I_{yy,pb} &= \sum_{j=1}^n m_j (d_x^2 + d_z^2)_j & I_{xz,pb} &= \sum_{j=1}^n m_j (d_x d_z)_j \\
 I_{zz,pb} &= \sum_{j=1}^n m_j (d_x^2 + d_y^2)_j & I_{yz,pb} &= \sum_{j=1}^n m_j (d_y d_z)_j
 \end{aligned} \tag{9-17}$$

where $d_{x,j}$, $d_{y,j}$ and $d_{z,j}$ are the directed distances from the *cg* of body j to the origin of the earth-fixed reference frame and, by consequence, equation (9-13) gives the inertia tensor $\mathbb{I}_{O_E,pb}^E$.

9-2-4 Angular Momentum macro

The Angular Momentum macro `Ang_Momentum.mac_cre` computes the angular momentum of a model as well as the time derivative of the angular momentum about the TKC global origin based on a particle approach.

Exact solution

First the exact solutions are given for the angular momentum of a multi-body system about the *cg* and the fixed global origin O_E . As explained in Reference [31] the total angular momentum of a *rigid body* with rotational speed $\boldsymbol{\Omega}$ about a *fixed* point on the body P with respect to the *fixed* global origin O_E is the angular momentum about the center of mass *cg* plus the moment of the linear momentum of *cg* about P :

$$\mathbf{B}_P = \int_{\mathcal{V}} \mathbf{r} \times (\boldsymbol{\Omega} \times \mathbf{r}) dm + \mathbf{r}_{Pcg} \times m \dot{\mathbf{r}}_P \tag{9-18}$$

where \mathcal{V} is the volume of the body, \mathbf{r} the position vector of *cg* to a mass element dm and \mathbf{r}_{Pcg} the position vector of point P to the *cg*.

If point P is fixed in space, then $\dot{\mathbf{r}}_P$ is zero, and if point P is chosen as the center of mass, then \mathbf{r}_{Pcg} is zero. In either case equation 9-18 reduces to:

$$\mathbf{B}_P = \int_{\mathcal{V}} \mathbf{r} \times (\boldsymbol{\Omega} \times \mathbf{r}) dm \tag{9-19}$$

Expanding the integrand and evaluating the integrand will eventually result in:

$$\mathbf{B}_P = \mathbb{I}_P \boldsymbol{\Omega} \tag{9-20}$$

where \mathbb{I}_P is the inertia tensor of the body with respect to point P .

Now, if a *multi-body* system is considered, using equation 9-18 and figure 9-10, for the angular momentum of a body j (for $j = 1$ to $j = n$) about the *moving* center of mass C of the multi-body system can be written:

$$\mathbf{B}_{C,j} = \int_{\mathcal{V}_j} \mathbf{r} \times (\boldsymbol{\Omega}_j \times \mathbf{r}) dm + \mathbf{r}_{cg_j C} \times m_j \dot{\mathbf{r}}_{cg_j} \tag{9-21}$$

where \mathbf{r} is the position vector of the local cg_j to a mass element dm , $\boldsymbol{\Omega}_j$ the rotational speed of body j with respect to the earth-fixed reference frame, $\mathbf{r}_{cg_j C}$ the position vector of cg_j to point C and $\dot{\mathbf{r}}_{cg_j}$ the velocity of the *cg* of the body j . See figure 9-10.

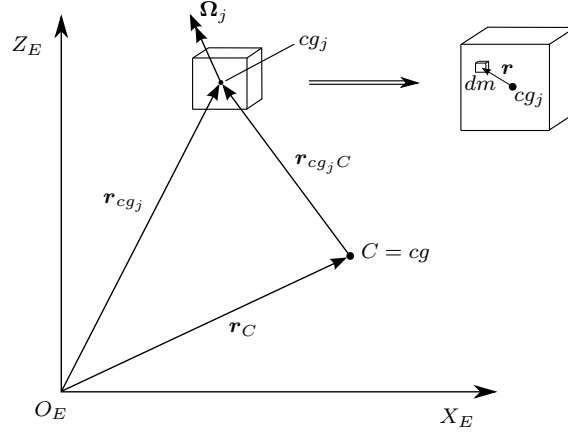


Figure 9-10: Angular momentum multi-body system

Equation (9-21) can be evaluated to:

$$\mathbf{B}_{C,j} = \mathbb{I}_{cg_j} \boldsymbol{\Omega}_j + \mathbf{r}_{cg_j C} \times m_j \dot{\mathbf{r}}_{cg_j} \quad (9-22)$$

where \mathbb{I}_{cg_j} is the inertia tensor of body j with respect to the center of gravity of body j cg_j .

Summing over all bodies gives:

$$\mathbf{B}_C = \sum_{j=1}^n \mathbb{I}_{cg_j} \boldsymbol{\Omega}_j + \sum_{j=1}^n \mathbf{r}_{cg_j C} \times m_j \dot{\mathbf{r}}_{cg_j} \quad (9-23)$$

Evaluating the second term in the latter expression, using $\mathbf{r}_{cg_j C} = \mathbf{r}_{cg_j} - \mathbf{r}_C$, gives:

$$\sum_{j=1}^n \mathbf{r}_{cg_j C} \times m_j \dot{\mathbf{r}}_C = \sum_{j=1}^n \mathbf{r}_{cg_j} \times m_j \dot{\mathbf{r}}_{cg_j} - \sum_{j=1}^n \mathbf{r}_C \times m_j \dot{\mathbf{r}}_{cg_j} \quad (9-24)$$

Using that the sum of linear momentum of all bodies is the linear momentum of C of the multi-body system, so:

$$\sum_{j=1}^n \mathbf{r}_{cg_j C} \times m_j \dot{\mathbf{r}}_C = \sum_{j=1}^n \mathbf{r}_{cg_j} \times m_j \dot{\mathbf{r}}_{cg_j} - \mathbf{r}_C \times m \dot{\mathbf{r}}_C \quad (9-25)$$

Finally, implementing equation (9-25) in (9-23), one obtains:

$$\mathbf{B}_C = \sum_{j=1}^n \mathbb{I}_{cg_j} \boldsymbol{\Omega}_j + \sum_{j=1}^n \mathbf{r}_{cg_j} \times m_j \dot{\mathbf{r}}_{cg_j} - \mathbf{r}_C \times m \dot{\mathbf{r}}_C \quad (9-26)$$

and is the angular momentum about the cg of a multi-body system expressed as the sum of the angular momenta of each body about their local cg_j plus the sum of the moments of the linear momentum of each body about the cg of the multi-body system minus the moment of the linear momentum of the cg of the multi-body system about O_E .

The latter term in equation (9-26) also arises when applying the *Translation Theorem for Angular Momentum* (Reference [31]), which states that the angular momentum about some moving point is equal to the angular momentum about the center of mass plus the moment of the linear momentum of the center of mass about the moving point.

Evaluating equation (9-20) for body j directly about the *fixed* global origin and summing over all bodies results in:

$$\mathbf{B}_{O_E} = \sum_{j=1}^n \mathbb{I}_{O_E,j} \boldsymbol{\Omega}_j \quad (9-27)$$

Particle approximation

As is explained in the section about the Inertia macro the computation of the inertia tensor is hard to be implemented in ADAMS. Therefore another approach is required for the angular momentum. Again, an approximation is proposed based on the particle method. According to Reference [31] the angular momentum about point P of a system of particles is:

$$\mathbf{B}_P = \sum_{j=1}^n \mathbf{r}_{Pj} \times m_j \dot{\mathbf{r}}_j \quad (9-28)$$

In the Angular Momentum macro the angular momentum is computed about the fixed global origin using the center of mass of each body:

$$\mathbf{B}_{O_E, pb} = \sum_{j=1}^n \mathbf{r}_{cgj} \times m_j \dot{\mathbf{r}}_{cgj} \quad (9-29)$$

which is exactly the second summation term in equation (9-26).

For the time derivative of the angular momentum only the derivative for the particle based method is given. Taking the time derivative of equation (9-29) gives:

$$\frac{d\mathbf{B}_{O_E, pb}}{dt} = \sum_{j=1}^n \dot{\mathbf{r}}_{cgj} \times m_j \dot{\mathbf{r}}_{cgj} + \sum_{j=1}^n \mathbf{r}_{cgj} \times m_j \ddot{\mathbf{r}}_{cgj} \quad (9-30)$$

and, by consequence,

$$\dot{\mathbf{B}}_{O_E, pb} = \sum_{j=1}^n \mathbf{r}_{cgj} \times m_j \ddot{\mathbf{r}}_{cgj} \quad (9-31)$$

which is the equation evaluated by the Angular Momentum macro.

9-2-5 Sum of General Forces macro

The Sum of General Forces macro `Sum_GForce.mac_cre` is created to compute the sum of all aerodynamic forces of the Multi-Body Kite model. The aerodynamic forces in ADAMS are modelled by so called ‘general force’ functions. The sum of all general forces can be expressed as:

$$\mathbf{F}_{GF} = \sum_{j=1}^n \mathbf{F}_{GF, j} \quad (9-32)$$

The evaluation in the macro file is done with function command `GForce`. In the `GForce` function the force name and the force component need to be specified.

9-2-6 Sum of General Moments macro

The Sum of General Moments macro `Sum_Mom_GF.mac_cre` computes the resulting moment of the general forces of the Multi-Body model in ADAMS. The Sum of General Moments macro is used to compute the sum of aerodynamic moments resulting from the aerodynamic forces. The expression evaluated by the macro file is:

$$\mathcal{M}_{GF} = \sum_{j=1}^n \mathbf{r}_{GF, j} \times \mathbf{F}_{GF, j} \quad (9-33)$$

9-3 Transformation of measures to body-fixed reference

To use the computed quantity components by the ADAMS function measures generated by the GUM files for aerodynamic parameter identification in chapter 10 the computed components need to be translated and transformed to the center of gravity and the body-fixed reference frame respectively.

As only the translation of the center of mass is computed the rotation is still undetermined. The orientation will be expressed in the body Euler angles $\langle \phi, \theta, \psi \rangle$ using the angular velocity vector.

9-3-1 Angular velocity and body Euler angles

Before the angular velocity is computed the inertia tensor and the angular momentum are first translated to the center of gravity cg of the multi-body system using the Parallel Axis Theorem on equation (9-17) and the Translation Theorem for Angular Momentum on equation (9-29) respectively:

$$\begin{aligned} I_{xx,cg} &= I_{xx,pb} - m(d_y^2 + d_z^2)_{cg} & I_{xy,cg} &= I_{xy,pb} - m(d_x d_y)_{cg} \\ I_{yy,cg} &= I_{yy,pb} - m(d_x^2 + d_z^2)_{cg} & I_{xz,cg} &= I_{xz,pb} - m(d_x d_z)_{cg} \\ I_{zz,cg} &= I_{zz,pb} - m(d_x^2 + d_y^2)_{cg} & I_{yz,cg} &= I_{yz,pb} - m(d_y d_z)_{cg} \end{aligned} \quad (9-34)$$

which can be written to the inertia tensor \mathbb{I}_{cg}^E , and,

$$\mathbf{B}_{cg} = \mathbf{B}_{O_E,pb} - \mathbf{r}_{cg} \times m \dot{\mathbf{r}}_{cg} \quad (9-35)$$

Now, using equation (9-20) with $P = cg$ the total angular velocity of the multi-body system in earth-fixed reference is:

$$\boldsymbol{\Omega}_{bE}^E = (\mathbb{I}_{cg}^E)^{-1} \mathbf{B}_{cg}^E \quad (9-36)$$

If the orientation is known at $t = t_n$ the rotational velocity, the inertia tensor and the angular momentum expressed in the body-fixed reference frame is evaluated using the transformation matrix \mathbb{T}_{bE} :

$$\boldsymbol{\Omega}_{bE}^b = \mathbb{T}_{bE} \boldsymbol{\Omega}_{bE}^E \quad (9-37)$$

$$\mathbb{I}_{cg}^b = \mathbb{T}_{bE} \mathbb{I}_{cg}^E \mathbb{T}_{bE}^\top \quad (9-38)$$

$$\mathbf{B}_{cg}^b = \mathbb{T}_{bE} \mathbf{B}_{cg}^E \quad (9-39)$$

Because of possible numerical inaccuracies it is not preferred to compute the time derivative of the angular velocity by numerical differentiation. Since the time derivative of the angular momentum is available the time derivative of the angular velocity is determined as follows. First the time derivative of the angular momentum about the global origin O_E is translated to the center of mass cg :

$$\dot{\mathbf{B}}_{cg} = \dot{\mathbf{B}}_{O_E,pb} - \mathbf{r}_{cg} \times m \ddot{\mathbf{r}}_{cg} \quad (9-40)$$

and using the time derivative of the angular momentum for a rigid body (from Reference [31]) the total angular acceleration of the multi-body system is:

$$\dot{\boldsymbol{\Omega}}_{bE}^E = (\mathbb{I}_{cg}^E)^{-1} \left(\dot{\mathbf{B}}_{cg} - \boldsymbol{\Omega}_{bE}^E \times \left(\mathbb{I}_{cg}^E \boldsymbol{\Omega}_{bE}^E \right) \right) \quad (9-41)$$

The angular acceleration is transformed to the body-fixed reference frame with \mathbb{T}_{bE} .

The time derivative of the Euler angles $\langle \dot{\phi}, \dot{\theta}, \dot{\psi} \rangle$ is obtained by using equation (6-22):

$$\begin{bmatrix} \dot{\phi} \\ \dot{\theta} \\ \dot{\psi} \end{bmatrix} = \begin{bmatrix} 1 & \sin \phi \tan \theta & \cos \phi \tan \theta \\ 0 & \cos \phi & -\sin \phi \\ 0 & \frac{\sin \phi}{\cos \theta} & \frac{\cos \phi}{\cos \theta} \end{bmatrix} \Omega_{bE}^b$$

Integrating the time derivatives of the Euler angles over time the Euler angles at every $t = t_n$ are determined:

$$\begin{aligned} \phi(t_n) &= \int_{t_0}^{t_n} \dot{\phi} \cdot dt + \phi_0 \\ \theta(t_n) &= \int_{t_0}^{t_n} \dot{\theta} \cdot dt + \theta_0 \\ \psi(t_n) &= \int_{t_0}^{t_n} \dot{\psi} \cdot dt + \psi_0 \end{aligned} \quad (9-42)$$

where ϕ_0 , θ_0 and ψ_0 are defined by the initial orientation of the Multi-Body model. ϕ_0 and ψ_0 are zero and θ_0 has been given in table 9-2.

With equations (9-42) the total orientation of the multi-body system at every time step has been determined. Both the inertia properties and the angular momentum vector are obtained based on the *particle* method. They both neglect the local body rotational inertia properties. As they are both used to determine the lumped rotational speed the error for the rotational speed is exactly the sum of the local rotational speeds of the bodies with respect to the rotational speed of the multi-body system. Because each body is connected on multiple locations this error can be assumed small.

Because both the inertia tensor and the angular momentum are computed by neglecting the contribution of the foil parts in the Multi-Body model, the center of mass position, velocity and acceleration, used in the Parallel Axis Theorem and the Translation Theorem, have to be computed again also without the foil parts. Otherwise the inertia tensor and the angular momentum about the *cg* would not be consistent.

The implementation of the matrix and vector computations given by equations (9-36) to (9-39) and (9-41) to (9-42) is done by a so called *ADAMS General State Equation* (GSE). The GSE is introduced in the model with the ADAMS/Controls plugin. With ADAMS/Controls a SIMULINK model can be attached to the model in the form of an executable dll-file. In this way the ability of MATLAB is used to perform the matrix and vector operations. In order to be accepted by ADAMS/Controls all values of the ADAMS function measures computed by the listed equations are transferred to ADAMS state variables.

Furthermore, in the SIMULINK model, the output of the Euler angles ϕ and ψ are bounded to $-\pi$ and $+\pi$. The angle θ is not bounded, because it is assumed not to pass -0.5π and $+0.5\pi$ during simulations. If it does, it is very likely that the kite has crossed the $X_E Y_E$ -plane. As the orientation of the body-fixed reference frame is defined, all quantities measured in the earth-fixed reference frame can be computed in the body-fixed reference frame. For example the control positions are transformed to the body-fixed reference frame with the GSE.

Centroid Dummy orientation control

It would be worthwhile if the Centroid Dummy would follow the orientation of the body-fixed reference frame during simulations. It is then possible to create ADAMS function measures directly expressed in the body-fixed reference frame. And, additionally, the structural deformation can be analyzed with respect to the Centroid Dummy. This is incorporated by applied moments about

the axes of the Centroid Dummy, which, like the position control, is modelled by a torsional spring-damper system to create a PD-controller.

The torsional spring-damper applies a moment expressed in the earth-fixed reference frame. For the reference of the rotational speed $\boldsymbol{\Omega}_{bE}^E$ is used as computed in equation (9-36). The rotational speed $\boldsymbol{\Omega}_{CD}^E$ of the Centroid Dummy can be easily measured in ADAMS. The difference between both can be directly used to compute the contribution to the control moment. The Euler angles of the Centroid Dummy can be easily measured as well. But, by definition, the Euler angles define the orientation by a 321-rotation sequence. Therefore the error between the computed Euler angles and the measured Euler angles must be transformed to earth-fixed reference. The proportional (P) contribution to the control moment is given by:

$$\mathcal{M}_{CD,P}^E = k_{CD,ori} \cdot \left(\mathbb{T}_{EE''} \begin{bmatrix} \varepsilon_\phi \\ 0 \\ 0 \end{bmatrix} + \mathbb{T}_{EE'} \begin{bmatrix} 0 \\ \varepsilon_\theta \\ 0 \end{bmatrix} + \begin{bmatrix} 0 \\ 0 \\ \varepsilon_\psi \end{bmatrix} \right) \quad (9-43)$$

where,

$$\begin{aligned} \varepsilon_\phi &= \phi_{CD} - \phi(t_n) \\ \varepsilon_\theta &= \theta_{CD} - \theta(t_n) \\ \varepsilon_\psi &= \psi_{CD} - \psi(t_n) \end{aligned}$$

and expanding equation (9-43) gives:

$$\mathcal{M}_{CD,P}^E = k_{CD,ori} \cdot \left(\varepsilon_\phi \begin{bmatrix} \cos \theta \cos \psi \\ \cos \theta \sin \psi \\ -\sin \theta \end{bmatrix} + \varepsilon_\theta \begin{bmatrix} -\sin \psi \\ \cos \psi \\ 0 \end{bmatrix} + \varepsilon_\psi \begin{bmatrix} 0 \\ 0 \\ 1 \end{bmatrix} \right) \quad (9-44)$$

The derivative (D) contribution is simply:

$$\mathcal{M}_{CD,D}^E = c_{CD,ori} \cdot \boldsymbol{\varepsilon}_\Omega^E \quad (9-45)$$

with,

$$\boldsymbol{\varepsilon}_\Omega^E = \boldsymbol{\Omega}_{CD}^E - \boldsymbol{\Omega}_{bE}^E$$

And the total control moment is given by:

$$\mathcal{M}_{CD}^E = \mathcal{M}_{CD,P}^E + \mathcal{M}_{CD,D}^E \quad (9-46)$$

Again, the values for the gains are verified by simulations not to pass an error value of 10^{-6} . See table 9-8.

$k_{CD,ori}$	$1.0 \cdot 10^8 \text{ N}\cdot\text{m}/\text{rad}$
$c_{CD,ori}$	$1.0 \cdot 10^5 \text{ N}\cdot\text{m}\cdot\text{s}/\text{rad}$

Table 9-8: Gains for Centroid Dummy orientation PD-controller

9-3-2 Aerodynamic forces and moments

The created measures by the Sum of General Forces macro for the aerodynamic forces applied at the TKC global origin do not change when they are applied at the cg of the multi-body system. The aerodynamic moment measures are applied at the TKC global origin and have to be transferred to the cg , which is given by:

$$\mathcal{M}_{aero,cg}^E = \mathcal{M}_{GF} - \mathbf{r}_{cg} \times \mathbf{F}_{GF} \quad (9-47)$$

9-4 Verification of created measures

The verification of the implementation of the macro files is performed with respect to a simulation test of the Surf Kite model and with respect to a double pendulum model. The double pendulum is used to verify the implementation of the rotational quantities based on the particle method. The simulation test is used to verify the implementation of the translation as well as the rotational quantities.

The simulation test is performed with a wind speed of 12 m/s. The stabilization time is set to 15 s, such that the accelerations are damped out to a great extent and the kite is at a stationary condition. One second after the stabilization time the input on the controls is introduced with a so called 131 input on the left cart, see figure 9-11. The stabilization time has been truncated from the responses and the new t_0 has been set to 0 s.

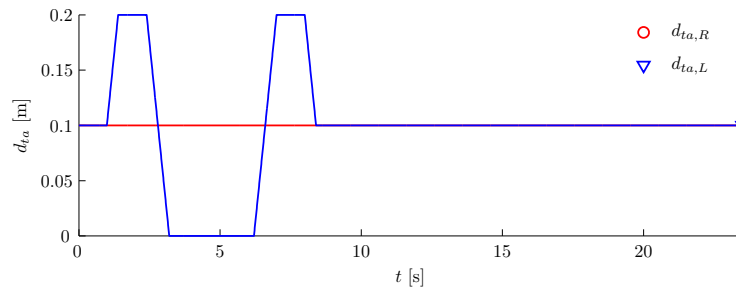


Figure 9-11: Surf Kite simulation test, inputs

The displacement and orientation of the Centroid Dummy is shown in figure 9-12.

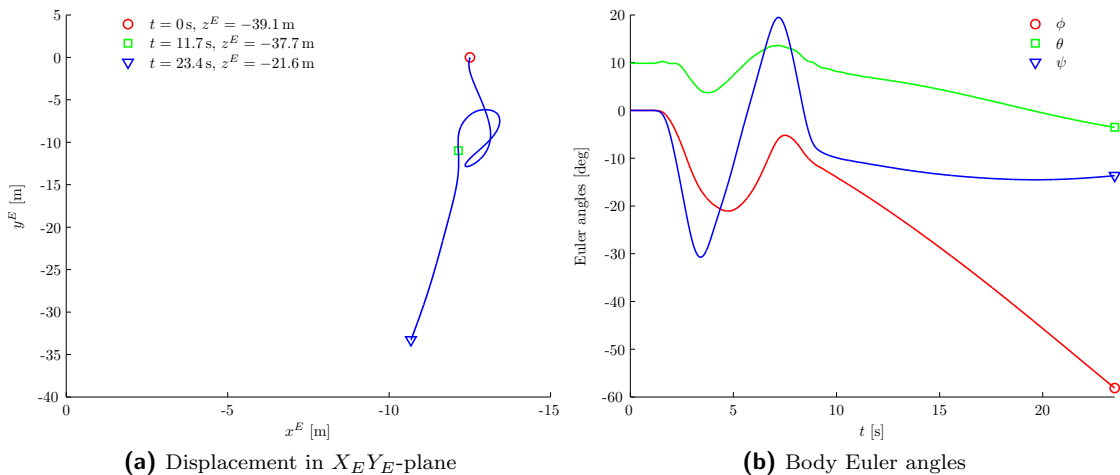


Figure 9-12: Surf Kite simulation test, translation and orientation of CD

The effectiveness of the PD-controllers for the translation and orientation of the Centroid Dummy is verified by illustrating the errors for the displacement, velocity, orientation and angular velocity, see figures 9-13 and 9-14.

Both figures clearly show that the maximum allowable error of 10^{-6} is met and that the Centroid Dummy effectively follows the reference signals for the translation and orientation.

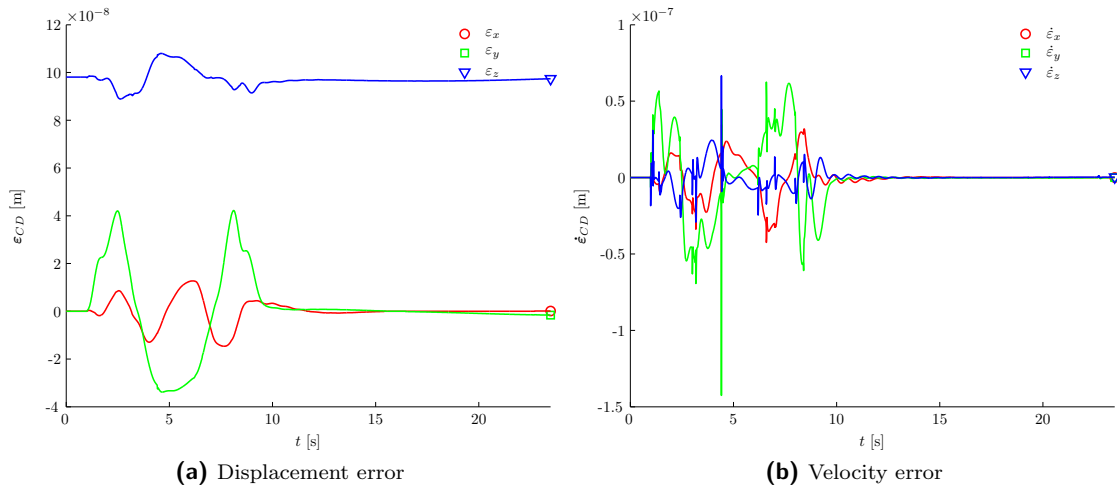


Figure 9-13: Surf Kite simulation test, translation error Centroid Dummy

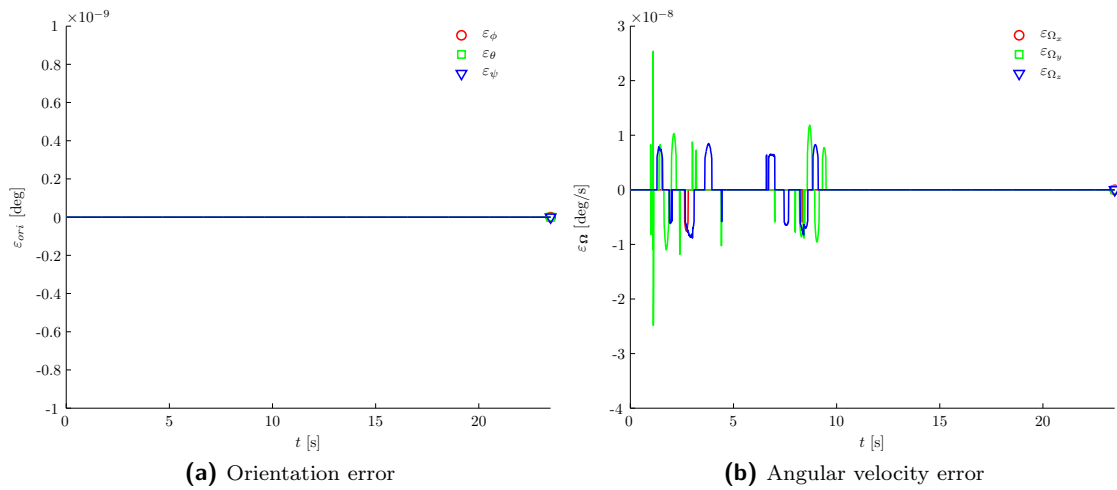


Figure 9-14: Surf Kite simulation test, rotation error Centroid Dummy

Still, it remains to verify if the reference signals, that is the actual displacement, velocity, orientation and angular velocity are implemented correctly. Although there is no direct check, since there was no data before the implementation of the macro files, there is another way to verify the correctness of the reference signals and with that the correctness of the implementation of the equations by the macro files.

9-4-1 Translation

The translation of the center of gravity is defined by the displacement, velocity and acceleration measures for the center of gravity.

Acceleration and aerodynamic forces The verification of the translation of the center of gravity of the multi-body system is done by comparing the measurements for the acceleration and the

resultant external forces. According to equation (9-12) the sum of the external forces must equal the acceleration of the center of gravity times the mass. As acceleration is obtained by the time derivatives of the displacement and velocity and the resulted equations are comparable (see equations (9-8), (9-9) and (9-11)) the comparison between the acceleration and external forces is also a verification for the velocity and displacement.

The verification is performed by transforming the quantities to the body-fixed reference frame. And, secondly, by rewriting equation (9-12) and equation (6-21) to:

$$\begin{aligned} X &= \sum F_{x,aero}^b = m \cdot A_x^b - (-mg_G \sin \theta + F) \\ Y &= \sum F_{y,aero}^b = m \cdot A_y^b - (mg_G \sin \phi \cos \theta + G) \\ Z &= \sum F_{z,aero}^b = m \cdot A_z^b - (mg_G \cos \phi \cos \theta + H) \end{aligned} \quad (9-48)$$

where

$$\mathbf{A} = \ddot{\mathbf{r}}_{cg}$$

The result is given in figure 9-15. The graphs show an excellent match. The graphs for the sum of aerodynamic forces are completely covered by the graphs representing the right side of equation (9-48).

9-4-2 Rotation

The rotation of the body-fixed reference frame is defined by the orientation, angular velocity and angular acceleration measures for the body-fixed reference frame.

The angular velocity is determined with the measures for the inertia tensor and the angular momentum (equation (9-36)) and, subsequently, the orientation of the body-fixed reference frame. The measures for the inertia tensor and the angular momentum are based on the particle method. For verification of this method, first, the method is implemented in another model, a double pendulum, and secondly, the Multi-Body Kite model simulation test is continued.

Double pendulum model

The double pendulum consists of three spherical bodies of equal mass m connected by massless links of equal length l . The connection with the ground is established by a spherical joint and at the second mass element m_2 there is a revolute joint. The spherical joint has three rotational degrees of freedom and the revolute joint has one rotational degree of freedom. The three spherical bodies have an inertia of mr^2 about each axis, where r is the radius of the sphere. Due to the equal masses m and equal length of the links l there is a symmetry plane parallel to the rotation axis of the revolute joint. See figure 9-16.

Furthermore the Centroid Dummy is shown with the Z_b and Y_b axes. The X_b -axis is directed downwards and parallel to the symmetry plane and lies, by definition of the center of gravity, in the symmetry plane. The Z_b -axis is directed parallel to the first two links and the Y_b -axis tangential to the first two links. A displacement vector \mathbf{r} is defined which represents the distance between cg and m_1 .

In figure 9-17 a snapshot of the model is shown at the initial condition in ADAMS/View. The center of mass position is again given by the Centroid Dummy and defines the body-fixed reference frame. The initial pitch angle θ_0 is +80 deg with respect to the earth-fixed reference. The Z_E -axis is positive upwards and gravity is negative with respect to the Z_E -axis.

The motion is initiated under the influence of gravity. Since there is no damping, friction or drag in the model the pendulum will stay in motion forever. The double pendulum is a classical example

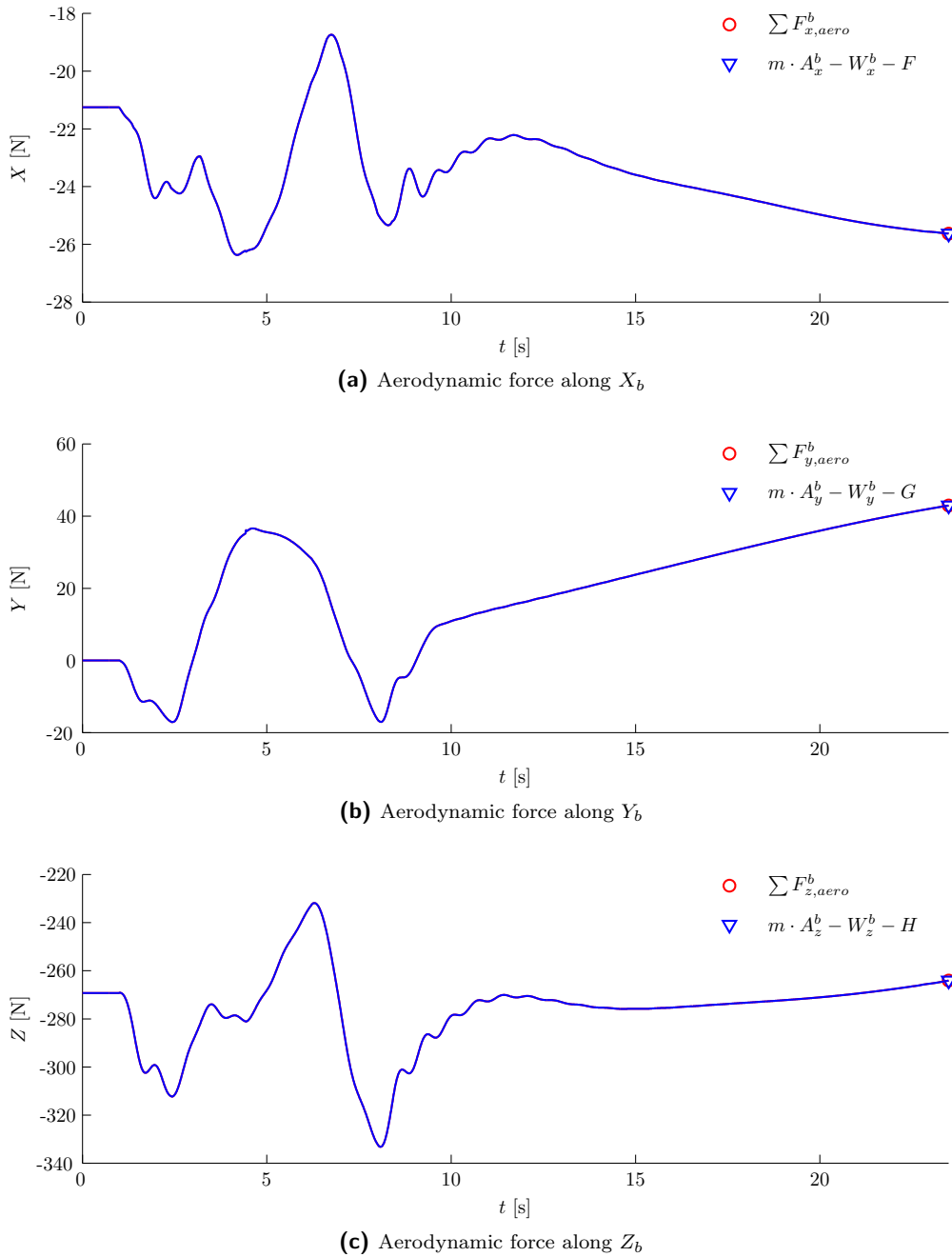


Figure 9-15: Surf Kite simulation test, verification of aerodynamic forces

of a system having *chaotic dynamics*. The chaotic behaviour is clearly visible from figure 9-18. Figure 9-18 shows the orientation of the body-fixed reference frame by the Euler angles ϕ , θ and ψ for a simulation time of 10 s.

For the *particle based* method to work the following should hold. From figure 9-16 can be seen that the Centroid Dummy must move along the dashed line of the symmetry plane for the verification of the center of gravity displacement. And, secondly, the distances between the Centroid Dummy and m_1 and between Centroid Dummy and m_3 expressed in the body-fixed reference frame must

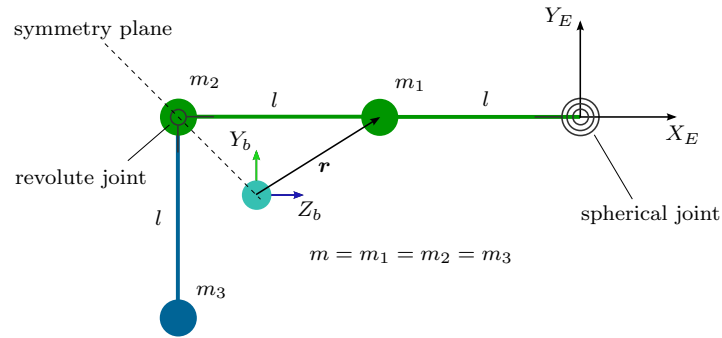


Figure 9-16: Double pendulum model

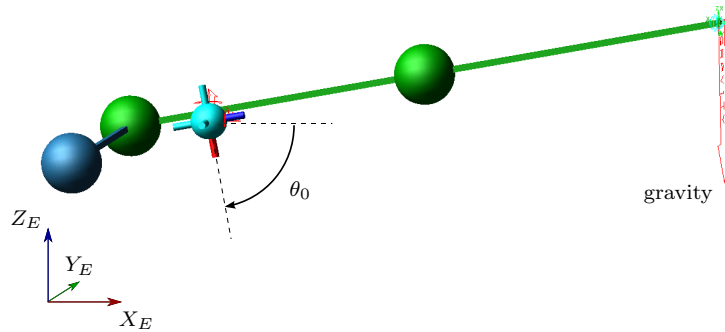


Figure 9-17: Double pendulum model, initial condition

be equal for the verification of the orientation. For both to hold it can be said that:

$$\begin{aligned} r_x^b &= x_{m_1}^b = x_{m_3}^b = 0 \\ r_y^b &= y_{m_1}^b = -z_{m_3}^b \\ r_z^b &= z_{m_1}^b = -y_{m_3}^b \end{aligned}$$

From figure 9-19 becomes clear that this is true. The values for r_x^b are within the integrator error setting of 10^{-3} .

Furthermore, the variation of the body Euler angles spans almost the full range of the Euler angles, which makes the particle method valid for this range of Euler angles.

Additionally, it can be said that the mass moment of inertia of the spherical bodies have no influence on the orientation of the body-fixed reference frame. Due to the plane of symmetry, the rotation of m_1 with respect to the Centroid Dummy is equal but opposite to the rotation of m_3 . Therefore the influence of the bodies on the angular momentum cancel.

The results of the simulation of the double pendulum verify two statements:

1. The implementation of the particle based method is done correctly
2. The particle based method works for a multi-body system as long as there is a symmetry plane, because then the influence of individual bodies left and right from the symmetry plane on the angular momentum cancel out

Note that the Kite model loses its symmetry when the kite deforms and under influence of control inputs, because the masses of the control parts are included in the inertia tensor and angular momentum computation. The influence of these two effects is investigated with a simulation test.

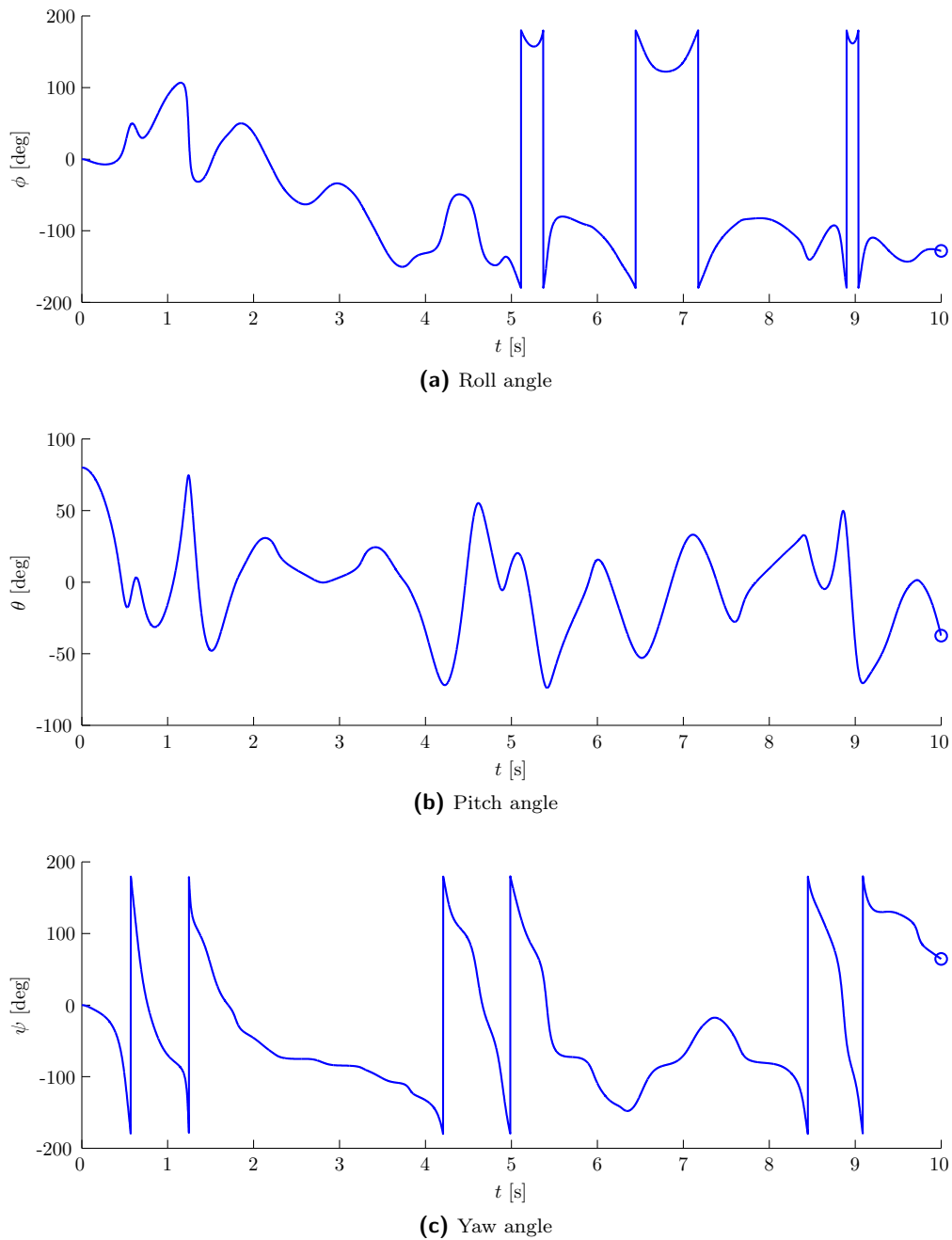


Figure 9-18: Double pendulum simulation, body Euler angles

Kite model

The verification of the Kite model continues with the simulation test given at the beginning of this section. Any irregularity with respect to the translation or rotation of the Centroid Dummy and the body-fixed reference frame, if there is any, is expected to be revealed, because the translational and rotational perturbations are relatively large.

In ADAMS the ‘camera view’ can be fixed to a specific part. Now, if the view is fixed at the Centroid Dummy the orientation and deformation of the kite with respect to the Centroid Dummy can be recorded during the simulation. Four snapshots are shown in figures 9-20 and 9-21: at the initial

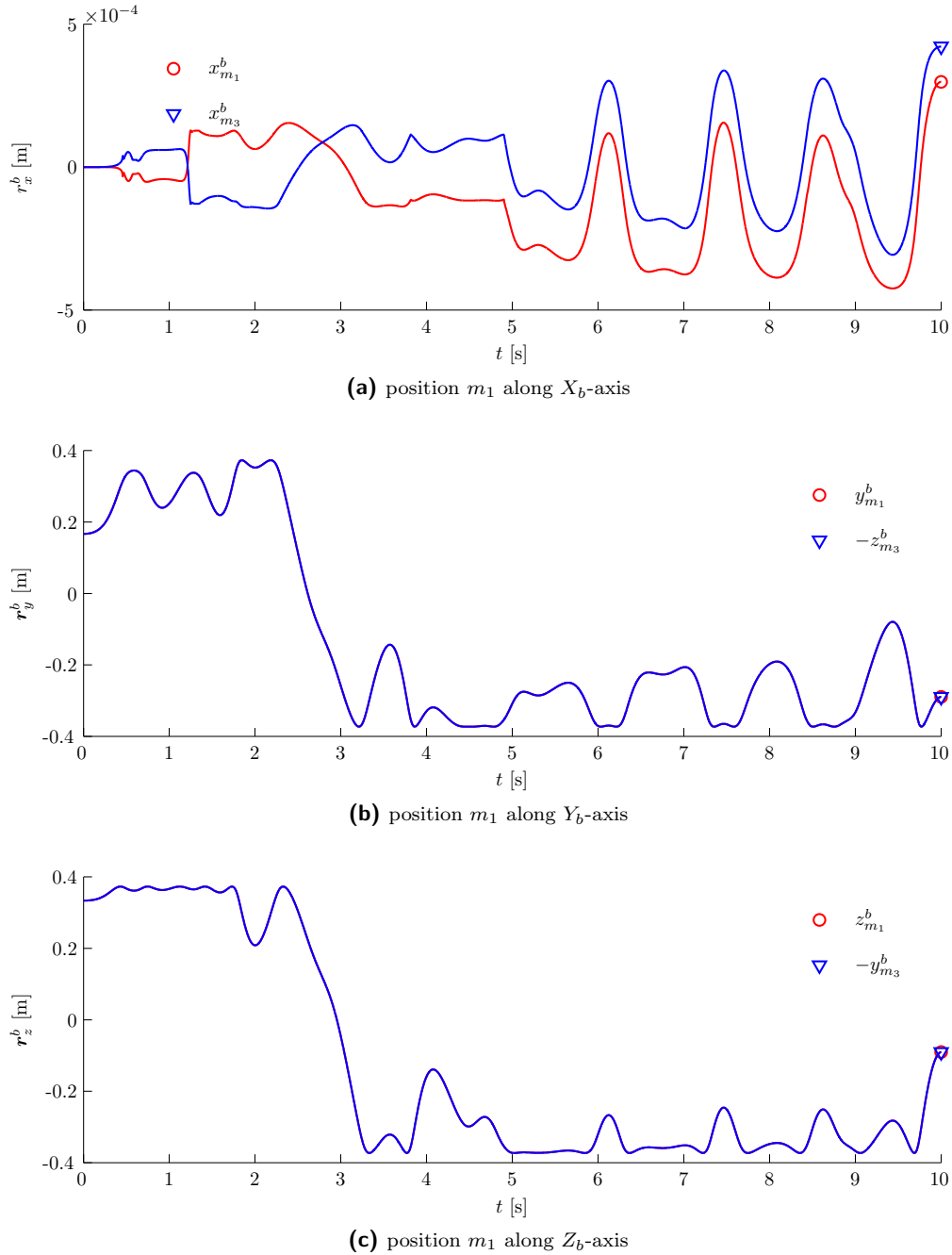


Figure 9-19: Double pendulum simulation, mass positions

condition, for an extreme value of d_{taL} and at approximately $t = 23$ s. The view on the left side of the figure gives an overall view in the earth-fixed reference frame. The view on the right side shows the kite fixed to the Centroid Dummy and in the body-fixed reference frame.

Figure 9-20a shows the snapshot of the kite at the initial condition. This snapshot is used as the reference, because there is no control input and no asymmetric deformation.

Figures 9-20b and 9-21a illustrate the kite when the left control is translated to 0.00 m and to 0.20 m along the rail respectively. It can be clearly seen in figure 9-20b that the right tip has

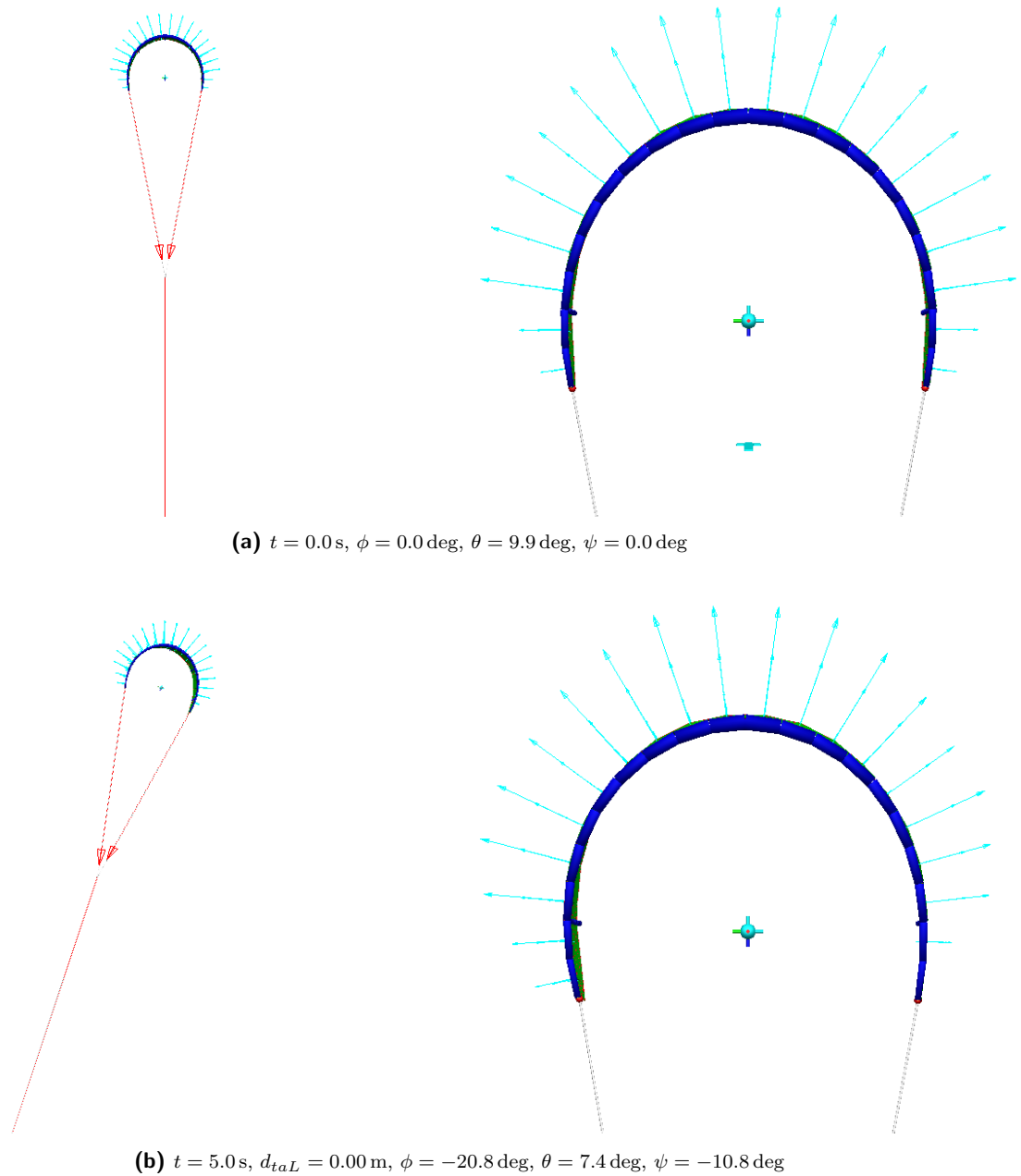


Figure 9-20: Surf Kite simulation test, $t = 0.0 \text{ s}$ and $t = 5.0 \text{ s}$

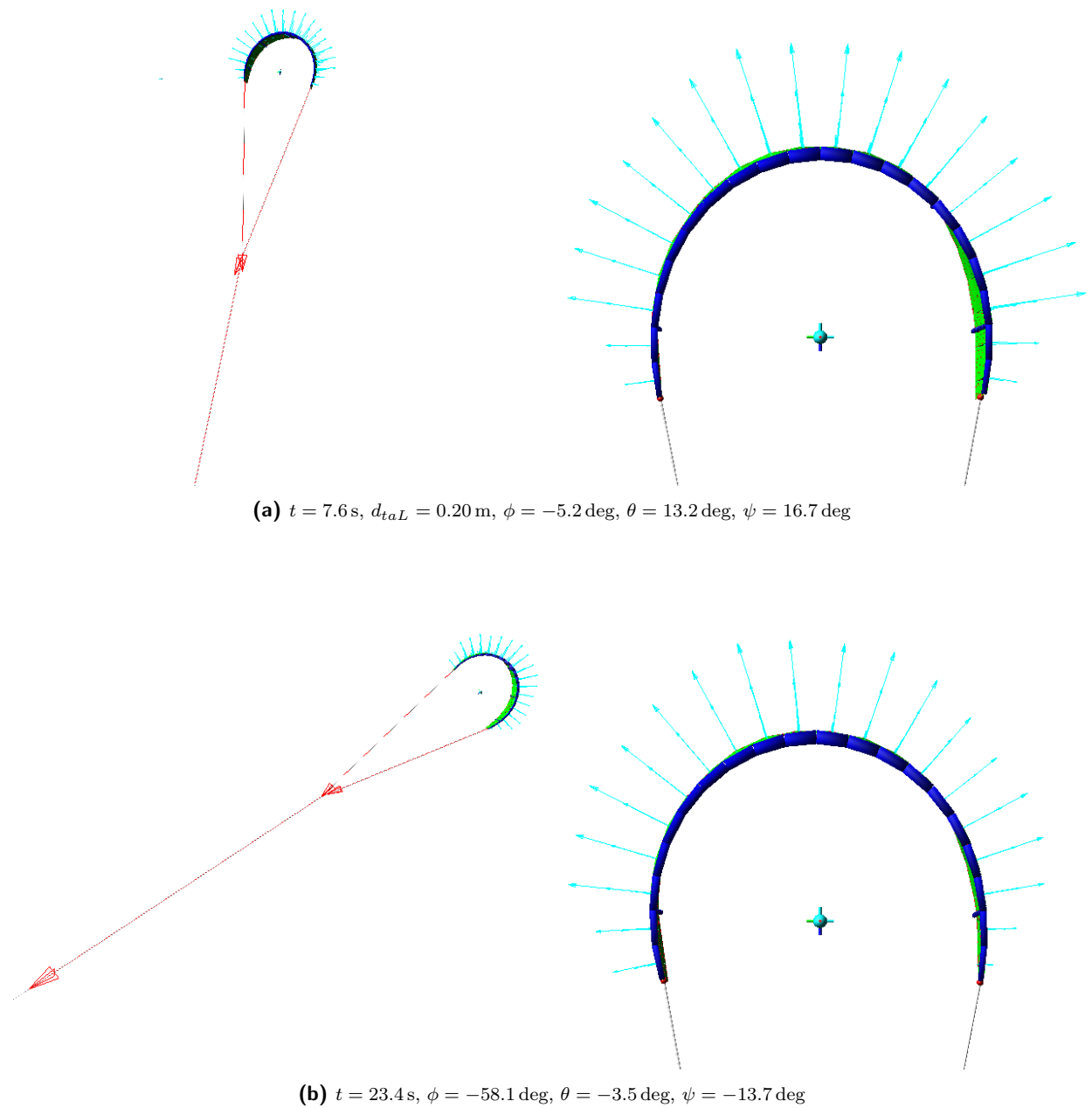


Figure 9-21: Surf Kite simulation test, $t = 7.6 \text{ s}$ and $t = 23.4 \text{ s}$

turned inwards and in figure 9-21a the left tip has turned inwards. Right is defined Y_b positive and left Y_b negative. The other tips are approximately unchanged with respect to the Centroid Dummy. This is an useful result, because the deformation of the tip with respect to the rest of the kite due to a control input becomes clear. Furthermore, the deformation of the tip results in an aerodynamic side force Y . First positive and then negative. Figures 9-20b and 9-21a confirm this by comparing the blue arrows on the left and right side of the kite. And, more clearly visible, the second graph in figure 9-15 proves this as well.

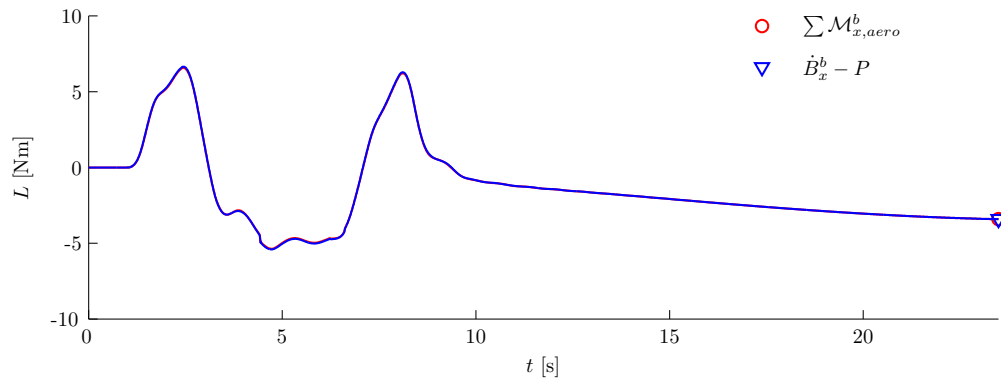
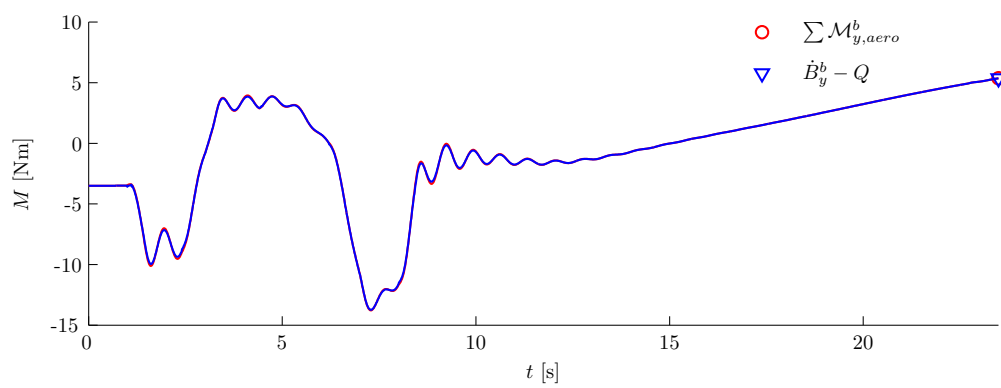
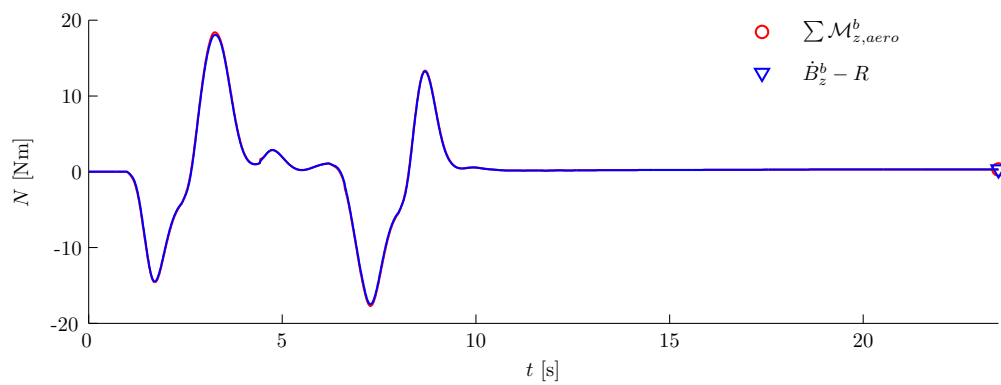
Figure 9-21b shows the kite at a roll angle of approximately -58 deg after 23 s. At this point the roll angle is increasing and the kite experiences some aerodynamic velocity from the negative Y_b -direction, resulting in a negative side slip angle β . When comparing figures 9-20a and 9-21b it can be noticed that the shape of the kite is a little bit skewed in figure 9-21b. This is a result of the side slip angle causing an increase of the aerodynamic forces on the right side and a decrease on the left side. These force differences give a resultant positive Y force as can be seen in figure 9-15.

Time derivative angular momentum and aerodynamic moments The verification of the time derivative of the angular momentum of the multi-body system is done by comparing the measurements with the resultant external moments. According to equation (6-2) the sum of the external moments must equal the time derivative of the angular momentum. This comparison gives also an indication of the error of the measurements for the angular momentum itself.

The verification is performed by transforming the quantities to the body-fixed reference frame. And, secondly, by subtracting the tether moments from the time derivative of the angular momentum:

$$\begin{aligned} L &= \sum \mathcal{M}_{x,aero}^b = \dot{B}_x^b - P \\ M &= \sum \mathcal{M}_{y,aero}^b = \dot{B}_y^b - Q \\ N &= \sum \mathcal{M}_{z,aero}^b = \dot{B}_z^b - R \end{aligned} \tag{9-49}$$

The result is given in figure 9-22. At first the graphs show a very good match. But looking more closely it can be seen that the extreme values of the sum of the aerodynamic moments are slightly higher in absolute sense. This difference can be clarified by the inaccuracy of the particle based method. On the other hand, the difference is quite small and therefore it can be said that the particle based method is a *very good approximation*.

(a) Aerodynamic moment about X_b (b) Aerodynamic moment about Y_b (c) Aerodynamic moment about Z_b **Figure 9-22:** Surf Kite simulation test, verification of aerodynamic moments

Review and final remarks

In this chapter a formal description is given for reducing the states of the Multi-Body Kite model to a set of rigid body states. Furthermore simulations are performed of a double pendulum model and the surf kite model for verification of the methodology and implementation in ADAMS. The states describing the rigid body motion are used for the aerodynamic model identification in chapter 10.

To conclude the following remarks are itemized:

- To ease the control input function description, the computation of vector and matrix operations and the output data handling the Multi-Body Kite model is implemented in SIMULINK in the form of co-simulation with ADAMS using ADAMS/Controls
- All functions and equations given in this chapter which are required to obtain the lumped parameters of the Multi-Body Kite model are programmed or automatically generated in a Surf Kite Assembly macro-file
- The verification of the implementation of the macro files and the method for obtaining the lumped parameters proves that the implementation and the method is excellent for the translational and very accurate for the rotational quantities of the rigid body states
- The state reduction methodology defines a very good basis for the aerodynamic model identification for the implementation in the Rigid Body model

Aerodynamic & Structural Model Identification

Chapter 9 describes the methodology for obtaining the rigid body states of a Multi-Body Kite system. Chapter 6 gives the derivation of the equations of motion of the Rigid Body Kite model. This chapter describes the model identification technique to derive functions for the aerodynamic model and structural model on parametric basis. Flight test simulations are performed of the Multi-Body Kite model described in chapter 9. Use is made of flight test techniques for aircraft from reference [23].

10-1 Theory of parameter identification

For the Rigid Body model the functions of the aerodynamic model are based on Taylor series. This is a proven method to describe the aerodynamic model of an aircraft. The aerodynamic model of the Rigid Body model is also given by Taylor series (see equation (7-5)). These functions can be restricted to the following form (reference [23]):

$$y(t_i) = \sum_{k=1}^r a_k \cdot x_k(t_i) + \varepsilon(t_i) \quad \text{for } i = 1 \dots n \quad (10-1)$$

where $y(t_i)$ is the aerodynamic force or moment coefficient at t_i , a_k the identifiable parameters and $x_k(t_i)$ the state and control variables. $\varepsilon(t_i)$ denotes modelling errors which describes everything not included. The modelling errors are not taken into account any further.

The variables $x_k(t_i)$ are independent and are called the observation variables. The observation variables are constructed by relations given in chapters 5 and 6 from the output variables of the ADAMS model. $y(t_i)$ is the dependent variable. The variable $y(t_i)$ results by dividing the measured aerodynamic forces and moments by the corresponding dimensional divisors representing the dynamic pressure. Both variables are assumed to be measured exactly from the ADAMS model. That is the measures are not subject to any bias or error.

The steps taken in the model identification process can be enumerated as:

1. Construct the kite state and control variables $x_k(t_i)$ from the ADAMS model output

2. Define on the knowledge at hand the aerodynamic model which describes the dependent variable $y(t_i)$
3. Identify and estimate the model parameters a_k for $t = t_1 \dots t_n$
4. Check the accuracy of the identified parameters
5. Repeat steps 2, 3 and 4 until no improvement can be obtained

Least squares estimate

The identification of the aerodynamic derivatives is done by a least squares estimate. MATLAB has a function `lsq` to apply the least squares estimate. This function computes additional to the identified parameters the standard errors of the parameters: σ_{a_k} , the mean squared error $\bar{\varepsilon}^2$ and an estimated covariance matrix S . Additionally the correlation matrix of the responses of the observation variables is computed. In short the least squares estimate computes the parameters a_k as described below (reference [23]).

Equation (10-1) can be written in more compact form by:

$$\mathbf{Y} = \mathbf{X} \cdot \mathbf{a} \quad (10-2)$$

where \mathbf{X} is the observation matrix given by:

$$\mathbf{X} = \begin{bmatrix} x_{1,1} & x_{2,1} & \cdot & \cdot & \cdot & x_{r,1} \\ x_{1,2} & x_{2,2} & \cdot & \cdot & \cdot & x_{r,2} \\ \cdot & \cdot & & & & \cdot \\ \cdot & \cdot & & & & \cdot \\ \cdot & \cdot & & & & \cdot \\ x_{1,n} & x_{2,n} & \cdot & \cdot & \cdot & x_{r,n} \end{bmatrix}$$

\mathbf{a} a vector with the identifiable parameters:

$$\mathbf{a} = \langle a_1, a_2, \dots, a_r \rangle$$

and \mathbf{Y} a vector with the dependent variables $y(t_i)$.

For a particular estimate of \mathbf{a} , $\hat{\mathbf{a}}$, the vector of residuals is defined as:

$$\mathbf{e} = \mathbf{Y} - \mathbf{X} \cdot \hat{\mathbf{a}} \quad (10-3)$$

The least squares estimate minimizes the squares of the residuals for $t = t_1 \dots t_n$. A minimum is found by setting the derivative with respect to $\hat{\mathbf{a}}$ to zero, which leads to the so called *normal equations*:

$$\hat{\mathbf{a}} = (\mathbf{X}^T \mathbf{X})^{-1} \mathbf{X}^T \mathbf{Y} \quad (10-4)$$

For a good estimate of \mathbf{a} the following conditions must hold:

- The time period as well as the discretization frequency of $t = t_1 \dots t_n$ must comply to a certain minimum
- The disturbance or input signal must have a certain power spectral density such that the most dominant frequency modes are excited
- There must be enough variation in the responses of the observation variables $x_k(t_i)$
- The dependency between the observation variables must be small

The first and second item make sure that amount of ‘information’ in \mathbf{X} is high. This means that the potential for a good estimate of $\hat{\mathbf{a}}$ is high. The third item makes sure that the influence of $x_k(t_i)$ on $y(t_i)$ is high enough and a_k can be fitted accurately. The fourth item comprises the influence of an observation variable on the parameter of another observation variable. The fourth item can be counteracted by defining cross terms of the Taylor expansion as an observation variable.

Input signals

The input signals, that is the disturbance on the system, influences the excitation of the specific modes that can be identified. One can think of all kind of inputs: step, doublet, 3211, frequency sweep and optimal inputs. The performance of the input signals can be represented by its power spectral density. Optimal inputs are optimized for a specific model and have a high power at the frequencies of interest. The most feasible input at hand is the 3211-input, because its power is distributed over a broad range of frequencies. The 3211-input signal is shown in figure 10-1. Reference [20] can be consulted for a comparison between the power spectral densities of different input signals.

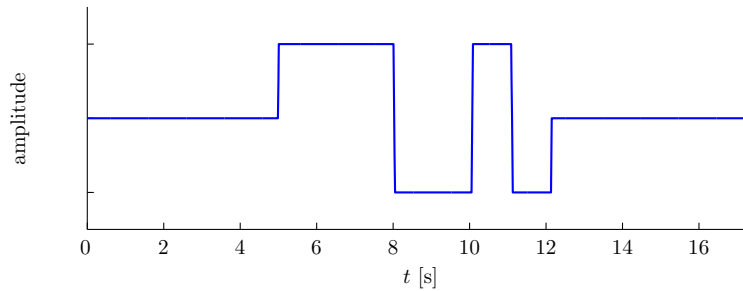


Figure 10-1: 3211-input signal

Initial condition

The initial condition for the test simulation for the identification of the aerodynamic parameters plays an important role. Not only will the values of the parameters or perhaps even the aerodynamic function differ from condition to condition, also the potential for an accurate fit of the aerodynamic function differs. A good starting point is to identify the aerodynamic functions around stationary dynamically stable conditions.

10-2 Aerodynamic model

The complete identification of the aerodynamic model of the ADAMS Kite model is potentially a tedious job and requires more advanced techniques than described here. Due to the complexity of the deformation, specific structural states need to be defined to take the effect of the structural modes into account. These states are not (yet) implemented in the Rigid Body Kite model. That is, there is no dynamic function to describe these states. From the final result of the model identification follows if this is a potential problem. The influence of the structural deformation on the responses is often a superposition on the ‘rigid body’ responses (reference [18]). The higher the effect of the structural modes on the aerodynamic forces and moments, the more the probability of an accurate fit degrades.

The dimensionless forces and moments are given by:

$$\begin{aligned}
 C_X(t_i) &= \frac{X(t_i)}{\frac{1}{2}\rho V_a(t_i)^2 S(t_i)} & C_l(t_i) &= \frac{L(t_i)}{\frac{1}{2}\rho V_a(t_i)^2 S(t_i) b(t_i)} \\
 C_Y(t_i) &= \frac{Y(t_i)}{\frac{1}{2}\rho V_a(t_i)^2 S(t_i)} & C_m(t_i) &= \frac{M(t_i)}{\frac{1}{2}\rho V_a(t_i)^2 S(t_i) \bar{c}(t_i)} \\
 C_Z(t_i) &= \frac{Z(t_i)}{\frac{1}{2}\rho V_a(t_i)^2 S(t_i)} & C_n(t_i) &= \frac{N(t_i)}{\frac{1}{2}\rho V_a(t_i)^2 S(t_i) b(t_i)}
 \end{aligned} \tag{10-5}$$

where the explicit time dependency of the variables V_a , \bar{c} , b and S is shown. In this way the dimensionless forces and moments are independent of the dynamic pressure and additionally any linear dependency on the variables \bar{c} , b and S is removed.

Model structure

The first step is to set up the *a priori model* as an initial guess for the model structure. In this case, this is based on the knowledge about the aerodynamic model in ADAMS. Chapter 3 showed that the aerodynamic forces and moment acting on each airfoil can be written as:

$$c_{x,j}, c_{z,j}, c_{m,j} \rightarrow f(\alpha_j, \zeta_j) \quad \text{for } j = 1 \dots n \quad (10-6)$$

where n is the number of airfoils and ζ_j a deformation vector containing the camber and airfoil thickness.

From equation (10-6) becomes clear that the resulting forces and moment on each airfoil j are only dependent on the *static* parameters α_j and ζ_j . This means that the local aerodynamic forces (distributed over the airfoil) at each time step are independent of the time derivative of these parameters and with that the time history.

This will not hold for the complete kite, as the lumped forces and moments C_X, C_Y, C_Z, C_l, C_m and C_n are dependent on all airfoils combined. And, therefore, on the complete shape of the kite. Not only on the static shape at each time step, but also on the shapes in the past due to the structural interference. Because the structural interference is unknown (yet), the *a priori model* is defined to be dependent of the local static variables.

Translating the local static variables to the overall body variables gives that the local angle of attack results in a dependency on the body rates p, q and r and the side slip angle β . And, of course, the control variables along the X -axis of the body-fixed reference frame x_{taL} and x_{taR} have a definite influence.

For the *a priori model* an additional assumption is made. The longitudinal and lateral forces and moments can be decoupled, that is the observation variables x_k describing the symmetric aerodynamic forces and moment have no influence on the asymmetric force and moments and vice versa. The *a priori model* is then given as:

$$\begin{aligned} C_X, C_Z, C_m &\rightarrow f\left(\alpha, \frac{q\bar{c}}{V_a}, \frac{x_{ta}}{\bar{c}}\right) \\ C_Y, C_l, C_n &\rightarrow f\left(\beta, \frac{pb}{2V_a}, \frac{rb}{2V_a}, \frac{x_{taL}}{b}, \frac{x_{taR}}{b}\right) \end{aligned} \quad (10-7)$$

where the states are made dimensionless by the time dependent variables V_a, \bar{c} and b .

The second step is to define the set of so called *candidate variables*, which will be added to the model consequently one after the other. The full set of candidate variables is given by the time derivatives, higher order terms, cross terms of the variables given in equation (10-7) as well as deformation states represented by the vector $\zeta(\cdot)$. The deformation states for the complete body still have to be determined except for \bar{c}, b and S . Note that (\cdot) defines the complete Taylor series backwards in time. The deformation states are restricted here to $\bar{c}(\cdot), b(\cdot)$ and $S(\cdot)$.

It is not necessarily that once a variable is added to the model it cannot be removed from the model. Because it is possible that a variable improves the fit, but can worsen the fit once other variables are added (reference [23]).

Note that in ADAMS almost any state variable of the multi-body kite model can be measured. This includes the lumped translational and rotational variables as well as any deformation state. For the aerodynamic model of Rigid Body only those state variables can be taken into account which are available from the Rigid Body model equations.

Initial conditions domain

The domain of the initial conditions defines greatly the validity domain of the obtained model. In ADAMS the initial condition is set by defining the parameters $W_{x,0}, d_{taL,0}$ and $d_{taR,0}$. For the

aerodynamic model these variables transform to $V_{a,0}$, $x_{taL,0}$ and $x_{taR,0}$. The boundaries for $V_{a,0}$ are given by the minimum velocity to keep the kite in the air and the maximum velocity for which no buckling of the tubes exists. The boundaries of the control positions are given by the most forward position along the rail and the most backward position for which still a statically stable condition is found. The domain is discretized to specific number of initial conditions. For each initial condition a *flight test simulation* is performed to obtain the corresponding aerodynamic functions.

A stationary dynamically stable condition is achieved by specifying a constant wind speed W_x and a symmetric initial condition for the control positions d_{taL} and d_{taR} . After the stabilization phase of 15 s the kite is assumed to be at a stable zenith position, that is the acceleration terms are damped to practically zero. At first this might not seem a condition which is often encountered for a kite in motion or even flying a figure of eight and therefore does not give much information for the full flight domain. But this is not entirely true, because the aerodynamic forces and moments are a reaction on the aerodynamic velocity (local velocities for the body rates) and attitude conditions and not on the kinematic conditions. In other words the kite does not ‘know’ whether the wind velocity or the velocity with respect to ground is the cause for the resulting aerodynamic velocity. Although, for the static conditions the question rises if dynamically or at least statically stable conditions can be found for the full domain of the angle of attack α and side slip angle β .

Furthermore, the minimum and maximum values of the observation variables define the validity region of the aerodynamic function. If a test simulation is performed from a statically stable condition and the fitting of the aerodynamic function is successful then the aerodynamic parameters are only a function of the initial condition and are valid for the region span by the observation variables. Now, if the aerodynamic functions are identified for multiple initial conditions the domain of the aerodynamic model is increased.

Finally, an additional assumption is made: the aerodynamic model structure is the same for all initial conditions. This is done to restrict the time consuming process of improving the fit to the very detail for every flight test simulation.

Control input

An additional complexity is given by the fact that the controls have mass. A change of the control positions causes a relative large shift of the center of gravity with respect to the body. This induces additional nonlinearities and restricts the amplitude of the control input to relative small values for the flight test simulations.

An example of the input curve, which is representative for most flight test simulations, is shown in figure 10-2. Figure 10-2a shows again the 3211-input curve. The curve has a slope towards the extreme values of the amplitude to avoid discontinuity in the signal as ADAMS can potentially crash. After the 3211-input, the d_{ta} is kept at the initial condition for 5 s to increase the information in the observation matrix \mathbf{X} .

Figure 10-2b illustrates the response curve of the cart position with respect to the center of gravity. Based on this curve a formula is found to *convert* the control input d_{ta} to x_{ta} . The relation is given in equation (10-8):

$$\begin{aligned} x_{taL} &= x_{taL,0} - \frac{2 \cdot m_c}{m - m_c} \cdot (d_{taL} - d_{taL,0}) - 0.1 \cdot \dot{x}_{taL} \\ x_{taR} &= x_{taR,0} - \frac{2 \cdot m_c}{m - m_c} \cdot (d_{taR} - d_{taR,0}) - 0.1 \cdot \dot{x}_{taR} \end{aligned} \quad (10-8)$$

where m is the mass of the complete system, m_c is the mass of one control unit and the value 0.1 has been found to improve the fit. The equations are also valid for the symmetric input d_{ta} to describe x_{ta} .

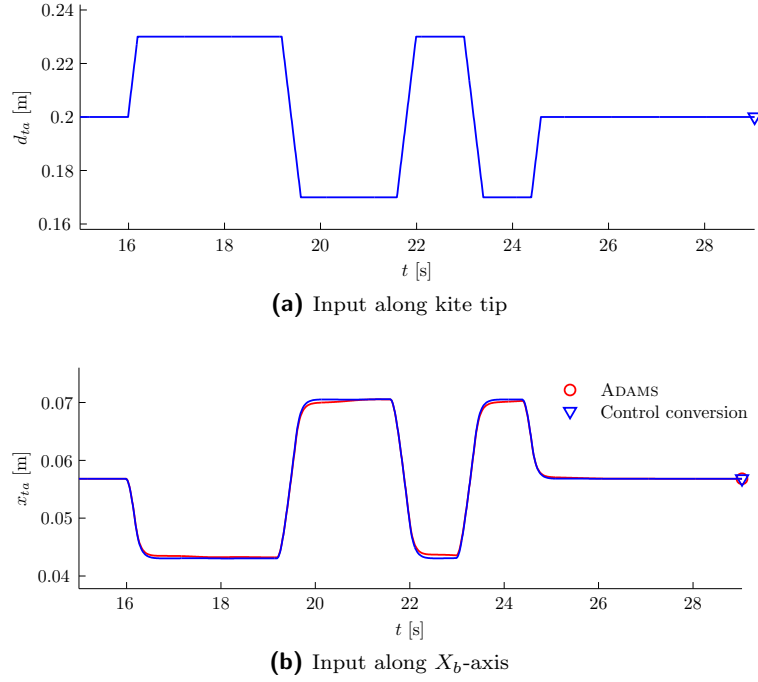


Figure 10-2: 3211-input with $W_{x,0} = -8$ m/s and $d_{ta,0} = 0.20$ m

Significance criterion

The probability of the accuracy of the fitted parameters can be explored to the very detail (see for example reference [23]). The analysis gives information on the significance of a parameter and how to improve the fit.

Here, the analysis is restricted to the standard deviation of the identified parameter σ_{a_k} . It is assumed that the parameters a_k are independent and normally distributed, so:

$$a_k \sim \mathcal{N}(\hat{a}_k, \sigma_{a_k}^2) \quad \text{for all } k \quad (10-9)$$

The probability for a good fit is defined when the following criterion is met:

$$\frac{|a_k|}{2\sigma_{a_k}} > 5.0 \quad (10-10)$$

which defines that the value of the fitted parameter is between $0.8a_k$ and $1.2a_k$ with a probability of approximately 0.95.

Now, an iterative process can be started where subsequently observation variables are removed and added to the model structures based on the significance criterion until no improvement is found.

Symmetric forces and moment

For the longitudinal forces and moment the following model structure is found:

$$\begin{aligned} C_X &= C_{X_0} + C_{X_\alpha} \cdot \alpha + C_{X_{x_{ta}}} \cdot \frac{x_{ta} - x_{d_{ta}=0}}{\bar{c}} \\ C_Z &= C_{Z_0} + C_{Z_\alpha} \cdot \alpha + C_{Z_q} \cdot \frac{q\bar{c}}{V_a} + C_{Z_{x_{ta}}} \cdot \frac{x_{ta} - x_{d_{ta}=0}}{\bar{c}} \\ C_m &= C_{m_0} + C_{m_\alpha} \cdot \alpha + C_{m_q} \cdot \frac{q\bar{c}}{V_a} + C_{m_{x_{ta}}} \cdot \frac{x_{ta} - x_{d_{ta}=0}}{\bar{c}} \end{aligned} \quad (10-11)$$

where all aerodynamic derivatives are dependent on the static variables by V_a and x_{ta} and $x_{d_{ta}=0}$ is x_{ta} at $d_{ta} = 0$.

It is found that more variables have a significant influence on the aerodynamic forces and moment. These states include $\dot{\alpha}$, \dot{q} , \dot{x}_{ta} and S . The values of the parameters corresponding to $\dot{\alpha}$ and \dot{q} appeared to be positive for most part of the initial conditions domain. This does not constitute to a physical meaning. The contributions of these time derivatives should govern damping in the model and must therefore be negative. On this basis the model structure is kept limited to the dependence shown in equation (10-11).

The flight test simulations are performed for all possible 48 combinations of the initial conditions given in table 10-1. All simulations are fed with the 3211-input signal with an amplitude of 0.03 m on d_{ta} . This amplitude value is based on a compromise such that there is a little overlap between the amplitude of the initial conditions, but not too high to reduce the shift of the center of gravity. A higher amplitude increases the amount of information in the variable responses, but is less linear. A lower amplitude decreases the information, but is more linear.

	min	max	step	#
W_x [m/s]	-22	-8	2	8
d_{ta} [m]	-0.05	0.20	0.05	6

Table 10-1: Initial conditions for the symmetric simulations

The relation between α_0 , V_a and x_{ta} is illustrated in figure 10-3. α_0 is in this case α at $t = 0$ s. The 48 data points are linearly interpolated such that the trend is more clear. Note that x_{ta} decreases towards the trailing edge. The first thing that is noticed is that the range of α_0 is rather low. But the most important conclusion that can be deduced is that the control of α with control displacement is rather poor. For lower velocities the angle of attack can be increased a little to approximately 11 deg, but for higher velocities the angle of attack even decreases with control input.

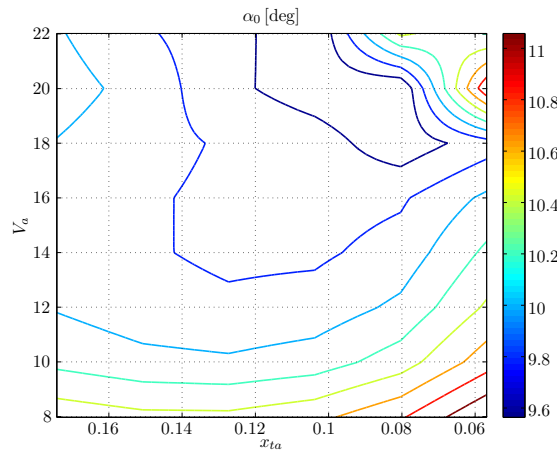


Figure 10-3: α_0 as a function of V_a and x_{ta}

In the following three simulations results are analyzed for the fitting of the forces and moment curves X , Z and M . Two extreme conditions will be analyzed with an initial wind velocity of -8 m/s and -22 m/s respectively and an initial control position of $d_{ta} = 0.20$ m. And thirdly one more central in the initial conditions domain of $W_{x,0} = -14$ m/s and $d_{ta} = 0.05$ m. The first one is shown in figure 10-4, the latter two in appendix B in figures B-1 and B-2.

To analyze the resulted values for a_k in more detail, σ_{a_k} and $|a_k|/(2\sigma_{a_k})$ for the fitted force curve M are given in table 10-2. The parameters which did not satisfy the criterion are highlighted in light gray.

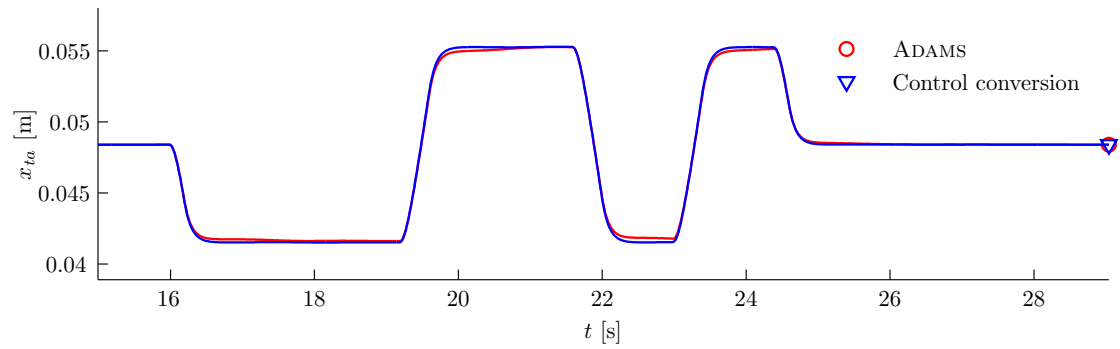
	C_{m_0}	C_{m_α}	C_{m_q}	$C_{m_{x_{ta}}}$
a_k	0.126	-0.733	-0.058	0.107
$ a_k /(2\sigma_{a_k})$	53.7	49.6	4.89	9.76

Table 10-2: Fitted parameters and significance criterion for M at $W_{x,0} = -8$ m/s and $d_{ta,0} = 0.20$ m

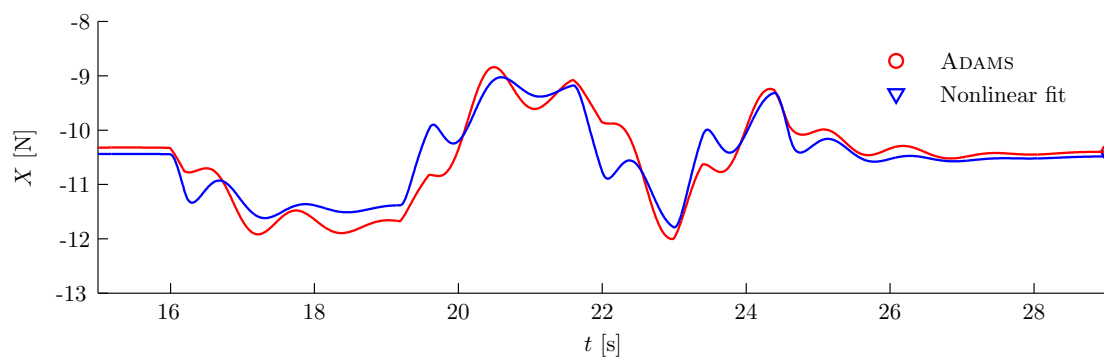
The fact that the significance of the value for C_{m_q} is low can have several causes. A cause can be that the dependency of $\frac{q\bar{c}}{V_a}$ on C_m is indeed low. Another cause can be that the responses have *data collinearity*. Data collinearity means that there is a high correlation between the responses of the observation variables. Collinearity problems are more a data problem rather than a statistical problem (reference [23]). Collinearity can be decreased or removed by choosing different input signals. The computed correlation matrix reveals that the correlation coefficient of α and $\frac{x_{ta}}{c}$ is -0.862 , which is high. This is a plausible cause for the decreased significance of C_{m_q} .

The fitted and ADAMS measured force and moment curves in figures 10-4 and B-1 have a reasonable to good match, especially for the curves of Z and M . The fitted and ADAMS measured force and moment curves in figure B-2 do not have a bad match, but is worse than the other two. Figure B-2a suggests that some other phenomenon plays a role as the control conversion formula is not quite valid. The cause are the internal forces, which have exceeded the structural limits as will be shown in section 10-3.

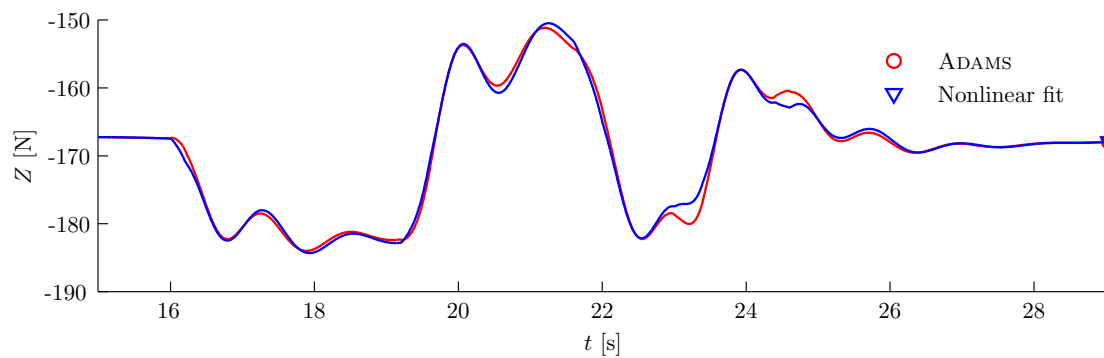
Furthermore the figures show that there is one dominant slow damped periodic mode. It is clearly visible that the frequency of this mode increases with $W_{x,0}$ and the damping decreases with $W_{x,0}$.



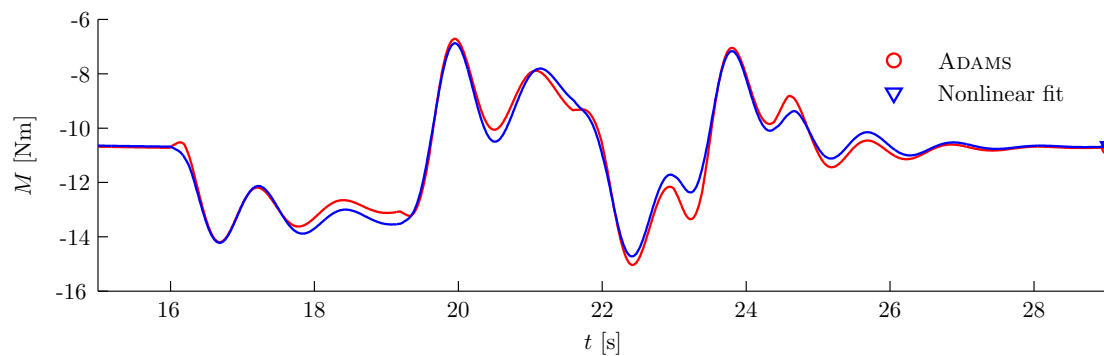
(a) Input along X_b -axis



(b) Force curve along X_b -axis



(c) Force curve along Z_b -axis



(d) Moment curve about Y_b -axis

Figure 10-4: Simulated and fitted symmetric forces and moment curves at $W_{x,0} = -8$ m/s and $d_{ta,0} = 0.20$ m

Asymmetric force and moments

The determination of the lateral force and moment functions have additional complexity compared to the longitudinal case. The initial condition is at least dependent on three variables instead of two, namely $V_{a,0}$, $x_{taL,0}$ and $x_{taR,0}$. When assuming that the initial condition for the asymmetric derivatives is only dependent of these three variables means that β_0 is given implicitly, just like the relation between the initial condition and α_0 for the symmetric case. Due to the three dimensional dependency of the asymmetric aerodynamic derivatives the amount of flight test simulations to determine them is increased. Referring to the symmetric case would imply that the amount of simulations increases six times. Another problem is that no statically stable initial conditions can be found for asymmetric positions of the controls. A solution is to find Taylor series which are valid for a larger domain.

The identification of the complete asymmetric model requires more research, therefore the determination of the parameters for the asymmetric model is restricted to symmetric initial conditions. This possibly constitutes a decrease of the validity of the model for more extreme asymmetric control positions. The model structure found for the asymmetric aerodynamic force and moments is given in equation (10-12). The initial conditions for which the parameters are determined are shown in table 10-3.

$$\begin{aligned}
 C_Y &= C_{Y_\beta} \cdot \beta + C_{Y_{\dot{\beta}}} \cdot \dot{\beta} + C_{Y_r} \cdot \frac{rb}{2V_a} + C_{Y_{x_{taL}}} \cdot \frac{x_{taL} - x_{d_{taL}=0}}{b} + C_{Y_{x_{taR}}} \cdot \frac{x_{taR} - x_{d_{taR}=0}}{b} \\
 C_l &= C_{l_\beta} \cdot \beta + C_{l_r} \cdot \frac{rb}{2V_a} + C_{l_{x_{taL}}} \cdot \frac{x_{taL} - x_{d_{taL}=0}}{b} + C_{l_{x_{taR}}} \cdot \frac{x_{taR} - x_{d_{taR}=0}}{b} \\
 C_n &= C_{n_\beta} \cdot \beta + C_{n_r} \cdot \frac{rb}{2V_a} + C_{n_{x_{taL}}} \cdot \frac{x_{taL} - x_{d_{taL}=0}}{b} + C_{n_{x_{taR}}} \cdot \frac{x_{taR} - x_{d_{taR}=0}}{b}
 \end{aligned} \tag{10-12}$$

where again all aerodynamic derivatives are dependent on the static variables V_a and x_{ta} . The derivatives with respect to the left and right control position have the same absolute values but are opposite in sign.

Also for the asymmetric force and moments is found that other variables play a role in the constitution of the model structure. Probably, this includes time derivatives and higher order terms of the variables shown in equation (10-12). Due to collinearity of the responses of the observation variables the significance of the estimated parameters is decreased and their contribution could not be taken into account.

	min	max	step	#
W_x [m/s]	-18	-8	2	6
d_{ta} [m]	0.00	0.25	0.05	6

Table 10-3: Initial conditions for the asymmetric simulations

The input of the asymmetric simulations is altered compared to the 3211-input for the symmetric simulations. The input signal is applied only to the left control d_{taL} . Furthermore the first block of 3 time units of the 3211-input possibly causes the kite to move away from the initial condition in such a way that the kite crosses the $X_E Y_E$ -plane even before the input signal has finished. Therefore a 1321-input is chosen such that the kite stays closer to the initial condition. Additionally a time factor of 0.5 is applied to the complete input signal. The amplitude of the input is set to 0.05 m. See figure 10-5.

Again the results of three flight test simulations are analyzed. The initial conditions of the three simulations are two extreme conditions at $W_{x,0} = -8$ m/s and $W_{x,0} = -18$ m/s with $d_{ta,0} = 0.25$ m and one at $W_{x,0} = -14$ m/s and $d_{ta,0} = 0.05$ m, see figures B-3, 10-6 and B-4. The fit of the

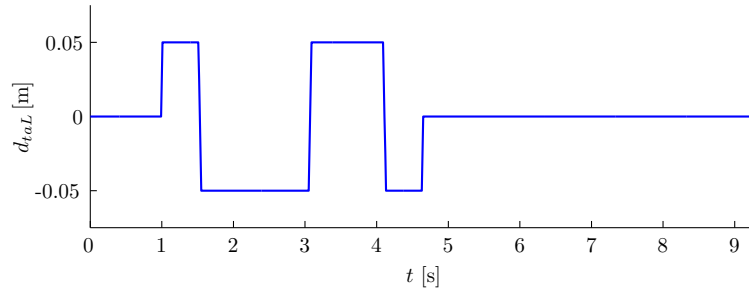


Figure 10-5: 1321-input signal on d_{taL}

asymmetric force and moment curves is reasonably accurate, but less than for the symmetric case. Especially the fit for the yaw moment N follows the ADAMS measurement closely. Note that the control conversion relation is less accurate as well.

The simulation shown in figure B-3 reveals that a critically damped oscillation is excited just after the control input has returned to the initial condition. Adding additional variables improves the fit, but did not add any significance. This means that either additional candidate variables need to be found or the input signal should be altered or both.

For initial conditions at and above $W_{x,0} = -10$ m/s the critically damped oscillation is almost or completely gone as can be seen in figure 10-6. The curves suggest that the found model structure is quite accurate, but also indicate that improvement is possible for the moment L . The derivatives which did not fulfill the significance criterion for this flight test simulation is $C_{l_{x_{taL}}}$ with a $|a_k|/(2\sigma_{a_k})$ of 2.89.

	C_{l_β}	C_{l_r}	$C_{l_{x_{taL}}}$	$C_{l_{x_{taR}}}$
a_k	-0.0120	-0.0201	0.0094	-0.0101
$ a_k /(2\sigma_{a_k})$	20.7	44.0	2.89	3.09

Table 10-4: Fitted parameters and significance criterion for L at $W_{x,0} = -14$ m/s and $d_{ta,0} = 0.05$ m

The third example, figure B-4, illustrates that when the kite moves away from the initial condition the fit does not completely follow the ADAMS measured force and moments as can be seen from the steep curve at the end of the flight test simulation. Although it is found that the time derivative of the yaw rate \dot{r} improves the fit of N drastically.

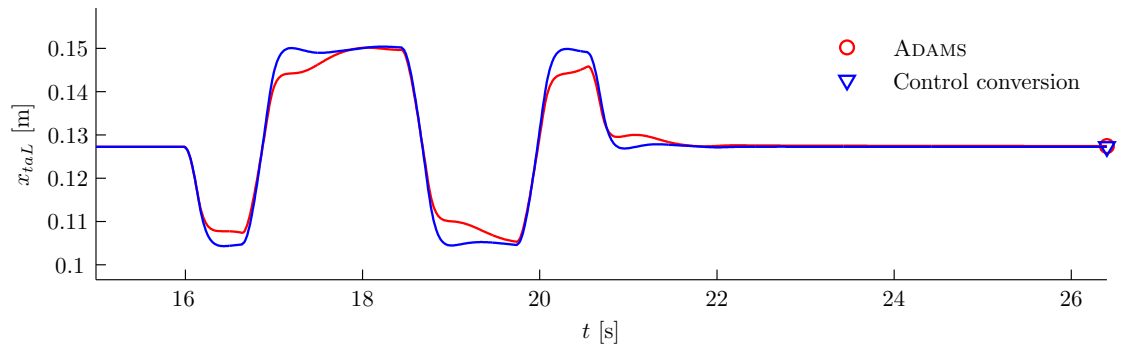
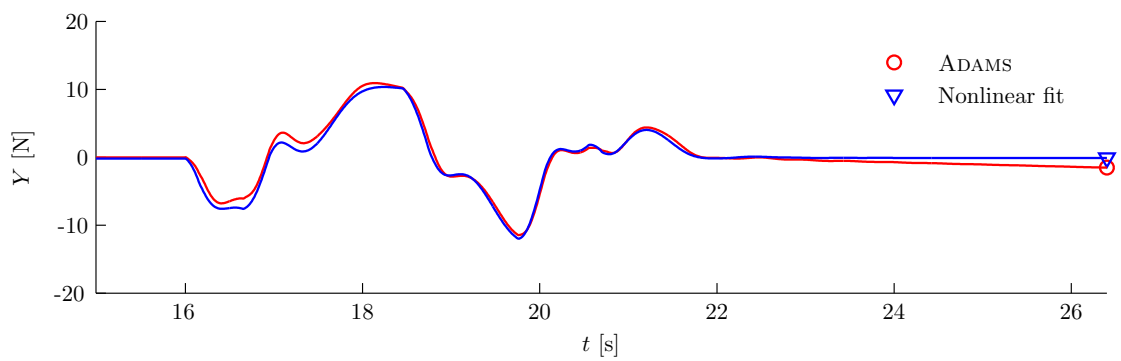
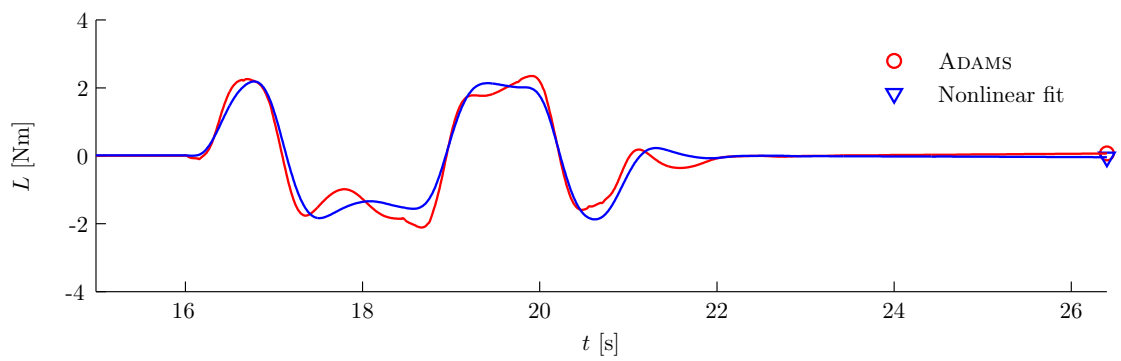
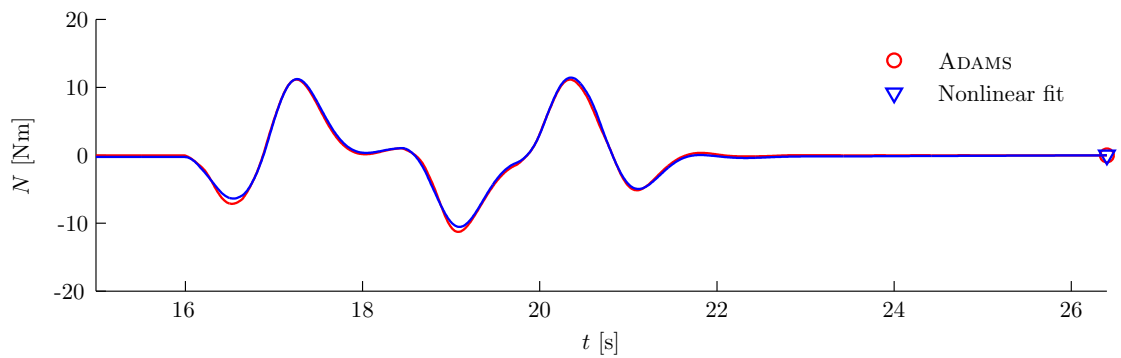
(a) Left input along X_b -axis(b) Force curve along Y_b -axis(c) Moment curve about X_b -axis(d) Moment curve about Z_b -axis

Figure 10-6: Simulated and fitted asymmetric force and moments curves at $W_{x,0} = -14$ m/s and $d_{ta,0} = 0.05$ m
Modelling the Dynamics of an Arc-shaped Kite for Control Law Design

The values of the symmetric and asymmetric aerodynamic derivatives as well as the statistical significance as a function of the initial conditions given by $V_{a,0}$ and $x_{ta,0}$ are shown in appendix C.

10-3 Inertia tensor & structural properties

As the aerodynamic derivatives vary as a function of the initial condition the variation of the moments and products of inertia, mean aerodynamic chord, projected surface area and wing span are also a function of the initial condition. Actually the variation of these properties are dynamic like the variation of the aerodynamic forces and moments. The analysis here is restricted to find a relation of the inertia tensor and structural properties as a function of the initial condition. In this way it is possible to incorporate the inertia tensor and the structural properties on a *quasi static* basis.

Inertia tensor

As the test simulations are performed for only symmetric initial conditions the moments and products of inertia can only be determined as a function of the symmetric initial variables $V_{a,0}$ and $x_{ta,0}$.

In the same sense as the aerodynamic forces and moments are made dimensionless in flight dynamics theory the moments and products of inertia can be made dimensionless. The relations are given in equations (10-13):

$$\begin{aligned}\mu_c K_X^2 &= \frac{I_{xx,0}}{\rho S_0 b_0^3} & \mu_c K_{XY} &= \frac{J_{xy,0}}{\rho S_0 b_0^3} \\ \mu_c K_Y^2 &= \frac{I_{yy,0}}{\rho S_0 c_0^3} & \mu_c K_{YZ} &= \frac{J_{yz,0}}{\rho S_0 b_0^3} \\ \mu_c K_Z^2 &= \frac{I_{zz,0}}{\rho S_0 b_0^3} & \mu_c K_{ZX} &= \frac{J_{zx,0}}{\rho S_0 b_0^3}\end{aligned}\quad (10-13)$$

where μ_c is the dimensionless mass:

$$\mu_c = \frac{m}{\rho S_0 \bar{c}_0}$$

The measured moments and products of inertia in ADAMS are particle based as discussed in section 9-2-3. From the translation theorem can be deduced that the error made by the particle based method is the sum of the moments and products of inertia of each body about its own center of mass. Table A-5 gives an indication of the order of magnitude of the error. The error is variable and depends on the orientation of each individual body. Since all bodies are connected and the error is rather small a constant correction factor is proposed. In ADAMS the actual inertia tensor can be measured with the `Aggregate Mass...` function and compared to the particle based measurement. The difference at $W_{x,0} = -12$ m/s is:

$$\mathbb{I}_{sl} = \begin{bmatrix} 0.625 & 0 & -0.685 \\ 0 & 0.715 & 0 \\ -0.685 & 0 & 0.622 \end{bmatrix}\quad (10-14)$$

which is added to the particle based values to obtain the estimate for the inertia tensor.

It appears that the moments and products of inertia can be described by a quadratic relation as a function of $x_{ta,0}$ where the parameters are a function of only $V_{a,0}$:

$$K = K_{0.15}(V_{a,0}) + K_{x_{ta,0}}(V_{a,0}) \cdot \frac{x_{ta,0} - 0.15}{\bar{c}} + K_{x_{ta}^2}(V_{a,0}) \cdot \frac{(x_{ta,0} - 0.15)^2}{\bar{c}^2}\quad (10-15)$$

where $x_{ta} = 0.15$ is equal to $d_{ta} = 0.0$.

In this way functions are derived for the moments and products of inertia on a quasi static basis described by dimensionless parameters. The model can be included in the Rigid Body Kite model using a lookup table.

Structural properties

The mean aerodynamic chord, wing span and projected surface area can be described by a quadratic relation as well. Opposite to the function for the inertia tensor the function is not made dimensionless, because there is no divisor for \bar{c} and b . The equations are:

$$\begin{aligned}\bar{c}_0 &= \bar{c}_{0.15}(V_{a,0}) + \bar{c}_{x_{ta,0}}(V_{a,0}) \cdot \frac{x_{ta,0} - 0.15}{\bar{c}} + \bar{c}_{x_{ta}^2}(V_{a,0}) \cdot \frac{(x_{ta,0} - 0.15)^2}{\bar{c}^2} \\ b_0 &= b_{0.15}(V_{a,0}) + b_{x_{ta,0}}(V_{a,0}) \cdot \frac{x_{ta,0} - 0.15}{\bar{c}} + b_{x_{ta}^2}(V_{a,0}) \cdot \frac{(x_{ta,0} - 0.15)^2}{\bar{c}^2} \\ S_0 &= \bar{c}_0 \cdot b_0\end{aligned}\quad (10-16)$$

The image plots for the dimensional values of the moments and product of inertia the structural properties \bar{c}_0 , b_0 and S_0 are shown in appendix D. The values of J_{xy} and J_{yz} are zero due to the symmetric initial conditions. The tether attachment points in Y_b and Z_b direction can also be given as a function of $V_{a,0}$ and $x_{ta,0}$. The corresponding image plots are also given in appendix D, where the position in Y_b -direction is given as $2 \cdot y_{taR,0}$.

For higher velocities it is expected that the wing span will decrease due to a higher tension in the tether. And consequently causes I_{xx} to decrease as well and I_{yy} to increase. As can be seen from the figures this holds only for control positions close to the leading edge. When the controls are displaced more towards the trailing edge the wing span, I_{xx} and I_{yy} become approximately invariable with the aerodynamic velocity. A rearward displacement of the controls causes the trailing edge of the rails to bend inwards due to the weight of the controls. This results in an increased local angle of attack, which increases the sideways force and causes the wing span to increase. The image plot of the mean aerodynamic chord, figure D-2a, shows a sudden decrease at the top right corner. This is explained by the fact that the chord tubes have buckled. This potentially clarifies the less accurate fit at $W_{x,0} = -22$ m/s in figure B-2. The increased angle of attack at the tips and the buckled tubes is shown in figure 10-7.

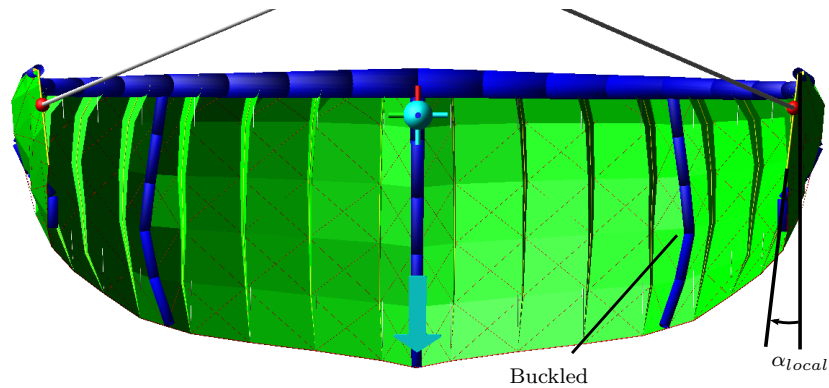


Figure 10-7: Bottom view of ADAMS Kite model at $V_{a,0} = 22$ m/s and $x_{ta,0} = 0.06$ m

Review and remarks

Parameter identification techniques are used to find a model based on Taylor series for the aerodynamic forces and moments expressed in the body-fixed reference frame. It is shown that this

results in functions depending on aerodynamic and structural variables and respective aerodynamic derivatives. The aerodynamic variables are constructed from the rigid body states of the reduced Multi-Body model. The aerodynamic derivatives are a function of the static variables V_a and x_{ta} . The initial angle of attack at $t = 0$ s is implicitly given by these two variables.

The following assumptions are made regarding the aerodynamic model:

- The symmetric and asymmetric aerodynamic forces and moments are decoupled
- The variables in the model functions have an independent contribution to the forces and moments
- The model structures for the symmetric and asymmetric forces and moments are valid for all symmetric conditions of V_a and x_{ta} within the specified domain
- The structural deformation variables are only given by \bar{c} , b and S

All effects which are not taken into account contribute to modelling errors. The aerodynamic model structure found is given in equations (10-11) and (10-12). Several resulting fits are discussed and show reasonable to good results. It is found that other variables have a contribution on the aerodynamic forces and moments, like time derivatives, quadratic terms and structural deformation. Due to data collinearity meaning high correlation coefficients these contributions are not taken into account. It is shown that data collinearity can give a low statistical significance of the estimated parameters. It is proven that time derivative and higher order contributions are a result of the flexible structure. Every state which is not in the a priori model is a result of the flexible structure.

The amplitude of the input signal of the flight test simulations defines the excitation of the observation variables and the validity domain of the model. Especially for the static variables α and β . Figure 10-3 shows that the range of α achieved by the control system is low.

To conclude it is recommended to perform more detailed research on the identification of the aerodynamic models. This comprises redesign of the input signals, increase the set of candidate variables and an extension of the validity domain.

Validation Rigid Body Kite Model

The identified aerodynamic model of chapter 10 is implemented in the Rigid Body Kite model. A validation simulation is performed by comparing the responses with the responses of the Multi-Body Kite model.

The symmetric aerodynamic forces and moment are identified with a 3211-input curve. To demonstrate the effectiveness of the identification, the Multi-Body model and Rigid Body model are simulated subject to another input curve. The resulted input curve on x_{ta} is shown in figure 11-1. The initial condition is $W_{x,0} = -12$ m/s and $d_{ta,0} = 0.0$ m.

Figures 11-2 to 11-6 show the response curves of the kinematic velocities u_k and w_k , the pitch angle θ , the pitch rate q and tether zenith angle θ_t . The position and orientation response curves illustrate a good comparison. It is clear that the damping of the rigid body model is less. The pitch angle θ damps out more slowly in the Rigid Body response curve. The pitch rate q response curve shows this even more clearly.

The eigenvalues of the symmetric periodic eigenmotions corresponding to the Rigid Body model at the initial condition $W_{x,0} = -12$ m/s and $d_{ta,0} = 0.0$ m are:

$$\begin{aligned}\lambda_{1,2} &= -0.320 \pm 8.880 i \\ \lambda_{3,4} &= -0.395 \pm 0.871 i\end{aligned}$$

where the $\lambda_{1,2}$ corresponds to the short period oscillating motion of 1.41 Hz and $\lambda_{3,4}$ to the low frequent pendulum motion of 0.152 Hz. The short period eigenmotion is visible in the response curve of the pitch rate q and the pendulum motion in the other response curves.

Choosing another initial condition at $W_{x,0} = -12$ m/s and $d_{ta,0} = 0.20$ m where the cart position is moved more towards the trailing edge results in the following eigenvalues for the symmetric oscillating modes:

$$\begin{aligned}\lambda_{1,2} &= 0.101 \pm 8.179 i \\ \lambda_{3,4} &= -0.431 \pm 0.962 i\end{aligned}$$

from which becomes clear that the short period motion has become unstable. For other wind velocity conditions the same phenomenon is verified.

So, the less damped short period oscillating motion of the Rigid Body model compared to the Multi-Body model becomes unstable for control positions more towards the trailing edge. This analysis shows that a damping contribution has been lost in the aerodynamic model identification process. When the cart is moved towards the trailing edge the kite tips bend inwards. This

deformation can be a cause for the decreased effectiveness of the model identification. It can be concluded that the application of the symmetric aerodynamic model identified in chapter 10 is limited. Also for the asymmetric motions unstable solutions are found. One cause is data collinearity representing high correlation coefficients of the responses of the observation variables. It is concluded that the identification of the aerodynamic models requires more research.

This should constitute a structural modal analysis, specification of deformation states to increase the set of candidate variables for the aerodynamic model identification and an advanced model identification technique. The latter comprises redesigned inputs and advanced estimation techniques, like weighted least squares or maximum likelihood estimation.

The simulation time of the shown simulation does prove that the reduction process is possible. The simulation time for simulating the approximately 27 s takes with the ADAMS model more than 300 s whereas the Rigid Body needs less than 3 s. The rigid body simulation is almost ten times faster than real-time, whereas the ADAMS model is ten times slower than real-time.

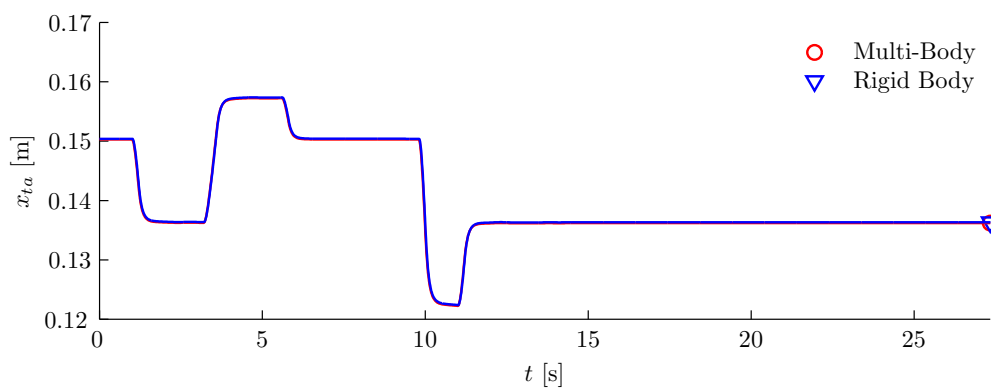


Figure 11-1: Multi-Body and Rigid Body, x_{ta} input curve at $W_{x,0} = -12$ m/s and $d_{ta,0} = 0.0$ m

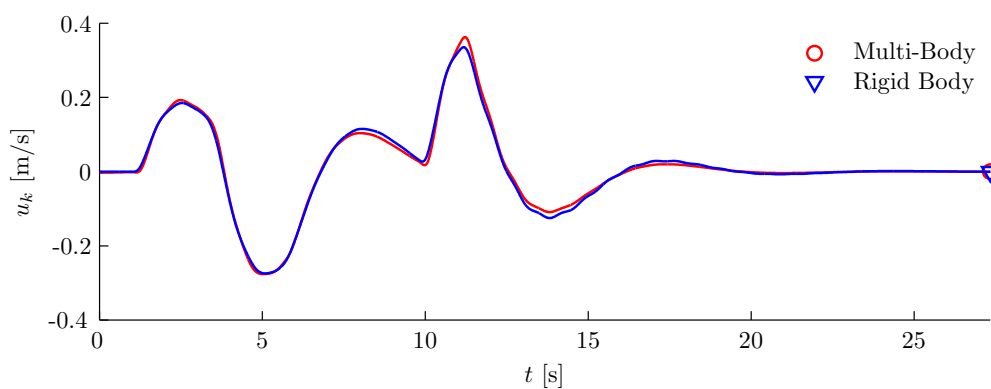


Figure 11-2: Multi-Body and Rigid Body, u_k response curve at $W_{x,0} = -12$ m/s and $d_{ta,0} = 0.0$ m

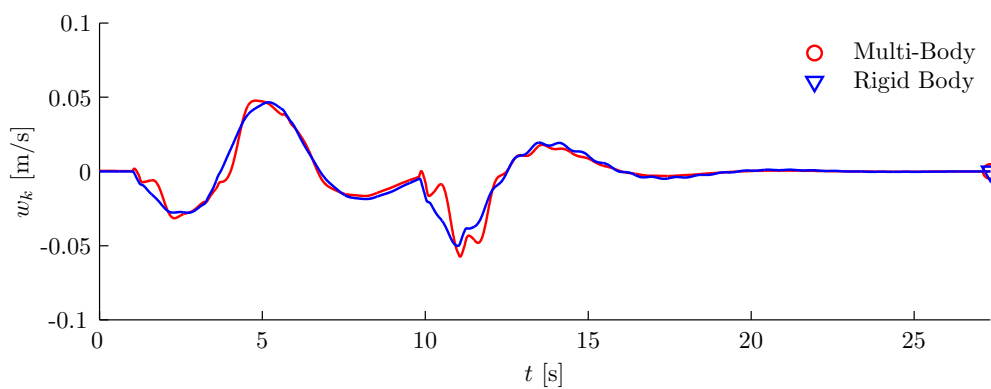


Figure 11-3: Multi-Body and Rigid Body, w_k response curve at $W_{x,0} = -12$ m/s and $d_{ta,0} = 0.0$ m

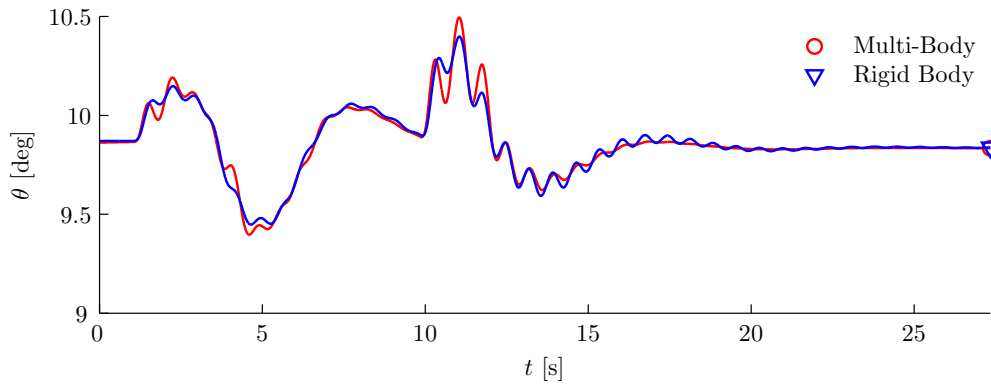


Figure 11-4: Multi-Body and Rigid Body, pitch angle response curve at $W_{x,0} = -12$ m/s and $d_{ta,0} = 0.0$ m

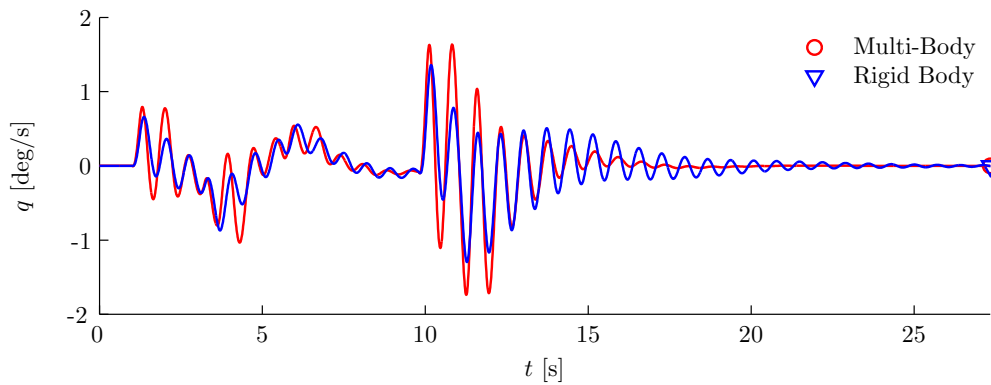


Figure 11-5: Multi-Body and Rigid Body, pitch rate response curve at $W_{x,0} = -12$ m/s and $d_{ta,0} = 0.0$ m

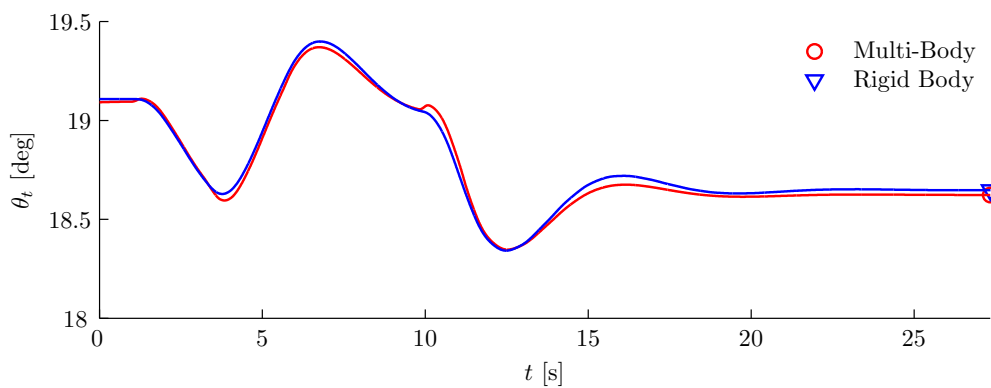


Figure 11-6: Multi-Body and Rigid Body, tether zenith angle response curve at $W_{x,0} = -12$ m/s and $d_{ta,0} = 0.0$ m

Conclusions & Recommendations

A formal methodology is developed to reduce the complex Multi-Body arc-shaped kite model to a rigid body arc-shaped kite model. In more general terms: the methodology presented here allows for any flying object modelled with multi-bodies to be reduced to a set of states describing the motion as a rigid body.

The multi-body reduction process developed is shown in figure 12-1, where U comprises the wind and controller input along the kite tip, Y_{mb} the output of the multi-body system, X_{red} the reduced state vector, X_{val} the state vector of the validation model and ε the error between the reduced model and the Multi-Body model. The error is fed back to the input to optimize the input and the model identification. X_{red} consists of translation and rotational quantities, the inertia tensor, the sum of aerodynamic forces and moments, the tether forces and the control input defined in the body-fixed reference frame.

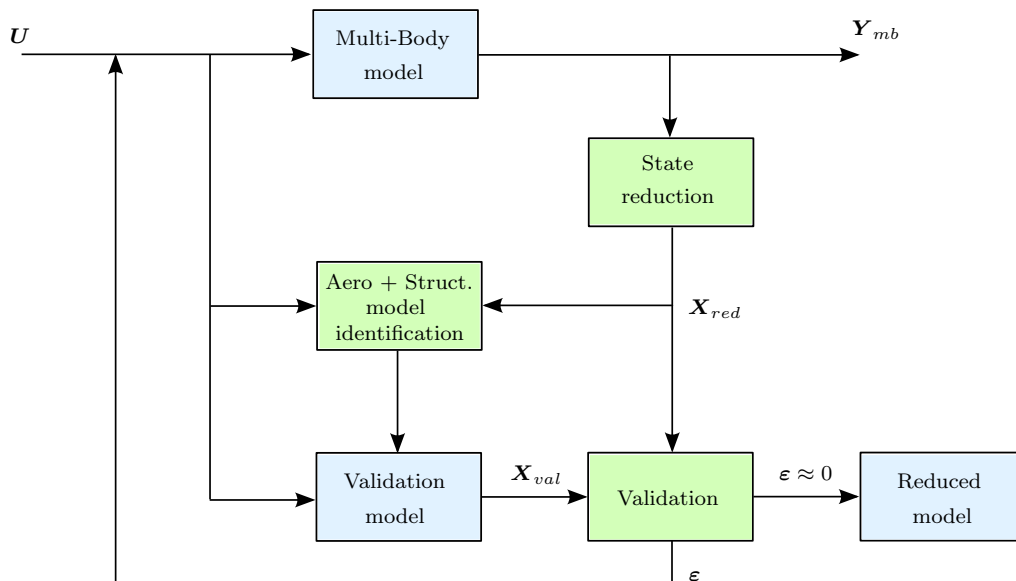


Figure 12-1: Multi-Body model reduction process

Conclusions

The particular Rigid Body model developed describes the dynamic motion of the Multi-Body model formulated by rigid body states. The Rigid Body model and the Multi-Body model are both attached to a spring-damper tether model such that only model reduction is required for the aerodynamics and the structure.

The complete set of equations to describe the dynamics of the Rigid Body Kite model is established and formulated with Newton's second law in Cartesian and spherical coordinates. The model describes a kite attached to a straight line tether with two bridle lines. The model is verified by referring to a rigid body aircraft model. The aircraft dynamics are known from a linear time invariant reference model from reference [24]. For completion of the verification LTI models are derived for an aircraft flying in wind conditions and for the Rigid Body model on the same basis as in reference [24]. Because the LTI models are on a parametric basis, they can be used to investigate the influence of specific parameters on the stability of the system.

The numerous states of the Multi-Body model designed in ADAMS are reduced to a set of states describing the motion as a single body. For every body, flexible and rigid, holds that the inertial linear and rotational acceleration follow Newton's second law: the sum of external forces is equal to the time derivative of the linear momentum and the sum of external moments is equal to the time derivative of the angular momentum. On this principle the state reduction is applied and verified for the Multi-Body model. The acceleration, velocity and displacement components of the center of mass are obtained by a mass weighted approach on the basis of conservation of linear momentum. To establish the rotational states the inertia tensor and angular momentum are required as a function of time. Because of programming issues in ADAMS the implementation of the measurement for the inertia tensor and angular momentum is applied with a particle based method. It is shown that the particle based method neglects the contribution of the sum of the local mass moments of inertia and angular momentum about the center of gravity of each body. It is proven that the particle based method makes up a very good approximation for the angular momentum and the time derivative of the angular momentum of the Multi-Body Arc-shaped Kite model. With the measurements of the inertia tensor, the angular momentum and the time derivative of the angular momentum the body rotational rates and accelerations are computed. By integrating the rotational rates through time the orientation of the body-fixed reference frame is tracked.

Specific ADAMS macro files are programmed which automate the generation of the function measures for the measurements of the displacement quantities, inertia tensor components, angular momentum and the time derivative of the angular momentum. A SIMULINK model is coupled to the ADAMS model to ease the matrix and vector operations for computation of the body angular acceleration, angular rate and orientation during run-time simulations. A visualization dummy is added to the model which tracks the position and orientation of the body-fixed reference frame. Now, any structural deformation aspect can be analyzed with respect to this centroid dummy.

To accomplish the reduction of the Multi-Body Kite model to a Rigid Body Kite model it is required that the aerodynamic and the structural model can be written by functions dependent on rigid body states. The rigid body states are defined by the state reduction process. Due to the tight interaction between the flight condition and kite shape the aerodynamic model and structural model vary with flight condition.

The aerodynamic model is formulated on the basis of Taylor expansions and written in dimensionless form making it independent of the dynamic pressure, mean wing chord, wing span and projected surface area. Taylor series results in a linear decomposition of the dependency of each state. The effective contribution of each aerodynamic state is given by respective dimensionless aerodynamic derivatives. Flight test simulations are performed for a predefined flight domain to find the model structure and to fit or estimate the values of the aerodynamic derivatives. The aerodynamic derivatives are then dependent of the flight condition, which is given by V_a and x_{ta} .

Roughly V_a accounts for the static body shape and x_{ta} for the shift of the center of gravity due to the weight of the control carts. The initial angle of attack α of each flight test simulation is implicitly given by these two variables. It is shown that the angle of attack control has a range of approximately 2 deg. The angle of attack control with cart position is very limited. For the symmetric as well as the asymmetric model the flight test simulations are performed from a stationary initial condition. It is found that the aerodynamic forces and moments depend on angle of attack, side slip angle, body rates and control positions, but also on respective time derivatives and higher order terms. Because the aerodynamic model for each airfoil in the Multi-Body model does not depend on time related parameters, but only on static states, the time derivative contributions in the aerodynamic model for the Rigid Body model are a result of the flexible structure.

The structural model is constituted on a quasi-static basis by formulating functions describing the initial conditions of the flight test simulations. Therefore the structural model is also dependent on the variables V_a and x_{ta} . Functions are formulated for the inertia tensor components, mean wing chord, wing span, projected surface area and the tether attachment points.

Test simulations are performed to validate the Rigid Body model with respect to the Multi-Body model where both models are subject to the same input. Comparisons are made for initial conditions which represent a dynamically stable condition. The main difference is shown with the damping of the short period eigenmotion. The damping of this eigenmotion is less for the Rigid Body model. It appears that dynamically unstable situations result for initial conditions where the control positions are moved towards the trailing edge. This is clarified by the positive real part of the eigenvalue of the short period motion for these conditions. In the model reduction process some damping term has been lost, which results in the fact that the reduced model is unstable for some flight conditions.

Accurate fits of the aerodynamic forces and moments response curves are found for a large part of the investigated domain. Implementation of the found aerodynamic model resulted in the unstable situations for some part of the flight domain. It is found from further investigation on the aerodynamic model identification process that the observation variables have data collinearity meaning high correlation coefficients. This degrades the statistical significance of the estimated derivatives and makes the independent contribution of the variables problematic to identify. The model identification technique fails to identify the aerodynamic model for a broader domain.

The validation proves that the proposed methodology for model reduction is a qualitative manner for model reduction of the Multi-Body Kite model and for multi-body model reduction of flying objects in general. It results in kite models almost ten times faster than real-time, whereas simulating the Multi-Body Kite model in ADAMS takes more than ten times real-time.

To answer the question '*Is it possible to simulate the overall dynamic behaviour of a flexible arc-shaped kite model with a rigid body model?*' it can be said that this is possible. The model reduction is proven for some part of the investigated flight domain. Advanced model identification techniques which can identify the aerodynamic model with higher statistical significance increase the validity domain.

A detailed Rigid Body arc-shaped kite model which is appropriate for controller design is developed. The system equations of the Rigid Body model are qualitatively formulated and verified. This modelling approach results in fast models. Advanced control techniques can be designed on the basis of this modelling approach.

Recommendations & future work

For future work multiple recommendations can be formulated.

Regarding the ADAMS Multi-Body model it is found that the simulation time is long. It is worthwhile to investigate in more efficient methods or applications to simulate complex multi-body models. The presented multi-body reduction process is appropriate for other multi-body applications.

For the aerodynamic and structural model identification the following recommendations can be itemized:

- Perform research into more advanced model identification techniques
- Perform a modal analysis to identify the dominant structural modes of an arc-shaped kite
- Identify the aerodynamic and structural models

Referring to the aerodynamic model a similar approach can be depicted for the structural model, where the dynamics are also described by parametric functions based on Taylor series or Fourier series. As the body-fixed reference frame of the Multi-Body Arc-shaped Kite model is defined it is now possible to perform an analysis of the deformation modes superimposed on the rigid body states. The governing structural states on the rigid body motion can be added to the aerodynamic models. With this approach a high interaction is established between the aerodynamic and structural model written as a set of parametric formulations. This will resolve the unstable solutions found in this thesis.

For faster simulations and better integration techniques the Rigid Body model should be designed in an other software application than SIMULINK. SIMULINK is advantageous for bookkeeping, but lacks in simulation speed and the use of custom integration methods. It is found that the aerodynamics of the Multi-Body Kite model have dependency on the rigid body acceleration states. Algebraic loops are found when these states are included in the aerodynamic models. Additionally the values of these respective parameters are positive. The algebraic loops and positive parameters resulted in unstable solutions. This can mean that unstable models are identified due to the positive parameters or that the numerical integration method in SIMULINK is limited to solve algebraic loops or both. For on-line application of the Rigid Body model these issues need to be resolved.

The kite is the main focus in this thesis. For the tether it is assumed that it can be represented by a straight line spring-damper model. This holds for short tethers. Further research is required to model tethers and to investigate the influence of the tether on the dynamics of the system. Specifically, this comprises tether drag and the limits of the straight line assumption.

References

- [1] J. Breukels and W. J. Ockels. A Multi-body Dynamics Approach to a Cable Simulation for Kites. Paper, ASSET, Delft University of Technology, 2007.
- [2] J. Breukels and W. J. Ockels. Analysis of Complex Inflatable Structures Using a Multi-body Dynamics Approach. In *Proceedings of the 49th AIAA/ASME/ASCE/AHS/ASC Structures, Structural Dynamics, and Materials Conference, Schaumburg, IL, USA*, The Netherlands, 2008. ASSET, Delft University of Technology.
- [3] J. Breukels and W. J. Ockels. A Multi-body System Approach to the Simulation of Flexible Membrane Airfoils. Paper, ASSET, Delft University of Technology, 2010. Under review by Aerotecnica Missili & Spazio (AIDAA).
- [4] J. Breukels and W. J. Ockels. Simulation of a flexible arc-shaped surf kite. Paper, ASSET, Delft University of Technology, 2010. Under review by AIAA, Journal of Aircraft.
- [5] J. Breukels and W. J. Ockels. Simulation of a Three Dimensional Flexible Sail Wing with an Inflated Tubular Spar. Paper, ASSET, Delft University of Technology, 2010. Under review by Aerotecnica Missili & Spazio (AIDAA).
- [6] M. Diehl, H.G. Bock, and J. P. Schlöder. A Real-time Iteration Scheme for Nonlinear Optimization in Optimal Feedback Control. Paper, University of Heidelberg.
- [7] B. Etkin. *Dynamics of Atmospheric Flight*. John Wiley & Sons Inc., 1972. University of Toronto.
- [8] L. Fagiano. *Control of Tethered Airfoils for High-Altitude Wind Energy Generation*. Phd. thesis, Technische Universiteit Delft, 2009.
- [9] A. Furey and I. Harvey. Adaptive Behavioural Modulation and Hysteresis in an Analogue of a Kite Control Task. Paper, Centre for Computational Neuroscience and Robotics, University of Sussex, Brighton, United Kingdom, 2008.
- [10] A. Furey and I. Harvey. Evolution of Neural Networks for Active Control of Tethered Airfoils. Paper, Centre for Computational Neuroscience and Robotics, University of Sussex, Brighton, United Kingdom, 2008.
- [11] A. Furey and I. Harvey. Robust adaptive control for kite wind energy using evolutionary robotics. Paper, Centre for Computational Neuroscience and Robotics, University of Sussex, Brighton, United Kingdom, 2008.

- [12] B. Houska. A 9 DOF Kite Model. Internal Paper, University of Heidelberg.
- [13] J. D. Jacob and S. W. Smith. Design of HALE Aircraft Using Inflatable Wings. In *46th AIAA Aerospace Sciences Meeting and Exhibition, Reno, Nevada, USA, January 2008*. Aerospace Engineering, Oklahoma State University & Mechanical Engineering, University of Kentucky.
- [14] B. Lansdorp, R. Ruiterkamp, and W. J. Ockels. Towards Flight Testing of Remotely Controlled Surf kites for Wind Energy Generation. Paper, ASSET, Delft University of Technology, Delft, The Netherlands, 2007.
- [15] B. Lansdorp, R. Ruiterkamp, and P. Williams. Long-Term Laddermill Modeling for Site Selection. Paper, ASSET, Delft University of Technology, Delft, The Netherlands, 2008.
- [16] B. Lansdorp and P. Williams. The Laddermill - Innovative wind energy from high altitudes in Holland and Australia. Paper, ASSET, Delft University of Technology, Delft, The Netherlands, 2006.
- [17] Chun-Liang Lin. Synthesis of Real-Time Robust Flexible Structure Controllers. *Journal of Guidance, Control, and Dynamics*, Vol. 21(No. 6), November-December 1998. Feng Chia University.
- [18] G. H. N. Looye. *An Integrated Approach to Aircraft Modelling and Flight Control Law Design, Control & Simulation*. Phd. thesis, Delft University of Technology, 2008.
- [19] M. L. Loyd. Crosswind Kite Power. *Journal of Energy*, Vol. 4(No. 3), May-June 1980. Lawrence Livermore National Laboratory, Livermore, California.
- [20] B. Lubbers. *A model of the Experimental Fly-By-Wire control system for the PH-LAB*. Master Thesis, Delft University of Technology, 2009.
- [21] T. Melin. Tornado, The Vortex Lattice Method. Royal institute of Technology in Stockholm Sweden and University of Bristol, United Kingdom. <http://www.redhammer.se/tornado/>, version 134.
- [22] MSC Software. ADAMS. <http://www.mscsoftware.com/Contents/Products/CAE-Tools/Adams.aspx>.
- [23] J. A. Mulder, J. K. Sridhar, and J. H. Breeman. *AGARDograph 300, Identification of Dynamic Systems - Applications to Aircraft, Part 2: Nonlinear Analysis and Manoeuvre Design*, volume 3 of *Flight Test Techniques*. AGARD, Advisory Group for Aerospace Research and Development, May 1994.
- [24] J. A. Mulder, W. H. J. J. van Staveren, J. C. van der Vaart, and E. de Weerd. Flight Dynamics. Lecture notes, Delft University of Technology, 2006. Flight Dynamics Course.
- [25] W. J. Ockels. Laddermill, a Novel Concept to Exploit the Energy in the Airspace. *Aircraft Design*, Vol. 4(No. 3):pages 81–97, 2001.
- [26] W. J. Ockels. Kite power and propulsion, The Laddermill principle. Paper, ASSET, Delft University of Technology, 2009. Submitted for publication.
- [27] C. O’Gairbhith. High-altitude Wind Energy The potential in Ireland. Report, Ireland, 2009.
- [28] A. Simpson, J. Rowe, S. W. Smith, and J. Jacob. Aeroelastic Deformation and Buckling of Inflatable Wings under Dynamic Loads. In *48th AIAA/ASME/ASCE/AHS/ASC Structures, Structural Dynamics, and Materials Conference, 15th AIAA/ASME/AHS Adaptive Structures Conference, Waikiki, Hawaii, Lexington, USA, April 2007*. Mechanical Engineering Dept., University of Kentucky. AIAA 2007-2239.

- [29] A. Simpson, M. Usui, J. Jacob, and S. Smith. Aeromechanics of Inflatable Airfoils. In *34th AIAA Fluid Dynamics Conference and Exhibition, Portland, Oregon, Lexington, USA*, June-July 2004. Mechanical Engineering Dept., University of Kentucky. AIAA 2004-2233.
- [30] E. J. Terink. *Kiteplane Flight Dynamics*. Master Thesis, ASSET, Delft University of Technology, December 2009.
- [31] Josef S. Török. *Analytical Mechanics*. John Wiley & Sons, Inc., 2000.
- [32] A. de Wachter. *Deformation and Aerodynamic Performance of a Ram-Air Wing*. Master Thesis, ASSET, Delft University of Technology, 2008.
- [33] C. Wielgosz, J. C. Thomas, and P. Casari. Strength of Inflatable fabric Beams at High Pressure. In *43rd AIAA/ASME/ASCE/AHS/ASC Structures, Structural Dynamics, and Materials Conference, Denver, Colorado, France*, April 2002. Facult des Sciences et des Techniques, Universit de Nantes. AIAA 2002-1292.
- [34] P. Williams and B. Lansdorp. Flexible Tethered Kite with Moveable Attachment Points, Part I: Dynamics and Control. Paper, ASSET, Delft University of Technology, The Netherlands, 2007.
- [35] P. Williams and B. Lansdorp. Flexible Tethered Kite with Moveable Attachment Points, Part II: State and Wind Estimation. Paper, ASSET, Delft University of Technology, The Netherlands, 2007.
- [36] P. Williams and B. Lansdorp. Modeling and Control of a Kite on a Variable Length Flexible Inelastic Tether. Paper, ASSET, Delft University of Technology, The Netherlands, 2007.
- [37] P. Williams and B. Lansdorp. Nonlinear Control and Estimation of a Tethered Kite in Changing Wind Conditions. Paper, ASSET, Delft University of Technology, The Netherlands, 2008.
- [38] P. Williams and B. Lansdorp. Optimal Crosswind Towing and Power Generation with Tethered Kites. Paper, ASSET, Delft University of Technology, The Netherlands, 2008.
- [39] P. Williams, B. Lansdorp, and R. Ruiterkamp. Modeling, Simulation, and Testing of Surf Kites for Power Generation. Paper, ASSET, Delft University of Technology, The Netherlands, 2008.
- [40] World Wind Energy Association. World Wind Energy Report 2008. Technical report, World Wind Energy Association (WWEA), Bonn, Germany, February 2009. <http://www.windea.org/home/index.php>.
- [41] T. Zandbergen. *Low Drag line*. Bachelor Thesis, ASSET, Delft University of Technology, 2008.

Appendix A

Additional Information Multi-Body Kite Model

Additional information is depicted of the Multi-Body Kite model with respect to the parts and joints, UDE function partitions and mass and inertia tensor properties.

Model overview

ADAMS has a function to verify the model on the number of parts, constraints and degrees of freedom. The result is shown in table A-1.

Degrees of Freedom	375
Moving parts	211
Revolute joints	22
Spherical joints	66
Translational joints	20
Hooke joints	120
Redundant constraints	0

Table A-1: Model verification

UDE function partitions

Table A-2 gives an overview of the parts with respect to their number and total weight. Additionally the subdivision of the Center of Gravity UDEs is shown. This subdivision is a result of the character limit of the ADAMS function measures created with the macro files. The filter string defines the parts selected for the creation of the UDE. More details are given in section 9-2.

Part	Filter string	UDE name CoG_	Number of parts	Total Weight [kg]
LE Tubes	Tube*	LE	20	1.2485
Side Tubes	Chord*	CH	25	0.5297
Foils	FoilC0C1_YNeg*	01L	32	$2.23 \cdot 10^{-2}$
	FoilC0C1_YPos*	01R	32	$2.23 \cdot 10^{-2}$
	FoilC1C2_YNeg*	12L	32	$1.73 \cdot 10^{-2}$
	FoilC1C2_YPos*	12R	32	$1.73 \cdot 10^{-2}$
	FoilC2tip_YNeg*	2tL	16	$5.42 \cdot 10^{-3}$
	FoilC2tip_YPos*	2tR	16	$5.42 \cdot 10^{-3}$
Cart, rail, kite top	Kite*	CO	5	3.61
Total		T	210	5.3062

Table A-2: Part overview and Center of Gravity UDE partition overview

Table A-3 gives an overview of the subdivision of the Angular Momentum and Inertia UDEs. For the angular momentum and inertia measures the contribution of the foil parts is ignored. This can be justified by the fact that the weight of the foil parts is very small.

Part	Filter string	UDE name AngM_, I_	Number of parts
LE Tubes	Tube_YNeg*	LEL	10
	Tube_YPos*	LER	10
Side Tubes	Chord0*	CH0	5
	Chord1*	CH1	10
	Chord2*	CH2	10
Cart, rail, kite top	Kite*	CO	5
Total		T	50

Table A-3: Angular Momentum and Inertia UDE partition overview

Table A-4 gives an overview of the subdivision of the General Force UDEs for the aerodynamic force measures.

Force	Filter string	UDE name SumGF_	Number of forces
GForce	*C0C1_YNeg_Fae*	01L	20
	C0C1_YPos_Fae	01R	20
	C1C2_YNeg_Fae	12L	20
	C1C2_YPos_Fae	12R	20
	C2tip_YNeg_Fae	2tL	10
	C2tip_YPos_Fae	2tR	10
Total		T	100

Table A-4: Aerodynamic forces overview and General Forces UDE partition overview

Mass and inertia tensor

The mass and inertia tensor properties at the initial condition ($t = 0$ s) are shown in table A-5. Inertia tensor properties obtained with `Aggregate Mass...` function as well as with the particle

based method are shown. The values are expressed in the body-fixed reference frame.

m , total mass	5.3062 kg	$d_{taL,0}$	0.05 m
m_c , cart mass	0.990 kg	$d_{taR,0}$	0.05 m
m_r , rail mass	0.724 kg		
Inertia property	Exact [kg·m ²]	pb [kg·m ²]	Error [%]
I_{xx}	30.88	30.25	2.0
I_{yy}	10.07	9.36	7.1
I_{zz}	22.34	21.72	2.8
I_{xy}	0.0	0.0	0.0
I_{yz}	0.0	0.0	0.0
I_{zx}	0.383	0.314	17.2

Table A-5: Mass and *initial* inertia properties, body-fixed reference

Appendix B

Examples of flight test simulations

Examples are shown of four flight test simulations, which are used for the aerodynamic parameter identification. The fitted forces and moments curves are corresponds to the the aerodynamic models in equations (10-11) and (10-12). The figures are analyzed and discussed in chapter 10.

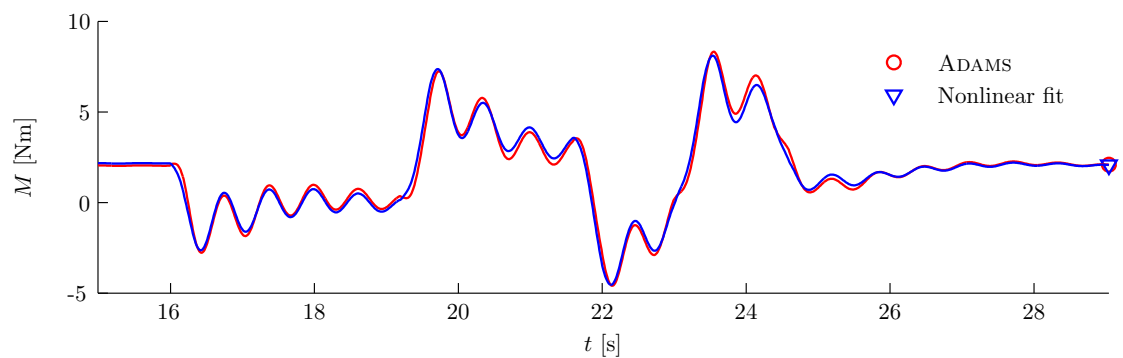
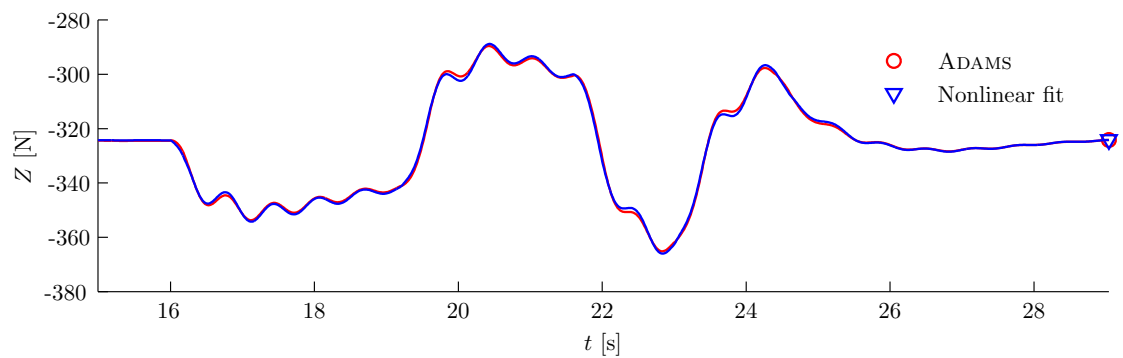
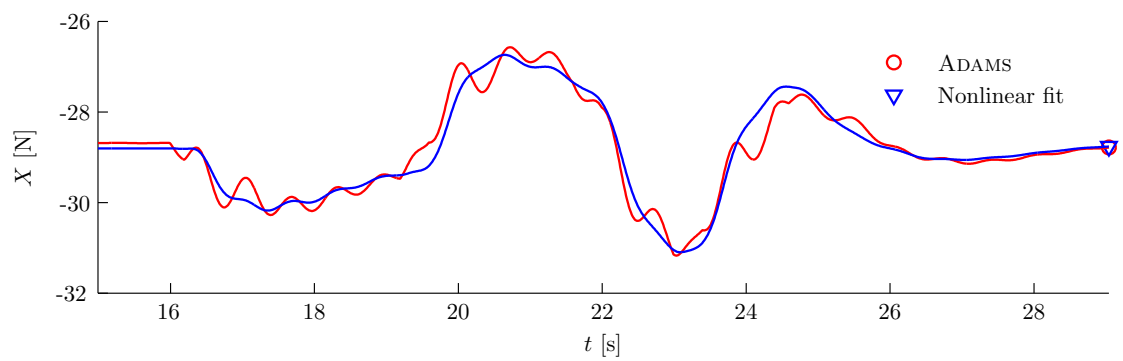
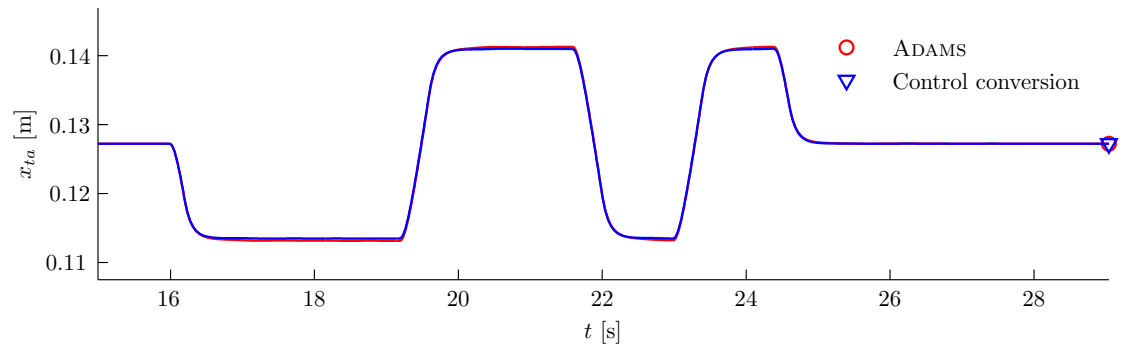


Figure B-1: Simulated and fitted symmetric forces and moment curves at $W_{x,0} = -14\text{m/s}$ and $d_{ta,0} = 0.05\text{m}$
Modelling the Dynamics of an Arc-shaped Kite for Control Law Design

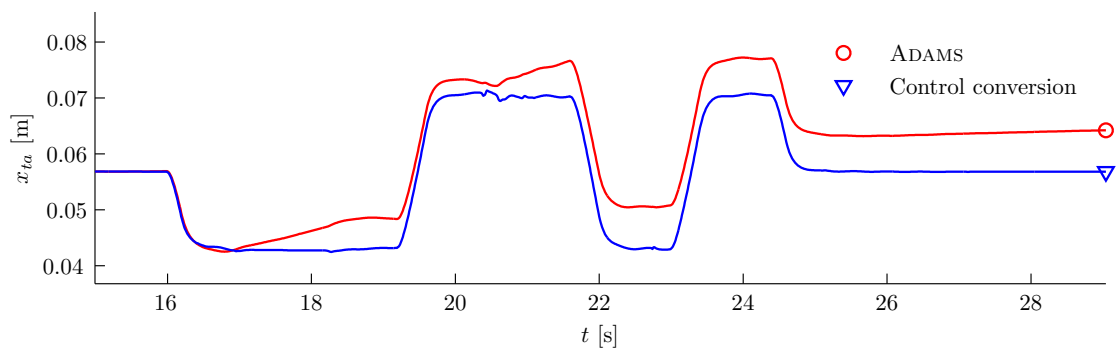
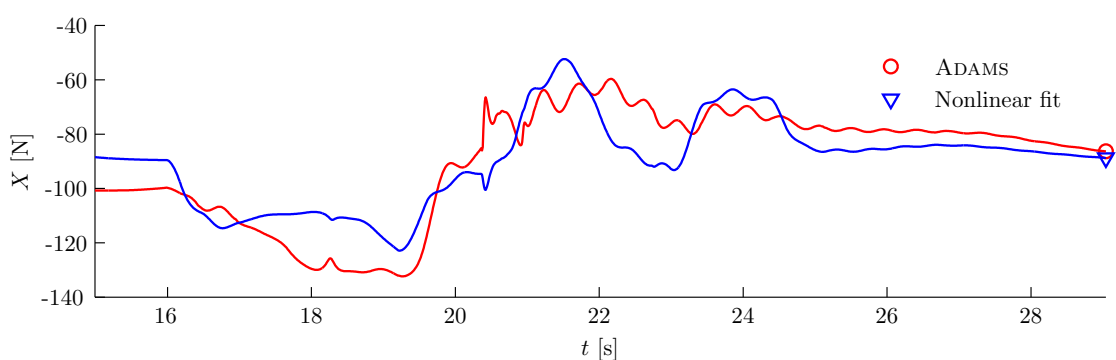
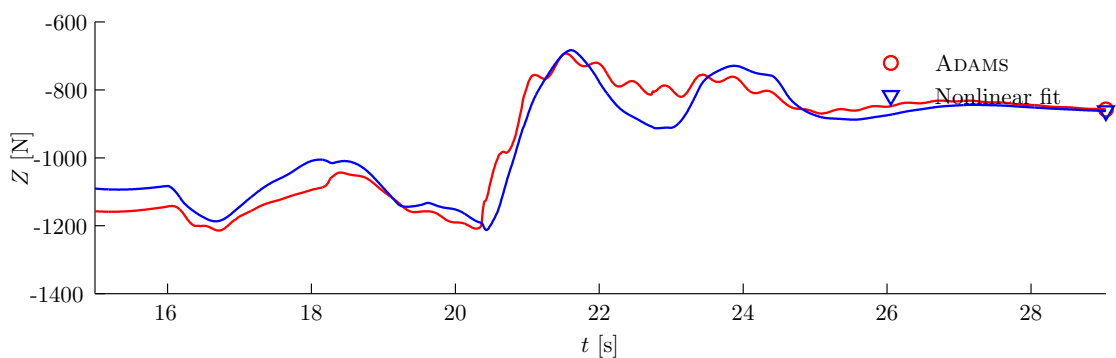
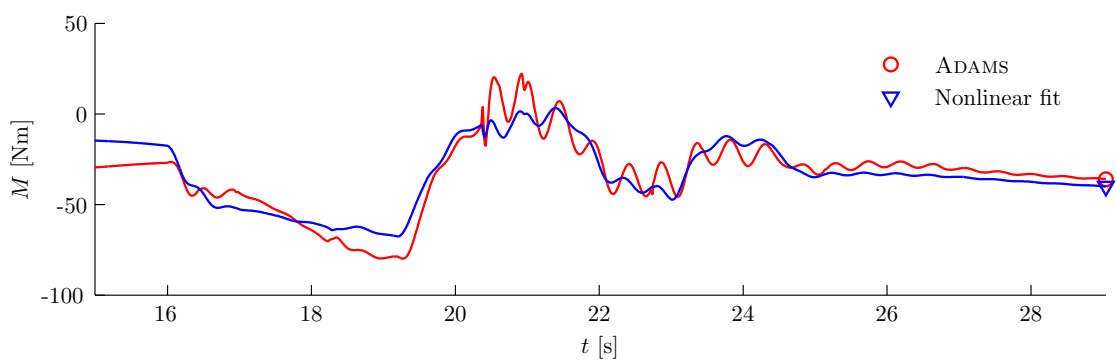
(a) Input along X_b -axis(b) Force curve along X_b -axis(c) Force curve along Z_b -axis(d) Moment curve about Y_b -axis

Figure B-2: Simulated and fitted symmetric forces and moment curves at $W_{x,0} = -22$ m/s and $d_{ta,0} = 0.20$ m

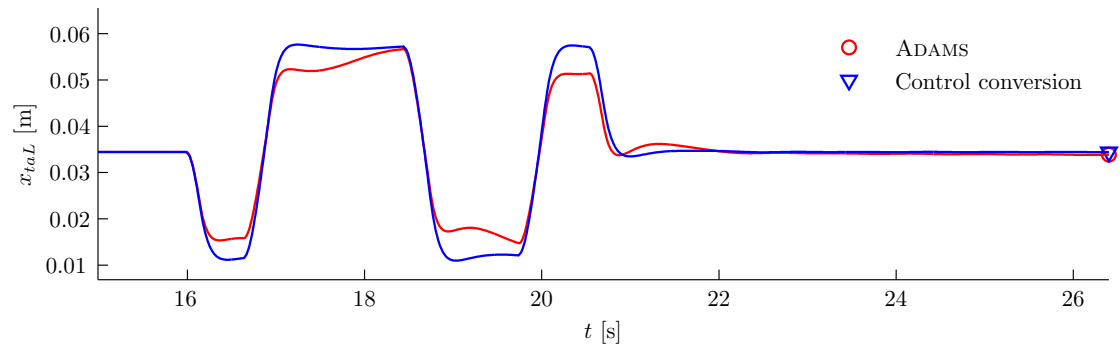
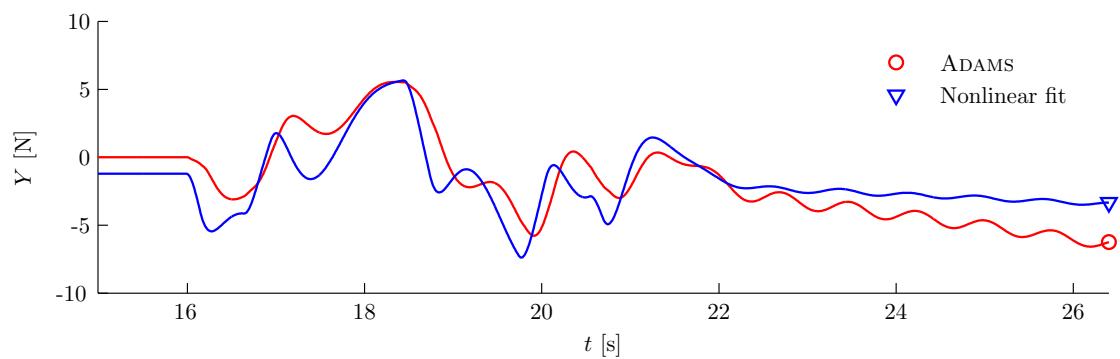
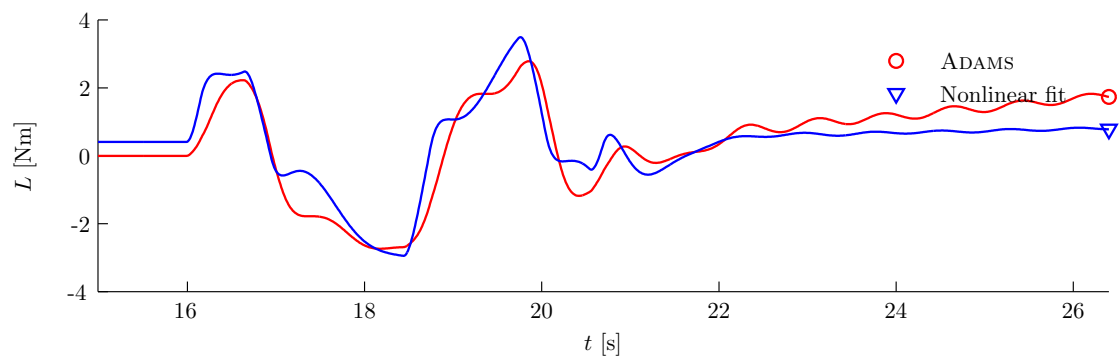
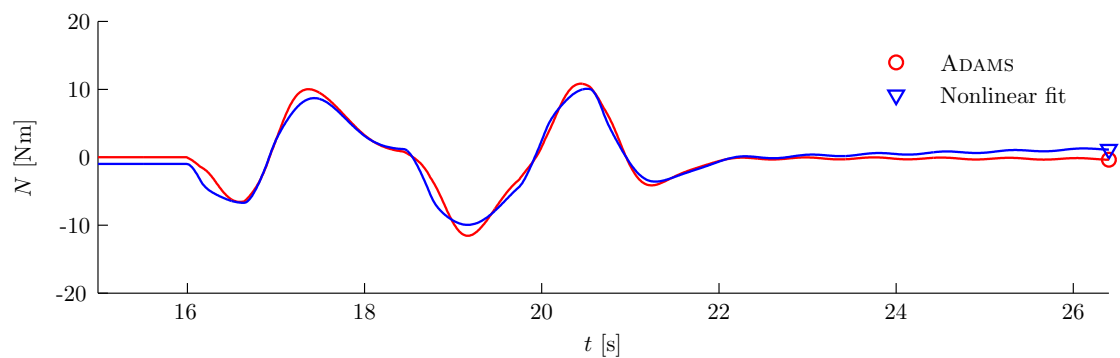
(a) Left input along X_b -axis(b) Force curve along Y_b -axis(c) Moment curve about X_b -axis(d) Moment curve about Z_b -axis

Figure B-3: Simulated and fitted asymmetric force and moments curves at $W_{x,0} = -8 \text{ m/s}$ and $d_{ta,0} = 0.25 \text{ m}$
Modelling the Dynamics of an Arc-shaped Kite for Control Law Design

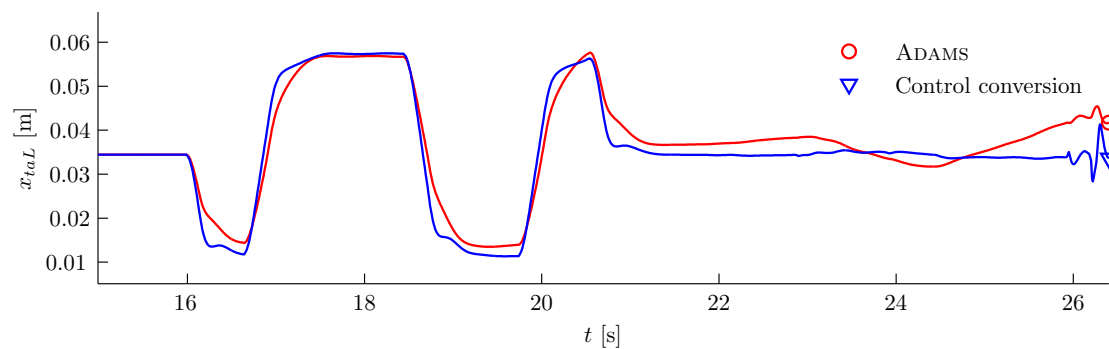
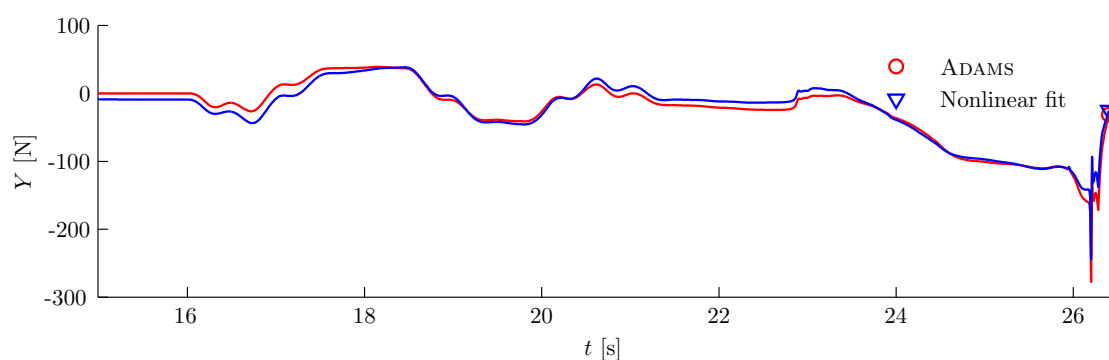
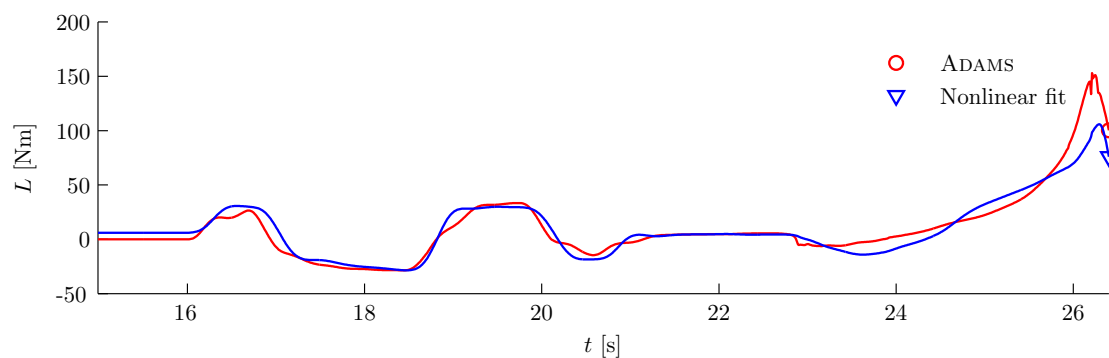
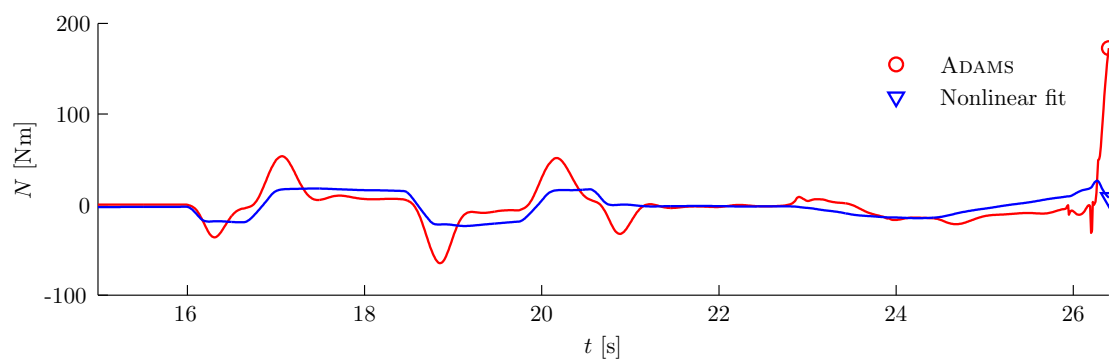
(a) Left input along X_b -axis(b) Force curve along Y_b -axis(c) Moment curve about X_b -axis(d) Moment curve about Z_b -axis

Figure B-4: Simulated and fitted asymmetric force and moments curves at $W_{x,0} = -18$ m/s and $d_{ta,0} = 0.25$ m

Appendix C

Aerodynamic derivatives

The dimensionless aerodynamic derivatives derived with the flight test simulations of chapter 10 are shown in subsequent figures on the left with the significance criterion on the right. The derivatives of the symmetric forces and moment are obtained from 48 flight test simulations and the asymmetric force and moments from 36 flight test simulations as given by tables 10-1 and 10-3.

The derivatives are shown with contour plots obtained with linear interpolation. The values of the significance criterion are illustrated with image plots and are not interpolated. The colors of the image plots represent the same value for every plot. All values of the significance criterion higher than 30 are truncated and represented by the color for 30, which defines that the value of the fitted parameter is approximately between $0.97a_k$ and $1.03a_k$ with a probability of 0.95.

C-1 Derivatives of the symmetric forces and moment

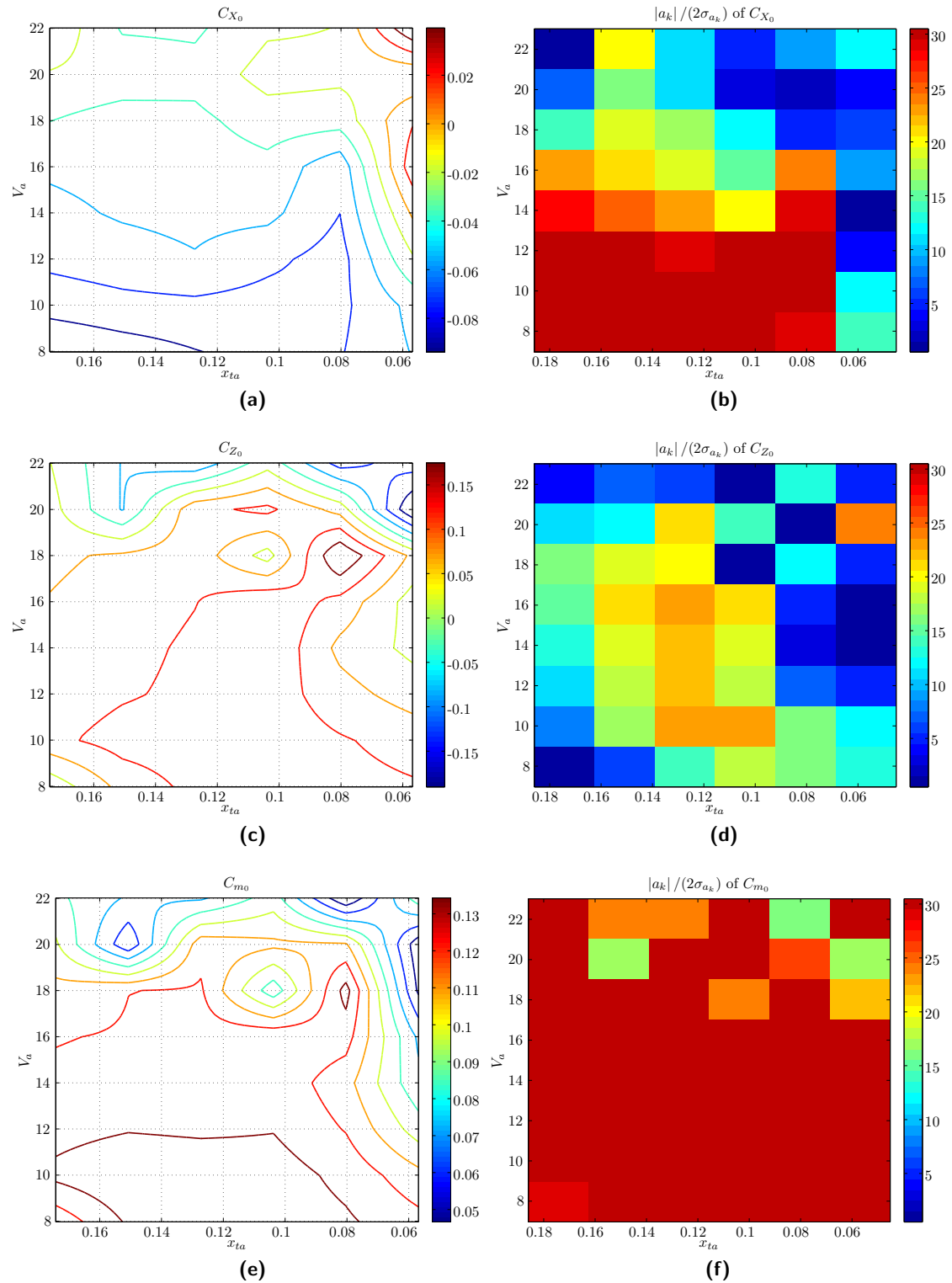


Figure C-1: Initial values of C_X , C_Z and C_m as a function of $V_{a,0}$ and $x_{ta,0}$

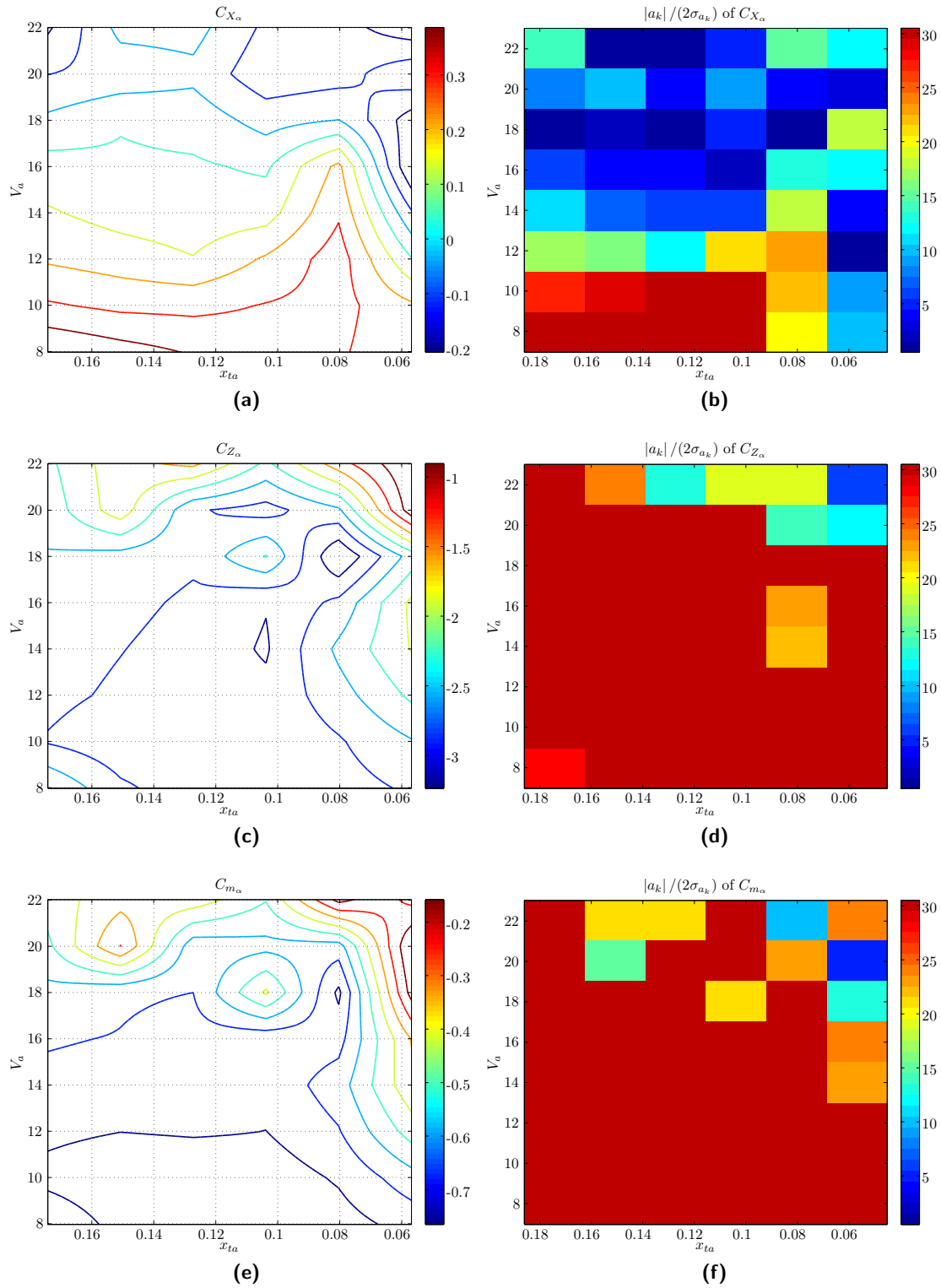


Figure C-2: Derivatives with respect to α as a function of $V_{a,0}$ and $x_{ta,0}$

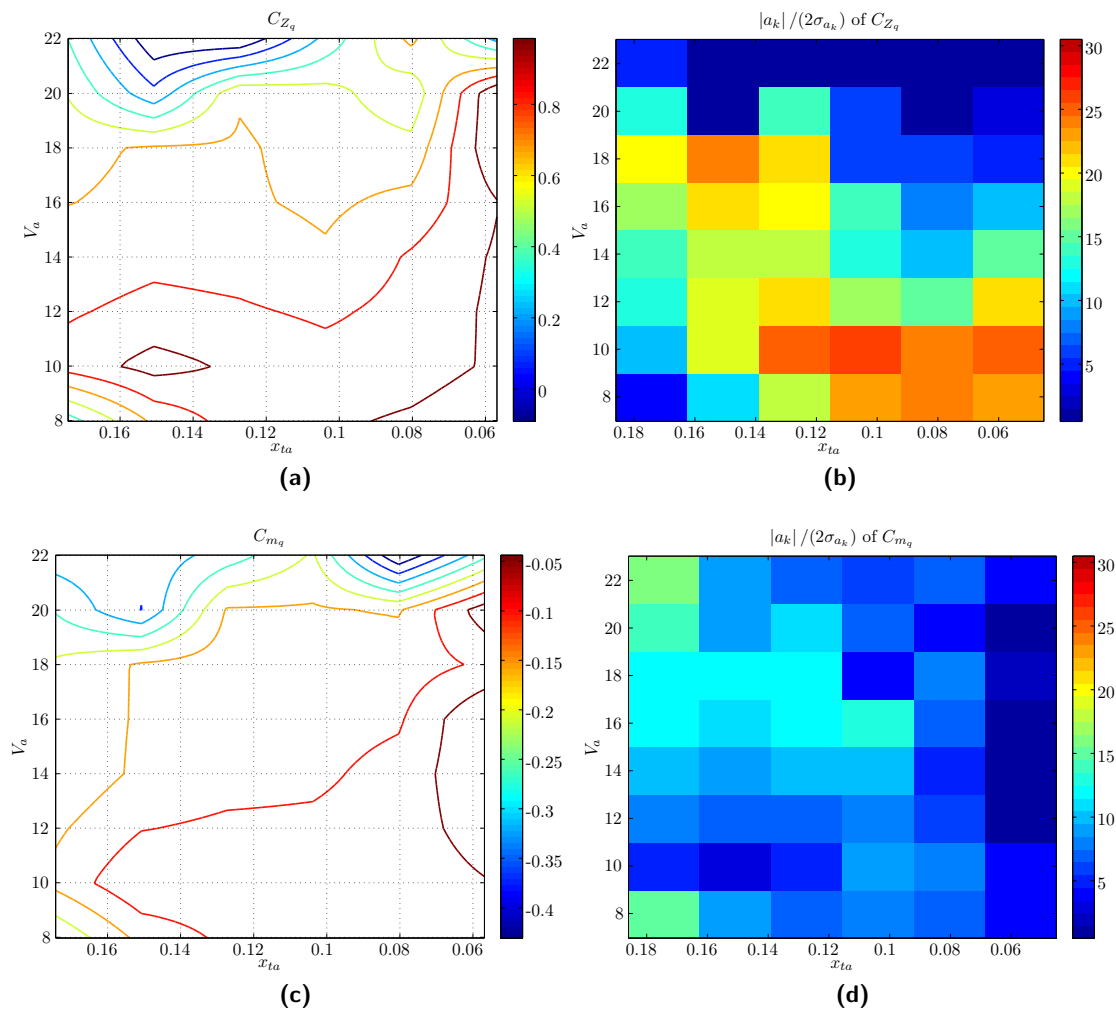


Figure C-3: Derivatives with respect to $\frac{q\bar{c}}{V_a}$ as a function of $V_{a,0}$ and $x_{ta,0}$

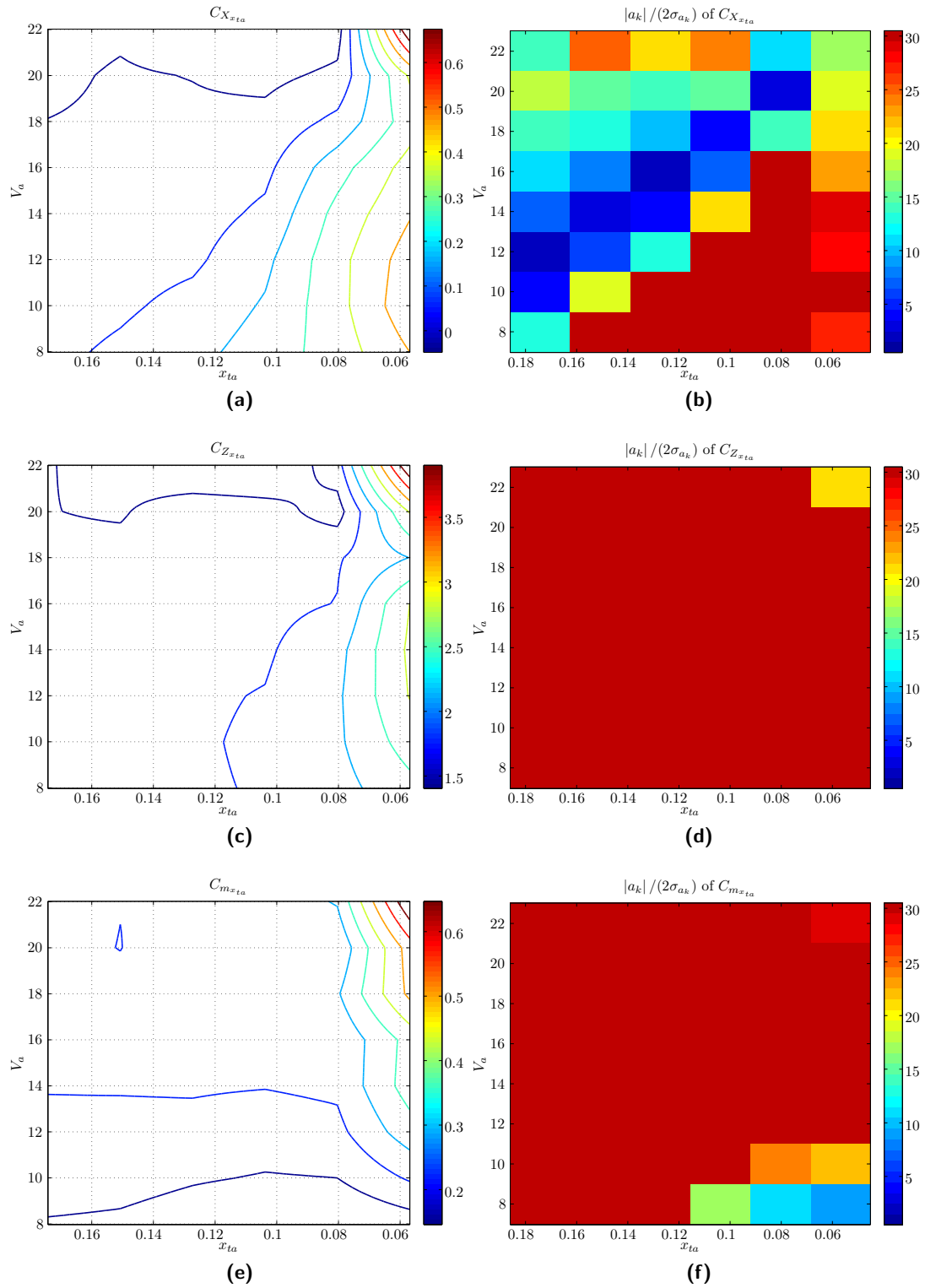


Figure C-4: Derivatives with respect to $\frac{x_{ta}}{c}$ as a function of $V_{a,0}$ and $x_{ta,0}$

C-2 Derivatives of the asymmetric force and moments

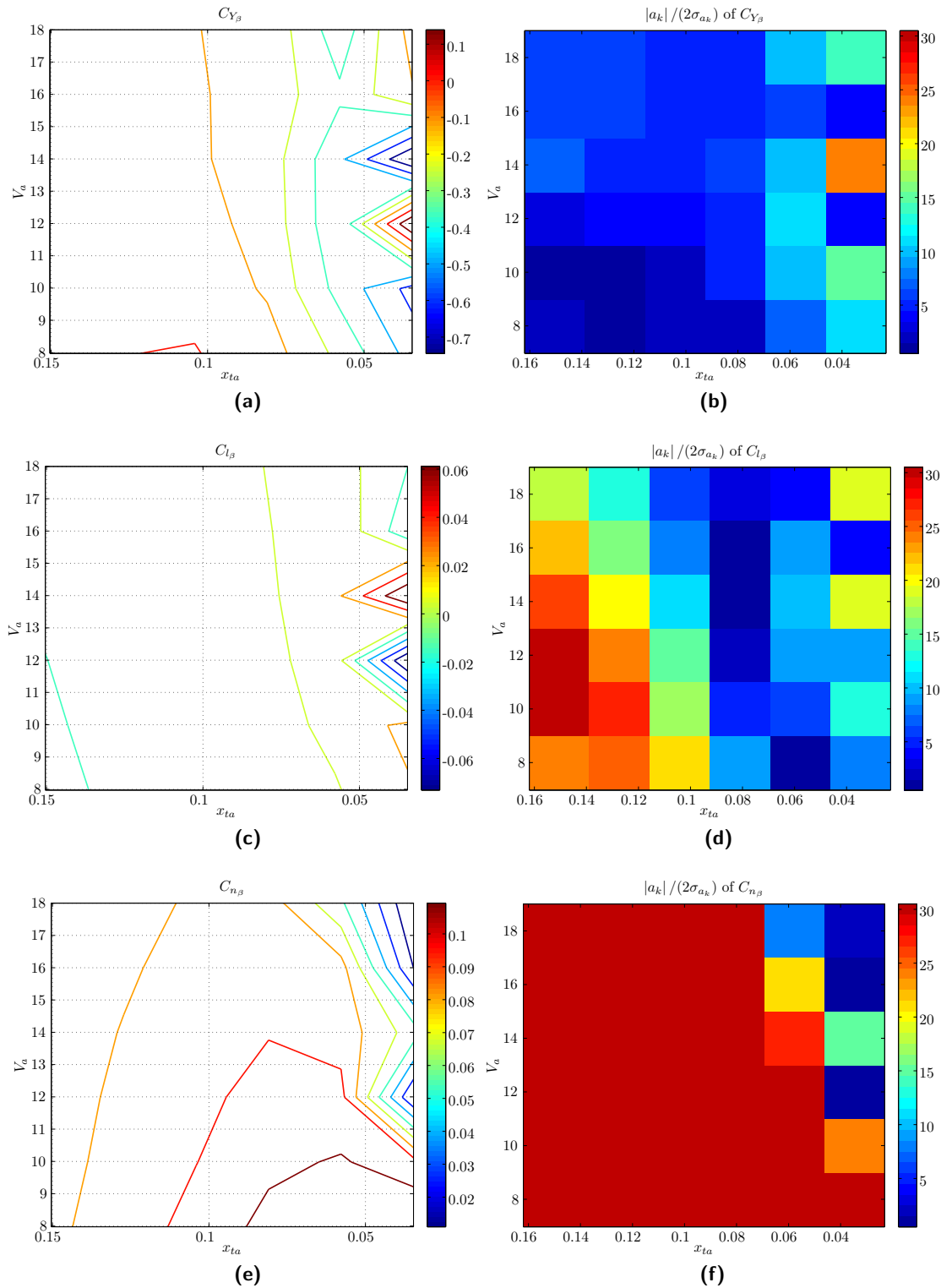


Figure C-5: Derivatives with respect to β as a function of $V_{a,0}$ and $x_{ta,0}$

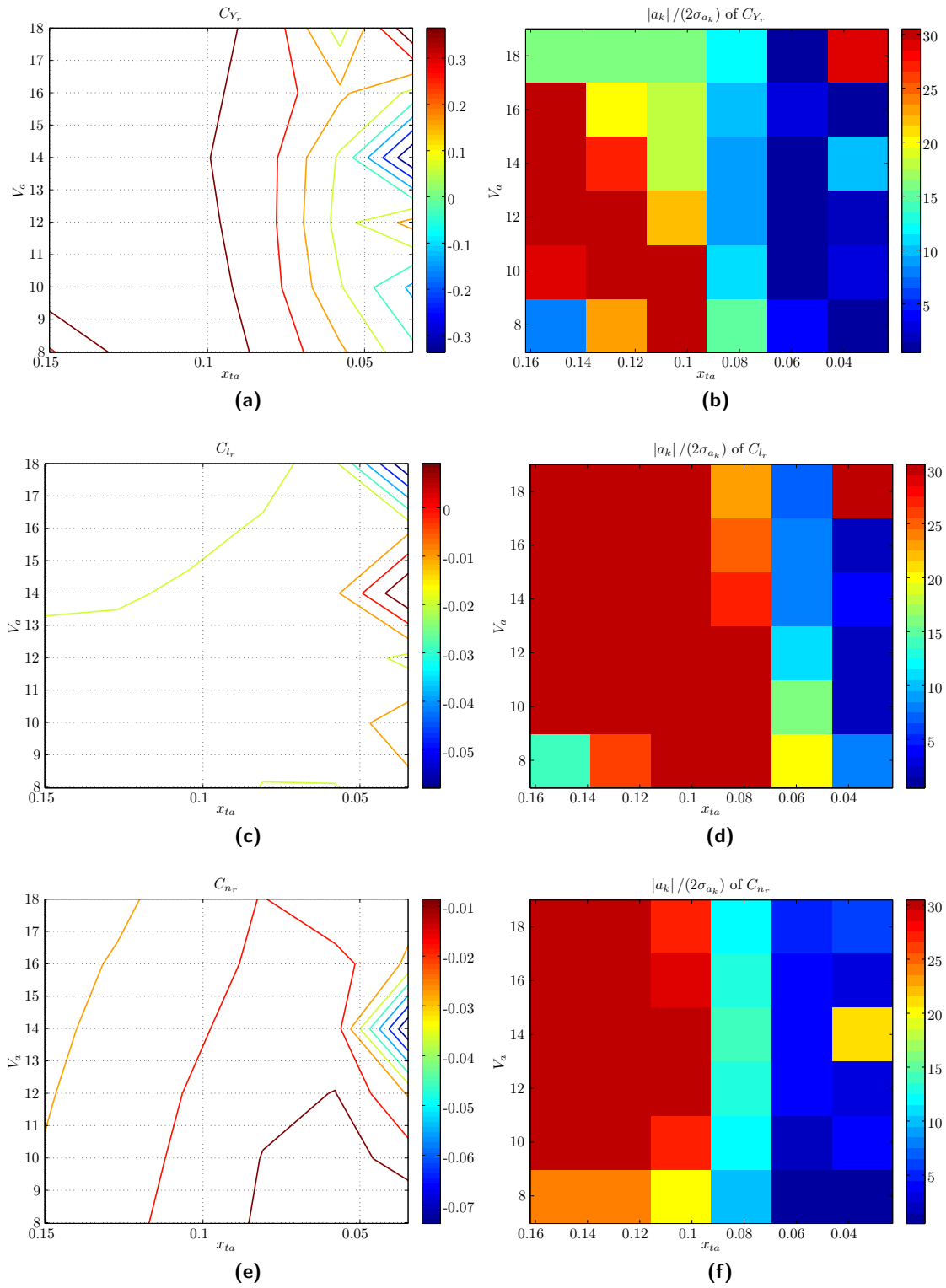


Figure C-6: Derivatives with respect to $\frac{r_b}{2V_a}$ as a function of $V_{a,0}$ and $x_{ta,0}$

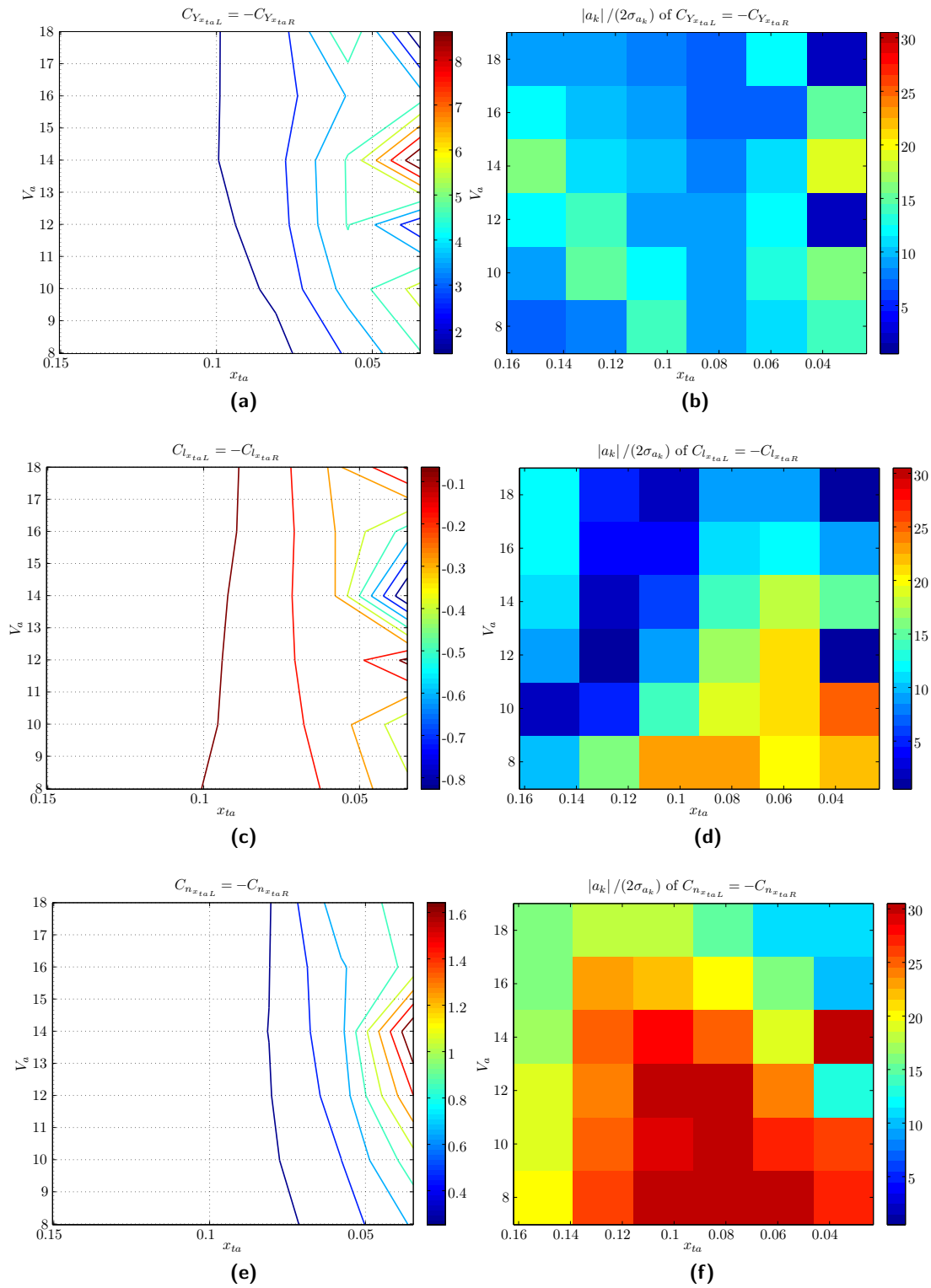


Figure C-7: Derivatives with respect to $\frac{x_{taL}}{b}$ as a function of $V_{a,0}$ and $x_{ta,0}$

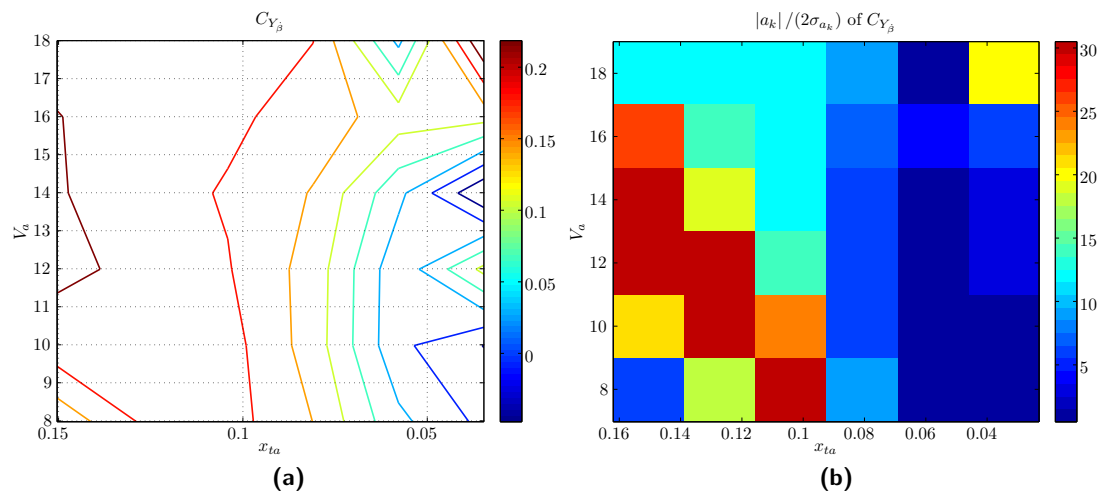


Figure C-8: Derivatives with respect to $\frac{\dot{\beta}b}{\beta a}$ as a function of $V_{a,0}$ and $x_{ta,0}$

Appendix D

Moments and product of inertia and structural properties

The image plots for the dimensional values of the moments and product of inertia the structural properties \bar{c}_0 , b_0 and S_0 and the control positions or tether attachment points along Y_b and Z_b -axis are given as a function of V_a and x_{ta} . The values of J_{xy} and J_{yz} are zero due to the symmetric initial conditions. And $2y_{ta}$ is equal to $2y_{taR}$.

Moments and product of inertia

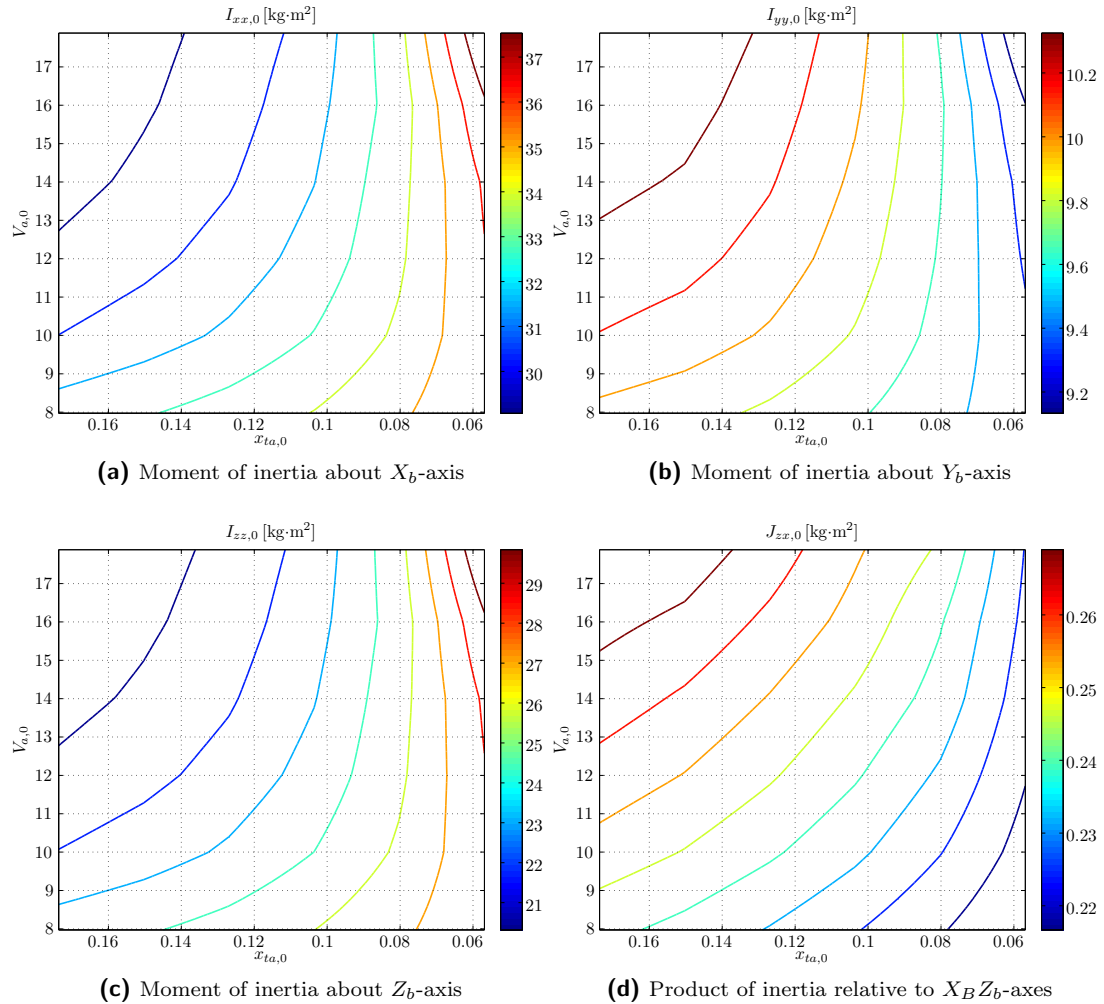


Figure D-1: Moments and product of inertia as a function of V_a and x_{ta}

Structural properties

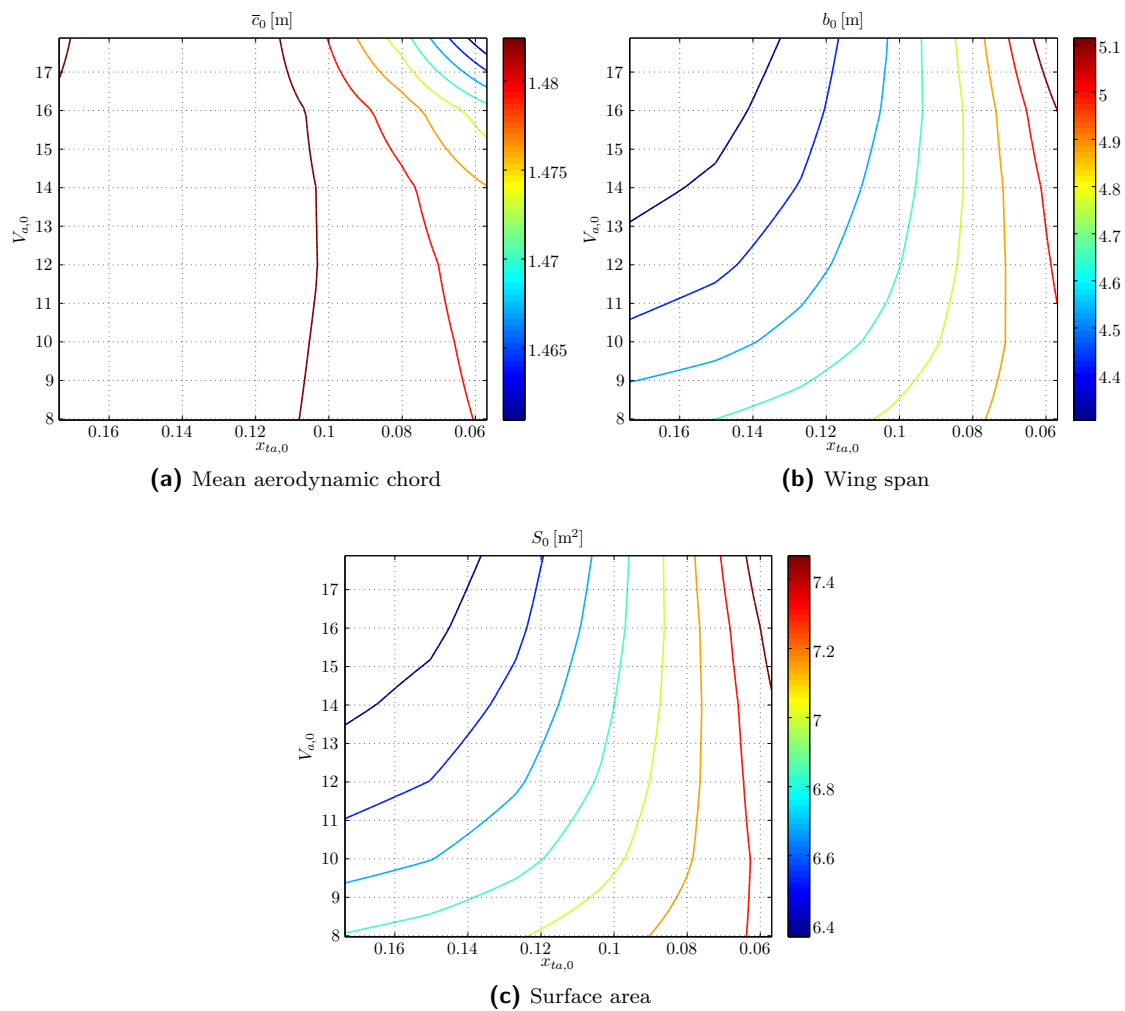


Figure D-2: Structural properties as a function of V_a and x_{ta}

Control positions

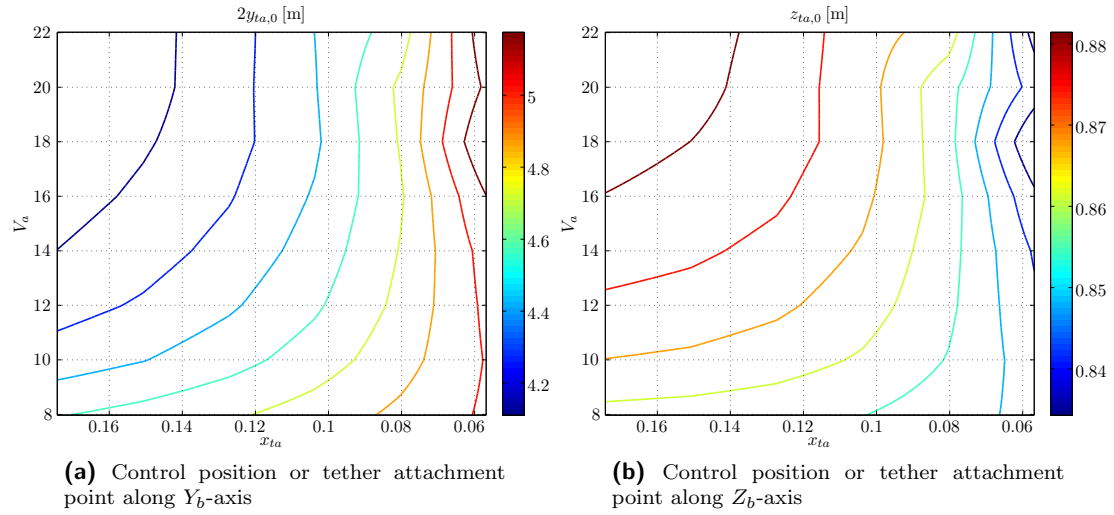


Figure D-3: Control positions as a function of V_a and x_{ta}

Appendix E

Response curves aircraft and Citation-Kite simulations

This appendix shows the response curves of the aircraft and Citation-Kite simulations for the verification of the Rigid Body Kite model as described in chapter 8.

E-1 Aircraft

Symmetric motions, phugoid responses

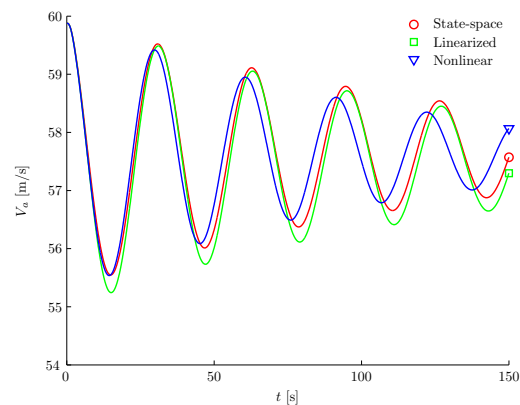


Figure E-1: V_a -response curve for a step elevator deflection ($\Delta\delta_e = -0.005$ rad) for Cessna Ce500 'Citation', phugoid

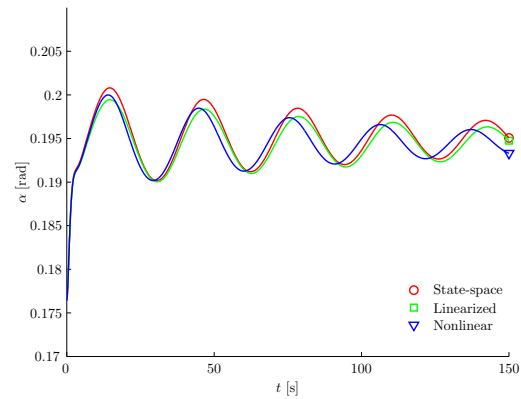


Figure E-2: α -response curve for a step elevator deflection ($\Delta\delta_e = -0.005$ rad) for Cessna Ce500 'Citation', phugoid

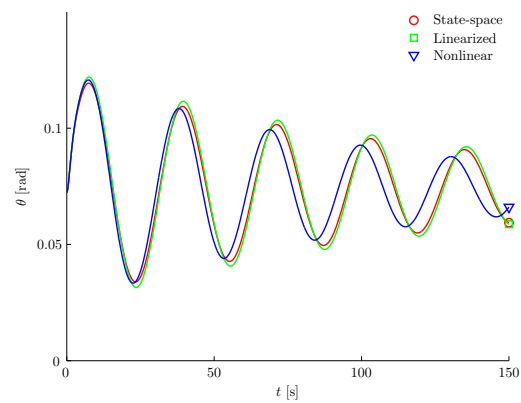


Figure E-3: θ -response curve for a step elevator deflection ($\Delta\delta_e = -0.005$ rad) for Cessna Ce500 'Citation', phugoid

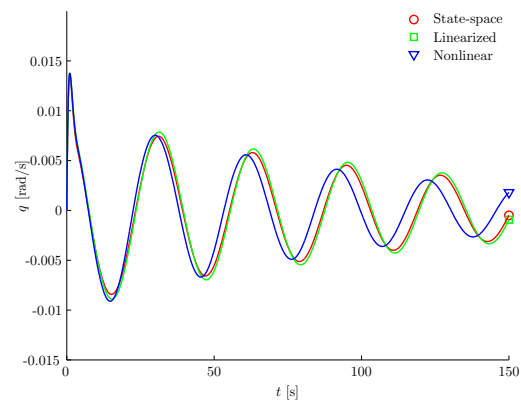


Figure E-4: q -response curve for a step elevator deflection ($\Delta\delta_e = -0.005$ rad) for Cessna Ce500 'Citation', phugoid

Symmetric motions, short period responses

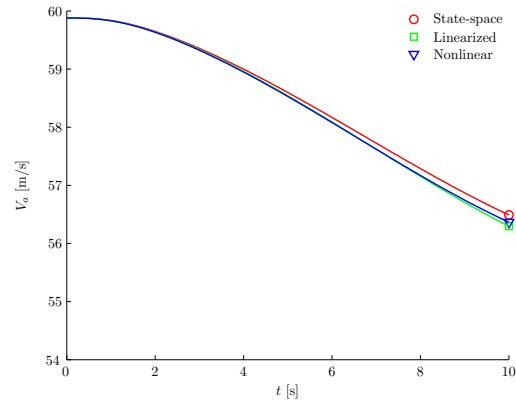


Figure E-5: V_a -response curve for a step elevator deflection ($\Delta\delta_e = -0.005$ rad) for Cessna Ce500 'Citation', short period

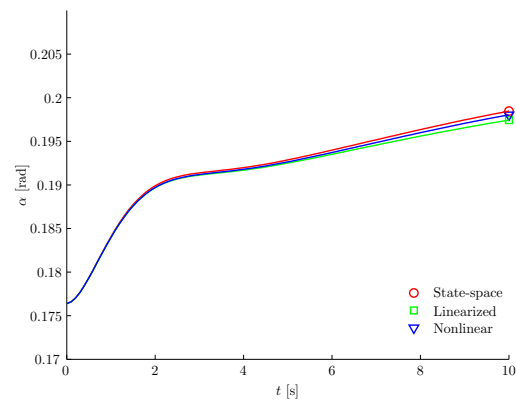


Figure E-6: α -response curve for a step elevator deflection ($\Delta\delta_e = -0.005$ rad) for Cessna Ce500 'Citation', short period

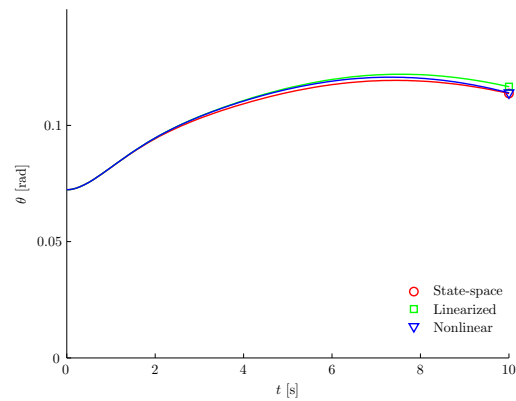


Figure E-7: θ -response curve for a step elevator deflection ($\Delta\delta_e = -0.005$ rad) for Cessna Ce500 'Citation', short period

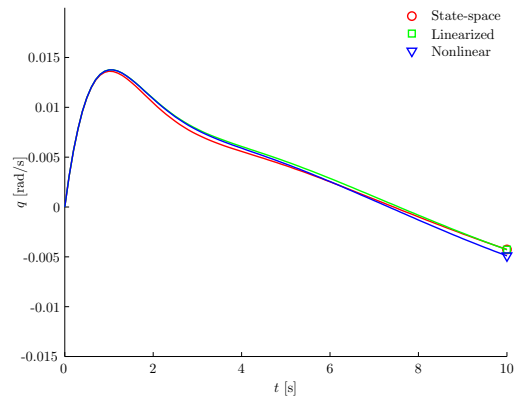


Figure E-8: q -response curve for a step elevator deflection ($\Delta\delta_e = -0.005$ rad) for Cessna Ce500 'Citation', short period

Asymmetric motions, rudder deflection

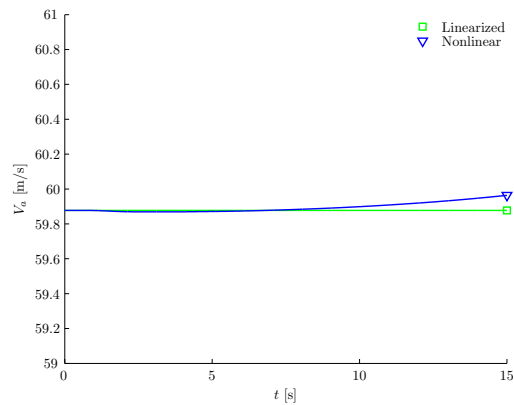


Figure E-9: V_a -response curve for a pulse rudder deflection ($\Delta\delta_r = 0.025$ rad during 1 s) for Cessna Ce500 'Citation'

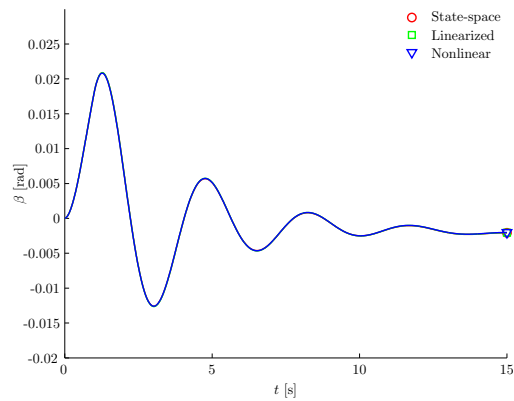


Figure E-10: β -response curve for a pulse rudder deflection ($\Delta\delta_r = 0.025$ rad during 1 s) for Cessna Ce500 'Citation'

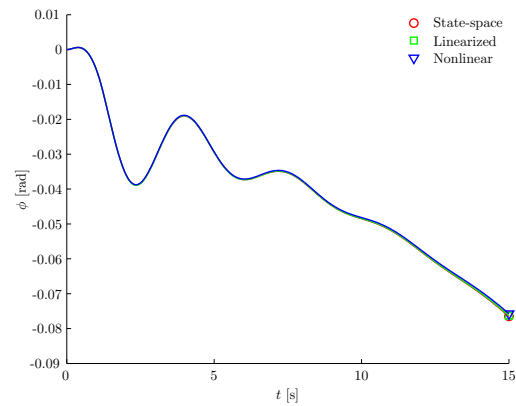


Figure E-11: ϕ -response curve for a pulse rudder deflection ($\Delta\delta_r = 0.025$ rad during 1 s) for Cessna Ce500 'Citation'

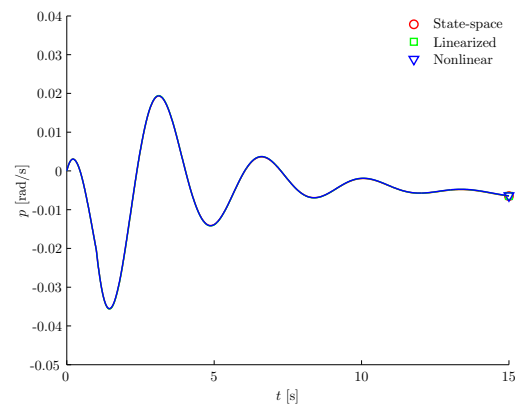


Figure E-12: p -response curve for a pulse rudder deflection ($\Delta\delta_r = 0.025$ rad during 1 s) for Cessna Ce500 'Citation'

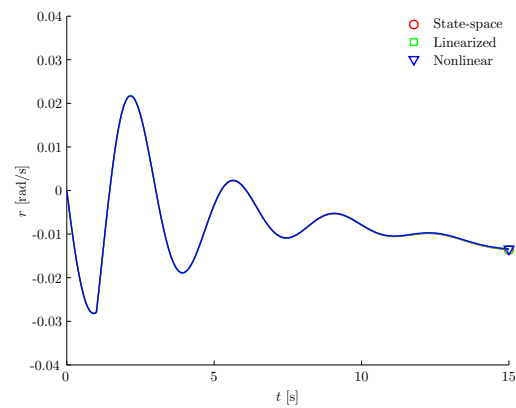


Figure E-13: r -response curve for a pulse rudder deflection ($\Delta\delta_r = 0.025$ rad during 1 s) for Cessna Ce500 'Citation'

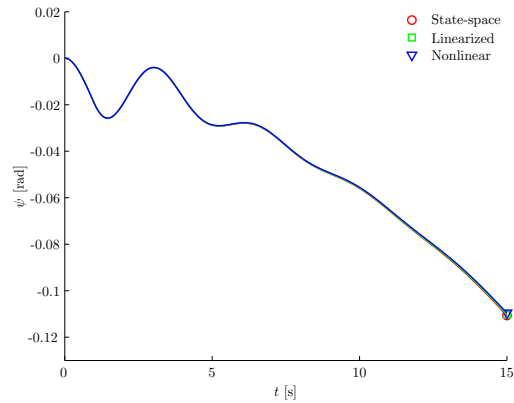


Figure E-14: ψ -response curve for a pulse rudder deflection ($\Delta\delta_r = 0.025$ rad during 1 s) for Cessna Ce500 'Citation'

Asymmetric motions, aileron deflection

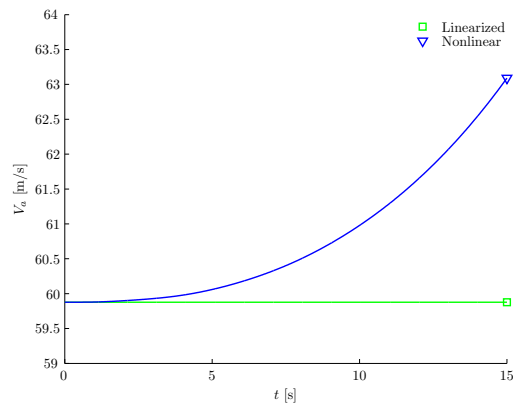


Figure E-15: V_a -response curve for a pulse aileron deflection ($\Delta\delta_a = 0.025$ rad during 1 s) for Cessna Ce500 'Citation'

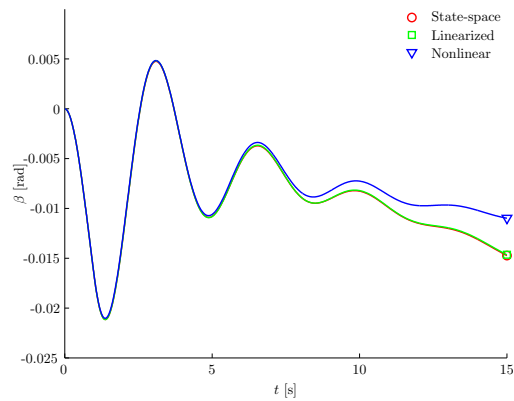


Figure E-16: β -response curve for a pulse aileron deflection ($\Delta\delta_a = 0.025$ rad during 1 s) for Cessna Ce500 'Citation'

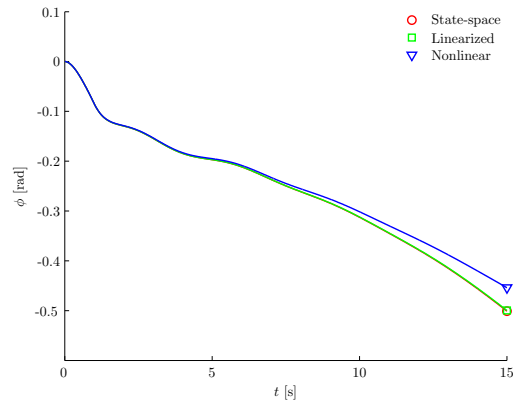


Figure E-17: ϕ -response curve for a pulse aileron deflection ($\Delta\delta_a = 0.025$ rad during 1 s) for Cessna Ce500 'Citation'

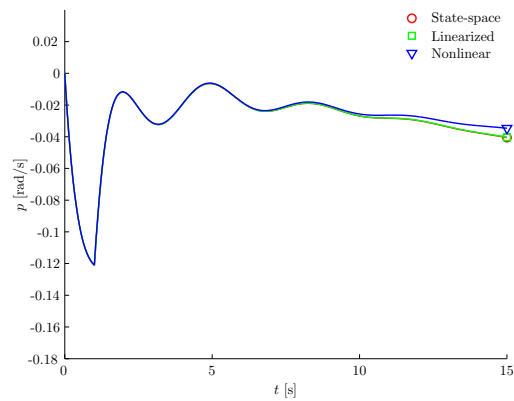


Figure E-18: p -response curve for a pulse aileron deflection ($\Delta\delta_a = 0.025$ rad during 1 s) for Cessna Ce500 'Citation'

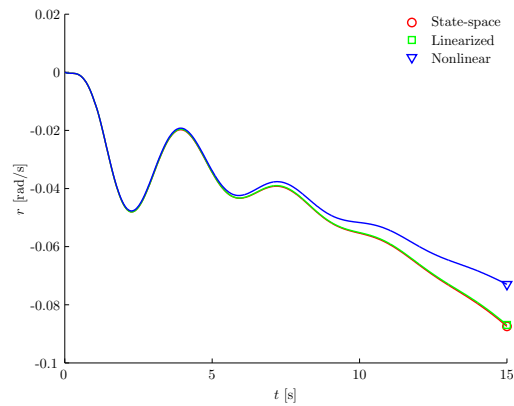


Figure E-19: r -response curve for a pulse aileron deflection ($\Delta\delta_a = 0.025$ rad during 1 s) for Cessna Ce500 'Citation'

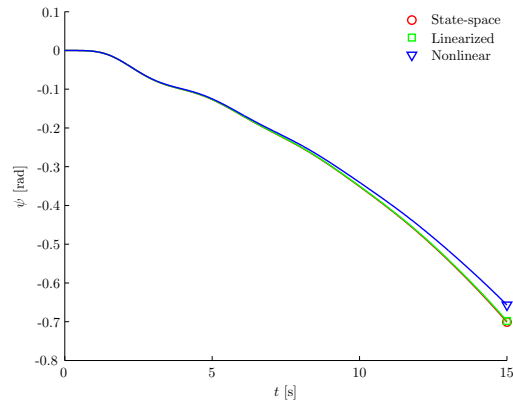


Figure E-20: ψ -response curve for a pulse aileron deflection ($\Delta\delta_a = 0.025$ rad during 1 s) for Cessna Ce500 'Citation'

E-2 Citation-Kite

The symmetric response curves give a comparison between the state-space, linearized and nonlinear model and are given for the six states in the state-space model: u_k , w_k , θ , q , θ_t and l_t . The pendulum motion as well as the short period motion are shown.

The asymmetric response curves give a comparison between the state-space, linearized and nonlinear model and are given for the six states in the state-space model and additionally β in the order: β , v_k , p , r , ϕ , ψ and ψ_t .

E-2-1 Symmetric motions, wind step input

Pendulum responses

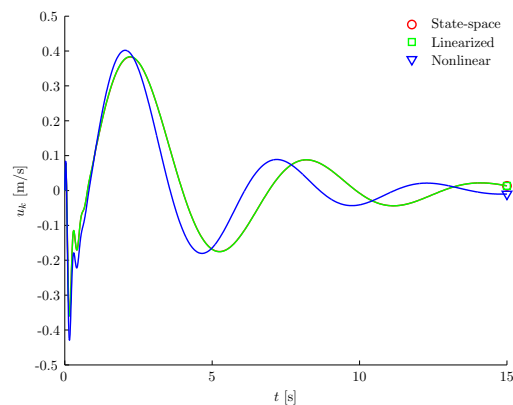


Figure E-21: u_k -response curve to a wind step input of $\Delta W_x = -10$ m/s of the 'Citation-Kite', pendulum motion

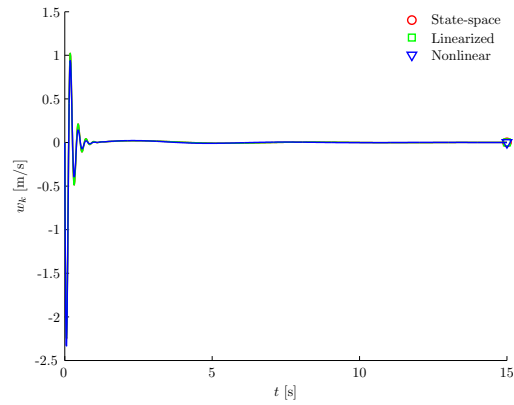


Figure E-22: w_k -response curve to a wind step input of $\Delta W_x = -10$ m/s of the 'Citation-Kite', pendulum motion

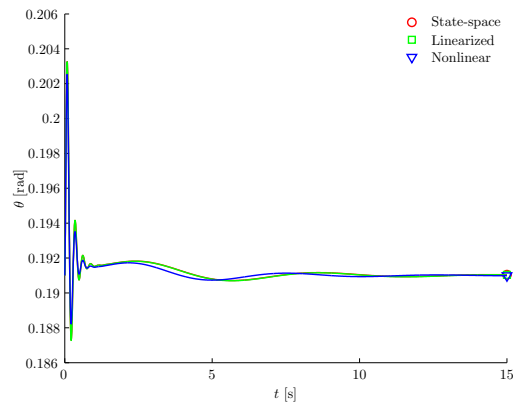


Figure E-23: θ -response curve to a wind step input of $\Delta W_x = -10$ m/s of the 'Citation-Kite', pendulum motion

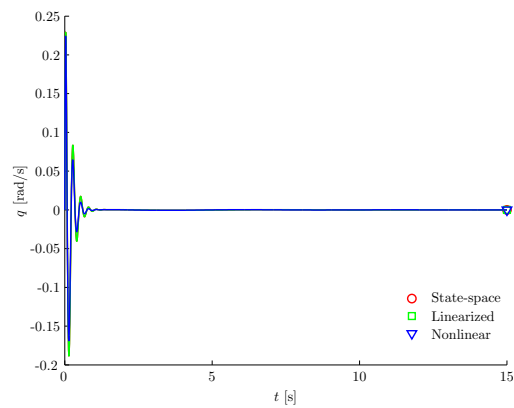


Figure E-24: q -response curve to a wind step input of $\Delta W_x = -10$ m/s of the 'Citation-Kite', pendulum motion

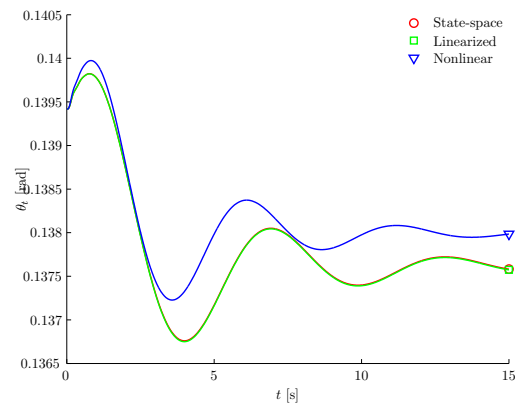


Figure E-25: θ_t -response curve to a wind step input of $\Delta W_x = -10$ m/s of the 'Citation-Kite', pendulum motion

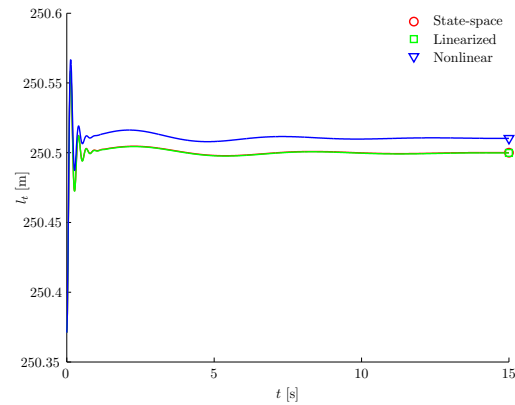


Figure E-26: l_t -response curve to a wind step input of $\Delta W_x = -10$ m/s of the 'Citation-Kite', pendulum motion

Short period responses

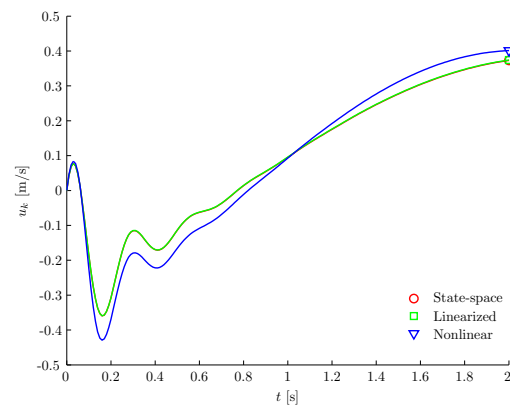


Figure E-27: u_k -response curve to a wind step input of $\Delta W_x = -10$ m/s of the 'Citation-Kite', short period motion

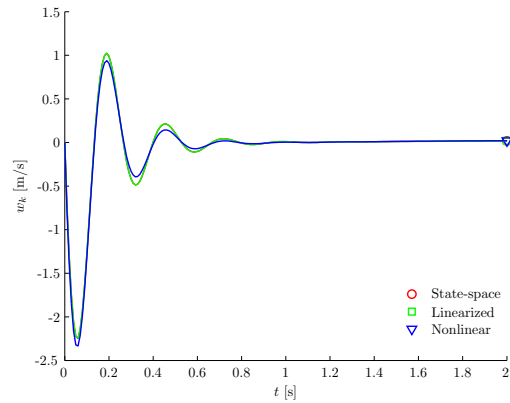


Figure E-28: w_k -response curve to a wind step input of $\Delta W_x = -10$ m/s of the 'Citation-Kite', short period motion

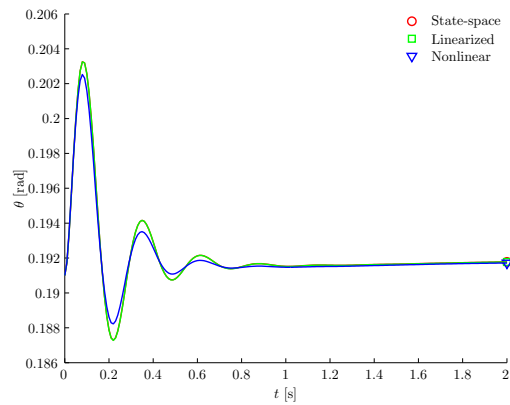


Figure E-29: θ -response curve to a wind step input of $\Delta W_x = -10$ m/s of the 'Citation-Kite', short period motion

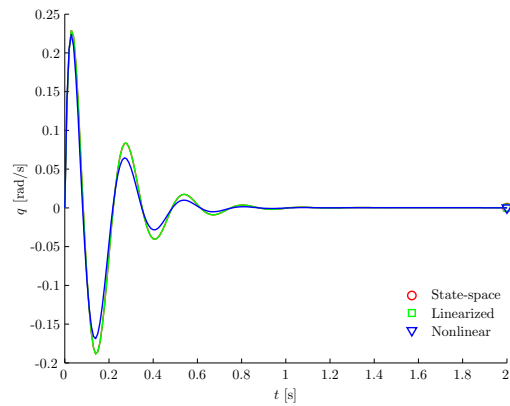


Figure E-30: q -response curve to a wind step input of $\Delta W_x = -10$ m/s of the 'Citation-Kite', short period motion

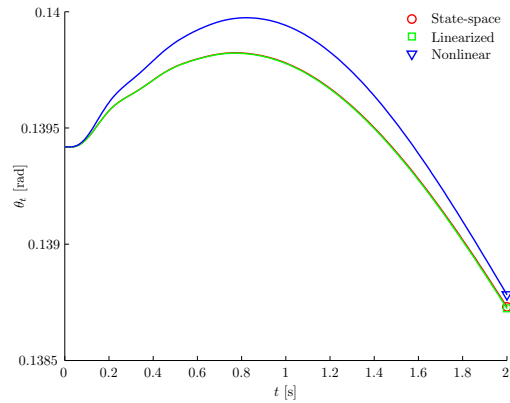


Figure E-31: θ_t -response curve to a wind step input of $\Delta W_x = -10$ m/s of the 'Citation-Kite', short period motion

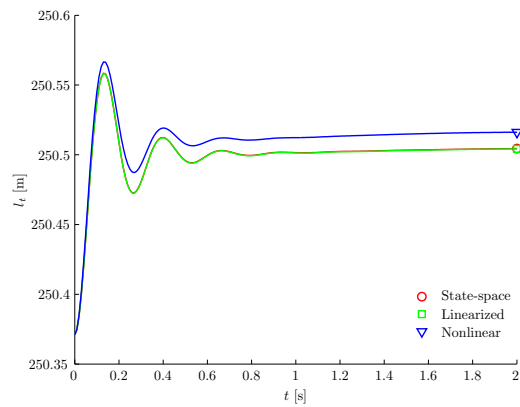


Figure E-32: l_t -response curve to a wind step input of $\Delta W_x = -10$ m/s of the 'Citation-Kite', short period motion

E-2-2 Symmetric motions, control step input

Pendulum responses

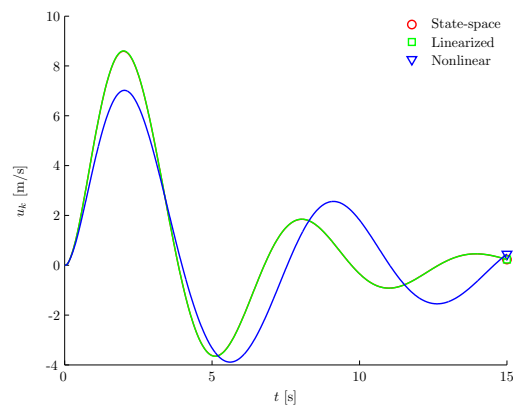


Figure E-33: u_k -response curve to a control step input of $\Delta x_{ta} = 0.05$ m of the 'Citation-Kite', pendulum motion

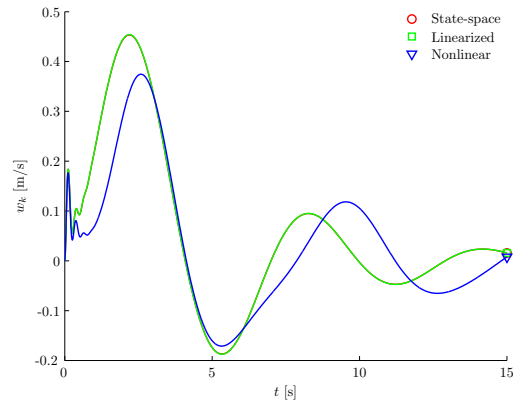


Figure E-34: w_k -response curve to a control step input of $\Delta x_{ta} = 0.05$ m of the 'Citation-Kite', pendulum motion

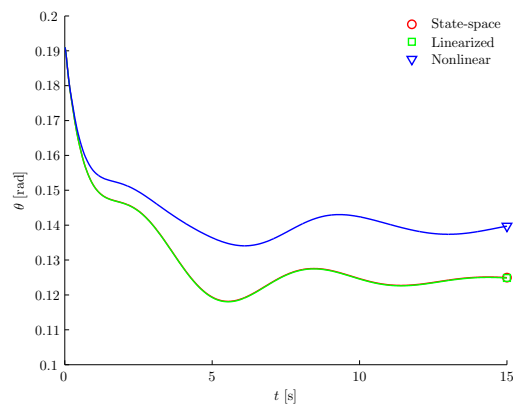


Figure E-35: θ -response curve to a control step input of $\Delta x_{ta} = 0.05$ m of the 'Citation-Kite', pendulum motion

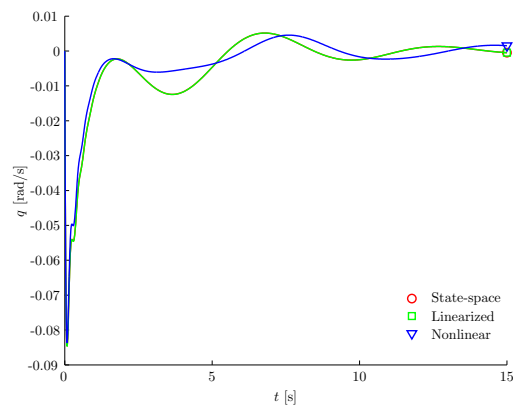


Figure E-36: \dot{q} -response curve to a control step input of $\Delta x_{ta} = 0.05$ m of the 'Citation-Kite', pendulum motion

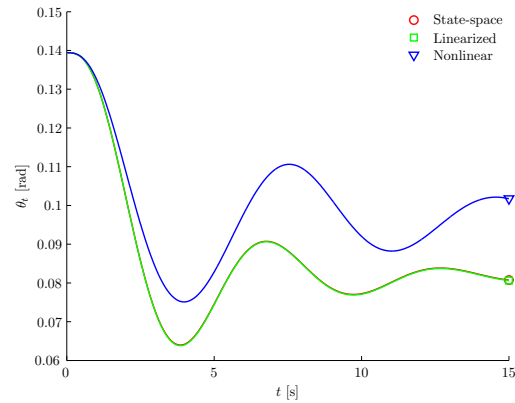


Figure E-37: θ_t -response curve to a control step input of $\Delta x_{ta} = 0.05$ m of the 'Citation-Kite', pendulum motion

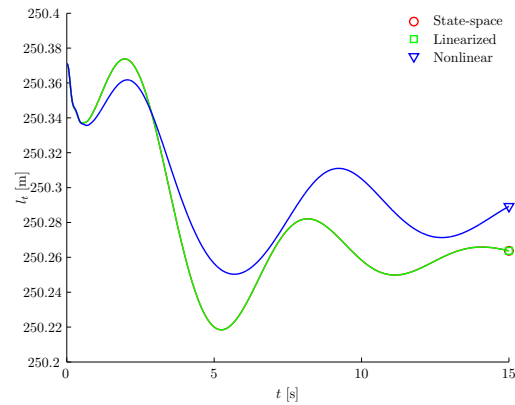


Figure E-38: l_t -response curve to a control step input of $\Delta x_{ta} = 0.05$ m of the 'Citation-Kite', pendulum motion

Short period responses

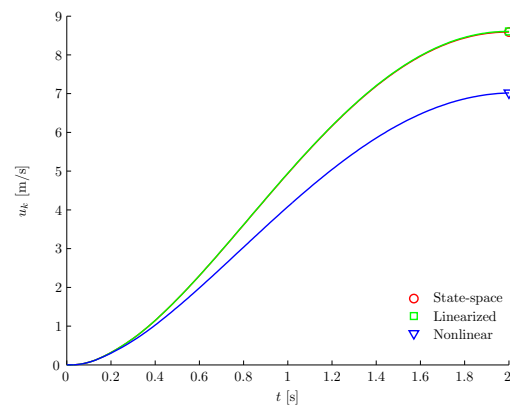


Figure E-39: u_k -response curve to a control step input of $\Delta x_{ta} = 0.05$ m of the 'Citation-Kite', short period motion

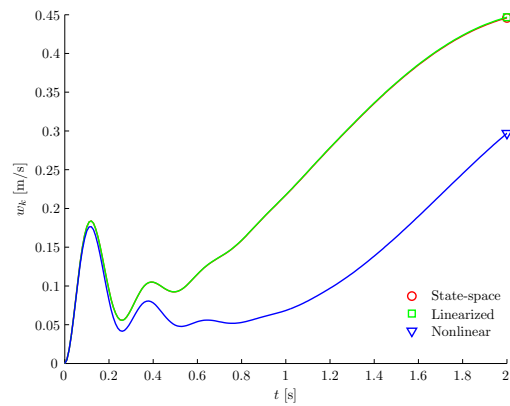


Figure E-40: w_k -response curve to a control step input of $\Delta x_{ta} = 0.05$ m of the 'Citation-Kite', short period motion

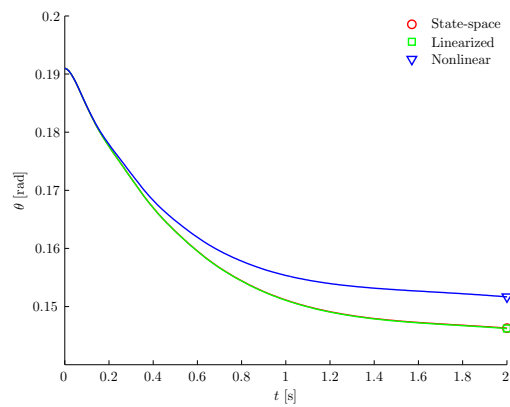


Figure E-41: θ -response curve to a control step input of $\Delta x_{ta} = 0.05$ m of the 'Citation-Kite', short period motion

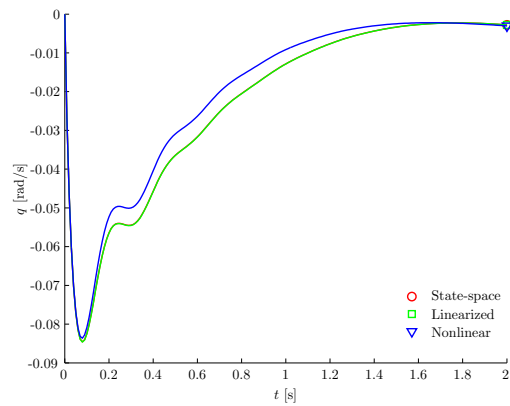


Figure E-42: q -response curve to a control step input of $\Delta x_{ta} = 0.05$ m of the 'Citation-Kite', short period motion

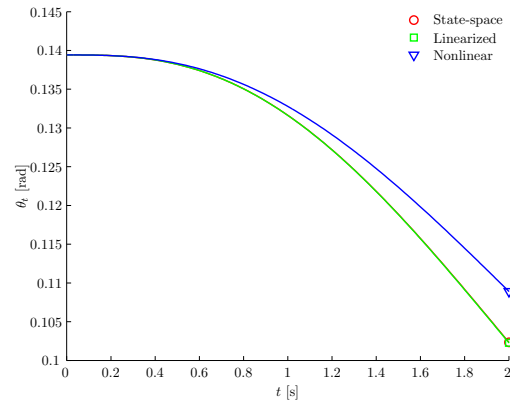


Figure E-43: θ_t -response curve to a control step input of $\Delta x_{ta} = 0.05$ m of the 'Citation-Kite', short period motion

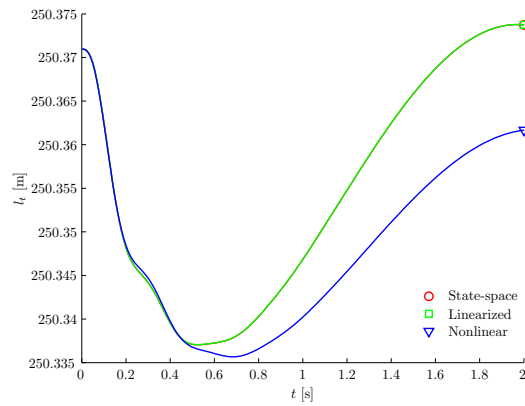


Figure E-44: l_t -response curve to a control step input of $\Delta x_{ta} = 0.05$ m of the 'Citation-Kite', short period motion

E-2-3 Asymmetric motions, lateral wind step input

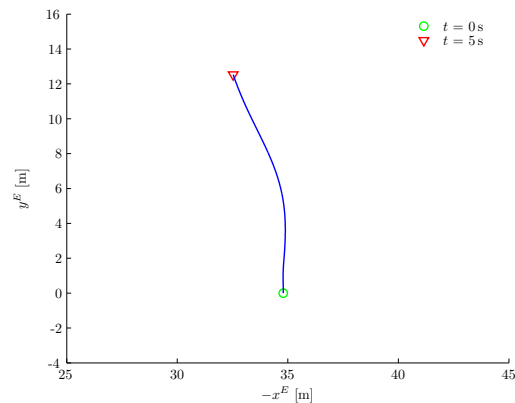


Figure E-45: Path in $X_E Y_E$ -plane to a wind step input of $\Delta W_y = 15$ m/s of the 'Citation-Kite', nonlinear simulation

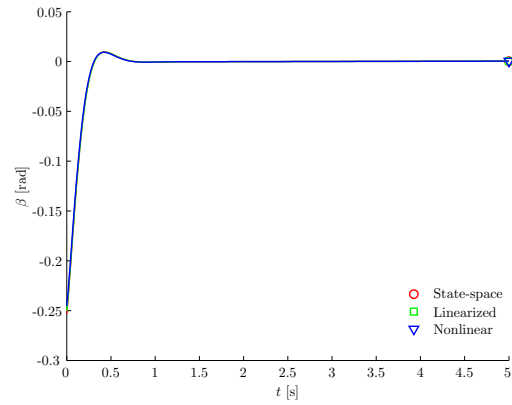


Figure E-46: β -response curve to a wind step input of $\Delta W_y = 15$ m/s of the 'Citation-Kite'

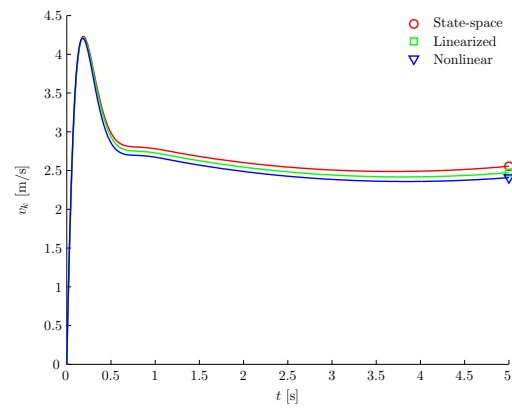


Figure E-47: v_k -response curve to a wind step input of $\Delta W_y = 15$ m/s of the 'Citation-Kite'

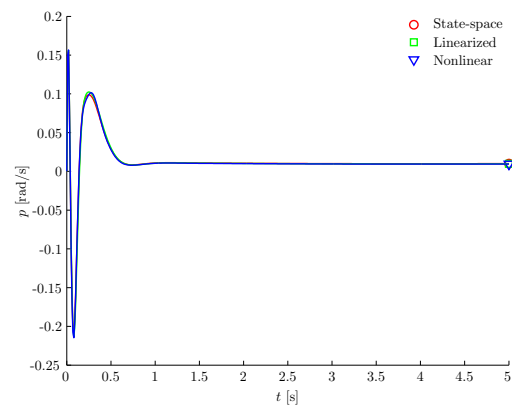


Figure E-48: p -response curve to a wind step input of $\Delta W_y = 15$ m/s of the 'Citation-Kite'

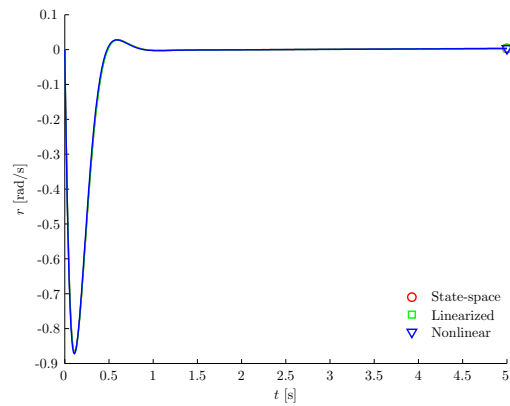


Figure E-49: r -response curve to a wind step input of $\Delta W_y = 15$ m/s of the 'Citation-Kite'

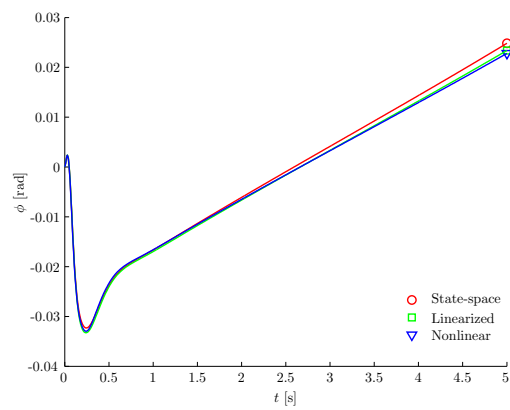


Figure E-50: ϕ -response curve to a wind step input of $\Delta W_y = 15$ m/s of the 'Citation-Kite'

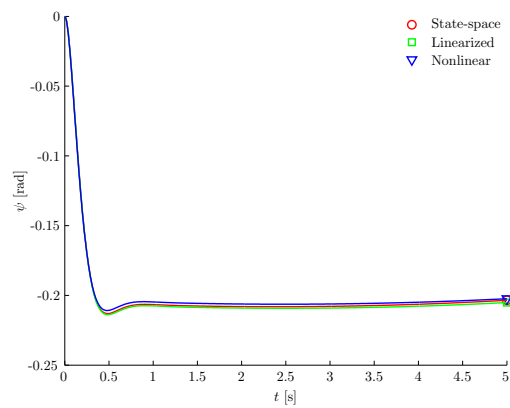


Figure E-51: ψ -response curve to a wind step input of $\Delta W_y = 15$ m/s of the 'Citation-Kite'

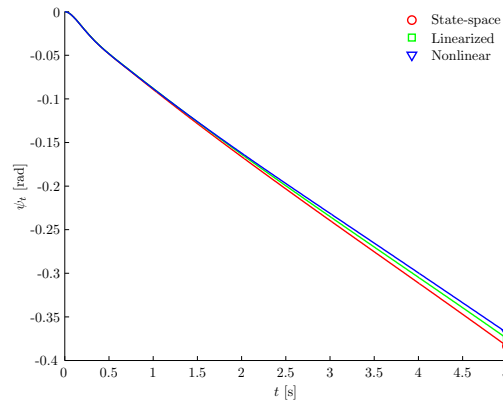


Figure E-52: ψ_t -response curve to a wind step input of $\Delta W_y = 15$ m/s of the 'Citation-Kite'

E-2-4 Asymmetric motions, asymmetric control step input

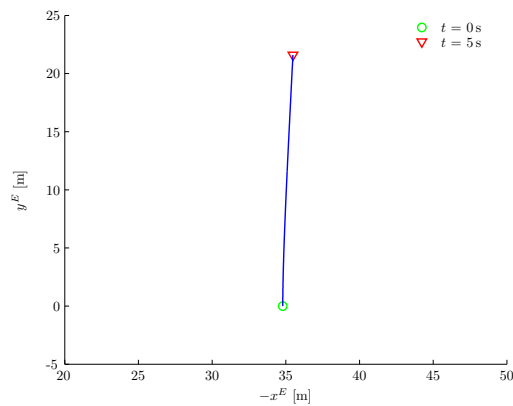


Figure E-53: Path in $X_E Y_E$ -plane to a control step input of $\Delta x_{ta}^L = 0.05$ m and $\Delta x_{ta}^R = -0.05$ m simultaneously of the 'Citation-Kite', nonlinear simulation

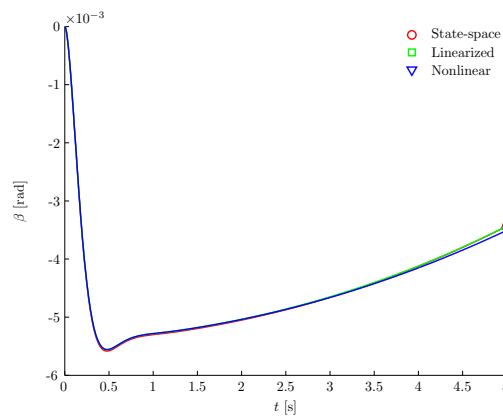


Figure E-54: β -response curve to a control step input of $\Delta x_{ta}^L = 0.05$ m and $\Delta x_{ta}^R = -0.05$ m simultaneously of the 'Citation-Kite'

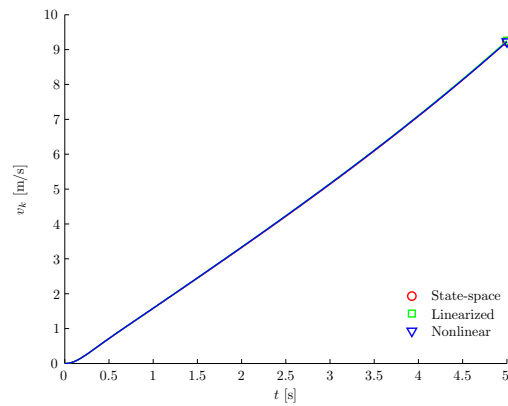


Figure E-55: v_k -response curve to a control step input of $\Delta x_{ta}^L = 0.05$ m and $\Delta x_{ta}^R = -0.05$ m simultaneously of the 'Citation-Kite'

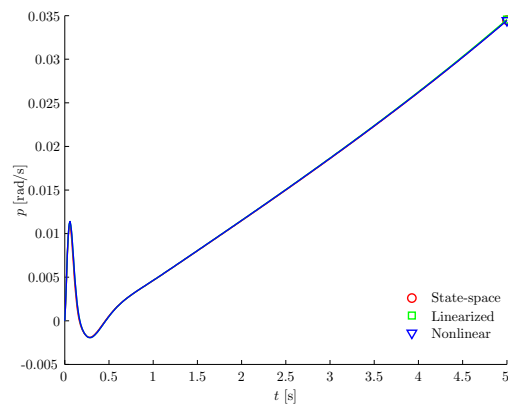


Figure E-56: p -response curve to a control step input of $\Delta x_{ta}^L = 0.05$ m and $\Delta x_{ta}^R = -0.05$ m simultaneously of the 'Citation-Kite'

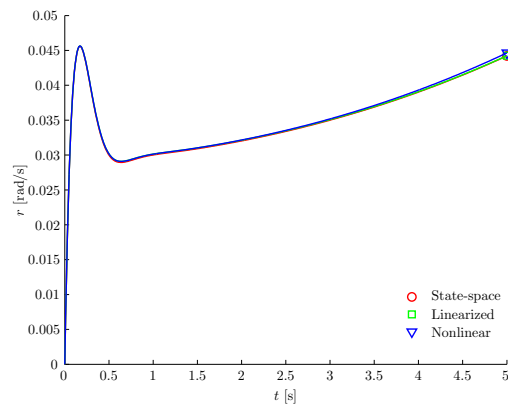


Figure E-57: r -response curve to a control step input of $\Delta x_{ta}^L = 0.05$ m and $\Delta x_{ta}^R = -0.05$ m simultaneously of the 'Citation-Kite'

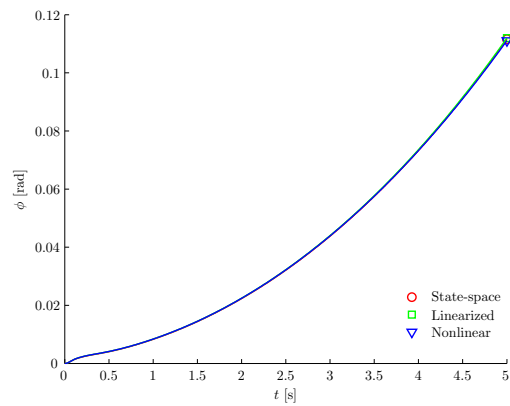


Figure E-58: ϕ -response curve to a control step input of $\Delta x_{ta}^L = 0.05$ m and $\Delta x_{ta}^R = -0.05$ m simultaneously of the 'Citation-Kite'

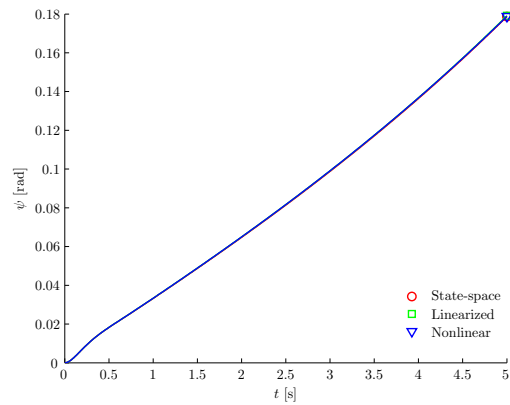


Figure E-59: ψ -response curve to a control step input of $\Delta x_{ta}^L = 0.05$ m and $\Delta x_{ta}^R = -0.05$ m simultaneously of the 'Citation-Kite'

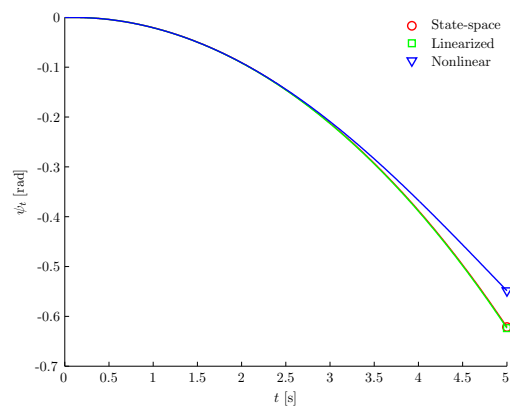


Figure E-60: ψ_t -response curve to a control step input of $\Delta x_{ta}^L = 0.05$ m and $\Delta x_{ta}^R = -0.05$ m simultaneously of the 'Citation-Kite'